STRONG MICROWAVES IN PLASMAS

1993

Volume 1

Institute of Applied Physics
Nizhny Novgorod

RUSSIAN ACADEMY OF SCIENCES
INSTITUTE OF APPLIED PHYSICS

STRONG MICROWAVES IN PLASMAS

PROCEEDINGS
OF THE INTERNATIONAL WORKSHOP
Moscow – Nizhny Novgorod – Moscow,
15 – 22 August 1993

Edited by
A.G. Litvak

In two volumes
Volume 1

Nizhny Novgorod – 1994

Printed in Russia,
Publishing-house «Chuvashia»
Ivan Jakovlev prospekt, 13, 428019 Cheboksary

ISBN 5-201-09298-5

Editor's Preface

This book is the collection of invited lectures and some interesting contributions made at the Second International Workshop on Strong Microwaves in Plasmas. The First Workshop was organized by the Institute of Applied Physics, Russian Academy of Sciences (Nizhny Novgorod) and held in Suzdal (Russia) in September 1990. Its aim was to bring together the researchers who develop powerful microwave sources and deal with applications of strong microwaves in plasma for heating and generation of currents in fusion set-ups, for basic investigations of nonlinear processes in plasmas, for studies of the freely localized gas discharge in microwave beams with a number of industrial applications, etc. Leading laboratories of all the world were represented at the First Workshop, therefore its scientific significance was high, and the Reader can judge about that from the published Proceedings. A specific feature of that Workshop was participation of a great number of researchers from the leading FSU laboratories including young scientists who reached the world level in this field, but had rather limited possibilities for international contacts. The Suzdal Workshop proved to be very useful for scientific collaboration between a number of Russian and foreign laboratories, and promoted, specifically, access of Russian gyrotrons to the foreign market. The explicit success of the Suzdal Workshop called for further meetings. We decided that the next workshop would be held in three years—this interval seems optimal for accumulation of research material that is to be generalized and categorized.

The II International Workshop on Strong Microwaves in Plasmas was held on August 15-22 on board the "Feliks Dzerzhinsky" river boat that cruised from Moscow to Nizhny Novgorod and back. Recently river boats have been quite often used for scientific

conferences in Russia. Experience of our Workshop proves that the idea is fruitful. The participants were confined within a "closed" space of the ship, and that greatly extended their communication beyond the scope of the official sessions, and stimulated further discussions and personal scientific contacts. Along with high scientific efficiency, the Workshop resulted in most pleasant memories of the participants about the sight-seeing in historical towns of Russia, about the magnificent landscape of middle Russia seen from the board of a comfortable ship, about the evening concerts performed by invited musicians and actors well-known in Russia. All that made the Workshop unforgettable for the participants and their families.

The Workshop brought together 179 participants from 13 countries. Plenary sessions in the mornings, and sessions of 4 sections in the afternoons excluded the necessity of poster papers. All in all, the Workshop participants listened to 117 communications, and 41 of them were invited. The topics of the contributions, as at the First Workshop, mainly focused on the problems of developing new sources of powerful microwaves and their plasma applications. Along with this, some new tendencies were revealed, which go beyond the framework of the plasma research area. Specifically, invited speakers discussed the problems of using strong microwaves for new radar and information systems, for material processing, and, in particular, new techniques for advanced material production, for example, production of advanced ceramic materials, for atmosphere purification of human-origin hazardous admixtures, etc. Great interest towards these problems can result in future in certain transformation and widening of the scope of our Workshop, if it becomes traditional.

We hope that the materials about the state-of-the-art of the study on powerful coherent sources of microwaves and interaction of strong electromagnetic waves with plasma will be useful for the Reader who is interested in this research area.

A.G. Litvak

CREATION AND HEATING OF PLASMA BY MICROWAVES IN FUSION DEVICES

HIGH POWER LOWER HYBRID CURRENT DRIVE ON JET: RESULTS AND PROSPECTS

C. Gormezano, Y Baranov, M Brusati, J Dobbing, A Ekedahl, P Froissard, A Kaye, M Lennholm, F Rimini, P Schild, J Jacquinot and F Söldner

JET Joint Undertaking, Abingdon, Oxfordshire, OX14 3EA, UK

JET has successfully developed high power auxiliary systems: the Neutral Beam Injectors (NBI), the Ion Cyclotron Resonance Frequency (ICRF) waves and the Lower Hybrid Current Drive (LHCD) system [1]. The LHCD system has been the latest system developed and only a prototype system has been tested. This method is aimed at the control of the plasma current profile by driving a significant part of the plasma current alone or in combination with the other two additional heating methods.

The frequency of the LHCD system has been chosen to be 3.7 GHz both for technical and scientific reasons. Such a frequency belongs to the so called "microwave" domain. This paper will concentrate mainly on the description of the achieved results and on the prospects of LHCD on JET in accordance with the main topic of the workshop.

The paper will be organised as follows:

- description of the technical features of the JET prototype system;
- achieved results and main physics output. In particular the "synergistic" effects between Lower Hybrid waves and Ion Cyclotron waves will be summarised;
- description and status of the full LHCD system;
- prospects for the use of LHCD on JET for the next campaign and some considerations on the long-term aspects of Lower Hybrid Current Drive on a reactor.

1. The JET LHCD Prototype System

The characteristics of the prototype system have been described elsewhere [2] and are summarised in Table 1. The choice of the frequency (3.7 GHz) takes advantage of the technical developments made previously for Tore Supra [3] and

TABLE 1: LHCD Prototype (full system in brackets)

Frequency	3.7 GHz
Number of klystrons	8, (24)
Power (generator)	
10s pulse	4.8 MW
20s pulse	4 MW (12 MW)
Duty cycle	1/30
Efficiency	42%
Phase control	10 degrees accuracy
Maximum VSWR	1.8
Length of transmission line	40 m
Estimated insertion losses	1 dB
Number of waveguides	128, (384)
Waveguide material	stainless steel and ZiCo (stainless steel)
Coating	copper + carbon, (copper)
Maximum temperature	350°C
Total weight	12 tons (15)
Stroke	210 mm
Response	12 mm/15 ms
Maximum coupled power	2.4 MW

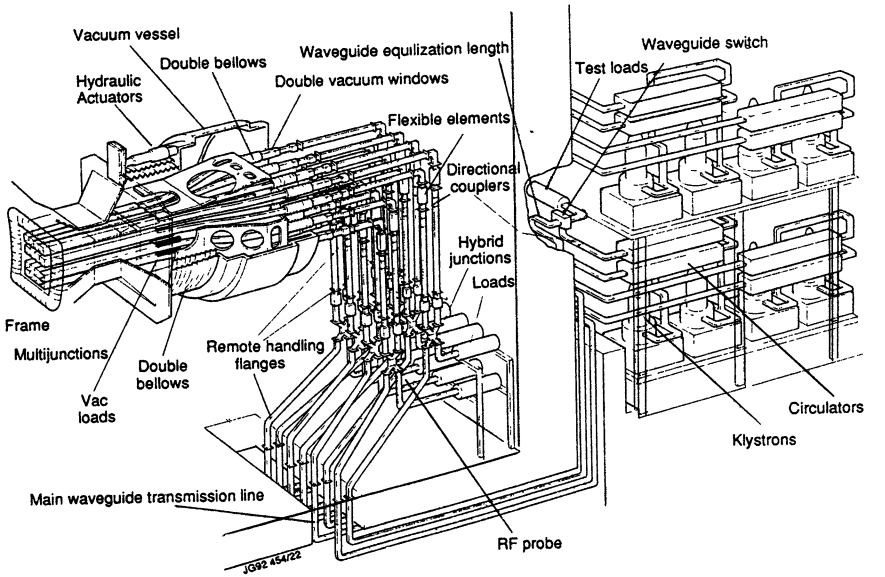

Fig.1 Schematic diagram of the LHCD prototype system

allows the wave to penetrate to the plasma centre for central densities up to $3\ 10^{19}\ m^{-3}$. The prototype system consists of 8 klystrons. The power generated by each klystron is split via one hybrid junction and 2 multi-junctions into 16 waveguides at the grill mouth as sketched in fig 1. The generation of a well defined and well controlled wave spectrum with a high directivity is essential for current drive applications. Therefore particular emphasis has been put on the control of the phase in each waveguide. The whole design of the JET LHCD system has been dictated by the constraints imposed by JET:

- no electronics in the torus hall;
- double tritium barrier;
- remote handling of sensitive parts;
- high degree of reliability;
- maximum automation of the control.

For instance the control of phase and amplitude has to be made far away from the torus (50m). Consequently, an accuracy of 10° in the phase control has only been achieved via a very tight control of mechanical dimensions of the splitting network and a sophisticated feedback control of the phase at the output of each klystron [4].

The resulting wave spectrum, as shown in fig 2, is centred at $N_{//} = 1.8$ with a width of $\Delta N_{//} = \pm 0.23$. The central value of the wave spectrum can be varied from 1.4 to 2.3 by varying the phasing between the multi-junctions from -90° to +90 °.

Eight of the multi-junctions were designed specifically for JET and are known as LOP (Launcher Zero, Physics) while the others were provided by CEN Cadarache using the same design as TORE SUPRA and are known as LOC (Launcher Zero, Cadarache). LOP is made of copper plated stainless steel, whereas LOC is made of zirconium copper. Both sets of multi-junctions were coated with a carbon anti-multipactor layer. They were also coated with a beryllium layer from the JET torus evaporators situated next to the launcher.

Operation with the JET machine started in June 1990 for an initial campaign of five months followed by a seven month machine shutdown to change a toroidal field coil. Operation resumed in June 1991. The second campaign ended in February 1992 with a shutdown to install the JET divertor coils. A total of 1700 pulses were achieved with JET plasmas during the two campaigns. Between campaigns the multi-junctions were inspected and found to be in generally good condition except for some flaking of the carbon anti-multipactor layer. The LHCD system operated on about 50% of all available plasma pulses.

Where operation was not possible it was usually due to the plasma conditions being unsuitable rather than equipment failure.

During the first campaign power levels were mostly below 200 kW per klystron. The multi-junctions did not loose conditioning during the seven month shutdown between campaigns. At the start of the second campaign power levels increased slowly but steadily as the multi-junctions conditioned. During the second campaign two uncontrolled air leaks occurred on the torus while it was at its operating temperature of 350°C. These had a serious effect on LOC which was unable to recover its output power level. LOP on the other hand recovered with only minor reconditioning and went on to reach the maximum klystron power (650 KW) on some multi-junctions at the end of the campaign. This long conditioning time is attributed to the lack of proper baking, which is the only way for proper conditioning of the vacuum waveguides.

The achieved generator power on LOP was 2.05 MW compared with an installed capability of 2.4 MW with 1.75MW coupled to the plasma. LOC managed 1.5 MW generator power with 1.2 MW coupled to the plasma prior to the air leaks but only achieved 600 KW generator power after the air leaks.
Coupling of the launcher has been studied in a variety of plasma configurations including limiter and double null X-point plasmas (L-mode and H-mode) with different launcher positions. Coupling of Lower Hybrid Waves is a direct function of the density at the grill mouth. This density in turn depends upon the connection length of the magnetic field line, $L_{//}$, near the launcher. The relevant coupling parameter is $d / L_{//}^{\frac{1}{2}}$ where d is the radial distance between the last close magnetic surface and the grill mouth. As shown in fig 3 there is a very good agreement with a detailed coupling theory [5].

In order to maintain a good coupling, which was required to achieve good power handling, the LH launcher is moveable by means of hydraulic actuators and flexible waveguides. The launcher can be moved during shots, following a preset position waveform or via a feedback control system, which adjusts the launcher position in order to maintain a requested power reflection coefficient for LOP. The position control with a preset position waveform was used during the 7MA shots in JET, where LH power was applied during the ramp up of the plasma current in order to save flux from the ohmic transformer. As the plasma elongation increased, the plasma edge moved inwards and the launcher was requested to follow the plasma movement by moving from 3mm behind the ICRH antennae to 25mm in front of the antennae with a speed of 10mm/s (fig 4).

The use of the feedback control system for the launcher position is exemplified in fig 5. The requested reflection coefficient for LOP was set to 10% in order to avoid trips due to the proximity to the plasma, especially for LOC. The feedback system was allowed to adjust the position within ±3mm from the preset position waveform, which in this case was constant, 4mm behind the ICRH antennae. The position of the plasma was constant, but as the electron density increased the reflection coefficient tends to decrease and as a result the launcher moved outwards.[6,7].

2. PHYSICS RESULTS

Although limited to 2.4 MW of coupled power, operation of the prototype launcher has brought a large amount of physics data reported in several conferences. In particular, the LHCD system has been used as a tool for several applications such as

- obtaining a one minute pulse duration discharge at 2MA where the application of 1MW of LH power for 50 sec has been instrumental in achieving these long pulses [8].

- Flux saving of 2V/s from the application of 1.5 MW of LH power during the low density current ramp-up phase of 7 MA limiter plasmas [9], allowing extension of the current flat top by 2 sec to a total duration of 9 sec.

Full current drive data and synergystic effects between Lower Hybrid and Ion cyclotron waves have been specifically studied [10,11,12]. Full non inductive sustainment of the current has been achieved up to:

- 0.4 MA with LH only;
- 1.5 MA for 6 sec and 2 MA for 1.5 sec in ICRF heated limiter plasmas.

Full current drive has been achieved in conditions where the LH waves can propagate to the plasma centre i.e. with the highest magnetic field (3.4 T) and central density lower than 3 $10^{19} m^{-3}$, as anticipated from theoretical considerations.

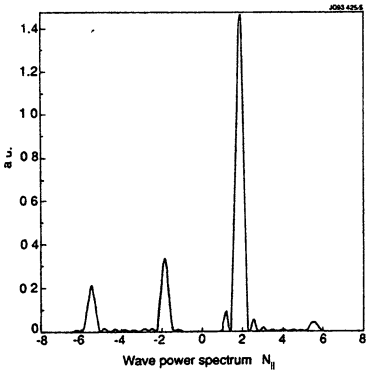

Fig.2: Wave spectrum of the Prototype Launcher

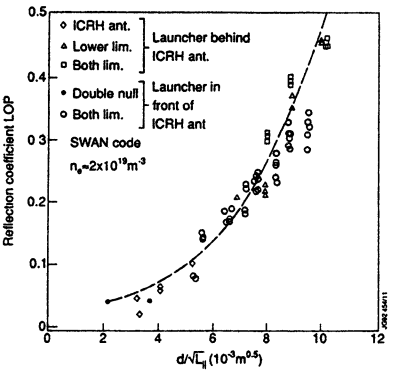

Fig.3: Reflection coefficient versus $dL_{//}^{-0.5}$ and comparison with the SWAN coupling code

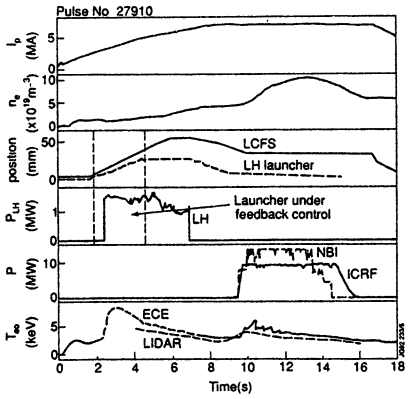

Fig.4: Combined operations of LHCD, ICRH and NBI during the long 7MA discharge.

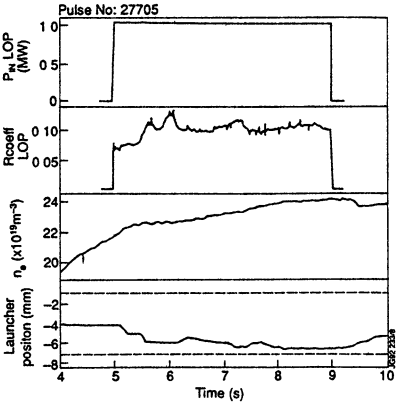

Fig. 5: Feedback control system for the launcher position - the reflection coefficient was set at 10%

In fig 6, LHCD power is applied after ramping down the plasma current from 3 to 1.5 MA in order to achieve a target plasma with higher internal inductance, ℓ_i, and more peaked electron temperature. During LHCD, the loop voltage is negative and ℓ_i is roughly constant or even increases. In addition, a reversal of the sign of the derivative of the primary current is observed indicating that some magnetic energy is supplied both to the plasma and to the transformer. The radial profile of the X-ray emissivity induced by fast electrons is very similar to the plasma current profile as determined from a combination of magnetic analysis and polarimetry measurements and no transients in loop voltage are observed.

In similar conditions, a 2 MA plasma is sustained with zero resistive loop voltage, no driving flux from the primary and constant plasma energy with 2 MW of LH power for about 1.5 second. This time duration is limited by density increase and by trips in the LHCD system.

The time duration of full LHCD current drive is limited by the toroidal field plateau available on JET at high magnetic field (8s). A maximum time of 6s at 1.5 MA with zero resistive loop voltage has been achieved [8]. This limited duration prevents the study of current diffusion.

An example of full current drive in combined LHCD and ICRF heated plasma in an X-point configuration is shown in fig. 7. Throughout all the ELMY phase of the H-mode, the loop voltage is zero, ℓ_i is constant and no primary flux is consumed. The central density reaches 3.6 10^{19} m^{-3} and the poloidal beta a value of 0.74 with a corresponding bootstrap current estimated to be about 40% of the total current. Quasi-stationary conditions are maintained up to the onset of the ELM-free H-mode phase where the density increases.

In some combined ICRF LHCD discharges, synergy between the two waves was quite apparent. The "signature" for such synergy is an acceleration of fast electrons in excess of the 1 MeV range, well above the expected range of acceleration in conditions where the full current was driven by the LH wave field in the absence of ohmic electric field. In these conditions, the total amount of driven current was above the values anticipated from theoretical considerations.

A 19 channel hard X-ray camera is the main tool for estimating the radial electron distribution. As shown in fig 8, photon energy distributions are given for two shots with full current drive with and without ICRF. This acceleration of electrons, in the presence of ICRF, beyond the domain of velocities corresponding to the LHCD parallel wave spectrum (100 keV), in the absence of

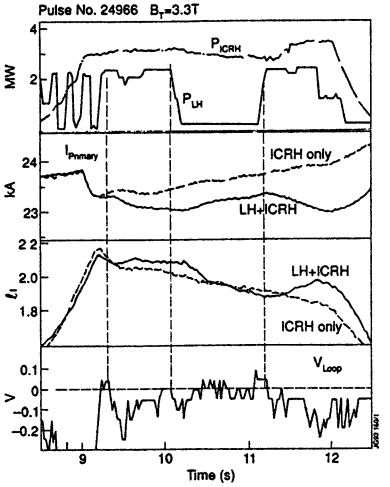

Fig.6: Full Current Drive in 1.5 MA limiter plasma

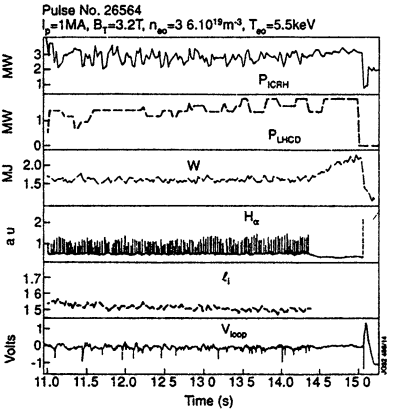

Fig.7: Full Current Drive in 1 MA H-mode plasma

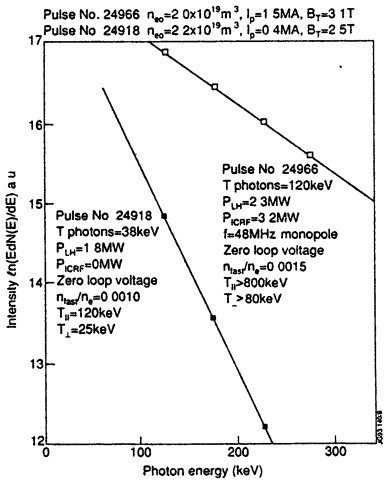

Fig.8 : Photon temperature at zero loop voltage with and without ICRF.

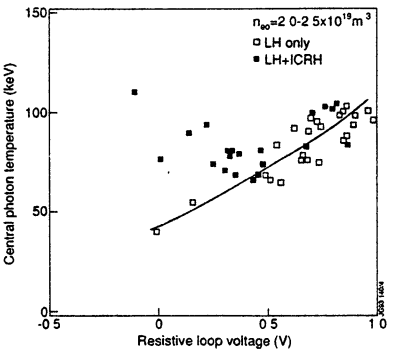

Fig. 9: Central photon temperature versus resistive loop voltage

electric field is the "signature" of the synergism which is described in this paper. As shown in fig 9, high photon temperatures can be achieved when the loop voltage is not zero, as anticipated from electric field acceleration.

This synergism is further confirmed by calculations carried out with an LHCD numerical simulation code [13]. The physics of Lower Hybrid waves is modelled via a ray-trajectory method, with the dispersion relation including both the electromagnetic part and thermal corrections. The electron distribution function is calculated by the two-dimensional relativistic Fokker-Planck equation, taking into account effects due to spatial fast electron diffusion and the residual toroidal electric field. In this model, the diffusion of fast electrons is due to the stochasticity of the magnetic field. Typical values of the diffusion coefficient are 0.5 m^2/s for thermal electrons and 1.5 m^2/s for 100 keV electrons. The output of the code is then used to simulate the hard X-ray spectrum emitted by the suprathermal population and compared with the output of the FEB camera. In fig 10a the results are shown for 4 different pulses: LHCD only at zero loop voltage, LHCD only at moderate power with residual electric field, LHCD only at high electron temperature (8 keV) and residual electric field, and finally (fig 10b) a combined LHCD-ICRF pulse at zero loop voltage. All cases with LHCD only are very well simulated, with only a small discrepancy at the plasma centre in the high electron temperature case: the large discrepancy between computation and experimental data in the LHCD-ICRF combined pulse is attributed to the synergism.

This synergism can also be substantiated from the estimation of the power coupled to the bulk electrons from electron power balance during LH power modulation with and without ICRF [14]. About 80% of the LH power is estimated to be coupled to the bulk electrons in pulses with LHCD alone. The power coupled to the electrons can slightly exceed the launched LH power in ICRF heated discharges in some specific conditions, as discussed later. Although error bars are large (±20%), there is a systematic difference between coupled power when synergism is present.

When synergism is observed, current drive efficiencies can be high. When the plasma current is fully non-inductively driven, the non-inductive current drive efficiency has been calculated in two ways [1]:

$$\text{an engineering efficiency } \gamma_{eng} = \frac{\bar{n}_e R I_p}{P_{LHCD} + P_{ICRF}}$$

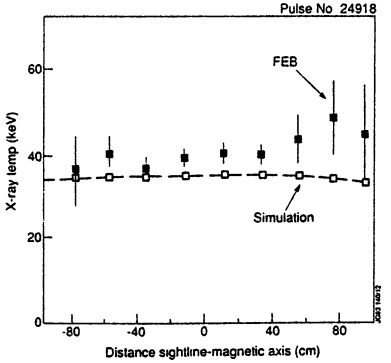

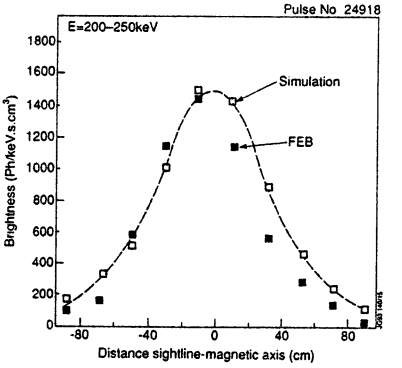

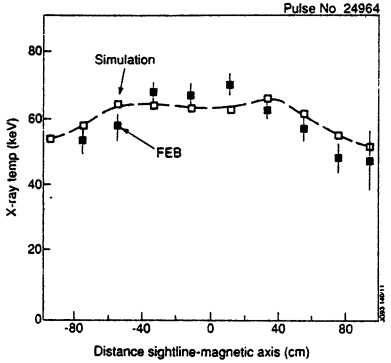

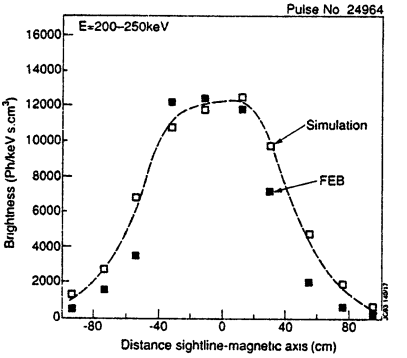

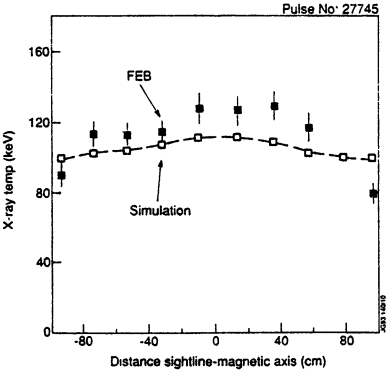

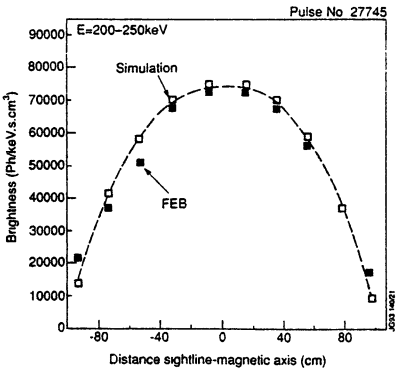

Fig. 10a *Comparison between FEB chord integrated signals and ray tracing simulation code.*

I_p (MA)	B_T (T)	n_{eo} ($10^{19}m^{-3}$)	T_{eo} (keV)	P_{LH} (MW)	P_{ICRF} (MW)	V_{Res} (V)
#24918 0.4	2.5	2.2	1	1.8	0	0
#24964 1.5	3.3	2.2	3	1.1	0	0.1
#27745 3.1	3.3	1.3	8	1.3	0	0.3

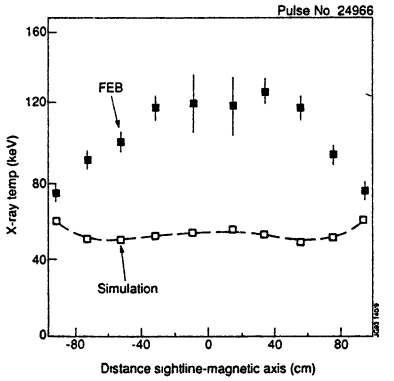

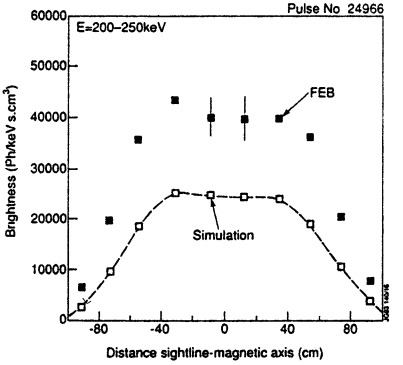

Fig.10b: Comparison between X-ray chord integrated signals and simulation code: $I_p = 1.5MA$, $B = 3.1T$, $n_{eo} = 2\ 10^{19}\ m^{-3}$, $T_{eo} = 8\ keV$, $P_{LH} = 2.3\ MW$, $P_{ICRF} = 3.2\ MW$, $V_{Res} = 0$

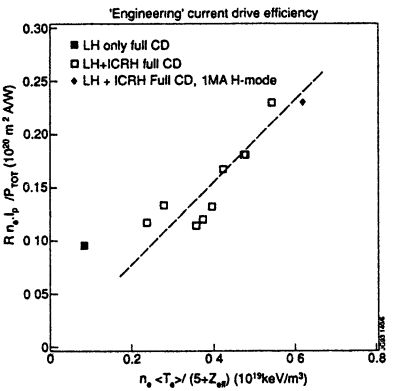

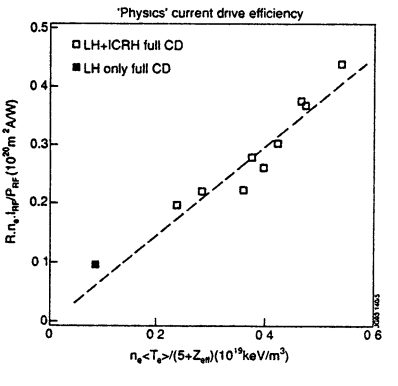

Fig.11: γ_{eng} *versus* $n_e < T_e > (5 + Zeff)$

Fig.12 γ_{phy} *versus* n_e *<Te>/(5 Zeff)*

a physics efficiency $\gamma_{phy} = \frac{\bar{n}_e R I_{RF}}{P_{LHCD} + P_{syn}}$ where $I_{RF} = I_p - I_{BS}$ (I_{BS} being the estimated bootstrap current) and P_{syn} being the part of the ICRF power which is transferred by synergy to the fast electrons created by LHCD. P_{syn} is determined from electron power balance as discussed above.

As discussed in [11], these efficiencies present a large scatter for full current drive when plotted against $<T_e>/(5 + Z_{eff})$, as in JT-60. This scattering disappears when data are plotted against $n_e <T_e>/(5 + Z_{eff})$ as in fig.11 and 12. No apparent saturation in γ_{eng} is observed in the domain of operation, i.e. for central densities up to 3.6 10^{19} m^{-3}. It is not clear if these features: (i) absence of saturation (ii) linear dependence with plasma pressure, are also a signature of the LHCD - ICRF synergism.

The already achieved high current drive efficiencies together with their apparent absence of saturation are very encouraging and we shall try to understand the underlying physics mechanism in order to optimise and make the full benefit of this synergy.

A decisive proof of principle experiment is still missing. With the experimental conditions, the density of the fast electron population is estimated to be rather low ($n_{fast}/n_e \cong 0.0015$) so the damping of ICRF wave on fast electrons via Transit Time Magnetic Pumping is unlikely to occur. Results from specific experiments:

- scan of ICRF power (fig 13) showing that up to 20% of the ICRF power can be transferred to the electron population;

- variation of the ICRF wave spectrum (fig 14) comparing very different k// spectrum;

- comparison between radial profiles of the photon temperature with and without ICRF (fig.15).

are all supporting the damping of an Ion Bernstein Wave created via mode conversion of the Fast ICRF wave at the ion-ion hybrid resonance layer [1]. This wave (IBW) has a low N// at birth and can be damped on a pre-existing fast electron population before being upshifted along its ray trajectory, as indicated in

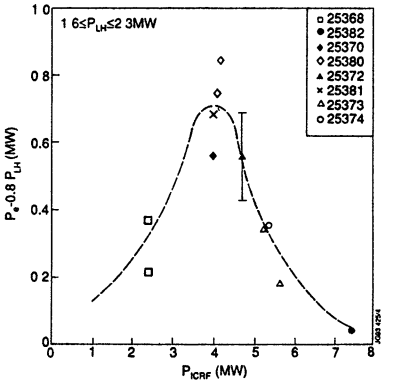

Fig.13: ICRF power coupled to electron ($B = 3.4T$, $n_{eo} = 2\ 10^{19}$ m-3

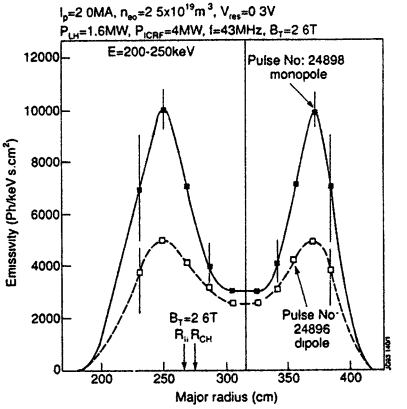

Fig.14: Comparison monopole dipole. R_{ii} corresponds to the ion-ion hybrid layer

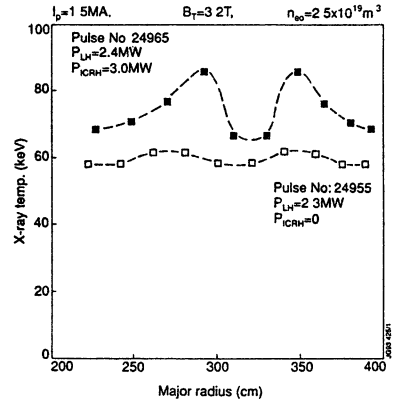

Fig.15: Comparison between ICRF and non ICRF X-ray profiles

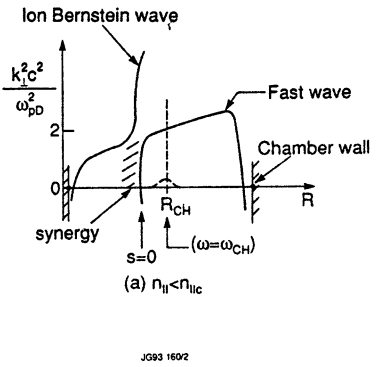

Fig.16: Mode conversion of an ICRF Fast Wave into an Ion Bernstein wave

fig 16. This scheme has been discussed by Jacquinot in [1] indicating that up to 25% of the ICRF power at a given $N_{//}$ can be converted in an IBW in optimum conditions: (i) low $N_{//}$ values for which damping at the resonance layer is not too high, (ii) low minority concentrations ($\leq$ 10%) so that the distance between cut-off and ion-ion hybrid layer remains small compared with the wavelength to allow tunnelling through the cut-off region, (iii) low fast ion tail energy to keep the minority damping low and to avoid blurring the ion-ion hybrid layer by the resonance layer.

The acceleration of LH fast electrons[15], which might take place near the ion-ion hybrid layer if the fast electron population is high enough (large LH power or peaked profiles) and if the Döppler broadening of the minority resonance is not too large (which occurs at high ICRF power with a low minority concentration) support the hypothesis of mode conversion to IBW. The observed localisation of synergistic effects is a strong experimental fact supporting mode conversion to IBW as the mechanism creating the synergy. However, preliminary quantitative calculations indicate that the mode converted power is lower than the experimental power coupled from ICRF to the electron population.

3. THE FULL JET LHCD SYSTEM

The characteristics of the full JET LHCD system are also listed in Table 1. It will have 3 times more power capability than the prototype with a narrower wave spectrum with 32 waveguides in an horizontal row instead of 16, the width of the spectrum $\Delta N_{//}$ is 0.13. The full launcher, L_1, has been assembled and tested at high power at the level of 100 kW for 2 sec per multi-junction in vacuum. A photograph of the L_1 mouth can be seen in fig 17. As sketched in fig 18, the L_1 launcher will be equipped with a 100 000 l/s cryopump allowing for a proper pumping in the L_1 vacuum vessel during initial conditioning and during long time duration high power pulses.

In order to achieve a speedier conditioning than during the previous JET campaigns, a procedure to produce heating of the vacuum waveguides through HF losses of the microwave power has been set up. It is intended to increase the temperature of the waveguides by 50 to 100° C above the operating temperature to insure a proper baking. For that purpose, HF will be launched into vacuum and high power loads (250kW) will be installed in the Torus Hall, behind the hybrid junctions. A new gas introduction system close to the L_1 mouth is being prepared in order to increase the local density.

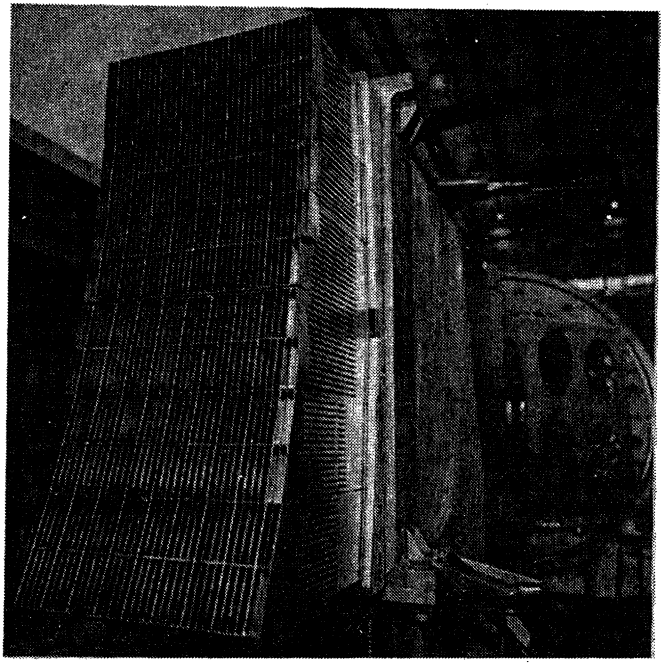

Fig.17: View of the L1 launcher mouth

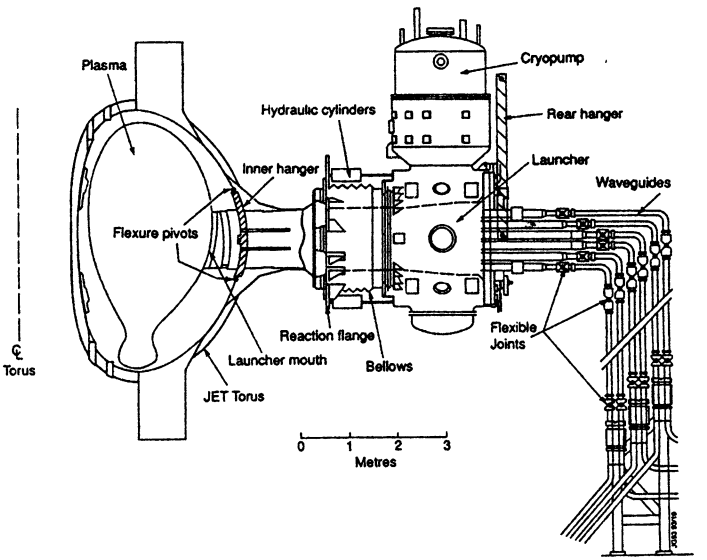

Fig.18: Sketch of the full LHCD system

The new L_1 launcher will be installed in JET during the present shutdown. Among the main modifications which are being done, the new pumped divertor configuration and the new set of ICRF antennae with their new phasing capability will have a significant impact on the operation of the LHCD system. A sketch of these new systems is shown in fig 19.

The new divertor configuration will allow longer connecting lengths for the magnetic field lines linking the grill mouth to the plasma configuration. The sensitivity of the launcher radial location to the plasma coupling should be consequently be reduced.

The new A2 antennae being grouped in modules of 4 adjacent straps will have a narrower spectrum. It will be possible to superimpose both wave spectra, as shown in fig.20, by setting a 40° phasing between straps, indicating that a gain by a factor of 2 in the available "synergistic" power appears possible.

Note that optimum synergism has been obtained with $P_{ICRF} \approx 1.5\text{–}2\ P_{LHCD}$, but synergistic effects disappeared for ICRF power above 4 MW in the last JET experiments. If mode conversion is the mechanism responsible for synergy, some scenarios will have to be developed in order to use the respective maximum power of 20MW and 10MW for ICRF and LHCD systems, for instance by spreading the synergy area by using slightly different frequencies for the ICRF system or by using ^3He as a minority for damping the ICRF wave.

It is also to be noted that special emphasis will be given to the use of feedback loops including:

- active feedback on the plasma position control combined with the L_1 launcher position control;
- active feedback on the total power of the LH plant;
- possibly active feedback on the phase between multi-junctions in order to maintain some control on the current profile.

4. PROSPECTS

Several studies have been made for the prospective use of Lower Hybrid waves in a reactor. They have been summarised in [16]. Although LH waves can be used as a very effective electron heating system, as shown in Tore Supra [17], their best role remains to produce non-inductive current drive. Present LHCD efficiencies are higher, by at least one order of magnitude, than efficiencies

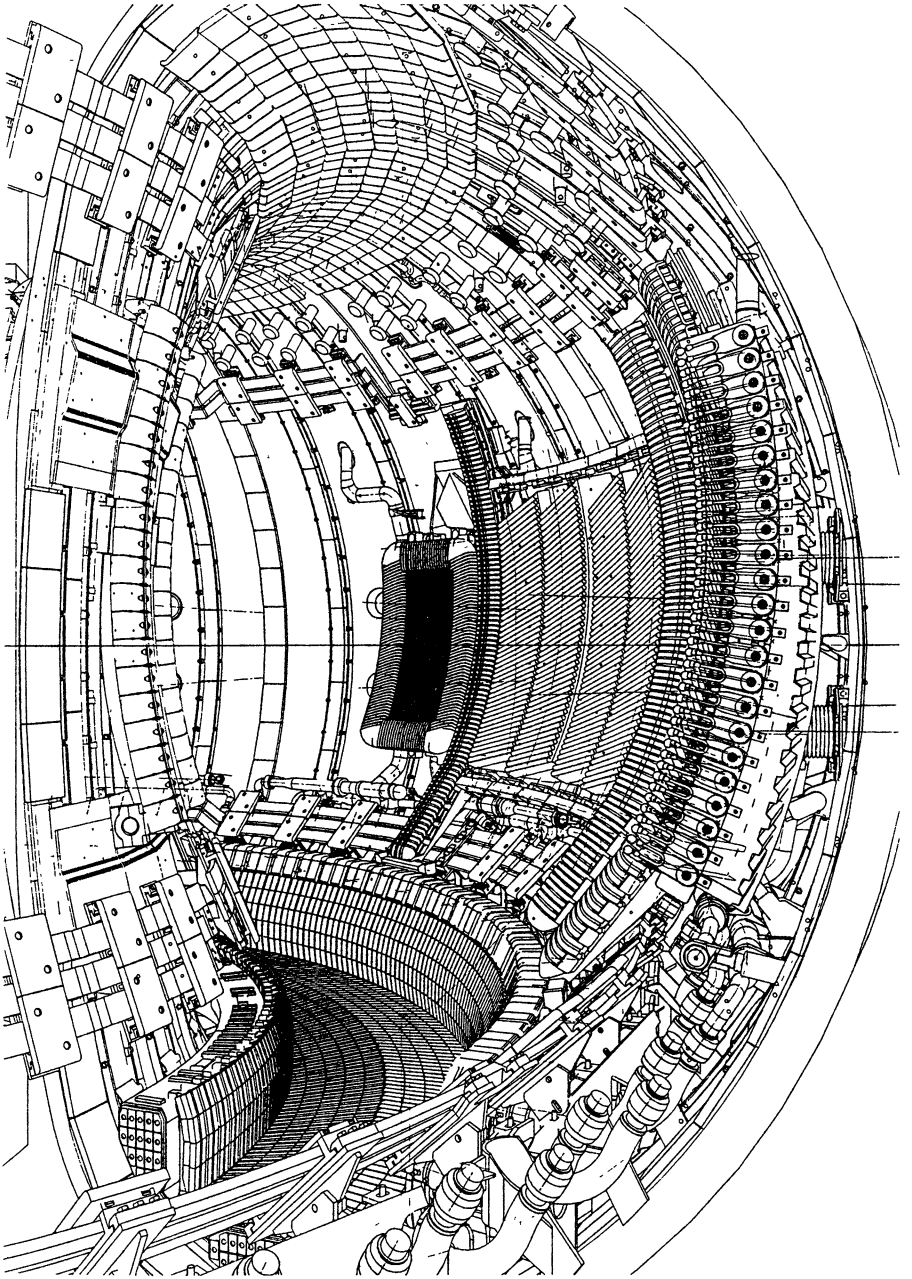

Fig.19: The new JET configuration

achieved with other methods. A record full driven current of 3.6MA with LHCD has been achieved recently in JT-60U [18].

Studies made for NET and ITER indicate that the frequency of an LHCD system should be in the range 5 to 8 GHz. Therefore, the corresponding coupler should be composed of thousands of waveguides. Several proposals have been made to overcome that difficulty, including launching LH slow waves via a quasi-optical grill [19]. JET is studying a solution using a transfer cavity: the hyperguide [20] between the grill mouth and the rest of the system as sketched in fig 21. The advantages of such a hyperguide are several:

- The mouthpiece is decoupled from the rest of the cavity, and can therefore be modified or replaced without requiring the rest of the system to be dismantled using remote handling techniques.

- The structures required in a hyperguide launcher are much lighter, simpler and cheaper to manufacture than in the conventional approaches.

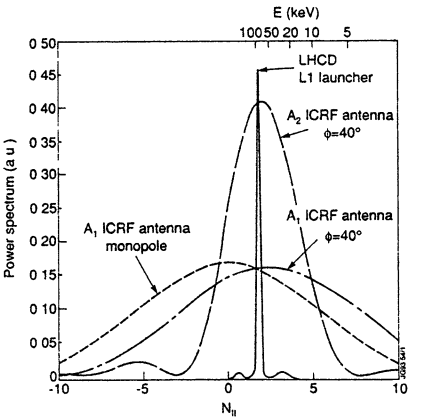

Fig.20: Wave spectrum of the L1 launcher and of the A1 and A2 antenna respectively

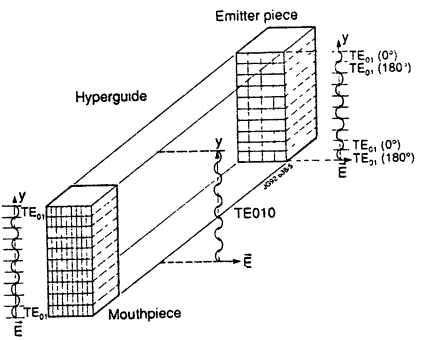

Fig.21: Principle of an hyperguide transfer cavity

- The hyperguide surface exposed to the microwave power is smaller than in the other types of antennas, and the cavity is much easier to pump. A hyperguide cavity replacing the present multi-junction system installed at JET would have an exposed surface area 4 times smaller than at present not including the mouthpiece. As the power goes through the electron cyclotron resonance within the hyperguide, this could solve the power handling problems linked to the accumulation of gas.

- Finally, as the hyperguide is not a resonant cavity, there is no inconvenience in extending its length. It is conceivable therefore to place the emitter surface outside the main shielding of the machine, allowing the vacuum windows and the associated electronics to be outside the high radiation area. In the same way, the possibility of replacing the numerous individual windows by a single one installed inside the hyperguide would further simplify the system and improve its reliability.

A low power hyperguide prototype is being prepared and will be tested at JET. It might lead, if successful, to a simplified version of L_1 allowing the LHCD system to accommodate smaller magnetic configurations.

It has been shown that the non-inductive current drive efficiency which is required to maintain an ignited steady-state reactor of the ITER EDA type, with a low aspect ratio and high plasma current, shall exceed $\gamma = 1.2\ 10^{20}\ m^{-2}\ A/W$ for densities in the range required for divertor operation [1,21]. The anticipated current drive efficiencies do not exceed about $\gamma = 0.5\ 10^{20} m^{-2}\ A/W$ for LHCD and for any other conventional method. Therefore, full current drive in a reactor can only be expected for high bootstrap current devices with improved confinement, i.e. low plasma current, unless much higher current drive efficiencies can be achieved.

A route to increase non-inductive current drive efficiency is to maintain the current with very high energy electrons, to avoid collisions even at the density required in a reactor. Fast electrons induced by LHCD have their energy limited to about 100 keV due to accessibility conditions. Acceleration of these electrons by a Fast Wave is a very attractive scheme. Synergy with Electron cyclotron waves as proposed for Tore Supra can also be an attractive scheme provided that electrons can be accelerated into the MeV range.

One of the aims in the next JET experimental campaign is to assess if this synergism can be used to achieve the current drive efficiencies required in an ITER type reactor, in plasma conditions which are reactor relevant. In addition

to experiments aimed at a better identification of the physics mechanisms of the synergy, it will be attempted to extend the operational range for which this synergy is effective to higher densities ($n_{eo} > 3\ 10^{19}\ m^{-3}$) and to identify ways of coupling a larger amount of ICRF power to the fast electron population.

Current profile control using Lower Hybrid waves is a major ingredient of the so called "advanced" tokamaks scenarios where most of the plasma current is produced via the bootstrap current. It can be shown that these "advanced" scenarios require operating the plasma at very high values of the ratio $\beta_N = \frac{aB}{I}\beta t$ for which stability can only possibly be achieved if the plasma current profile is properly tailored.

The new LHCD experiments on JET during the next operational phase will not only allow a better understanding of the physics of a large tokamak but should help to assess the potential application of Lower Hybrid waves to a reactor type plasma.

REFERENCES

1. J Jacquinot, V P Bhatnagar, C Gormezano and the JET Team, in Proc. Europhysics topical Conf. on RF Heating and Current Drive of Fusion devices Plasma Phys. and Cont. Fusion 35 (1993) A35.
2. C Gormezano, et al, 1, Proceedings 12th Symp. on Fus. Eng., Vol 1 (Monterey, 1987)
3. G Tonon and Equipe Tore Supra, 14th Symp. on Fus. Tech., San Diego, 1991.
4. C Gormezano, et al in 32nd APS meeting, Cincinatti, Nov 1990 (JET-IR(90)07)
5. X Litaudon, D Moreau, Nucl. Fusion 30 (1990) 471.
6. A Kaye et al, in proc. Machine Actuators and Control Seminar, London, March 1993.
7. A Ekedahl, et al, in Proc. Europhysics topical Conf. on RF Heating and Current Drive of Fusion devices (Brussels, July 1992) 221
8. M Brusati, M, et al, in Proceedings 19th Eur. Conf. Cont. Fusion and Plasma Phys., Innsbruck (1992) I, 307
9. The JET Team, High Power Heating of 7MA Limiter Plasmas in JET, presented by P Lomas, 14th Int. Conf. on Plasma Phys. and Cont. Nucl. Fusion, Wurzburg, Germany, 1992 (CN-56/A-3-2).
10. F Rimini, et al, in Proc. Europhysics topical Conf. on RF Heating and Current Drive of Fusion devices (Brussels, July 1992) 229

11.The JET Team, Non Inductive Current Drive in JET, presented by C Gormezano, 14th Int. Conf. on Plasma Phys. and Cont. Nucl. Fusion, Wurzburg, Germany, 1992 (CN-56/E-1-1)
12.C Gormezano, In Proc. 10th Top. Conf. on RF Power in Plasmas, Boston, April 1993.
13.Y Baranov, et al, in Proc. 20th EPS Conf. on Cont. Fusion and Plasma Phys. Lisbon 1993, III-881.
14.C Gormezano, et al in Proc. IAEA Tech. Com. Meeting on Fast Wave Current Drive in Reactor Scale Tokamaks, Arles 1991, 244
15.A K Ram et al, in Proc.20th EPS Conf. on Cont.Fusion and Plasma Phys., Lisbon 1993 II-897
16.Report of the Coordinating Committee for Lower Hybrid Waves and Current Drive - NET, January 1993.
17.B Saoutic, in Proc. 10th Top. Conf. on RF Power in Plasmas, Boston, April 1993.
18.Y Ikeda, et al., in Proc. 20th EPS Conf. on Cont. Fusion and Plasma Phys., Lisbon 1993, III-909.
19.M I Petelin, E V Suvorov, Soviet Journal of Tech. Phys. (Lett) Vol.15, P.23, 1989.
20.M Pain et al, Fus. Eng. and Design 22 (1993) 251.
21.P H Rebut, D Boucher, C Gormezano, B E Keen, M L Watkins, Plasma Phys. and Cont. Fusion, 35 (1993) A1

RF HEATING AND CURRENT DRIVE ON TORE SUPRA : STATUS, RESULTS AND APPROACH TO STATIONARY DISCHARGES

Gianfranco TONON

Association Euratom-CEA sur la Fusion Contrôlée
CE Cadarache, 13108 - St Paul lez Durance Cedex,
France

I - INTRODUCTION

Tore Supra is a large superconducting Tokamak ($R \sim 2.35$ m ; $a \leq 0.8$ m ; B_T up to 4.5 T ; I_p up to 2 MA) [1] which made possible achievement of quasi-continuous discharges at more than 1 MA level if the plasma current is driven non-inductively [2]. Indeed power and particle exhaust components (pump limiters, inner first wall, ergodic divertor) are actively cooled with a pressurized water loop ($T < 230°C$; 40 bars ; flow rate : 540 tons/h) able to exhaust 25 MW.

Two RF systems are operating actually on Tore Supra : (i) a lower hybrid current drive (LHCD) system, (ii) an ion cyclotron resonance heating (ICRH) system. A third system at the electron cyclotron resonance frequency (ECRH) is under development.

In section 2 the status of the RF systems is presented with emphasis on long pulse wave coupling capabilities. In section 3, the main results concerning volt second saving, heating, current drive and current profile control are given. In section 4, deduced from actual experiments, the expected flat top durations as a function of plasma current and electron density on Tore Supra are determined. Finally a summary is given in section 5.

2 - RF SYSTEMS OF TORE SUPRA

2.1 - The characteristics of the RF generators operating or planned for Tore Supra are summarized on Table 1.

The ICRH generator is composed by six tetrodes while the

LHCD transmitter uses 16 klystrons. It is planned, for the ECRH system, to install six gyrotrons delivering 0.5 MW each at 118 GHz in HE_{11} mode using an internal Vlasov converter ; the gyrotrons will have cryogenic windows.

Coaxial lines and rectangular waveguides are used for the ICRH and LHCD generators respectively in order to transfer the RF power from the sources to the antennas.

System	Source	Frequency	Total power on load (MW)	Pulse length (s) (duty cycle)
ICRH	Tetrode (TH526) 2 MW	35 to 80 MHz	12	30 (0.125)
LHCD	Klystron (TH2103) 0.5 MW	3.76 GHz	8	210 (0.35)
ECRH*	Gyrotron Cavity mode TE22.6 0.5 MW	118 GHz	3	210 (0.35)
* Under development				

Table 1

For the ECRH system, pumped corrugated circular transmission lines (ϕ = 63.5 mm) with mitre bends are developed.

2.2 - The RF antennas are installed in the equatorial ports of Tore Supra, the principle is shown in figure 1 and they are schematized in figure 2 .

For the ICRH system 3 antennas based on the principle of the resonant double loop antenna (fig. 1a) are used [3]. Variable capacitors permit to match the circuit between 35 and 80 MHz. Two multijunction-type grills are operated routinely in the LHCD system [4]. One grill is composed of 16 electrically insulated modules cooled at the top and bottom, each of them connected to one vacuum RF window (pill box type BeO). The launcher mouth represents a matrix of 128 active (32×4) and 8 passive waveguides

giving a very narrow $N_{//}$ power spectrum ($\Delta N_{//} \approx 0.5$). The six ECRH antennas are composed by three assemblies of two beams (fig. 1c) which are independently variable in horizontal and vertical directions by means of movable mirrors.

2.3 - It has been possible to couple up to 4 MW with one ICRH antenna (f = 57 MHz), which corresponds to a power density through the Faraday screen of 16 MW/m^2 [2].

The full available power 3.6 MW in one grill and 6.6 MW total was achieved with 2 s pulses length : this corresponds to an injected RF power density of 45 MW/m^2 through the waveguides [6].

As seen in figure 3, where we have plotted the evolution of the RF power density achieved on various devices as a function of frequency, the value obtained with the ICRH antenna on Tore Supra corresponds to a record value in this frequency domain. Taking into account of the multi-passage of the wave in the multijunction grill, the value of the electric field compared to the value in the standard grill has to be multiplied by a factor of around 1.5 [7] giving an "effective" RF power density of the order of 100 MW/m^2 which is near to the limits for this frequency. The planned RF power density on the mirrors of the ECRH antenna is about 60 MW/m^2 well below as seen in figure 3, the maximum value achieved actually in this frequency domain.

2.4 - In order to allow long pulse operations new Faraday screen with :

- one row of tubes actively cooled,
- thin (150 µm) boron carbide coating on plasma facing tube,
- tubes tilted along the magnetic field line,
- angled tubes to approximate the plasma external shape

and with cooled septum have been developed and installed [5]. Tests on B_4C coatings, using the European beam electron facility FE 200, have demonstrated as indicated in figure 4, that a thermal heat flux up to 10 MW/m^2 can be tolerated. On Tore Supra after 5 months use, 30 second pulses and 4 MW level operations, no

erosion sign could be noticed on the boron carbide coating. Using the new Faraday screen, steady pulses have already been obtained as indicted in figure 5 [5] where the time evolution of the temperature measured with an IR camera in some parts of the antenna is shown. For a 27 s, 2 MW level pulse the antenna thermal equilibrium is reached after 10 s and up to 54 MJ of energy have been delivered to the plasma in a single pulse. With this new Faraday screen design, the coupling to the plasma has been improved and the total radiated power by the plasma decreased compared to the old Faraday screen configuration [5].

2.5 - Good coupling has been achieved with the multijunction grill [8] and a mean power reflection coefficient $\overline{R}$ below 4 % is routinely obtained when the electronic density at the grill mouth n_{eg} is at least twice time the cut-off density (2.10^{17} m^{-3} at 3.7 GHz) [8]. The coupling remains linear until the maximum available power density [8] and a stationary coupling can be maintained during the one minute flat top discharge as shown in figure 6. On this shot, the LH injected power reaches 3 MW and the mean reflection coefficient $\overline{R} \approx 3\ \%$ remains constant ; the maximum injected LH energy reaches 180 MJ which constitutes a record value in this frequency domain. It is important to note that a low stationary pressure is maintained inside the antenna by a titanium getter pump.

3 - MAIN EXPERIMENTAL RESULTS

3.1 - LH assisted current ramp-up

On Tore Supra about half of the plasma surface flux is consumed in compensating the resistive losses during the current ramp [10]. So far LHCD is an attractive method to reduce the flux consumption ϕ_{RU} during the current rise phase. Consequently the current flat top duration τ_{FT} given by :

$$\tau_{FT} = (\phi_{AV} - \phi_{RU}) / V_L \qquad (1)$$

can be increased (ϕ_{AV} = 15 Wb represents the available flux swing

on Tore Supra and V_L the resistive loop voltage). We have defined a resistive magnetic flux saving efficiency ξ_{res} [9] :

$$\xi_{res} = \Delta\phi_{res} \Big/ \left(\int \frac{P_{LH}\, dt}{a^2 K \bar{n}_e} \right) \qquad (Wb/J/m^{-1}) \quad (2)$$

where a and K represent the plasma minor radius and elongation respectively and $\Delta\phi_{res}$ is the resistive flux saved during current ramp. The evolution of ξ_{res} as a function of P_{LH} is plotted in figure 7. We see that ξ_{res} is enhanced at low LH powers due to the OH-LH synergetic effects and reaches a constant value for powers greater than 1 MW and we have $\xi_{res} \approx 0.25$ to $0.4.10^{13}$ Wb/J/m^{-1} ; a value of $\xi_{res} \approx 0.4.10^{13}$ Wb/J/m^{-1} has been measured for the one minute discharge [10].

3.2 - Heating

Up to near 8 MW of the total power (ohmic + ICRH + LHCD) have been injected on Tore Supra [6]. A significant dependence of the global energy confinement time τ_E is observed with the plasma density as indicated in figure 8 [11]. On the other hand the measured kinetic electron energy W_e is well fitted by the global REBUT-LALLIA-WATKINS scaling [12] :

$$W_e^{R.L.W.} = 0.146\, \bar{n}_e^{3/4} Z_{eff}^{1/4} B_t^{1/2} I_p^{1/2} \left(Ra^2K\right)^{11/12}$$
$$+ 1.2\, 10^{-2} I_p\, Z_{eff}^{-1/2}\, P_{TOT} \left(Ra^2K\right)^{1/2} \qquad (4)$$

in units of 10^{20} m^{-3} , T , MA , MW , MJ and meters, as shown in figure 9. The global energy confinement time computed from $W_{TOT}^{R.L.W.} = W_e^{R.L.W.} + W_{ion}$ where the kinetic ion energy W_{ion} is deduced from charge exchange measurements, is also in good agreement with the experimental values as shown in figure 8.

Steady-state improved confinement regime with lower hybrid current drive has been obtained as shown in figure 10, where the time evolution of the main plasma parameters is represented. A steady state ℓ_i value of about 1.7 (instead of 1.4

in the ohmic case) is reached giving a τ_E enhancement of about 1.4 over both REBUT-LALLIA-WATKINS and GOLDSTON predictions. As shown in figure 11, this enhancement rises approximately as $(\ell_i/\ell_{io})^{0.7}$ for ℓ_i varying between 0.9 to 2.8, where ℓ_{io} is a standard value ($\ell_{io} \sim 1.25$ for $q_\psi \approx 3$ to 4).

3.3 - Current drive

In figure 10 is represented a stationary zero loop voltage discharge (full LH driven current 0.8 MA) obtained using a 2.7 MW, 10 s LH pulse in deuterium with $\bar{n}_e = 1.6.10^{19}$ m^{-3}. The RF generated current I_{RF}, calculated from the loop voltage drop taking into account the change of resistivity due to changes in T_e and Z_{eff} produced by the LH power, was determined in a large domain of density and plasma current as shown in figure 12 where the variation of the ratio I_{RF}/I_p is plotted as a function of $P_{LH}/\bar{n}_e$ RI_p (the points in the dashed region correspond to He plasma values).

A non inductively driven current of 1.6 MA has been achieved with an electron density $\bar{n}_e = 1.5.10^{19}$ m^{-3}. As indicated by the results plotted in figure 13, the current drive efficiency $\gamma_{LH} = \bar{n}_e.R.I_{RF}/P_{LH}$ lies between 0.15 to $0.2.10^{20}$ m^{-2} A/W.

As shown in figure 14, the plasma responses of LHCD assisted discharges (X-rays signals, EC emission, loop voltage drop) are well correlated with the antenna performances ($N_{//}$-spectrum evolution with the phase shift $\Delta\phi_m$) which exhibit a similar behaviour when measured by the "$N_{//}$-weighted directivity" δ_{CD} [8].

3.4 - Current profile control

The current profile can be modified by the application of the LH power during the low density current ramp-up phase. In this case LH waves are centrally absorbed and the current profile can be peaked. The influence of the LH antenna phasing in modifying the current profile can be seen in figure 15, where the internal inductance parameter ℓ_i is plotted versus time, for $\Delta\phi_m = -\pi/2$, 0, $\pi/2$ ($N_{//} = 1.4$, 1.8, 2.2 respectively) and

$dI_p/dt = 0.4$ MA/s . The application of LH power produces a peaking of the current profile with respect to the ohmic ramp-up and this peaking is maintained during the flat-top phase.

Sawtooth stabilization on low density ($\bar{n}_e \sim 1.5.10^{19}$ m^{-3}) discharges has been achieved with LH waves alone [13]. On axis ICRF minority heating permits to increases the sawtooth-free period [14]. As shown in figure 16 the duration of a sawtooth-free period due to hot ion stabilization by ICRF minority heating increases when applying LH power to the plasma. With the following parameters ($I_p = 1.5$ MA hydrogen minority ($\simeq 10$ %), (deuterium, dipole configuration) the sawtooth stabilized phase period lengthens from 0.45 s (4 MW ICRH alone) to almost 1 s (4 MW ICRH + 3.4 MW of LHCD). Analysis of polarimetric data shows that, instead of the continuous decrease of the central safety factor observed when using ICRH alone, the q value "freezes" when LHCD power exceeds 3 MW. This demonstrates a current profile control effect opening the way towards steady state sawtooth stabilization.

Local transport analyses, showed the influence of the shear $s = \frac{\nu}{q_\psi} \nabla q_\psi$ and, consequently, the important role played by the control of the current profile on the confinement [11] [14]. Figure 17 shows the evolution of the electron thermal diffusivity χ_e in the confinement region ($0.5 < r/a < 0.7$) as a function of the shear for different confinement modes : ICRH and LHCD modes (open symbols), LHCD high internal inductance mode (dark triangles) and ICRH sawtooth stabilized phase (dark squares) [14]. Low values of the electron thermal diffusivity in the confinement region are correlated with high values of the shear.

4 - PROSPECTS FOR LONG PULSE DISCHARGES ON TORE SUPRA

4.1 - Model

In all expressions, MKS units are used with temperature in units of 10 keV, current in MA , power in MW , energy in MJ

and densities in units of 10^{20} m^{-3} .

a) The flat-top duration is calculated using the relation (1) with $\phi_{RU} = 4.5\ I_p$ on Tore Supra. In the model we assume a parabolic dependence of the density, electron temperature on radius :

$$Y = \hat{Y}\left(1-\frac{r^2}{a^2}\right)^{\alpha_y}$$ where Y is replaced by n_e , T_e respectively.

The profile factors are determined considering some data observed on Tore Supra namely :

$$\begin{cases}\alpha_n = 0.25\ P_{TOT}^{0.28}/< n_e >^{0.6} \\ \alpha_t = 0.63\ P_{TOT}^{0.2}/< n_e >^{0.5}\end{cases}$$ and $P_{TOT} = P_{OH} + P_{LH} + P_{FW}$,

P_{TOT} represents the total power in the plasma taking into account the ohmic, lower hybrid and eventually fast wave power contributions. The electron energy content $W_e = 0.24 <n_e> <T_e>_n V_p$ is calculated considering the REBUT-LALLIA-WATKINS scaling (3) ($V_p = 2\pi^2 R a^2 K$ is the plasma volume and $<T_e>_n$ the density weighted volume averaged electron temperature). The Z_{eff} value is given by an empirical scaling valid for Tore Supra : $Z_{eff} \approx f + 0.25 \cdot P_{TOT}^{1/2}/< n_e >$ with $f = 1$ or 2 for hydrogen (deuterium) or helium plasmas respectively.

b) The current plasma I_p is given by :

$$I_p = I_{OH} + I_{LH} + I_{FW} + I_{BS}$$

The bootstrap current I_{BS} is determined using the following expression :

$$I_{BS} = <\beta_p> I_p \cdot J_{BS}(\alpha_n , \alpha_t , \alpha_j , Z_{eff})/2\ (R/a)^{1/2}$$

where the profile factor $J_{BS}(\alpha_n...)$ is calculated using WILSON'S data [15] and $<\beta_p>$ represents the averaged poloidal beta value.

The resistive loop voltage V_L :

$$V_L = 8.10^{-3} Z_{eff}\left[0.29+\frac{0.457}{1.077+Z_{eff}}\right] R\ I_{OH} \Big/ \left(1+\frac{\sigma_{LH}}{\sigma_{OH}}\right) a^2 < T_e >_n^{3/2}$$

includes the modification of the conductivity by the LH waves $((1+\sigma_{LH})/\sigma_{OH})$ determined by FISCH [16] :

c) We use an analytical expression for the LH current drive efficiency γ_{LH} deduced from a model [17] based on 2D FOKKER PLANK calculations made by KARNEY and FISH [18]. We have :

$$\gamma_{LH} = \frac{< n_e > R\, I_{LH}}{P_{LH}} = \frac{0.68 \cdot B_T \cdot < T_e >_n^{1/2}}{(5+Z_{eff}) < n_e >^{1/3} \left(\frac{\Delta N_{//}}{\overline{N}_{//}}\right)^{1/3}} \frac{(1+\alpha_n+\alpha_t)^{1/2}}{(1+\alpha_n)^{7/3}}$$

where B_T is the value of the toroidal magnetic field on plasma center and $\Delta N_{//}$, $\overline{N}_{//}$ represents the full width and the average index value of the main peak of the radiated $N_{//}$-spectra. As shown in figure 18, the LH current drive efficiency calculated using this analytic expression agrees well with the values obtained by HARVEY et al [19] and KUPFER and MOREAU [20].

The fast wave current drive efficiency γ_{FW} is given by [21] :

$$\gamma_{FW} = < n_e > \cdot R\, I_{FW}/P_{FW} = 0.63 < T_e >_n /(2+Z_{eff})$$

which gives results in agreement with the values obtained for Tore Supra by the ALCYON code [22].

4.2 - Comparison with experimental data

The model has been checked on the results obtained on Tore Supra when lower hybrid waves are applied. In figure 19, we have plotted the experimental points and the calculated values of the "effective" LH efficiency given by : $\eta_{eff} = \overline{n}_e\, R\, I_p \cdot \Delta V_L / V_{OH}\, P_{LH}$ (where ΔV_L represents the loop voltage drop and V_{OH} the resistive loop voltage before RF), as a function of the LH power. We see that the agreement between experimental and calculated values is fairly good and that, in particular, the OH-LH synergetic effects are well taken into account. The same general good agreement is observed when we consider the evolution of $\Delta V_L/V_{OH}$ for various electron density in deuterium (Fig. 20) or helium (Fig. 21) plasmas.

4.3 - Long pulse possibilities

We have indicated in figure 22 the LH power necessary to assure a given flat-top duration τ_{FT} for various plasma current values and $\langle n_e \rangle = 0.2\ 10^{20}\ m^{-3}$.

On this figure some achieved experimental flat-top duration values are also indicated for pure OH discharges ($P_{LH} = 0$) and with various LH powers : the agreement seems satisfactory. We see that, at moderate electron density, very long pulse can be achieved on Tore Supra with the actual LH system.

In future, in view to achieve good particle control with the pump limiters, higher densities are suitable [23]. In the limit of 25 MW of the total injected power, we have considered the case where we use 10 MW of fast wave power and 15 MW of LH power. The evolution of the flat-top duration τ_{FT} for a 2 MA plasma, as a function of $\langle n_e \rangle$ is plotted in figure 23 where H represents the enhancement factor of the energy confinement. We see that long pulse discharges (well above the skin time and the first wall saturation time values) can be achieved with $\langle n_e \rangle \sim 0.5\ 10^{20}\ m^{-3}$.

5 - SUMMARY

Various RF systems are operating (ICRH, LHCD) or planned (ECRH) on Tore Supra.

The ICRH antenna and LHCD grill have demonstrated (i) the capability to achieve high RF power density values (ii) long pulse possibility.

Significant experimental results concerning the resistive flux saving efficiency, the heating, the current drive and the current profile control have been obtained.

Based on simulations obtention of very long pulse (some minutes) seems possible on Tore Supra at moderate density ($\langle n_e \rangle \approx 0.2\ 10^{20} m^{-3}$) with the actual LHCD system and at high density ($\langle n_e \rangle \sim 0.5\ 10^{20} m^{-3}$) if the LH injected power is increased up to 15 MW.

Acknowledgements

The author is grateful to the contributions of all members of the TORE SUPRA TEAM. Stimulating discussions with G.T. HOANG, B. SAOUTIC and D. VAN HOUTTE are warmly acknowledged.

REFERENCES

1. Equipe Tore Supra presented by Aymar K., 12th Ind. Conf. Nice, 1988, Vol. 1, p. 9, IAEA Vienna, 1989.
2. Equipe Tore supra presented by Tonon G., Plasma Phys. Control. Fus. 35, 1993, A105-A112.
3. Beaumont B., Agaraci A., and Kuus H. Fusion Technology 1988, 503.
4. Rey G. et al. Proc 15th Symp. on Fus. Tech. Utrech, 1988, p. 514.
5. Agarici G. et al. 19th EPS Conference, Innsbruck, 1992.
6. Equipe Tore supra presented by Tonon G. The 14th IEEE/NASS Symposium, San Diego, 1991, Vol. 1, p. 168.
7. Rey G. et al. 17th Symposium on Fusion Technology, Rome 1992, Vol. 1, p. 628.
8. Litaudon X. et al. Nuclear Fusion, Vol. 32, n°11, 1992, p. 1883.
9. Van Houtte D. et al. 19th EPS Conf. Innsbruck, 1992, Vol. 16C, Part II, p. 945.
10. Van Houtte D. and Equipe Tore Supra, Nuclear Fusion, 1993, Vol. 33, n° 1, p. 137.
11. Hoang G.T. et al. EUR-CEA-FC, 1475, Report to be published on Nuclear Fusion.
12. Rebut P.H., Lallia P.P. and Watkins M.L., 12th Ind. Conf. Nice, 1988, Vol. 2, p. 191, IAEA Vienna, 1989.
13. Equipe Tore Supra presented by Parlange F., 13th Conf. on Plasma Phys. and Control. Nucl. Fus. Research, Washington DC, Nuclear Fusion Supplement, Vol. 1, p. 541.
14. Saoutic B. et al. 10th Topical. Conf. on Radiofrequency Power in Plasma, Boston, USA, 1993, EUR-CEA, FC-1486.
15. Wilson H.R., Nuclear Fusion 32, 1992, p. 257.
16. Fisch N.J., Phys. of fluids 28 (1), January, 1985, p. 245.
17. Tonon G., Tokamak Start-Up Edited by H. Knoppel, 1985.

18. Karney C.F.F. and Fisch N.J., Phys. of Fluids 22, 1979, p. 1817.
19. Harvey R.W., Europhysics Topic Conf. on Radiofrequency Heating and Current Drive of Fusion Devices, Brussels, 1992, Vol. 16E, p. 205.
20. Kupfer K. and Moreau. D., Europhysics Topic Conf. on Radiofrequency Heating and Current Drive of Fusion Devices, Brussels, 1992, Vol. 16E, p. 257.
21. ITER Physics Design Guidelines 1989, Compiled by N.A. UCKAN and ITER Physics Group - ITER Documentation Serie N 10, IAEA, 1990.
22. Bécoulet A., private communication.
23. Chatelier M. et al. Plasma Physics and Controlled Nuclear Fusion Research, 1992, Wursburg, IAEA, Vol. 1, p. 341.

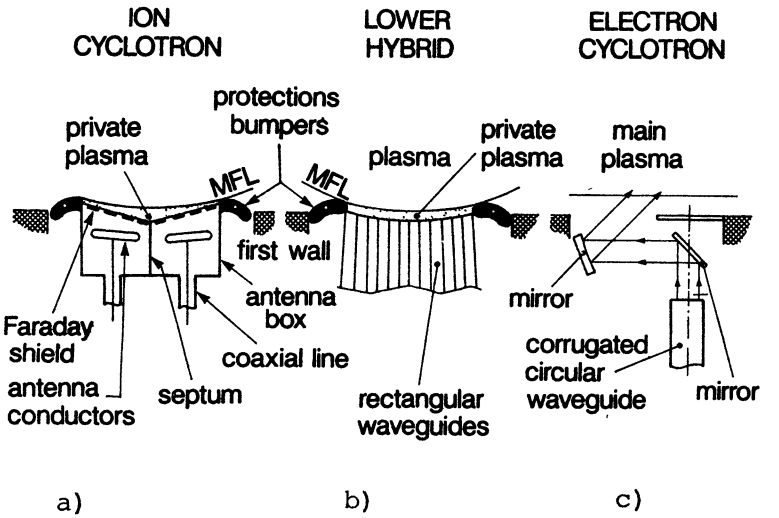

Fig. 1

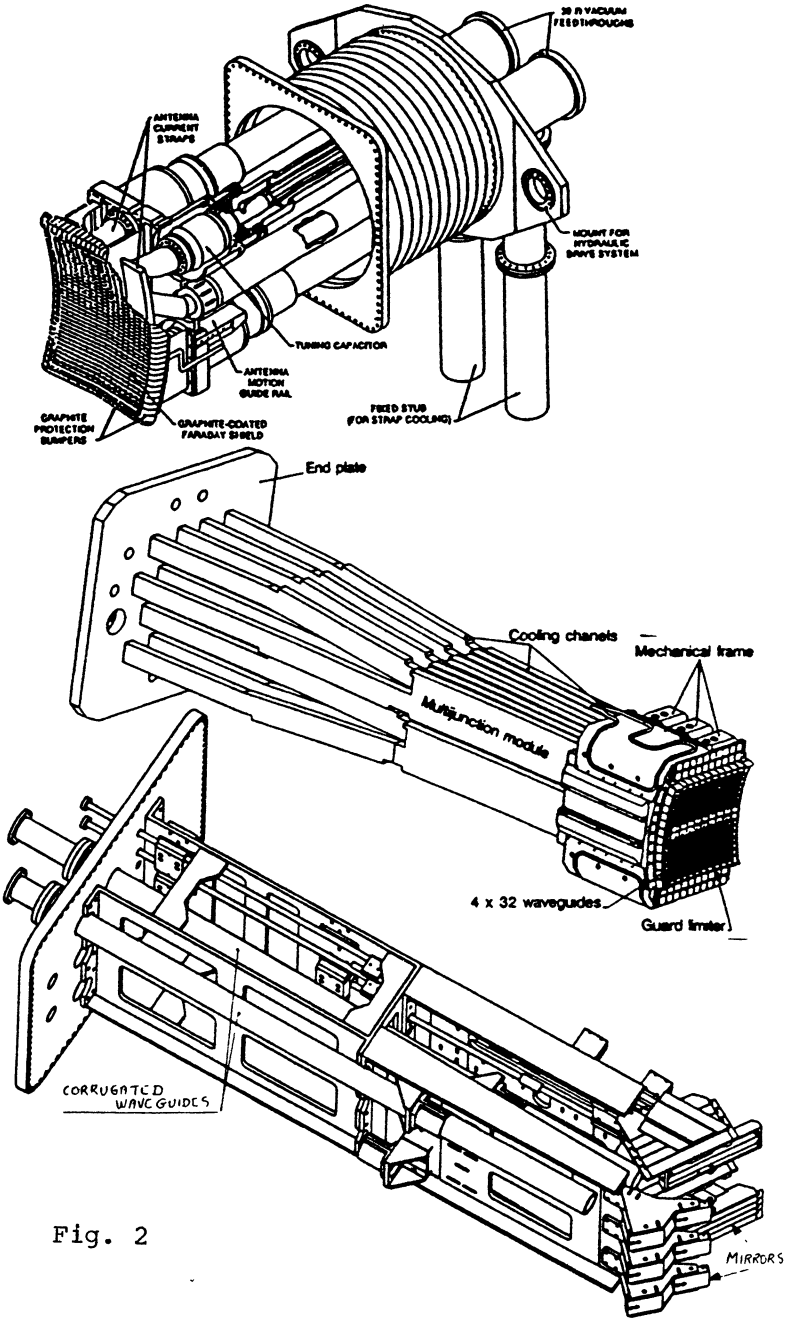
ANTENNA CURRENT STRAPS
TUNING CAPACITOR
ANTENNA MOTION GUIDE RAIL
GRAPHITE PROTECTION BUMPERS
GRAPHITE-COATED FARADAY SHIELD
FEED STUB (FOR STRAP COOLING)
End plate
Cooling channels
Mechanical frame
Multijunction module
4 x 32 waveguides
Guard limiter
CORRUGATED WAVEGUIDES
MIRRORS

Fig. 2

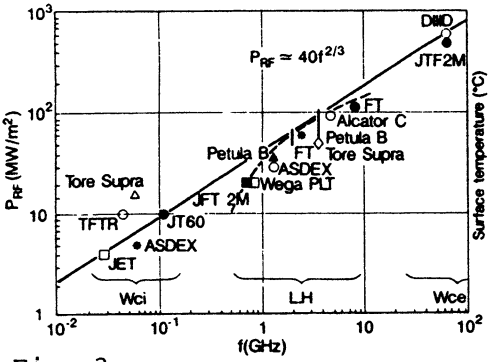

Fig. 3

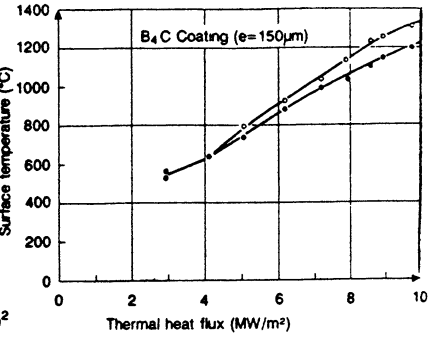

Fig. 4

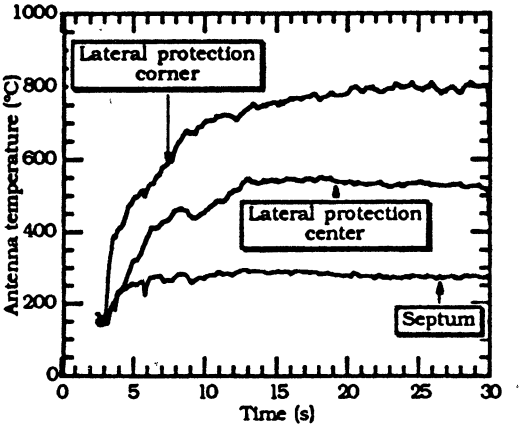

Fig 5

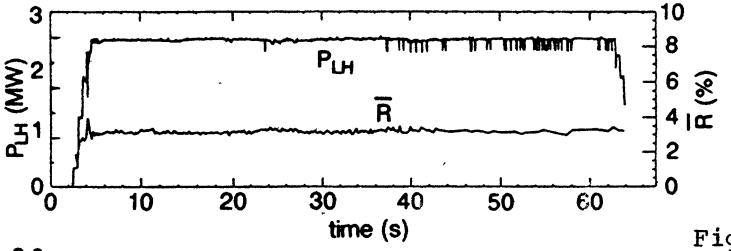

Fig. 6

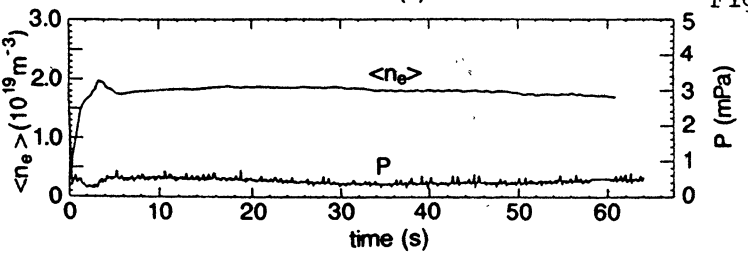

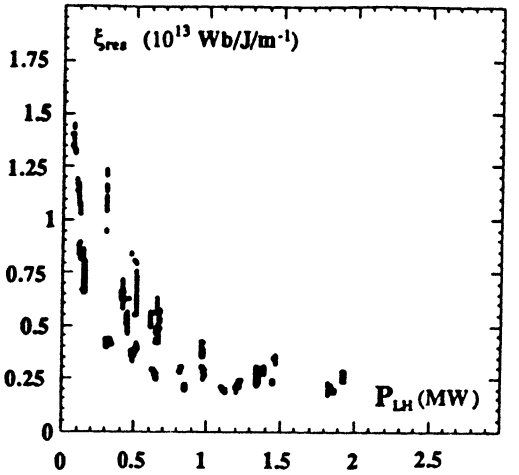

Fig. 7

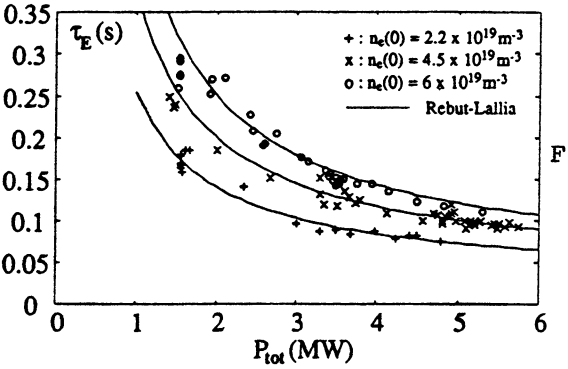

Fig. 8

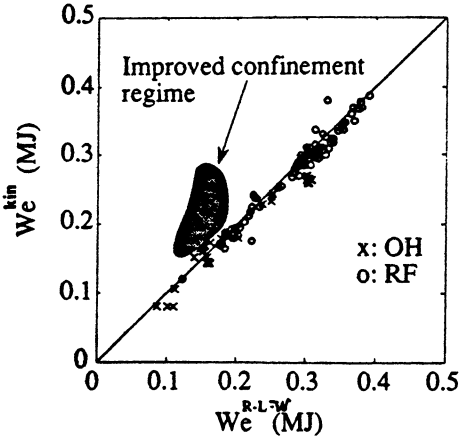

Fig. 9

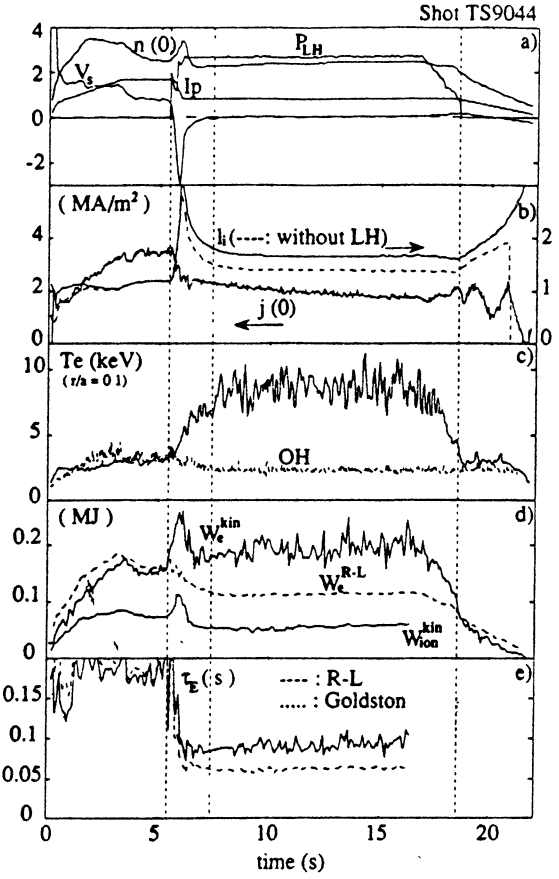
Shot TS9044
n (0)
P_{LH}
a)
V_s
Ip
(MA/m²)
b)
l_i (----: without LH)
j (0)
Te (keV)
(r/a = 0.1)
c)
OH
(MJ)
d)
W_e^{kin}
W_e^{R-L}
W_{ion}^{kin}
τ_E (s)
e)
---- : R-L
..... : Goldston
time (s)

Fig. 10

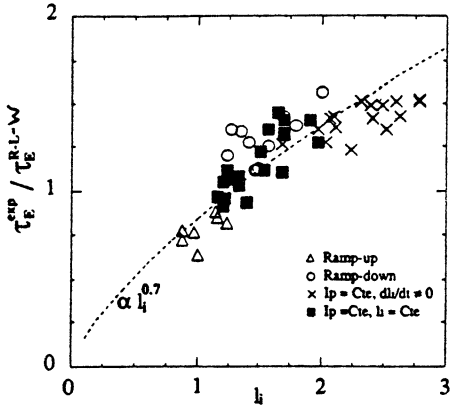
$\tau_E^{exp} / \tau_E^{R-L-W}$
$\alpha\ l_i^{0.7}$
Ramp-up
Ramp-down
Ip = Cte, dli/dt ≠ 0
Ip =Cte, li = Cte
l_i

Fig. 11

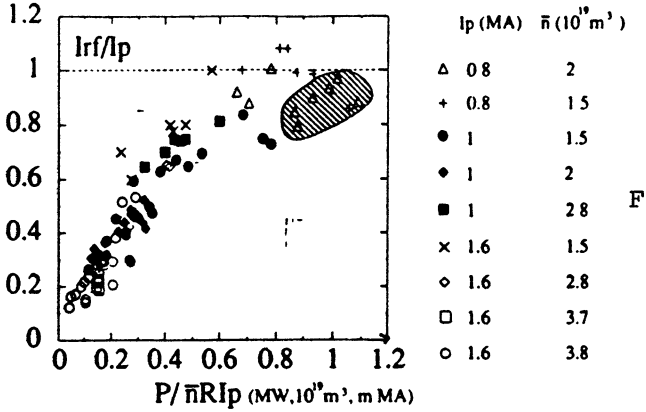

Fig. 12

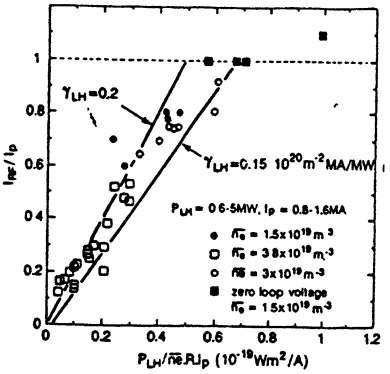

Fig. 13

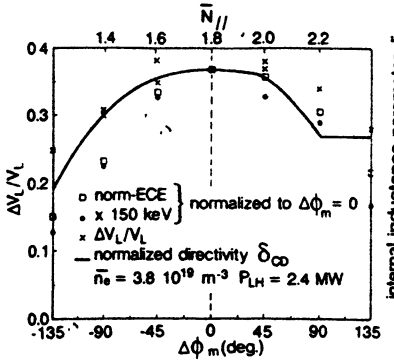

Fig. 14

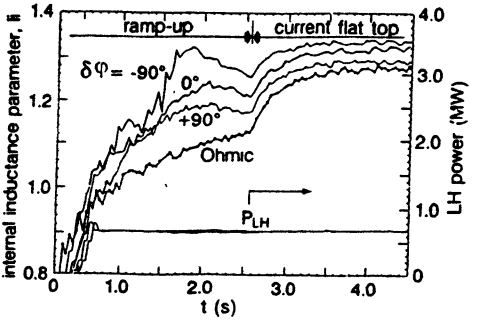

Fig. 15

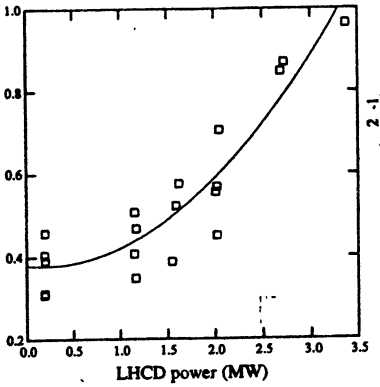

ig. 16

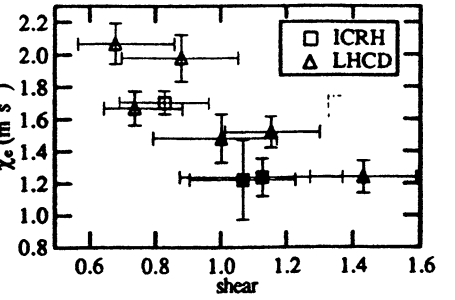

Fig. 17

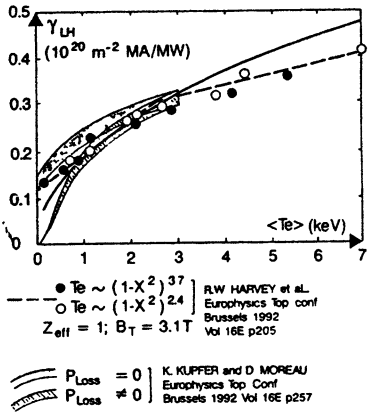

Fig. 18

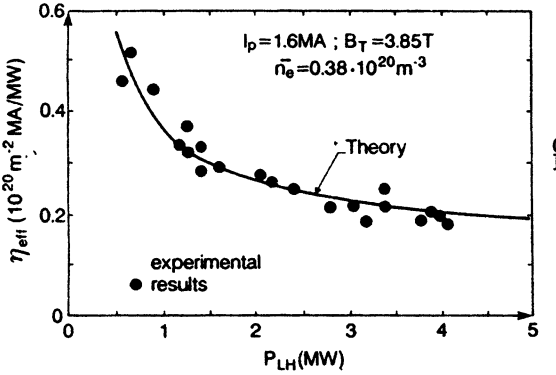

G
Fig. 19

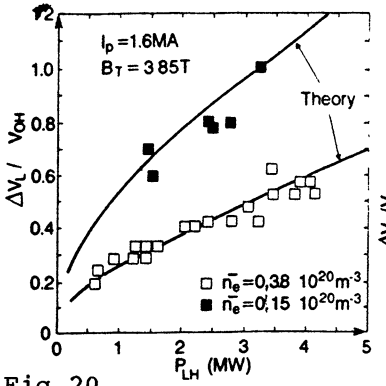

Fig.20

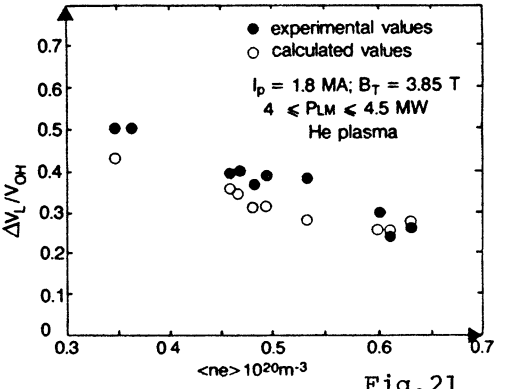

Fig.21

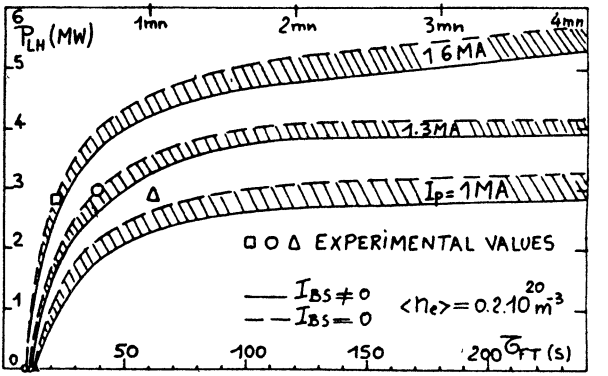

Fig.22

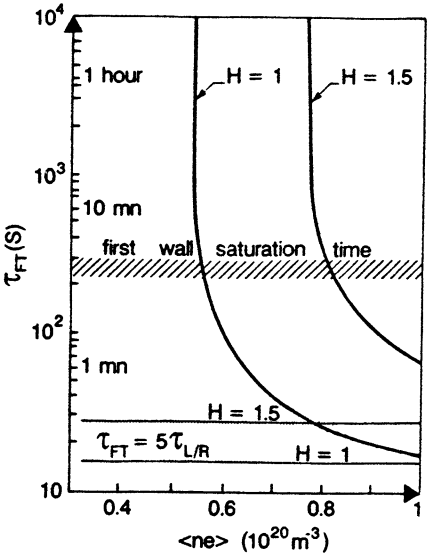

Fig. 23

8 GHz experiment on FTU

A.A. Tuccillo, E. Barbato, L. Gabellieri, G. Granucci*, S. Ide†
P. Micozzi, L. Panaccione, V. Pericoli, S. Podda, F. Santini, G. Tonini
F. Alladio, M.L. Apicella, G. Apruzzese, R. Bartiromo, F. Bombarda,
G. Bracco, G. Buceti, P. Buratti, A. Cardinali, R. Cesario, M. Ciotti,
V. Cocilovo, A. Coletti, I. Condrea, F. Crisanti, R. DeAngelis,
F. DeMarco, B. Esposito, T. Fortunato, D. Frigione, E. Giovannozzi,
M. Grolli, A. Imparato, H. Kroegler, L. Lovisetto, G. Maddaluno,
G. Maffia, M. Marinucci, G. Mazzitelli, S. Migliori, F. Mirizzi,
A. Moleti, F. Orsitto, M. Panella, L. Pieroni, G.B. Righetti,
M. Roccon, D. Santi, M. Sassi,E. Sternini, O. Tudisco, F. Valente,
V. Vitale, V. Zanza, M. Zerbini

Associazione EURATOM-ENEA sulla Fusione
Centro Ricerche Energia Frascati,
C.P. 65 - 00044 Frascati, Rome (Italy)

Abstract

The FTU 8 GHz Lower Hybrid system started operation with the first of its 9 gyrotrons. The 1 MW power output of the tube feeds a 12 x 4 waveguides grill obtaining, in routine operations, a net specific power higher than 10 kW/cm^2. Good power coupling to the plasma is observed with reflection coefficients close to the theoretical expectations. Interaction of the launched waves with plasma electrons is detected up to a density $\overline{n}_e \sim 10^{20} m^{-3}$

*Istituto di Fisica del Plasma,CNR, Milano, Italy
†Naka Fusion Research Establishment, JAERI, 311-01 Japan

while waves at $N_{||} = 1.56$ have fully driven a plasma current of 230 kA at $\overline{n}_e \sim 3.5 \times 10^{19}\ m^{-3}$ yielding an efficiency $\eta \sim\ 1.4[10^{19} m^{-2} A/W]$. In this condition strong central electron heating occurs producing very peaked temperature profiles. Preliminary results on the modification of pellet ablation due to fast electrons created by Lower Hybrid waves are also reported.

Introduction

The Frascati Tokamak Upgrade (FTU) is a high magnetic field device with major radius 0.935 m and minor plasma radius 0.3 m. Its power supplies allow for 1.5 sec discharges at a plasma current of 1.6 MA with a toroidal field of 8 T. Main aim of the experiment is to study plasmas of thermonuclear interest with strong additional RF heating in regimes were electron and ion species are strongly coupled. To satisfy these requirements, with Lower Hybrid (LH) waves, a frequency of 8 GHz was chosen and a 1 $MW - 1$ sec gyrotron has been developed as RF power generator . This combination of "high frequency - gyrotron oscillator - LH" could give an important contribution to the assessment of LH scenarios for the next generation of reactor relevant devices like ITER.

We will report on the results obtained during the first months of operation with the first prototype tube that, despite some problem connected with the low flexibility in the power handling capability, already has permitted the successful beginning of the FTU LH experiment.

The LH system

The complete FTU LH system will have nine identical transmitter modules. Each transmitter is powered by a 8 $GHz - 1$ $MW - 1$ sec gyrotron fed, through a modulator and crow-bar unity, by a 100 $kV -$ 30 A power supply. The $TE^{\bigcirc}_{511}$ oscillation mode of the gyrotron is converted in the $TE^{\bigcirc}_{01}$ and transmitted to a mode converter and

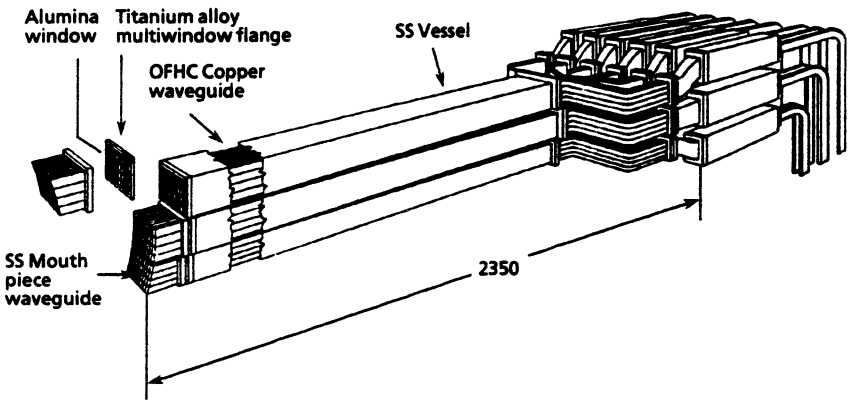

Figure 1: FTU LH antenna

power splitter by a 30 m long oversized circular waveguide (C_{18}), with negligible attenuation. The RF power is then available in the torus hall in 12 rectangular WR 137 waveguides in the $TE_{10}^{\square}$ mode. Each of these waveguides is phase controlled and then splitted in four to feed one column of a grill. Three of such grills are superimposed, as shown in Fig. 1, to be inserted in a FTU port. The whole structure has 7 cm stroke to allow to match all plasma conditions. The stainless steel mouth piece of the grills is gold plated and consists of 4 rows of 12 waveguides with inner dimensions 4.2×28 mm^2 and 0.8 mm wall allowing the production of the directional and symmetric spectra, shown in Fig. 2, with $1 \lesssim N_{\|} \lesssim 3.8$ and $\Delta N_{\|} \cong 0.6$ full width at half maximum. The mouth pieces are 15 cm long and are separated from the air filled section of the grill by a multiwindow array where 48 bricks (3.6×28 mm^2) of Al_2O_3 are brazed on a Ti alloy frame, with overall dimension 13.7×9 cm^2.

The total power losses, from the end of the circular waveguide up to the plasma, amounts to $\sim$ 40 % and are mainly due to the splitter - converter and to the reduced rectangular waveguides. Taking into account reflection from the plasma, still the net power available at mouth piece gives a specific power higher than 10 kW/cm^2, cor-

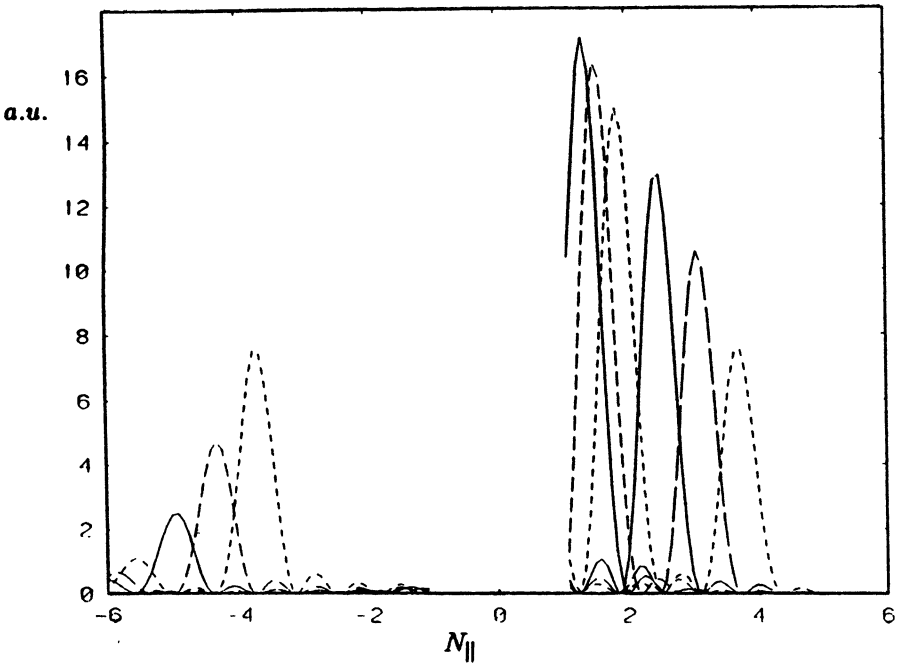

Figure 2: Spectra produced by FTU grill: 65, 75, 90, 120, 150,180deg phasing

responding to a total coupled power of about 0.5 MW. Moreover the proper oscillation mode of this prototype gyrotron is maintained in a very narrow space of its electrical parameters, allowing for the production of only full power RF pulses. Nevertheless long pulses operation can be routinely carried out with a 30 % probability to have the RF pulse modulated on-off by the protection of reflected power in the single waveguides. The possibility of independent phasing of each column, together with the measurement of direct and reflected power in each waveguide of the grill[1], gives to the system very high flexibility for physics studies.

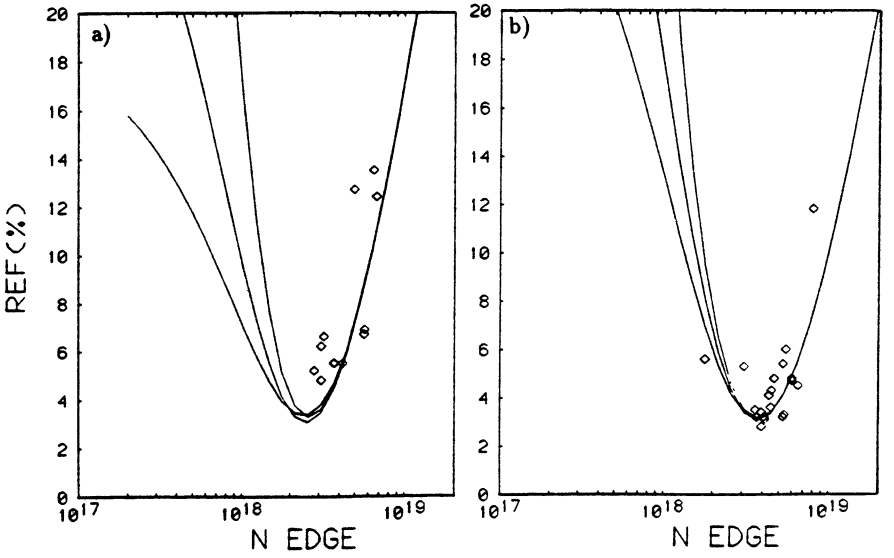

Figure 3: Reflection coefficient: a) 75 deg; b) 90 deg. Lines are Brambilla calculation with finite density at grill mouth followed by three different gradients, from the top: 1, 4, 8×10^{20} m^{-4}

Coupling

As already mentioned all LH experiments on FTU are carried out at the maximum output power of the gyrotron with a specific transmitted power, averaged on the 48 waveguides of the mouth piece, higher than 10 kW/cm^2 corresponding to a value $\gtrsim$ 11 kW/cm^2 on the Al_2O_3 windows. Despite this high value we obtain a very good power coupling to the plasma with a global reflection coefficient $R \lesssim$ 10 % that can be reached in all the experimental conditions[2].

It turns out that the minimum obtained reflection coefficient, for a given phasing, is $\sim$ 5 % higher of the theoretical expected one. Partly this discrepancy can be attributed to the intrinsic reflection of the launcher that is estimated to be $\sim$ 2 %.

In order to compare the measured reflected power with the prediction of the theory we have deduced, when possible, the scrape-off

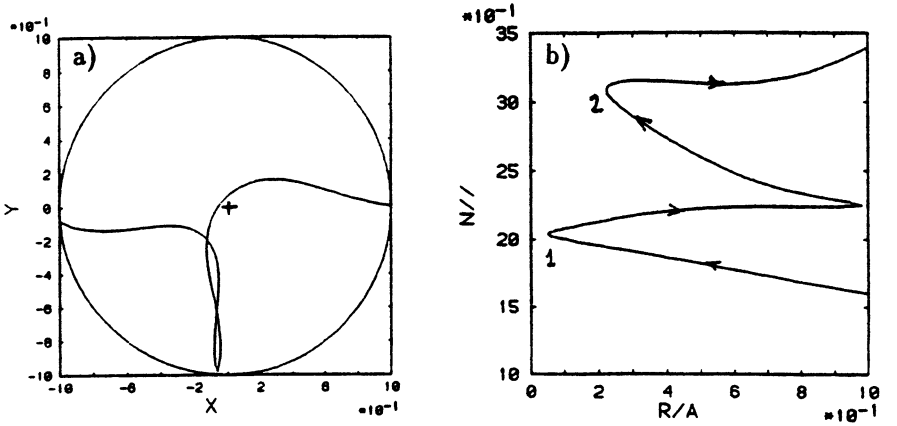

Figure 4: a) Projection in a poloidal section of a LH ray trajectory; b) Variation of $N_{||}$ along the trajectory. Plasma parameter: $I_p = 300\ kA, B_T = 6\ T, \overline{n}_e = 3 \times 10^{19}\ m^{-3}$

density at the grill mouth using movable Langmuir probes located on the equatorial plane 60 deg toroidally away from the LH antenna. With the FTU equilibrium code[3] we follow a field line starting from the grill mouth up to its crossing with the radial excursion of a Langmuir probe. The density measured in this position is then used together with the actual measurement of the reflection coefficient to compare with the predictions of a Brambilla code[4]. In this calculation a finite density at the grill mouth is assumed, followed by a density gradient. The data obtained with this procedure qualitatively reproduce the expected behaviour of the reflection coefficient as a function of the local plasma density. If we further correct the data by the 5 % higher reflection coefficient, systematically measured, we obtain the very good agreement documented in Fig. 3 a,b. In these figures data from 75 deg and 90 deg are compared with the results of the Brambilla code (continuous lines), the splitting of the computed curves on the left side being due to three different density gradients 1, 4, $8 \times 10^{20}\ m^{-4}$ following the density step at the grill mouth.

The lack of data in the left side of the figures reflects the FTU scrape-off conditions with fully circular plasmas. To explore this

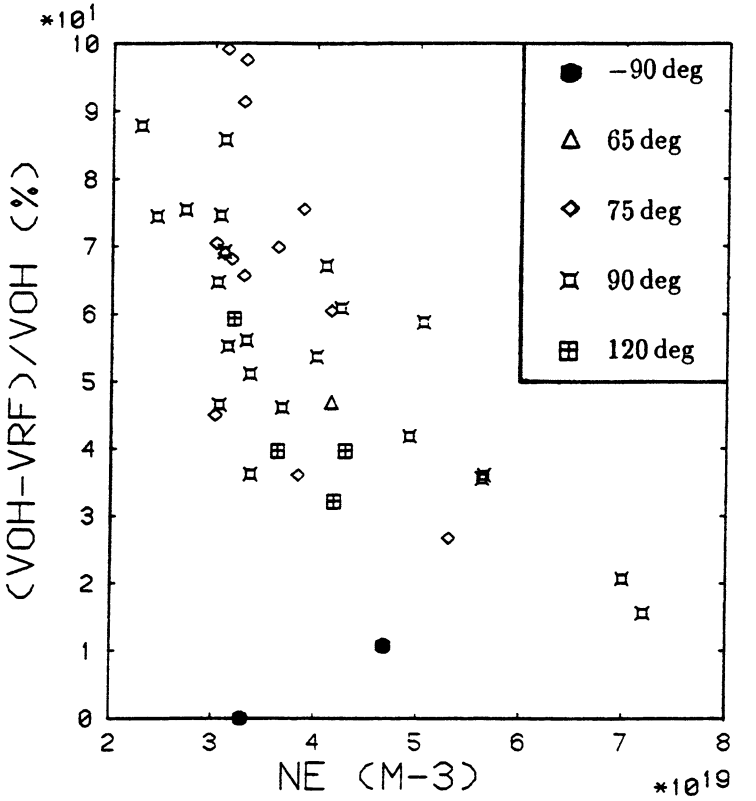

Figure 5: Relative loop voltage drop versus line averaged density. Plasma parameter: $I_p = 220 \div 300\ kA, B_T = 6\ T$

range of coupling densities it would be necessary to increase the distance between the grill and last closed magnetic surface by pushing the plasma toward the inner wall or by non circular shaping.

Heating and Current Drive

Operations with the prototype gyrotron allow to couple to the plasma a net power of 500 kW with a variability of 10 % mainly due to the variations of the coupling conditions. As a consequence the plasma

parameter range that can be explored is limited. In order to increase the fraction of driven current most of the experiments are then carried out at low plasma current $I_p \lesssim$ 300 kA (B_T = 6 $T, q_a \gtrsim$ 10) and electron density $\overline{n}_e \lesssim 4 \times 10^{19}$ m^{-3} , conditions that are at the lower limit of FTU operation space.

A typical ray-trajectory[5] for such a plasma, with the LH grill phased for current drive (CD), is shown in Fig. 4 a. It is possible to see that the wave goes straight to the centre and then suffers a reflection at bottom border of the plasma. From Fig. 4 b we see that a moderate up-shift is already present in the first pass, $N_{||}$ goes from 1.6 to 2.1, while a larger one occurs after the bottom reflection up to $N_{||} \sim 3.2$, close to the plasma centre. These data suggest high RF power absorption in agreement with the estimate obtained from the rate of change of equilibrium energy at the switch-on of RF, where a fraction of absorbed power $\alpha \sim 0.7 \div 0.8$ is generally found.

In Fig. 5 we summarise our results plotting the relative loop voltage drop versus the line averaged density. During the injection of LH power the plasma current is kept constant by feedback control. The large dispersion of experimental data is partly due to differences in the net LH power coupled to the plasma and partly to the differences in Z_{eff}. As the figure shows the CD effects, at this level of LH power, become very small as the density increases. For $\overline{n}_e \sim 10^{20}$ m^{-3} the evidence of wave interaction with electrons is recorded only by electron cyclotron and hard x-ray emission[6]. In the scatter of points it is difficult to recognise a difference in the effectiveness of the different phasing except for the reversed 90 deg where hardly any reduction of loop voltage is measured. Some minor differences can be detected with the 120 deg phasing where the directivity reduces to $\sim$ 80 %. For the 65 deg, where accessibility to the centre is not any more satisfied, the only point available does not show evident differences from the other phasing.

In the Fig. 5 two points at $\overline{n}_e \lesssim 3.3 \times 10^{19}$ m^{-3} exhibit $\sim$ 100% of loop voltage drop. They refer to full CD with 75 deg phasing and a lower plasma current I_p = 230 kA. Assuming that the residual electric field has a negligible effect ($V_{loop} \lesssim 50$ mV) we evaluate a CD

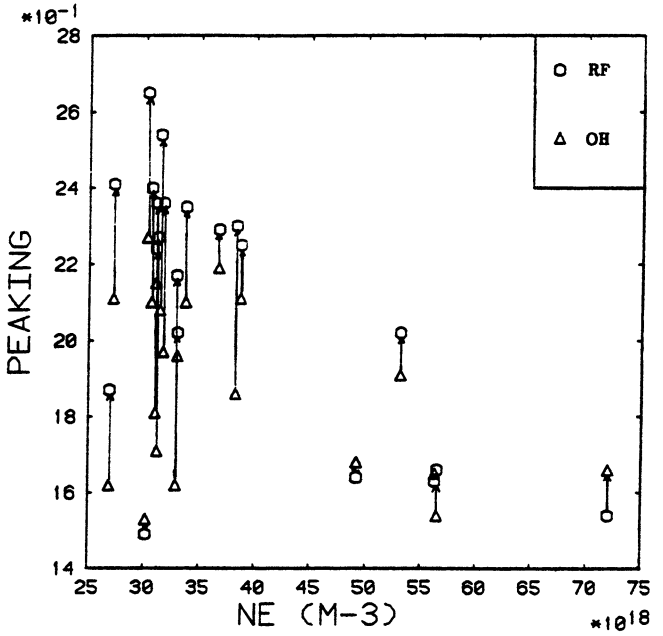

Figure 6: Peaking factor with LH versus line average density. Plasma parameter: $I_p = 220 \div 300\ kA, B_T = 6\ T; phasing = 65, 75, 90$ deg

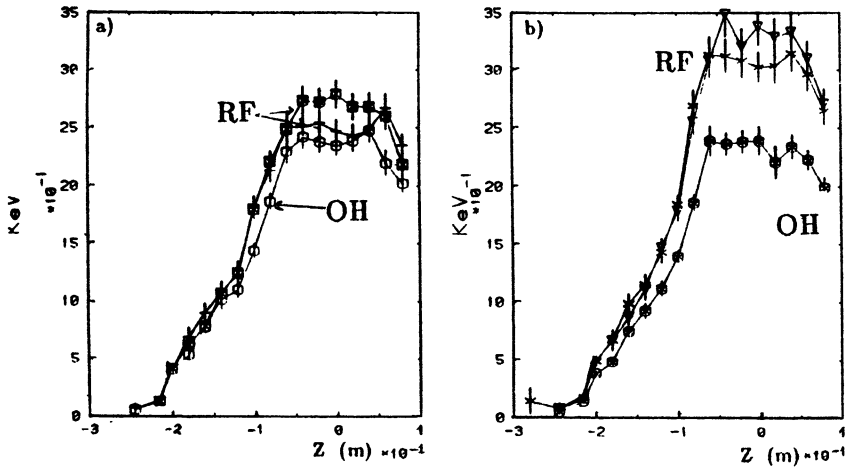

Figure 7: Electron temperature profiles: a) 90 deg; b) -90 deg. Plasma parameter: $I_p = 500\ kA, B_T = 6\ T, \overline{n}_e \sim 5 \times 10^{19}\ m^{-3}$

efficiency $\eta \sim 1.4\ [10^{19} m^{-2} A/W]$. This value must be considered a lower limit of the FTU capability because of the particular discharge conditions (low density, high Z_{eff}, poor confinement). Furthermore it must also be considered that the strong up-shift suffered by the waves at first pass can play a role in lowering the CD efficiency.

In CD discharges the LH generated fast electrons stimulate a strong central electron heating[2,7,8], leading to strong peaking of the electron temperature profiles[8]. Only minor changes are detected on the electron density profile, that generally slightly broadens. In Fig. 6 we report the change of the peaking factor $P = T_{e0}/\overline{T}_e$ versus line average density. It is evident that, because of the high value of the safety factor ($q_a \gtrsim 10$), already in the ohmic phase the profiles are peaked, nevertheless they further peak in the LH phase.

Comparing with the data of Fig. 5 we see that the peaking effect reduces according with the loop voltage drop and ultimately with CD effects. This is further demonstrated in discharges at lower q_a; $I_p = 500\ kA$ that also exhibit small or no modifications of the peaking factor either with or without consistent heating effects. An example is reported in Fig. 7 where two profiles obtained at $\overline{n}_e \sim 5 \times 10^{19}\ m^{-3}$ and $q_a \lesssim 6$ are shown. A CD phasing of 90 deg was applied to the discharge of the case a) obtaining $\sim 20\%$ reduction of loop voltage and only $\sim 200\ ev$ of heating; in the case b) the anti CD -90 deg was used, no reduction of loop voltage and $\Delta T > 1\ Kev$ was recorded: in both case the peaking factor stayed at the ohmic value of 1.7.

Furthermore we want to point out that from a preliminary estimate of global energy balance in discharges at $I_p = 300\ kA$ and $\overline{n}_e = 3 \div 5 \times 10^{19}\ m^{-3}$ confinement times within the dispersion of the ohmic values, in the same plasma conditions, are obtained. A more detailed analysis is absolutely necessary before we can try any conclusion. Open questions are the LH power deposition and a complete evaluation of radiation balance mainly in the lower density cases where high value of Z_{eff} are present already in the ohmic plasmas.

Finally we want to point out that, because of our high values of q_a, the discharges generally do not have sawtooth activity, that can occasionally be triggered by the LH pulse. When sawteeth are present

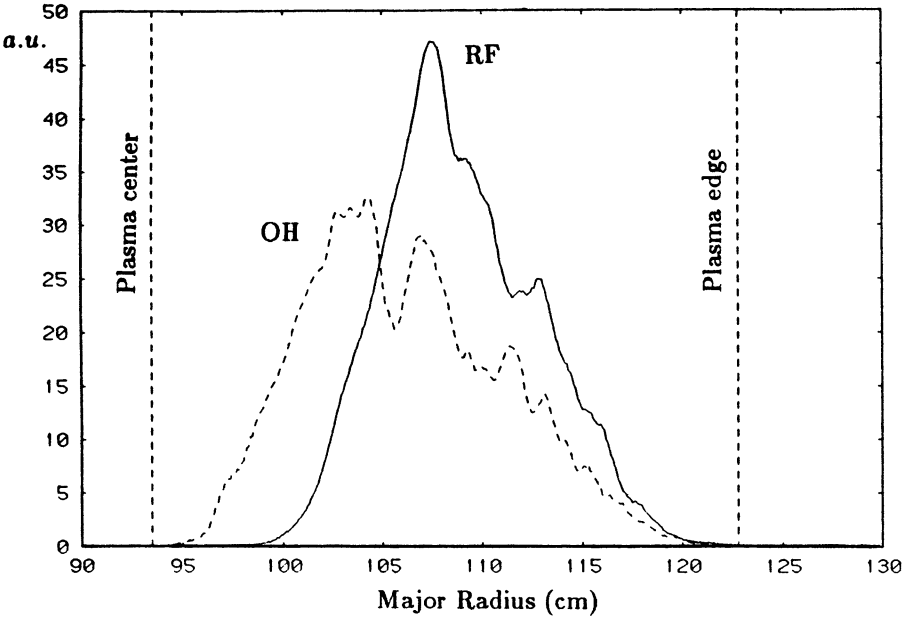

Figure 8: H_α emission during pellet injection with and without LH. Plasma parameter: $I_p = 300\ kA, B_T = 6\ T, \overline{n}_e \sim 3 \times 10^{19} m^{-3}$; $phasing = 90\,\mathrm{deg}$

in the target plasma their period strongly increase with LH phased for CD and according to the magnitude of CD effects[2]. With opposite CD phasing the period hardly change or slightly decreases. Also MHD activity in this conditions is mostly quiescent and generally stays unchanged during LH injection.

Pellet Ablation

In order to infer information on the fast electron population, created by LH waves, an experimental program has started to study the modification induced by the fast particles on the pellet ablation. On the other hand this modification of ablation mechanisms is of major importance in order to investigate the possibility of pellet injection

to fuel reactor relevant plasmas.

D_2 pellets are fired in the FTU plasmas by the Frascati high velocity ($V_{pellet} \leq 2.5\ Km/s$) injector[9]. The ablation is monitored by an H_α signal looking at the pellet path from the injector. Assuming constant velocity, the penetration depth can be estimated from this measurement.

A preliminary result is reported in Fig. 8 where the H_α emission of an ohmic discharge is compared with one from a 200 ms LH CD discharge where in both cases a pellet of approximately 10^{20} deuterium atoms was injected. The X-axis as been reconstructed assuming constant the pellet velocity $V_{pellet} = 1.8\ Km/s$. The parameters of the ohmic target plasma were: $I_p = 300\ kA, B_T = 6\ T, \overline{n}_e \sim 3 \times 10^{19}\ m^{-3}$, with a central electron temperature $T_{e0} = 2\ Kev$. In the OH discharge a penetration $\lesssim 25\ cm$ is obtained. Firing the pellet after 200 ms of 90 deg phased LH, with 50 ms of delay with respect to the LH pulse switch-off, a penetration shorter of about 10 cm is obtained. This difference does not change up to a firing delay, with respect to LH switch-off, of 100 ms suggesting a longer confinement time of energetic electron as found in other experiments[10]. This conclusion is very preliminary, more informations are necessary mostly regarding fast electrons energy and radial localisation. To diagnose these quantities an array of hard x-ray detectors, looking perpendicularly at the plasma, is under construction and will be in operation next year.

Conclusion

For the first time a high power gyrotron has successfully permitted a LH experiment. The gyrotron based LH experiment of FTU started operation obtaining very encouraging result in view of its extension at the full power of 9 MW. Very good coupling of LH power to FTU plasmas has been obtained, in agreement with theoretical expectations, with a transmitted power density $> 10\ kW/cm^2$. Encouraging heating and current drive effects have been obtained with a full CD efficiency $\eta \sim 1.4\ [10^{19} m^{-2} A/W]$. From preliminary results of modifications of pellet ablation a confinement time of energetic electrons

higher than 100 *ms* is evaluated.

References

[1] S. Di Giovenale et al., XVII SOFT, Roma, Italy 1992.

[2] F. Alladio et al., Tenth Topical Conference on RF power in Plasmas, Boston, USA 1993.

[3] F. Alladio and F. Crisanti Nuc. Fusion **1143**, 26 (1986).

[4] M. Brambilla, Nuc. Fusion **16**, 47 (1976).

[5] E. Barbato, Joint Varenna-Lausanne Work. on theory of fusion plasmas, Lausanne 1988, **577**, Ed. Compositori Bologna (1989).

[6] F.Alladio et al., XII Int. Conference on Plasma Physics and Controlled Fusion, Nice, France 1988.

[7] F. Alladio et al, LH Heating experiments in FT Tokamak, IX Int. Conf. on Plasma Physics, Baltimore, USA, 1982.

[8] F.X. Soeldner et al., XIII Int. Conference on Plasma Physics and Controlled Fusion, Washington, USA 1990.

[9] F. Alladio et al., Proc. of the IAEA Technical Committee Meeting on Pellet Injection, Japan JAERI, Naka Ibaraki-Ken, Japan 1993.

[10] R. Bartiromo et al., Fast electron confinement during LH experiments in Asdex, RT/NUCL/92/35, To be published on Nuc. Fusion

Development of ECH System for Large Helical Device at NIFS

K. Ohkubo, S.Kubo, M.Sato,
H. Idei, Y. Takita and T.Kuroda
National Institute for Fusion Science,
Furo-cho, Chikusa-ku, Nagoya, 461-01, Japan

ABSTRACT

An overall ECH system for LHD is described and how to create the elliptic gaussian beam for LHD antenna is discussed. The numerical and experimental results from the square corrugated waveguide and the parallel corrugated plate are given. By using the eigen mode expansion, coupling of circular to rectangular corrugated waveguides and the mode purity calculation are examined.

1 ECH system for LHD

R&D for 84 GHz-ECH system of the large helical device (LHD) in National Institute for Fusion Science is being carried out from the viewpoint of progress in handling the high-power CW millimeter waves. The gyrotron required to generate large amounts of power for LHD ECH- system with 3 MW for CW and 10 MW for 10 sec is still under the development. For the first stage a gyrotron with radial beam extraction and split waveguide was tested upto 0.9 MW for short pulse. The trials to increase the pulse length are now under the way. At the same time, the gyrotron power supply (Fig.1) with two deck modulator (TH5188), a series tube (CQK400-4A) and the performance of beam current 25(CW) $-$50A($\leq$ 10 s) is being tested

with a gyrotron load for the purpose of stable and long-pulse operation. The design of a gyrotron with an internal Vlasov coupler and a curved mirror is being performed for second stage of development. As for the transmission system, quasi-optical transmission and waveguide transmission are discussed. Out of the vaccum vessel the corrugated waveguide will be used and in the vessel the combination of both methods is introduced. The main subject of the paper is discussed analytically and experimentally on components of newly developed square corrugated waveguide and parallel corrugated plate for getting a elliptic gaussian beam.

2 Rectangular corrugated waveguide

An elliptic gaussian beam with the waist size w_x of x-direction different from that of y-direction w_y is necessary for the limitation of port size of the LHD vaccum vessel and for the rectangular window in the gyrotron installing the Vlasov convertor. To produce the elliptic gaussian beam, a candidate is that HE_{11} mode in the circular corrugated waveguide is mode-converted to HE_{11} mode in the square corrugated waveguide and that the aspect ratio of waist sizes in the output is changed. The other is an application of curve mirrors including the correction of amplitude and phase of the gaussian beam. Let discuss rectangular waveguide of $a \times b$ with two parallel walls having isotropic impedance surfaces at $x = 0$ and $x = a$, the other two walls being anisotropic at $y = 0$ and $y = b$ as shown in Fig.2. The dispersion relation, EM field and attenuation constant of the rectangular corrugated waveguide are discussed by the x-component Π_x of a Hertz vector [1,2];

$$(1) \qquad \Pi_x = A\sin(n\pi x/a)[\exp(-i\gamma y) \pm \exp(i\gamma(y-b))]\exp(-i\beta z).$$

Here, $\Pi_y = 0$, $\Pi_z = 0$ and plus (minus) sign represents symmetric (anti-symmetric) mode and n the mode number along x-direction. The EM field is calculated from

$$(2) \qquad \vec{E} = -i\omega\mu_0 \nabla \times \vec{\Pi},$$

(3) $$\vec{H}=k_0^2\vec{\Pi}+\nabla\nabla\cdot\vec{\Pi}.$$

The constant A normalized by $\int \vec{E}\times\vec{H}\cdot d\vec{S}=1$ is given by

(4) $$A=(k_0\beta Z_0)^{-1/2}[k_0^2-(n\pi/a)^2]^{-1/2}[\pm(\sin\gamma b)a/\gamma+ab]^{-1/2},$$

where β is given by

(5) $$\beta=\sqrt{k_0^2-(n\pi/a)^2-\gamma^2}\quad .$$

The dispersion relation is calculated from the condition where the surface impedance Z_{cor} on the corrugated surfaces is equal to the wave impedance $Z_w=\pm E_y/H_z$ on the surface of $y=0$ and $y=b$;

(6) $$Z_{cor}=\frac{iWZ_0}{P}\frac{\tan(k_0d\sqrt{1-(n\lambda/2a)^2})}{1-(n\lambda/2a)^2},$$

(7a) $$Z_{ws}=-\frac{i\gamma Z_0}{k_0}\frac{\tan(\gamma b/2)}{1-(n\lambda/2a)^2},$$

(7b) $$Z_{wa}=\frac{i\gamma Z_0}{k_0}\frac{\cot(\gamma b/2)}{1-(n\lambda/2a)^2}.$$

where, d, P and W is the depth, the pitch and the width of corrugation. For symmetric (asymmetric) mode $Z_{ws}(Z_{wa})$ is used. For body mode, γ is real and for surface mode γ imaginary. In Fig.3 (a) and (b), $|\beta|$ (rad / cm) and $|\gamma b/\pi|$ as a function of $D(=d/(\lambda/4))$ are shown for $W/P=0.5$, $n=1$, $a=b=82.1$ mm and $\omega/2\pi=84$ GHz. It is shown that γ is equal to $l\pi/b$ (l = odd (even) number for symmetric (anti-symmetric) mode) at $D=1$.

In the case of $D=1$, EM field is given by

(8a) $$E_x=0,$$

(8b) $$E_y=i2Ak_0\beta Z_0\sin\frac{n\pi x}{a}\sin\frac{m\pi y}{b}\exp(-i\beta z),$$

$$(8c) \qquad E_z = 2A\frac{m\pi}{b}k_0 Z_0 \sin\frac{n\pi x}{a}\cos\frac{m\pi y}{b}\exp(-i\beta z),$$

$$(8d) \qquad H_x = -i2A[k_0^2 - (\frac{n\pi}{a})^2]\sin\frac{n\pi x}{a}\sin\frac{m\pi y}{b}\exp(-i\beta z),$$

$$(8e) \qquad H_y = -i2A\frac{n\pi}{a}\frac{m\pi}{b}\cos\frac{n\pi x}{a}\cos\frac{m\pi y}{b}\exp(-i\beta z),$$

$$(8f) \qquad H_z = -2A\beta\frac{n\pi}{a}\cos\frac{n\pi x}{a}\sin\frac{m\pi y}{b}\exp(-i\beta z).$$

where $Z_0 = \sqrt{\mu_0/\varepsilon_0}$. Because the orders of E_y, E_z, H_x and H_z are $O(k_0^2)$, $O(k_0/b)$, $O(k_0^2)$, $O(1/(ab))$ and $O(k_0/a)$, respectively, EM field mainly consists of E_y and H_x.

From the perturbation method, the attenuation constant α is determined from calculating the surface current $\vec{J}_s = \vec{n} \times \vec{H}$ on the walls at $x = 0, x = a, y = 0$ and $y = b$. Here, $\vec{n}$ is the normal vector at the wall. Results from the calculation of

$$(9) \qquad \int_L \frac{R_\Omega}{2}\vec{J}_s \cdot \vec{J}_s^* dL = 2\alpha\frac{1}{2}\int \vec{E} \times \vec{H}^* \cdot d\vec{S}$$

determine attenuation constant α and is shown in Fig.3(c). Here, R_Ω is the surface resistance and L is the circumstance of the waveguide cross section. The main field components E_y and H_x have a function of $\cos(n\pi\xi/a)\cos(m\pi\eta/b)$ when the corrugated depth is equal to $\lambda/4$. Here, the origin of (ξ, η) is in the center of waveguide. For $n = m = 1$ and $a = b$, the function is well approximated as $J_0(r\chi_{01}/R)$ of HE $_{11}$ mode in the circular corrugated waveguide with the radius R within the second order of expansion when $a = \sqrt{2}R\pi/\chi_{01} = 1.84\ R$. Also, it is wothnoted that the abovementioned sinusoidal function is the same as the gaussian function $\exp[-(\pi\xi/a)^2/2 - (\pi\eta/b)^2/2]$ within the second order in expansion. These profiles of the function are shown in Fig. 4.

To analyze the mode in rectangular corrugated waveguide injected with arbitrarily polarized HE $_{11}$ mode from the circular corrugated waveguide, it is necessary to discuss the cross polarized mode

where main electric and magnetic fields are in x-direction and y-direction in the same rectangular corrugated waveguide. The cross polarized mode called as tall waveguide modes was earlier discussed for the only fundamental mode from the viewpoint of low attenuation constant [2]. To calculate EM field in the cross polarized mode including higher modes, we use y-component of Hertz vector Π_y :

$$\Pi_y = \cos\frac{n\pi x}{a}\sin\frac{m\pi y}{b}\exp(-i\beta z). \tag{10}$$

By substituting Π_y into Eqs.(2) and (3), EM field is calculated as follows:

$$E_x = Bk_0\beta Z_0\cos\frac{n\pi x}{a}\sin\frac{m\pi y}{b}\exp(-i\beta z), \tag{11a}$$

$$E_y = 0, \tag{11b}$$

$$E_z = iB\frac{n\pi}{a}k_0 Z_0\sin\frac{n\pi x}{a}\sin\frac{m\pi y}{b}\exp(-i\beta z), \tag{11c}$$

$$H_x = -B\frac{n\pi}{a}\frac{m\pi}{b}\sin\frac{n\pi x}{a}\cos\frac{m\pi y}{b}\exp(-i\beta z), \tag{11d}$$

$$H_y = B[k_0^2 - (\frac{m\pi}{b})^2]\cos\frac{n\pi x}{a}\sin\frac{m\pi y}{b}\exp(-i\beta z), \tag{11e}$$

$$H_z = -iB\beta\frac{m\pi}{b}\cos\frac{n\pi x}{a}\cos\frac{m\pi y}{b}\exp(-i\beta z). \tag{11f}$$

Here, B and β are determined by the orthnormal relation and the Helmholtz equation, respectively;

$$B = 2(k_0\beta Z_0)^{-1/2}(ab)^{-1/2}[k_0^2 - (\frac{m\pi}{b})^2]^{-1/2}, \tag{12}$$

$$\beta = \sqrt{k_0^2 - (n\pi/a)^2 - (m\pi/b)^2}. \tag{13}$$

It is easily confirmed that the surface impedances at all the walls are zero. The profiles are not affected by the presence of the corrugated walls for the cross polarized mode.

3 Coupling of the circular to the square corrugated waveguide

In this section, mode purity accompanying with the mode conversion to square corrugated waveguide is discussed as abovementioned on the base of field profile fitting. In the rectangular corrugated waveguide, the orthnormal relation can be satisfied:

$$\int \vec{E}_i \times \vec{H}_j^* \cdot d\vec{S} = \delta_{ij}, \tag{14}$$

where δ_{ij} is 1 for $i = j$ and 0 for $i \neq j$. The EM field in the circular corrugated waveguide injected into the square one is written by superposition of the eigenmode in the square corrugated waveguide as

$$\vec{E} = \Sigma A_j(z)\vec{E}_j, \tag{15a}$$

$$\vec{H} = \Sigma A_j(z)\vec{H}_j, \tag{15b}$$

Since the coefficient A_j is calculated from

$$A_j = \int \vec{E} \times \vec{H}_j^* \cdot d\vec{S} = (\int \vec{E}_j \times \vec{H}^* \cdot d\vec{S})^*. \tag{16}$$

The mode purity $|A_j|^2$ is able to estimate easily due to

$$\Sigma|A_j|^2 = \int \vec{E} \times \vec{H}^* \cdot d\vec{S} = 1. \tag{17}$$

The injected $\vec{E}$ and $\vec{H}$ in the circular corrugated waveguide with $2R = 88.9$ mm , $W/P = 0.5$ and $\omega/2\pi = 84$ GHz are calculated by solving the dispersion equation. In Fig. 5, the calculated content $P_{11} = |A_0|^2$ of fundamental HE $_{11}$ mode in the rectangular corrugated waveguide and total transmitted flux $P_{in} = \int \vec{E} \times \vec{H}^* \cdot d\vec{S}$ to the waveguide mouth are plotted as a function of a, where the integal is carried out over the crosssection of the square waveguide. As earier discussed the maximum of $|A_0|^2$ is obtained when $a_{opt} = 1$.

$84R$. Here, the transmitted power to square corrugated waveguide is $P_{in} = 99.3$ %. On the power transmission including higher modes, the length a should be equal to $2R$. In Fig. 6, the content of mode purity in the square corrugated waveguide with $a = 2R$ for a various mode of HE $_{nm}$ is examined. As expected, all the higher modes with the even mode number have relatively large content, though absolute value is very small. The sum of total power flux $\Sigma|A_j|^2$ within the range of m and n less than 5 is 0.991.

4 Elliptic gaussian beam

It is planed for the LHD machine that the elliptic gaussian beam with large waist size w_x in toroidal direction is injected into plasmas. How to modify the aspect ratio w_y/w_x of waist size is an use of the taper waveguide with the rectangular cross section or an application of the parallel corrugated plates connecting to the circular or square corrugated waveguide. If the tapered corrugated waveguide would be used for $w_y/w_x \approx 2$, the analysis by using the raise cosine profile shows that the waveguide length is as long as 7 m for the input size of 82.1×82.1 mm ^{2}. The second method by parallel corrugated plates is discussed here (Fig.7). The analysis is based on the calculation of radiation by superposition of plane wave (SPW) [1], but the formulation is slightly changed due to the boundary corrugated plates. When a wave whose amplitude is orthnormalized propagates along z-direction, EM field at any z can be written in terms of their spectrum functions $\vec{S}_t(k_x, k_y)$ and $\vec{Q}_t(k_x, k_y)$ which calculated from the Fourier transformation of the transverse EM field $\vec{E}_{twg}(x_1, y_1)$ and $\vec{H}_{twg}(x_1, y_1)$ at the input of the parallel corrugated plates ($z_1 = 0$);

$$(18) \qquad \vec{S}_t(k_x, k_y) = \int\int \vec{E}_{twg}(x_1, y_1)\exp[i(k_x x_1 + k_y y_1)]\mathrm{d}x_1\mathrm{d}y_1$$

$$(19) \qquad \vec{Q}_t(k_x, k_y) = \int\int \vec{H}_{twg}(x_1, y_1)\exp[i(k_x x_1 + k_y y_1)]\mathrm{d}x_1\mathrm{d}y_1$$

The longitudinal spectrum functions for $\vec{E}_z$ and $\vec{H}_z$ are determined by $\vec{k} \cdot \vec{S} = 0$ and $\vec{k} \cdot \vec{Q} = 0$. The EM field at any output position z of the parallel plates is given by

$$(20)\quad \vec{E}(\vec{r}) = \int\int \frac{k_z \vec{S}_t - (\vec{k}_t \cdot \vec{S}_t)\vec{i}_z}{4\pi^2 k_z} \exp[-i(k_x x + k_y y + k_z z)] \mathrm{d}k_x \mathrm{d}k_y$$

$$(21)\quad \vec{H}(\vec{r}) = \int\int \frac{k_z \vec{Q}_t - (\vec{k}_t \cdot \vec{Q}_t)\vec{i}_z}{4\pi^2 k_z} \exp[-i(k_x x + k_y y + k_z z)] \mathrm{d}k_x \mathrm{d}k_y$$

Here, k_z depends only k_x due to $k_y = 0$

$$(22a)\qquad k_z = \sqrt{k_0^2 - k_x^2} \quad \text{when} \quad k_0 \geq k_x,$$

$$(22b)\qquad k_z = -i\sqrt{k_x^2 - k_0^2} \quad \text{when} \quad k_0 \leq k_x,$$

In Fig.8, E_y profile at the output mouse of the parallel corrugated plate with $z = 1$ m injected by HE $_{11}$ mode in the square corrugated waveguide (82.1×82.1 mm ^{2}) is shown.

The fundamental and higher modes contents of orthnormalized gaussian beam are analyzed by using the eigen value expansion which is earier discussed in Eqs.(15a) and (15b). In general, orthnormalized EM field of any gaussian beam [3] is written by

$$(23)\quad E_y(\vec{r}) = \frac{\sqrt{2/\pi}}{\sqrt{2^{l+m} l! m!}} \frac{\sqrt{Z_0}}{\sqrt{w_x(z) w_y(z)}} H_l\left(\frac{\sqrt{2}x}{w_x}\right) H_m\left(\frac{\sqrt{2}y}{w_y}\right)$$

$$\times \exp\left[-x^2\left(\frac{1}{w_x^2(z)} + \frac{ik_0}{2R_x(z)}\right) - y^2\left(\frac{1}{w_y^2(z)} + \frac{ik_0}{2R_y(z)}\right)\right]$$

$$\times \exp\left[-ik_0 z + i(l + \frac{1}{2})\tan^{-1}\frac{\lambda(z - z_x)}{\pi w_{0x}^2}\right.$$

$$\left. + i(m + \frac{1}{2})\tan^{-1}\frac{\lambda(z - z_y)}{\pi w_{0y}^2}\right],$$

(24) $$H_x(\vec{r}) = -\frac{E_y}{Z_0}.$$

where H_l is the Hermite polynomial of order l, and $w_x(z)$, $R_x(z)$ are the spot size and the radius of curvature of the very nearly spherical wavefront along x-direction at z. The parameters $w_x(z)$ and $R_x(z)$ are defined by w_{0x} which is the minimum spot size:

(25) $$w_x^2(z) = w_{0x}^2[1 + (\frac{\lambda(z - z_x)}{\pi w_{0x}^2})^2],$$

(26) $$R_x(z) = (z - z_x)[1 + (\frac{\pi w_{0x}^2}{\lambda(z - z_x)})^2].$$

It should be noted that no inclusion of exponential term without dependence of x and y is necessary for the calculation of $|A_{lm}|^2$. The radiation pattern shown in Fig. 8 is analyzed for the fundamental gaussian beam of $l = m = 0$ and contour of $|A_{00}|^2$ in the plan of (w_x, R_x) is plotted in Fig. 9. Here, in the parameter survey, we use that the elliptic gaussian beam can be considered as two independent beams. The maximum point of $|A_{00}|^2 = 0.975$ can be obtained at ($w_y = 28.8$ mm, $1/R_y = 0$) and ($w_x = 49.5$ mm , $R_x = 1580$ mm). It should be pointed out that there is no reason why we choose the maximum of fundamental mode $|A_{00}|^2$ and that any combination of fundamental and higher modes for reconstruction of the profile is possible. In Fig.10 (a)-(c), $|A_{00}|^2$, $|A_{20}|^2$ and $|A_{40}|^2$ for $z = 1$ m are plotted in (w_{0x}, z_x) plane in stead of (w_x, R_x) by using Eqs.(23)-(26). The maximum of $|A_{00}|^2$ is located at ($z_x = 0$ mm, $w_{0x} =$ 28.8 mm), while, the mimima of $|A_{20}|^2$ and $|A_{40}|^2$ are in the same position. For $z = 600(1400)$ mm, contour plots of $|A_{00}|^2$ shows the same figure, but maximum of $|A_{00}|^2$ is ($z_x = 400(0)$ mm, $w_{0x} =$ 28.8(28.8) mm). The results shows that the output patterns from the parallel corrugated plate is explained by gaussian beams with the same minimum waist size at $z_x = 0$ except near fields such as $z = 600$ mm .

5 Experiment and results

The HE $_{11}$ mode with the frequency of $\omega/2\pi = 84.05$ GHz excited in 88.9 mm-corrugated waveguide is injected into the polarizer. The output waveguide of the polarizer is connected to the 82.1 × 82.1 mm ^{2} square corrugated waveguide. The field pattern in front of the waveguide mouth is measured by means of the WR-12 waveguide antenna. Fig.11(a) shows the results from the E_y measurement when the input $\vec{E}$ from the polarizer is adjusted so as to satisfy $E_x = 0$. The contour of E_y is almost axi-symmetric near the center and shows expected pattern of HE $_{11}$. The measured cross polarized field E_x is less than − 20 db. In order to excite the cross polarization mode, the polarization angle is increased by 90 degrees. In Fig.11(b) the measured field pattern of E_x at the waveguide mouth is shown. The pattern is the sum of two modes with the mode number ($n = 0$, $m = 1$) and ($n = 2$, $m = 1$). When each mode propagates along the square waveguide, field pattern is changed due to the presence of difference of propagation constant $\Delta\beta$. The measured E_y is as small as − 20db. The comparison with exact calculation is now under the way.

By removing the smooth walls from the square corrugated waveguide, EM field from parallel corrugated plate is investigated. The preliminary experiment on propagation in the parallel corrugated plate is carried out. The corrugated plate with width $a = 116$ mm and the length $z = 1000$ mm is placed in parallel with the distance $b = 82.1$ mm. In the present experiment, the value a is small compared with $w_x = 49.5$ mm and the distance between plates b = 82.1 mm. It is required for full-scale experiment where a is as large as 3 w_x. The experimental result for $E_y(E_x)$ is shown in Fig. (a) ((b)) when injected HE $_{11}$ from the circular corrugated waveguide is polarized along y(x)-direction. Both field patterns are elliptic and however are still circular near the center due to the smallness of a. To begin the full-size test of parallel corrugated plate, the preparetion of wider currugation plate and the theoretical analysis is now under t he way.

6 Figure captions

Fig.1: Block diagram of ECH power supply.
Fig.2: Schmatic drawing of the rectangular corrugated waveguide with two parallel corugated plates and two smooth plates.
Fig.3: Charachteristics of the rectangular corrugated waveguide of $a = b = 82.1$ mm , $W/P = 0.5$ and $n = 1$ for $\omega/\ 2\ \pi = 84$ GHz.
(a) The porpagation constant $|\beta|$ (rad / cm) as a function of the normalized corrugated depth D. (b) Eigen value of $|\beta|$ as a function of D. (c) Attenuation constant α (db / m) as a function of D.
Fig.4: Profile functions for the rectangular and circular corrugated waveguide and gussian beam.
Fig.5: Mode purity of $|A_0|^2$ and total injected power P_{in} into the waveguide.
Fig.6: Mode purity of $|A_{ij}|^2$ up to $i = j = 5$.
Fig.7: Schmatic drawing of parallel corrugated plates.
Fig.8: The output profile of E_y in the parallel corrugated plate
Fig.9: Gaussian mode purity $|A_{00}|^2$ in the (w_x, R_x) plane.
Fig.10: Gaussian mode purity of fundamental and higher modes.
(a) $|A_{00}|^2$ in the (w_{0x}, z_x), (b) $|A_{20}|^2$ in the (w_{0x}, z_x),(c) $|A_{40}|^2$ in the (w_{0x}, z_x).
Fig.11:(a) E_y profile at the mouse of the square corrugated waveguide. (b) E_x profile at the mouse of the corrugated waveguide when the cross polarized mode is excited.
Fig.12:(a) E_y profile at the mouse of the parallel corrugated plate. (b) E_x profile at the mouse of the parallel corrugated plate when the cross polarized mode is excited.

7 References

1. Ohkubo K., Hosokawa M., Kubo S., Sato M., Takita Y., Kuroda T., Proc. of 8th Joint Workshop on Electron Cyclotron Emission and Electron Cyclotron Heating vol.2 pp561 – 573 (Gut Ising 19 – 21 Oct. 1992)

2. Dybdal R. B., Peters, R.Jr., Peake, W.H., IEEE Trans. Microwave Theory Tech. vol.MMT – 19, 2 – 9 (1971).
3. Yariv A., Quantum Electronics (John Wiley & Sons, Inc., New York)

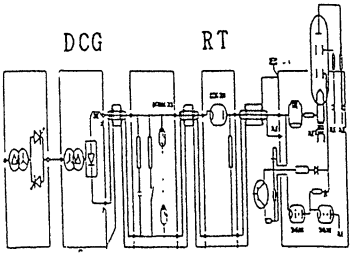

Fig. 1

Fig. 2

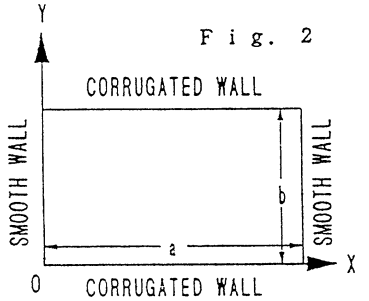

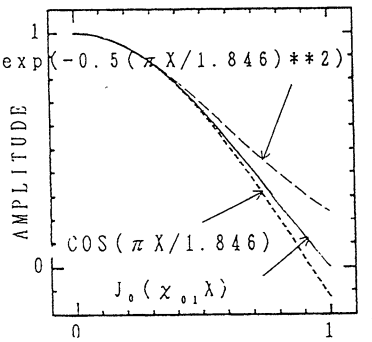

Fig. 4

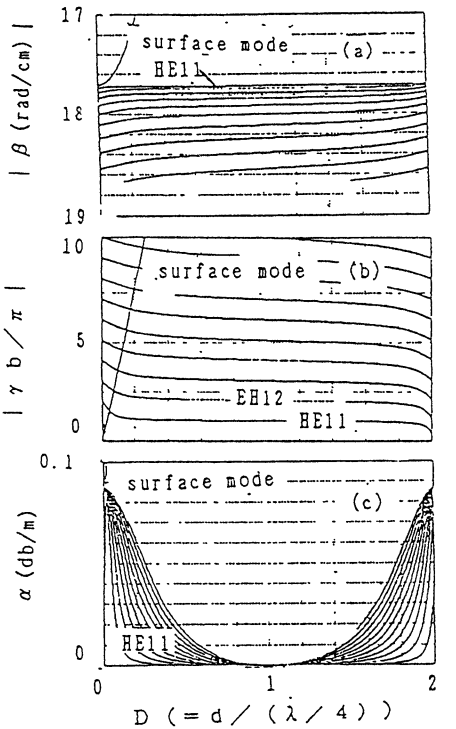

Fig 3

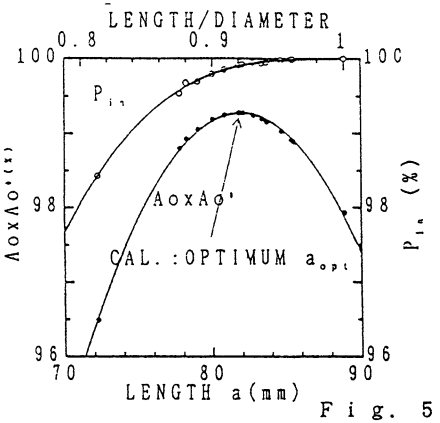

Fig. 5

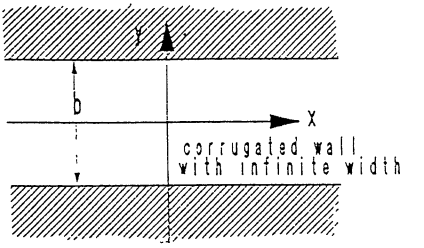

Fig. 7

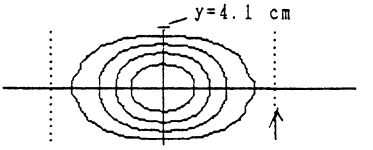

Fig. 8

88.9 mmϕ -88.9X88.9mm□

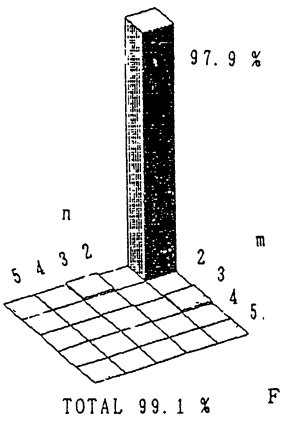

Fig. 6

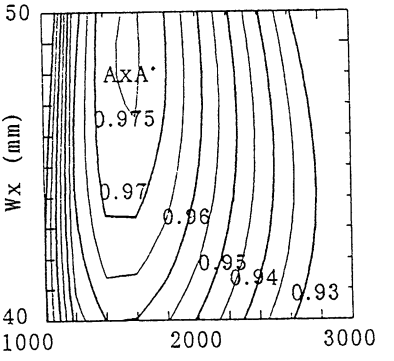

Fig. 9

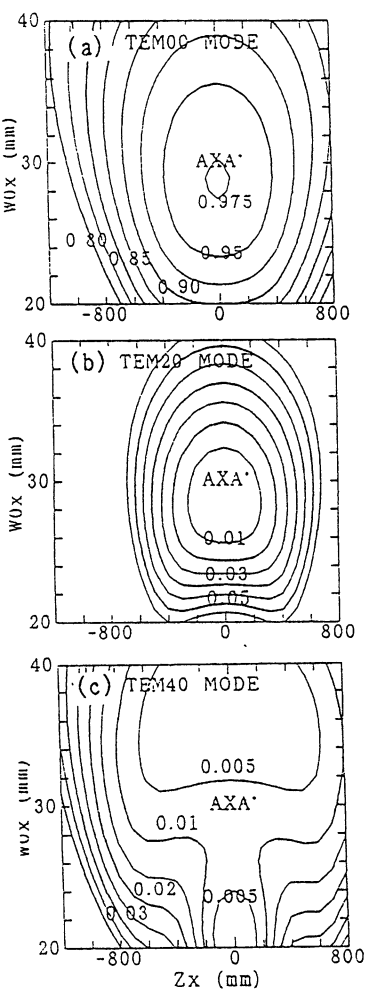
(a) TEM00 MODE
AXA
0.975
0.95
0.90
0.85
0.80
WOX (mm)
40
30
20
-800
0
800
(b) TEM20 MODE
AXA
0.01
0.03
0.05
(c) TEM40 MODE
0.005
AXA
0.01
0.02
0.03
0.005
Zx (mm)

Fig. 10

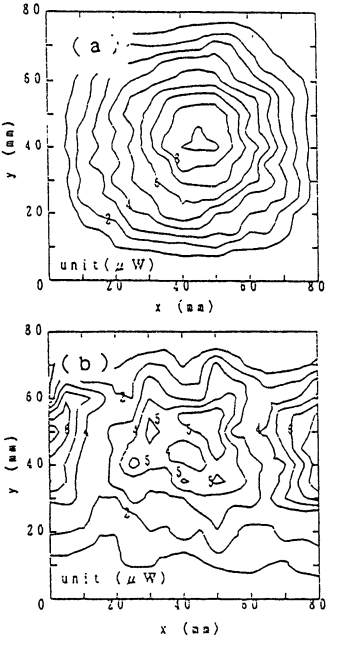
(a)
(b)
unit(μW)
x (mm)
y (mm)
0
20
40
60
80

Fig. 11

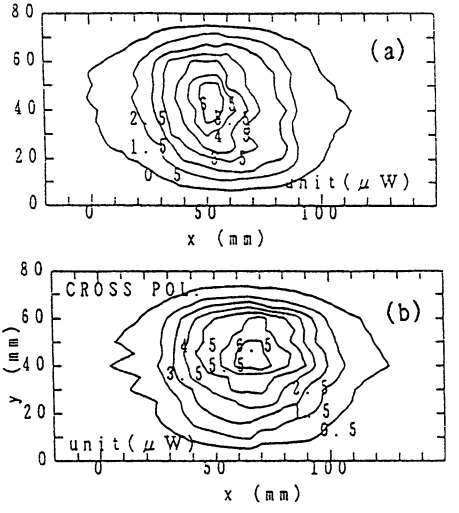

Fig. 12

Transport Study and MHD Control by Local Electron Cyclotron Heating in the WT-3 Tokamak

Y. Terumichi, S. Yoshimura, K. Hanada,
T. Maekawa, M. Nakamura*, T. Maehara,
S. Tabuchi, K. Nakamura and T. Iinuma
Department of Physics, Faculty of Science, Kyoto University
Kyoto, Japan

1: Heat transport in Lower Hybrid Current Drive Plasma

A short electron cyclotron heating ($2\Omega_e$ECH) pulse can locally perturb the electron temperature. The temperature perturbation can be observed in the soft X-ray signal intensity. The radial thermal diffusion coefficient, χ_e, is estimated by propagation delay of the perturbed signal (time-to-peak method). It is found that there is a threshold of lower hybrid power above which χ_e falls to 1/2 - 1/3 times that of the target ohmic heating plasma. The improvement of χ_e is confirmed as effective $2\Omega_e$ECH that the central electron temperatuire rises up to 3 times that of the target plasma.

2: Stabilization of m=2 MHD Activity by $2\Omega_e$ECH

The stabilization or destabilization of the m/n=2/1 MHD activity by local $2\Omega_e$ECH was studied systematically in the WT-3 tokamak. The toroidal magnetic field was carefully scanned for signs of suppression or enhancement of the activity. It is found that the m/n=2/1 and 1/1 activities can be suppressed simultaneously when the electron cyclotron resonance in the equatorial plane is located in the narrow region near q=2 or 1 surface and the width of the region near q=1

*On leave from Osaka Institute of Technology, Osaka, Japan

depends on ECH power and the region spread inward q=1 surface with ECH power.

Introduction

Local heating of plasma is a feature of ECH on tokamaks. It can be used to active diagnostics and profile control of tokamak discharge. In this paper, propagation of heat pulse generated by short ECH pulse is studied to estimate the electron heat transport coefficient in the lower hybrid current drive plasma and the suppression of MHD activities by ECH is studied by using a focusing ECH launcher.

1: Lower hybrid current drive is expected to be one of the candidates of profile control. In the previous papers, some effects of LHCD were reported, that is, tokamak discharge assisted with LHCD has good particle confinment [1] or energy confinment [2] in low density region, sawtooth, m=1 or/and m=2 MHD activities can be stabilized by LHCD[3]. But there is few report about the radial transport coefficient measured directly. In this paper, it is tried to estimate the electron heat transport coefficient, χ_e, using a heat pulse propagation. A short electron cyclotron heating (ECH) pulse can locally perturb the electron temperature of a tokamak plasma. The temperature perturbation can be observed as the perturbation of soft X-ray signal intensity. The radial thermal diffusion coefficient, χ_e of the plasma can be estimated by propagation delay of the perturbed signal in the radial direction. By using this method, χ_e is studied in LHCD plasmas with various lower hybrid power levels (P_{LH}) which have or have not sawtooth or MHD activities.

2:Stabilization of low mode number MHD activity is a very interesting subject related to the major disruption of tokamak plasma. In previous papers[4][5][6], stabilization of m/n=2/1 MHD activity by local ECH was studied. The instability can be stabilized when the outside of q=2 surface is heated and enhanced when the inside of q=2 surface is heated. However, the study is not systematic so much. In this paper, the stabilization or enhancement of the activity by local ECH is studied systematically in WT-3. The 2nd harmonic

electron cyclotron resonance ($2\Omega_e$ECR) layer is carefully scanned for signs of suppression or enhancement of the activity. Pickup coils and soft X-ray computerized tomography are used to know the behaviour of the activity.

1 Experimental apparatus

Schematic diagram of the experimental setup is shown in Fig.1. WT-3 is a small standard tokamak which has a circular cross section. The major radius R_0 is 65cm, minor radius a=20cm, maximum toroidal field B_T=1.75T, the maximu plasma current I_p=150kA and discharge duration is about 100ms. LHCD power source is a 2GHz, 350kW, 100ms klystron. LH power is launched by a two stacked 4 waveguide arrays. ECH power source is a 56Ghz, 200kW, 100ms gyrotron. EC power is launched from the low field side by a focusing antenna which is consisted of a Vlasov converter, eliptical and plane reflectors (Fig.2). Microwave is injected into plasmas nearly perpendicular (84 degrees) to the toroidal magnetic field in the extraordinary mode.

Main diagnostics used in this experiment are two sets of soft X-ray computerized tomography (CT) systems, soft X-ray pulse height analyzer for electron temperature measurement and pickup coils (magnetic probe). One of the CT systems is consisted of 3 soft X-ray pin hole cameras located at the top, bottom, and horizontal port in a poloidal cross section (3 port soft X-ray detector array). The spatial resolution of this system is 1.5cm and time resolution is 5μs. Another has 5 cameras (5 port soft X-ray detector array) and the arrangement is shown in Fig.3. Each camera has 20 detectors on the movable image plane which are sensitive to soft X-ray in the range of 0.2-27keV and has changable Be absorber foils (5, 15 and 100μm). The spatial resolution of this system is 1 - 2cm depending on the sweep range and the time resolution is 5μs. The sweep range of the pin hole camera can be changed by changing the distance between the pinhole and the imaging plane. This helps to observe the wide range of the plasma cross section. Magnetic signal is detected by 12 pickup coils which

sorround the plasma in a poloidal cross section. There are 4 sets of pickup coils and they are located 90 degrees apart each other in toroidal direction.

2 Heat transport in Lower Hybrid Current Drive Plasma

When LHCD is superimposed on Ohmic heating plasma with sawtooth oscillations, sawtooth oscillations can be stabilized above the threshold power level of lower hybrid power P_{LH}. It is interesting to investigate the thermal diffusion coefficient with sawtooth and without sawtooth. Thermal perturbation is generated by short (0.2-1ms) $2\Omega_e$ECH pulse injected into the center of the plasma. The temperature perturbation can be detected as perturbation of soft X-ray signal intensity on the detectors of 3 port CT system. The waveform of the detected signals are shown in Fig.4. Each trace in Fig.4 shows a signal intensity of different viewing chord and 'r' shows the distance from the plasma center. The heat pulse propagation can be seen in Fig.4(a) in OH plasma with sawtooth oscillations and in Fig.4(b) without them. There are apparent difference of the propagation velocity of the thermal pertubations (see r=10.1cm curves). It seems that χ_e with sawtooth is larger than χ_e without sawtooth. It is interesting in the P_{LH} dependence of χ_e. So, χ_e is estimated from the propagation delay in various P_{LH} level. χ_e is plotted versus P_{LH} in Fig.5. χ_e of OH plasma with sawtooth is about $6m^2/s$. Sawtooth can be stabilized above P_{LH}=40kW and simultaneously χ_e decreases and is about $2m^2/s$ above P_{LH}=100kW. In the range of P_{LH}=50-90kW, sawtooth is stabilized but m=1 MHD oscillation appears. Above 100kW, there is no sawtooth and no m=1 oscillation. To confirm the improvement of χ_e, $2\Omega_e$ECH is applied to the plasma with χ_e=$2m^2/s$ at the plasma center. Waveform of soft X-ray signal intensity of the central chord is shown in Fig.6. Open and solid circle shows the electron temperture measured by soft X-ray pulse height analysis. Electron temperture at the center increase up to 0.75 keV which is about 3 times that of the target plasma.

To confirm whether the improvement of χ_e depends on sawtooth stabilization or not, a plasma with high safety factor, q_L=7.5, is selected as a target plasma. There is no sawtooth in OH target plasma. LHCD is superimposed the sawtoothless plasma. Power dependence of χ_e is found to be similar to the low q_L=3.7 plasma with sawtooth. There is a threshold power level of about 100kW above which χ_e can be improved. χ_e of OH plasma is about $8m^2/s$ and that of the LHCD plasma with $P_{LH} > 100kW$ is about $3.5m^2/s$. It can be concluded that sawtooth stabilization is not essential for the improvement of χ_e. The mechanism is not known yet, but LHCD makes the current profile rather broad. $2\Omega_e$ECH at the center also raises the central temperature in this case.

3 Stabilization of m=2 MHD Activity by $2\Omega_e$ ECH

Stabilization and enhancement of m=2 MHD activity by $2\Omega_e$ ECH are studied systematically. Stable m/n=2/1 MHD activity can be observed in a plasma with q_L=2.7. Identification of the oscillation mode is made by getting the phase difference of magnetic probe signal detected 2 sets of magnetic probes located 180 degree apart each other in toroidal direction. To change the location of $2\Omega_e$ECR layer, toroidal magnetic field is scanned with keeping q_L constant. Fig.7 shows the typical waveforms of the magnetic probe signal. The upper left diagram shows the location of the ECR layer in the poloidal cross section where (1), (2) and (3) correspond to the waveform (1), (2) and (3) respectively. The most inner thin circle shows q=1 surface and the next one shows q=2 surface estimated by 5 port CT system. Waveform (1) and (3) show that the magnetic fluctuations can be stabilized when the ECR zone in the equatorial plane is located near q=2 or q=1 surface. Enhancement of the oscillation can be observed when ECR layer is located in the region between q=1 and 2 surfaces. The oscillation can be observed in the soft X-ray signal detected by the 5 port CT detectors. The frequency is the same as the magnetic signal. The coutour map of the amplitude of the oscillation in the

polodal cross section is reconstructed by CT method for OH plasma and the temporal evolution every 10μs is shown in Fig.8. There can be seen something like islands. One island can be seen in th inner space and two islands about 180 degrees apart each other are in the periphery. The inner island rotates faster than the peripheral islands. Rotating velocity of the inner one is 2 times that of the peripheral one. The inner island shows m=1 MHD oscillation. From this figure, q=1 surface is estimated as the trace of the most inner maximum amplutude and q=2 surface is estimated as that of the peripheral one. In Fig.9, signal ratio of ECH case to OH case for magnetic probe, soft X-ray signal detected on the chord tangential to near q=2 (r/a=0.75) and q=1 (r/a=0.3) surfaces are plotted versus position of the ECR in the equatorial plane. All signal amplitudes are suppressed when the ECR zone is near q=1 and 2 surfaces. This clearly shows that m=2 and m=1 modes are strongly coupled each other. Coupling mechanism is not yet clear experimentally but toroidal coupling seems to be the most available mechanism.

Summary

Heat Transport in Lower Hybrid Current Drive Plsma

1:χ_e of LHCD plasma is measured at first by using ECH heat pulse propagation.

2:There are some threshold power level for improvement of χ_e.

3:Stabilization of the sawtooth oscillation is not essential for improvement of χ_e.

4:Improvement of χ_e is confirmed by effective ECH of central electron temperature.

Stabilization of m=2 MHD Activity by $2\Omega_e$ECH

1:Stabilization and enhancement of m=2 MHD activity by $2\Omega_e$ ECH are studied systematically.

2:m/n=1/1 and 2/1 MHD activities can be simultaneously stabilized when $2\Omega_e$ECR is located in the narrow region near the q=1 and

2 surfaces in the equatorial plane.

3:The width of the region near q=1 surface depends on the ECH power and the region spreads inward q=1 surface with ECH power.

4:m=1 and m=2 activities are strongly coupled each other.

References

1. Nakamura M. et al., Nucl. Fusion, 1991, **31**, 1485.
2. Bell R. E. et al., Phys. Rev. Lett., 1988, **60**, 1294.
3. Iida M. et al., J. Phys. Soc. Japan, 1988, **57**, 3661.
4. Alikaev V. V. et al., Proc. of Intern. Conf. of Plasma Phys. Contr. Nucl. Fusion Res., 1984, **1**, 419.
5. TFR GROUP, Nucl. Fusion, 1988, **28**, 1995.
6. Hoshino K. et al., Phys. Rev. Lett., 1992, **69**, 2208.

Fig. 1

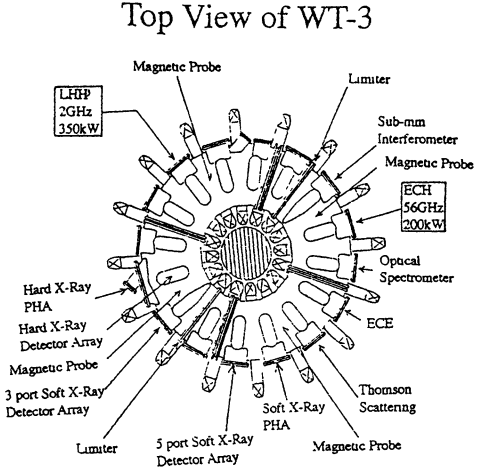

Fig. 2

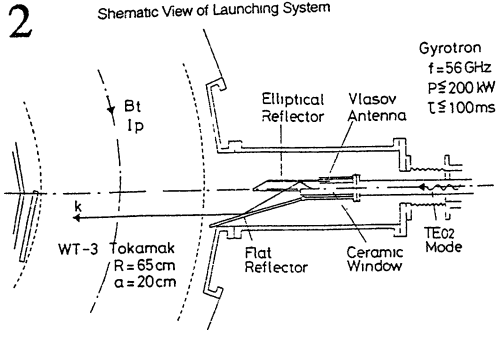

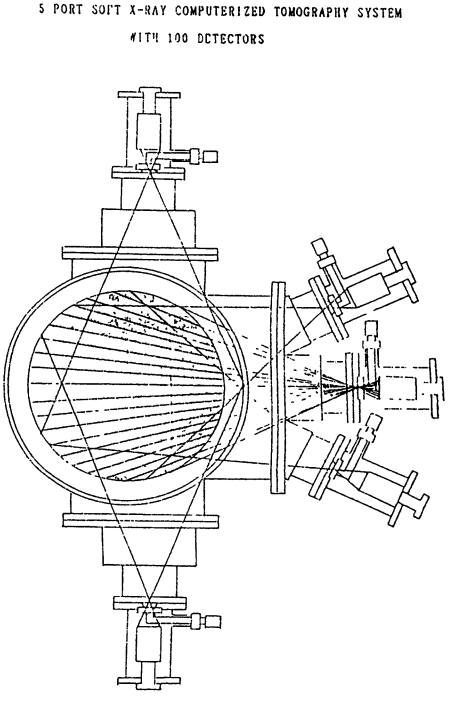

Fig. 3

Fig. 4 ECH heat pulse propagation in STO and no STO plasmas

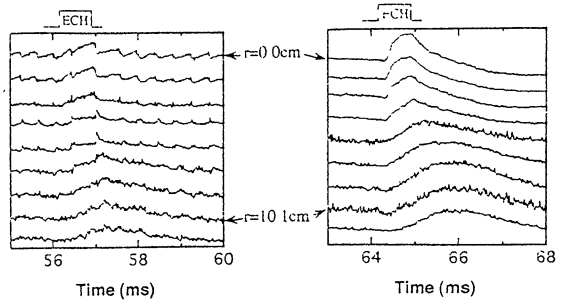

(a) OH plasma (b) OH + LHCD plasma

Fig. 5

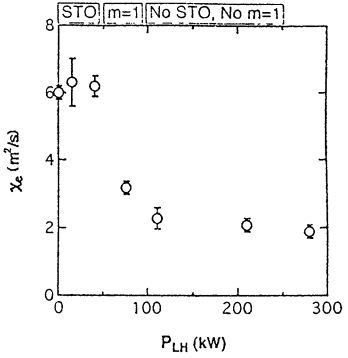

Waveforms of LHCD+ECH plasma

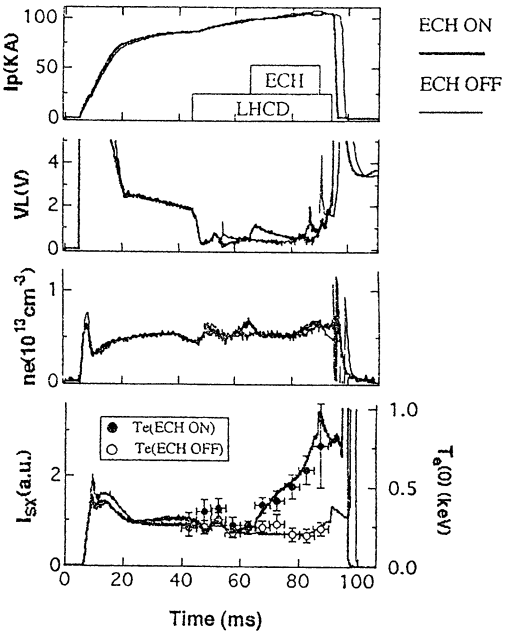

Fig. 6

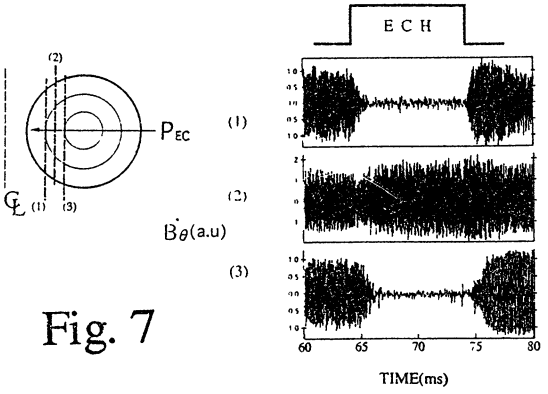

Fig. 7

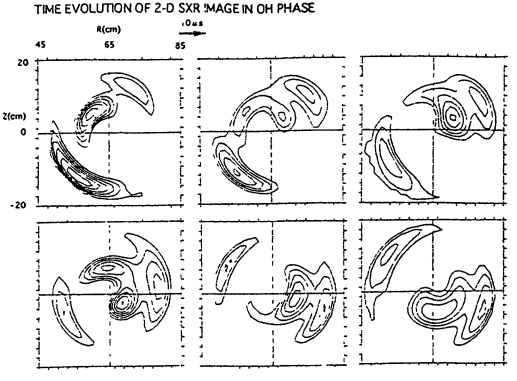

Fig. 8

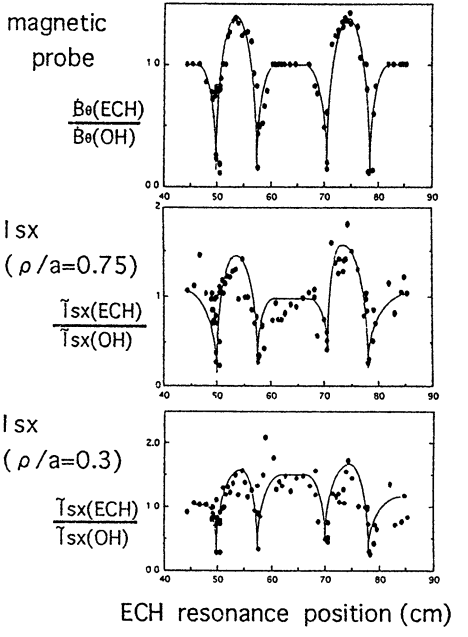

Fig. 9

ALPHA PARTICLE DIAGNOSTICS USING 140 GHz MICROWAVE SCATTERING ON JET

J.A. Hoekzema, A.E. Costley, T.P. Hughes, P.E. Stott
JET Joint Undertaking, Abingdon, Oxfordshire, OX14 3EA, UK

Abstract

To evaluate the efficiency of alpha particle heating in the DT phase of JET, measurement of the energy distribution of the fast alpha particle population is necessary. The fast ion and alpha particle diagnostic at JET will use collective Thomson scattering of high power microwave radiation to determine the alpha particle velocity distribution between their birth energy (3.5 MeV) and ~0.5 MeV with a typical spatial resolution <0.1 m and time resolution ~0.1 s. The diagnostic uses a high power long pulse 140 GHz gyrotron as the source of probing radiation and a heterodyne receiver system to measure the spectrum of scattered radiation.

1 Introduction

It is expected that JET will reach plasma parameters near scientific breakeven during the D(euterium)T(ritium) phase. Since the alpha particle heating power will amount to only 20% of the additional heating power, the energy balance will not be dominated by alpha particle heating (except possibly locally) and a detailed analysis of the fast alpha particle behaviour will be necessary to determine the efficiency of alpha particle heating. Fast (i.e. not yet thermalised) alpha particle densities are expected to amount to a few tenths of a percent of the electron density, n_e, at higher values of n_e ($\sim 10^{20}$ m^{-3}) and to a few percent at low n_e where the slowing down is relatively slow.

Collective effects, including alpha particle pressure effects can therefore be reactor relevant.

A variety of diagnostics will be used for alpha particle measurements. They include measurement of the source profile (neutron diagnostics), slowed down (ash) and fast alpha particle distributions up to at least 0.5 MeV (charge exchange diagnostics), edge densities (Ion Cyclotron Emission) and escaping alphas. The fast ion and alpha particle diagnostic [1] is aimed at measuring the velocity distribution of alphas between 0.5 and 3.5 MeV and will therefore be especially relevant to study anomalous fast alpha losses (if they occur) which could reduce the efficiency of alpha particle heating.

Use of the diagnostic is not limited to the DT phase of JET. Important fast ion populations are already created by the heating systems and can be measured. The measurement of the thermal ion feature, which dominates the spectrum in a different frequency range can give important information on several plasma parameters. Also, the power of the probing radiation necessary for alpha particle measurements is sufficient to be used for heat pulse propagation measurements.

2 Principle

When a beam of electromagnetic radiation is launched into the plasma, a very small fraction of the power will be scattered from fluctuations in the dielectric properties of the plasma. If the incident beam has wave vector $\mathbf{k}_i$ and frequency ν_i than the scattered radiation detected with wave vector $\mathbf{k}_s$ and frequency ν_s will be due to fluctuations with wave vector $\mathbf{k}$ such that

$$\mathbf{k} = \mathbf{k}_s - \mathbf{k}_i$$

and if $|\mathbf{k}_s|$ and $|\mathbf{k}_i|$ are almost equal,

$$|\mathbf{k}| = 2|\mathbf{k}_i|\sin(\theta/2)$$

where θ is the angle between the incident and scattered directions.

In many experimental situations the main contribution to the scattering comes from electron density fluctuations. In this case the theory is well known. If the wave vector of the fluctuations is small compared to the reciprocal of the Debye length in the scattering volume, the shielding electrons moving with each ion will scatter collectively and the scattered spectrum will be affected by the ion velocity distribution. The components along $\mathbf{k}$ of the ion velocities $\mathbf{v}_i$ of unmagnetised ions are mapped on to the frequency shift of the scattered radiation from the incident beam frequency:

$$\Delta\nu = \nu_s - \nu_i = \mathbf{k}.\mathbf{v}_i/2\pi$$

The thermal ions have relatively low velocity and form a narrow central feature in the scattered spectrum. Alpha particles, slowing down in the plasma from a birth energy of 3.5 MeV, and other fast ions form a distinctive feature which extends to larger frequency shifts. In relativistic, magnetised plasmas such as those in JET, the magnetic field affects the motion of the particles. The dielectric properties of the plasma are important and have been extensively investigated theoretically. In particular for eX(traordinary) to X mode scattering the scattering for frequencies between the fundamental Electron Cyclotron frequency and the R cutoff is much stronger than for O(rdinary) to O mode scattering [2]. The parameters determining the R cutoff have been discussed by Bindslev ([3,4]), who has given expressions convenient for numerical evaluation. Use of the X mode is however more restricted than the O mode due to the lower density cutoff.

If the scattering wave vector **k** is in a direction nearly perpendicular to **B** strong resonances can occur in the scattering spectrum. Fluctuations in other quantities such as the magnetic field and the electron velocity also become important. In this case a more detailed theoretical treatment is necessary. Extensive calculations are in progress following initial work by Aamodt and Russell [5,6], Chiu [7] and Bindslev [8]. Although the scattered power is much enhanced in these conditions, interpretation of the scattered spectrum in terms of fast ion velocity distributions will be difficult (if at all possible). On the other hand, when the scattering geometry is chosen such that these effects are avoided (i.e. by avoiding **k** close to perpendicular to **B**), mapping of the scattered spectrum to the alpha particle velocity distribution in the region where the alpha feature dominates the spectrum is straightforward [1].

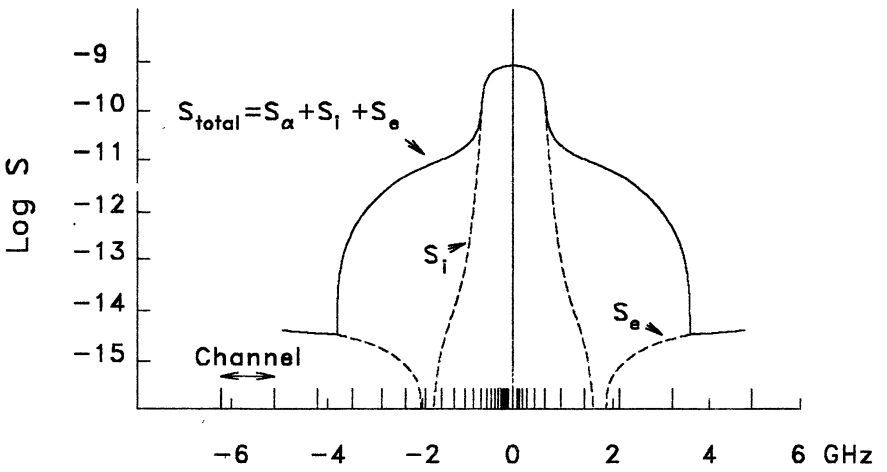

Fig 1: Typical calculated spectrum of scattered radiation showing the contributions of thermal ions, alpha particles and electrons to the spectrum. In part of the spectral region, corresponding to alpha energies between ~0.5 and 3.5 MeV the alpha feature dominates the scattered spectrum.

3 Parameters of the diagnostic system

3.1 Frequency

The probing frequency for the diagnostic is 140 GHz and this is the optimum value when JET is operated at full field (3.4 T). This is in the Electron Cyclotron frequency range. Below the fundamental EC frequency the density cut-off severely limits the densities at which measurements can be made (this is less so for a higher field tokamak, e.g. TFTR, where operation at a frequency below the fundamental is of interest) while at frequencies above the EC spectrum no suitable source exists (with possibly an exception for the CO_2 laser frequency which however would necessitate very small scattering angles, $\sim 0.1^{o}$, with a consequent loss of spatial resolution). At 140 GHz both the fundamental and second harmonic EC resonance are present in the plasma, located at the very edges. This means that EC emission, against which the scattered radiation has to be discriminated, has a minimum around this frequency. The plasma still acts as an efficient dump for the radiation after reflection(s) off the wall. The plasma is accessible for the radiation if near vertical injection is used up to densities $> 2 \times 10^{20}$ m^{-3} when radiation is coupled to the O(rdinary) mode in the plasma. The alpha-feature dominates part of the spectrum even at large scattering angles (up to at least 60^{o}) as long as the scattering vector is not near perpendicular to the magnetic field direction, and good spatial resolution for the measurements can be obtained.

3.2 Geometry

The probing radiation will be launched from a top port using a mirror assembly which launches a focused Gaussian beam which reaches a waist radius of 30 mm in the midplane of the torus. A similar Gaussian beam is collected by a receiver mirror assembly in the bottom part of the torus. The scattering

volume, determined by the overlap of injected and detected beams is cigar shaped, with a height dependent on the scattering angle. The spatial resolution for the measurement depends on θ but will generally be better than 100 mm.

Both the launch and receive front mirrors are steerable in two independent directions (poloidal and toroidal). In the poloidal direction, mirror rotation by up to $\pm 15^{o}$ is possible and this is sufficient to scan the scattering volume across the plasma midplane. In the toroidal direction the mirror rotation is limited to $\pm 7.5^{o}$. A small angle in the toroidal direction is necessary to allow the choice of a scattering geometry with **k** away from perpendicular to **B**. Changing the angle in the toroidal direction also makes it possible to measure the velocity distribution along different **k** directions to determine the anisotropy (if any) of fast ion populations.

3.3 Polarisation

The polarisation of injected and detected radiation will be chosen such that the radiation is coupled either to the O mode or the X mode in the plasma. In general this will mean elliptic polarisation both for the X and the O mode. For propagation near perpendicular to **B** access is possible up to the density cutoff at $n_e = 2.4\ 10^{20}\ m^{-3}$, although severe refraction effects will complicate measurements when n_e approaches this value. Measurements using the X mode will be limited to $n_e < 6\ 10^{19}\ m^{-3}$ due to the R cutoff and refraction. Accessibility is more restricted for the X mode because the 2nd harmonic resonance is very wide and absorption excludes access to the outboard plasma region.

4 Expected performance

4.1 Overlap of injected and detected beams

At higher densities refraction of the radiation in the plasma can be important. Ray tracing calculations will therefore be done to define the proper antenna orientations on the basis of expected plasma parameters. After the measurement the actual location of the scattering volume can be recalculated using the actual plasma parameters. The injected and detected beams are affected somewhat differently by refraction. This is due to the fact that neither the plasma nor the scattering geometry will be up-down symmetric after the installation of the pumped divertor in JET. As a result, the overlap of the beams may not be optimal if plasma parameters change or are different from expected. In the worst case the beams may even miss each other. At low densities refraction is less important but even here there is some concern that the overlap could be less than optimal due to differential movement of the antenna assemblies. These are mounted on the vessel wall (support independent of the vessel is no longer possible after the divertor installation) which is subject to up to a few cm. movement due to thermal effects and electromagnetic forces.

For these reasons a feedback system is being developed which will adjust the orientation of the steerable receive mirror to obtain optimum overlap. The feedback system will use signals from slave receivers which look in directions slightly displaced from the main beam and with wider antenna patterns (see fig. 2). There are 4 slave receivers but only 2 will be used at any one time (i.e. an opposite pair). The pair that is used depends on which angle (toroidal or poloidal) of the mirror is best adjusted for the selected scattering geometry. Signals collected by the slave receivers will be integrated over the spectrum, with a band surrounding the gyrotron frequency being filtered out by a notch filter to avoid stray light. Since part of the thermal ion feature is still included, the signals will be relatively strong and short integration times (1 ms) can be used. The feedback response time is however limited by mechanical constraints (mirror inertia) and fast changes in overlap (e.g. as a result of MHD events) can only be slowly corrected ($\sim$ 100 ms).

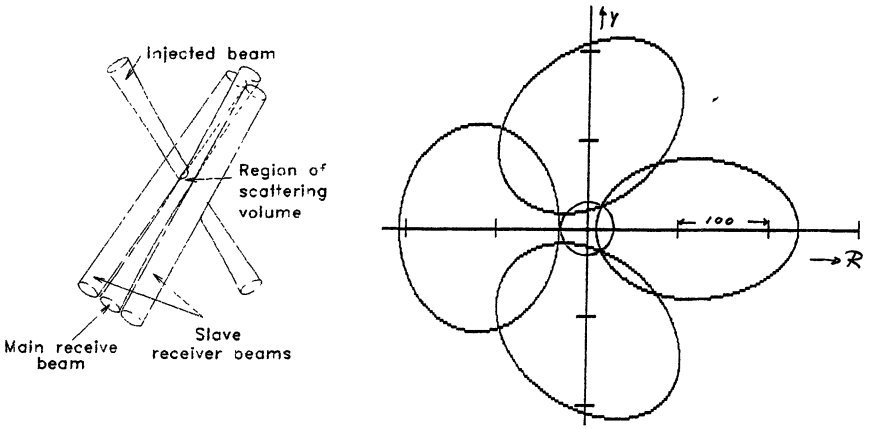

Fig 2: Schematic view of the scattering volume with two "slave" beams and the intersection of the main beam and surrounding slave beams with the torus midplane (1/e intensity contours).

4.2 Signal to noise

The scattered signal will have to be detected against background EC Emission with measured effective blackbody temperature of several hundred eV [9]. For comparison, the scattered signal will have an effective blackbody temperature of only a few eV in the spectral range dominated by the alpha feature. In order to discriminate between the scattered signal and the background, the injected power will be modulated (generally between maximum and zero power although part modulation is also possible).

Statistical fluctuations on the background radiation will be the main source of noise for the measurement. The signal to noise ratio can be increased by increasing the integration time, using pulse addition techniques. Values of the signal to noise ratio vary with plasma conditions, scattering geometry, mode and frequency. Assuming 5 MW of alpha heating, classical slowing down, no anomalous diffusion, a scattering angle of 20^{o},

background temperature 500 eV, modulation depth of injected power 400 kW, integration time 200 ms and O to O mode scattering with the scattering volume located in the central plasma region, average signal to noise ratios (i.e. averaged over the alpha feature) of 5 (at $n_e = 1.5 \times 10^{20}$ m^{-3}) to 50 (at $n_e = 2 \times 10^{19}$ m^{-3}) have been calculated. Signal to noise values can be increased slightly by reducing the spectral resolution (i.e. by combining detection channels) and dramatically if the X mode can be used.

4.3 Frequency of modulation

Since most of the injected radiation will be absorbed in the plasma after reflection off the vessel wall, this will affect the electron velocity distribution and therefore the ECE [10] which will also show a slight modulation. Although this modulation is mainly out of phase with the scattered radiation, it should be kept fairly small (at most at a level comparable to the scattered radiation). This is possible by choosing a high modulation frequency. Detailed calculations (taking non-thermal effects into account) indicate that a modulation frequency of 10 kHz should be sufficient and this will be the normal choice.

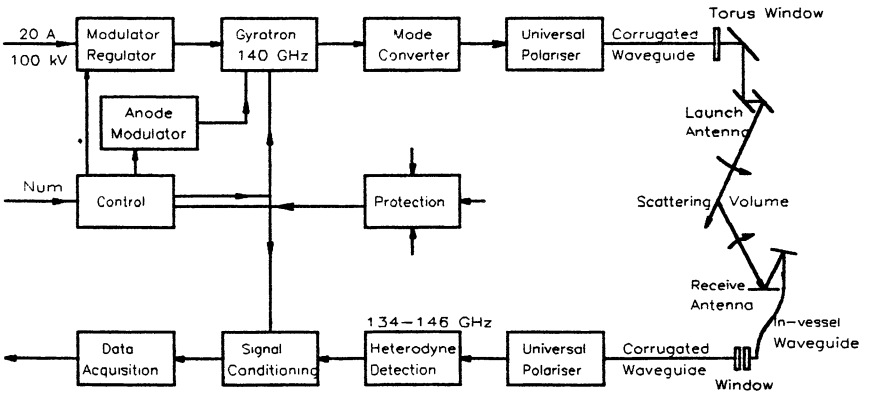

Fig 3: Schematic overview of the diagnostic system

5 Technical implementation

The main components of the diagnostic system, shown schematically in fig.3, are a high power gyrotron with associated equipment, RF transmission lines and antennae and a heterodyne detection system.

5.1 Source of probing radiation

A high power, long pulse RF source is necessary for the diagnostic to obtain sufficient signal to noise for alpha particle measurements. The selected gyrotron is capable of operation at up to 300 kW average in long pulses (5 s.). The output of the gyrotron is in the $TE_{15,2}$ mode and this mode is converted to a Gaussian beam external to the gyrotron. The gyrotron has a modulating anode and anode voltage modulation can be used to modulate the RF output power. For full anode modulation (i.e. between -3 kV and $\sim$25 kV relative to the cathode), the electron beam is suppressed during the down phase and for 50% modulation duty cycle the peak RF power can be above 500 kW. The existing Anode Modulator is not capable of full modulation at sufficiently high frequency but can part modulate (i.e. by a few kV) the anode voltage. In this case the electron beam is not suppressed and the peak power has to be reduced. Therefore, a special Anode Modulator is being developed which is capable of full anode voltage modulation at frequencies well above 10 kHz. Power dissipation in this unit is limited by storing the energy, removed from the stray anode capacitance in an external capacitor (gated sinusoidal oscillator) [11].

The gyrotron frequency is stable to within $\sim$100 MHz and the spectral purity is high (noise power outside the main frequency $P_N < 10^{-18}$ Po/Hz, where Po is the total RF power, in the frequency of interest). These properties are necessary to avoid stray light problems:

Some stray radiation will inevitably be collected by the receiver and also radiation scattered by coherent density fluctuations (waves, instabilities) with very small frequency shifts will be at a level many orders of magnitude above the level of radiation scattered on thermal fluctuations. It is estimated that the received radiation with frequency close to the gyrotron frequency will only be 70 dB down on the injected power. This is at a level where it will upset detection (the power in the fast ion feature is $\sim$130 dB down). For this reason frequencies close to the gyrotron frequencies are attenuated (~ -40 dB) by means of a notch filter. Obviously the frequency of the gyrotron should be sufficiently stable to stay within the notch bandwidth, which should not be very wide to avoid losing important spectral information. A high spectral purity is necessary because stray radiation at different frequencies cannot be discriminated from scattered radiation at these frequencies.

The gyrotron filament is heated by an AC current. Since the filament current (the associated magnetic field) has some effect on the gyrotron RF output, the frequency of the filament supply will be chosen equal to the anode modulation frequency and phase locked to it, to produce a reproducible RF waveform. The filament current will be boosted for long pulses using an adaptive boost control (i.e. it learns from experience) [11].

A control system to control the parameters of gyrotron operation as well as the scattering parameters (angle of injection, polarisation) and settings of the detection system has been implemented local to the gyrotron area. It is being extended to remote control from the diagnostic control room. A link to the mainframe IBM will make it possible to set up the optimum scattering geometry on the basis of numerical computations (e.g. ray tracing).

The technical systems are protected by a fast protection system which has several levels of intervention, dependent on the fault condition. Intervention ranges from interruption of the pulse for a short time (by rolling back the main Regulator tetrode) to full crowbar of the 100 kV supply voltage. Protection features include protection against operation at the wrong frequency, against operation with a too hot torus window, against excessive power collected by the receiver, against operation without plasma as well as all features standard to a gyrotron system (arcing, reflected power etc.).

5.2 High power transmission

The RF power is transmitted to the torus using a combination of quasi-optical and in-waveguide transmission [12,13].The transmission system is wide band (110-180 GHz) and could therefore be used at other frequencies, which would for instance be of interest if stepped tunability of the gyrotron would be possible. The system is schematically shown in fig. 4.

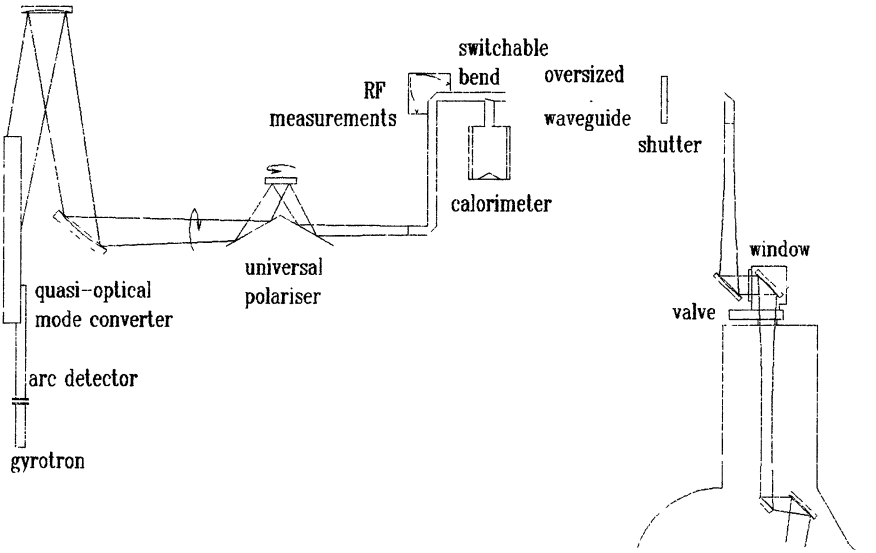

Fig 4: The high power transmission system

The $TE_{15,2}$ mode generated by the gyrotron is converted to a Gaussian beam using a quasi-optical mode converter. A high efficiency converter, using deformations of the feed waveguide, is in preparation at Stuttgart University to replace the existing standard converter. The feed waveguide of the converter has an internal diameter of 88.9 mm, equal to the gyrotron output waveguide. This requires large dimensions (the total height of the converter is 4 m.) but avoids a downtaper and consequent reflection of spurious high order modes and should give high power (MW) handling capability at atmospheric pressure. The converter is mounted inside an airtight and radiation tight box (PVC with Al cladding) and stray radiation is mainly absorbed by water in low velocity cooling channels. The required polarisation of the radiation is also produced quasi-optically. The linear polarisation at the output of the mode converter is converted to the required elliptical polarisation by means of a universal polariser. This consists of a rooftop mirror facing a corrugated mirror [12]. Rotation of the polariser as a whole rotates the polarisation while rotation of the corrugated mirror creates the required amount of ellipticity. The polariser is also mounted inside an airtight box. An arc detector, looking at the corrugated mirror, will be incorporated.

After the polariser, the radiation is coupled at the beam waist into 88.9 mm ID corrugated waveguide, using the excellent coupling of a Gaussian beam to the $HE_{1,1}$ mode. The waveguide run is 60 m. long and includes 7 mitre bends. The relatively large diameter of the waveguide will allow high power transmission at atmospheric pressure. In fact the whole transmission system will be at a slight under pressure, equal to the pressure inside the torus hall. Precise alignment of the waveguide (radius of curvature > 3 km) is crucial to avoid mode conversion. Alignment is achieved by precise machining of the 2 m. long waveguide sections and supporting them by constant spring supports which are adjusted individually to counterbalance the weight of the sections. Alignment is then

determined by the quality of machining of waveguide and flange connections and the waveguide can move to eliminate the effect of moving support structures (e.g. due to thermal effects). Expansion joints are included and allow fixed positions of the waveguide at both ends and at the torus hall penetration. Most of the waveguide is made of electroformed copper with NiP coating but more resistive sections (plasma sprayed stainless steel) are included after each bend. The increased resistivity has negligible effect on transmission of the $HE_{1,1}$ mode, but attenuates any high order modes created at the bends. Forward and reflected power measurements are done by coupling some radiation through an array of small (cut-off) holes in one of the mitre bends. By switching a mitre bend the radiation can be re-routed to a silicon oil cooled calorimeter. A mechanical shutter is included in the line for safety reasons.
Near the torus the transmission switches back to quasi-optical transmission. The Gaussian beam, launched from the waveguide is allowed to expand to reduce the power density at the torus window. Two slightly ellipsoidal parallel mirrors mounted on the vessel at the top of the port correct for differential movement between the end of the waveguide and the vessel (the vessel moves up and out due to thermal expansion and atmospheric and magnetic pressures). A focused beam is launched down the port which reaches a waist radius of 27.8 mm in the port (optimum waist to avoid beam truncation in the narrow port).

5.3 Torus windows

The gyrotron window is a double disk sapphire window with fluorocarbon face cooling between the disks. This type of window is not suitable as a torus window because the transmission capability is much less for a Gaussian beam than it is for the $TE_{15,2}$ mode, because safety margins for JET torus windows are larger than for gyrotron windows and because of the risk of fluorocarbon contamination of the vacuum vessel.

The high power torus window is an inertially cooled waterfree fused silica disk with 190 mm clear view. This material has been selected because of the low loss, low expansion, relatively low refractive index and limited temperature dependence of this index [14]. In view of the large beam radius at the window (45.5 mm) the temperature rise during a pulse should be tolerable. The main drawback of this material is the low thermal conductivity which will limit the duty cycle. By allowing the start of a new pulse before the window is completely cooled down (but still at a temperature of a few hundred ^{o}C in the centre), radiative cooling should be sufficient in between JET pulses. The window is resonant at 140 GHz, 200 ^{o}C to avoid reflection as much as possible and the thickness is chosen at 10 wavelengths. This thickness would be suitable for stepped tuning of the gyrotron to neighbouring $TE_{n,2}$ modes (the window would still be resonant to good approximation).

The high power window will be replaced (like all JET windows) by a double disk window assembly before the DT phase (1996). For this window assembly several options are being considered, including a double disk sapphire window with cryogenic (liq. N_2) edge cooling.

On the receiver side, double disk crystal quartz windows, already suitable for the DT phase, will be installed. Over a wide bandwidth these window assemblies show wild variations of transmission efficiency (between 20 and 100%) as a function of frequency. Although some loss of signal could be tolerated, since also the main source of noise would be attenuated (ECE), calibration would be difficult especially if thermal effects would be important. Fortunately the required bandwidth of the scattered signals is restricted. The bandwidth of the slave signals is < 1 GHz in which case it is sufficient to choose a resonant thickness for both disks to obtain almost full transmission. For the main scattered signal a reasonable behaviour of the transmission over the bandwidth of 134 to

146 GHz can be obtained by also controlling the distance between the disks precisely at a few half wavelengths [15], as illustrated in fig.5.

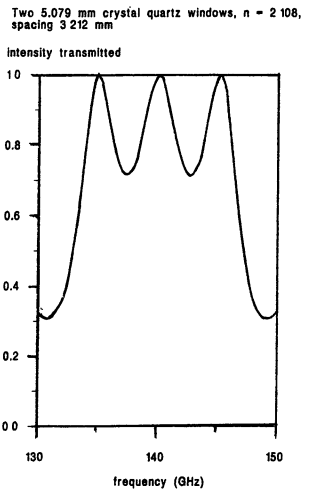

Fig 5: Transmission efficiency between 134 and 146 GHz of a double disk crystal quartz window (optimum interspace).

5.4 In-vessel components

The launch mirror assembly consists of a defocusing hyperboloidal fixed mirror and an ellipsoidal steerable mirror. The required orientation of the last mirror will be set up from a rest position (to which the mirror tends to return due to springs which are incorporated in the assembly) by means of pull rods. The start of movement (in poloidal and toroidal direction) from the rest position is detected by switches. The pull rods are controlled by stepper motors at the top of the port.

Scattered radiation is collected by a receive antenna, consisting of two mirrors; a flat mirror which can be rotated in two independent directions and a fixed ellipsoidal mirror. Mirror movement is again effected by pull rods, which in this case controlled by more powerful servo motors to minimise feedback response times. The curved mirror focuses a Gaussian beam (with 30 mm waist in the centre of the torus) into a 10 mm ID corrugated waveguide. This small diameter is chosen to allow bending the waveguide around the divertor structures in the torus. Four additional corrugated "slave" waveguides, with ID 7.5 mm are bundled with the main receive waveguide. They view the plasma through the same mirror assembly. The waveguide bundle is supported by an inconel structure which is

sufficiently flexible to allow the movement of the antenna end of the waveguides, mounted on the torus wall, with the torus while at the other end the waveguides are supported on the transformer limbs. The main receive waveguide is tapered up to 31.75 mm, before going through a mitre bend and the double disk crystal quartz window. The radiation from the slave waveguides leaves the vacuum quasi-optically.

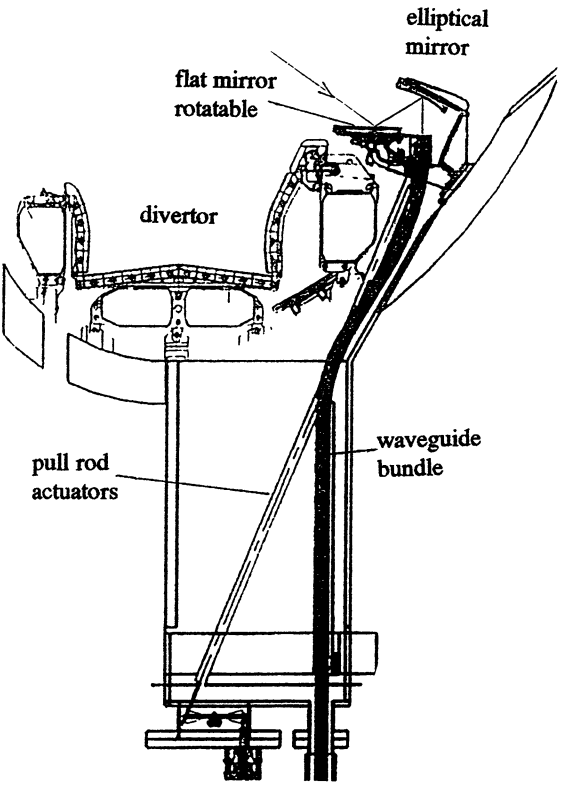

Fig 6: Receiver antenna assembly and waveguide bundle, containing a main and 4 slave corrugated waveguides, in the bottom part of the vessel.

Relative alignment of the launch and receive mirrors is possible by injecting low power radiation (which is coupled into the high power waveguide) and finding the angles for which the received signal is maximum. This determines the orientation where launch and receive are oriented such that they directly view each other.

5.5 Low power transmission

The main corrugated waveguide is continued to the detection area (40 m.) where the radiation is launched into a quasi optical polariser [16] to select the correct mode ($HE_{1,1}$) and polarisation. The polariser uses two mirrors with rotatable wire grids which act as quarter and half wave plates and can select the desired elliptical polarisation. The slave waveguides end before the vacuum windows and radiation is transmitted through the windows quasi-optically. Outside the vacuum the 2 signals to be used for feedback will be selected. Polarisers (again using mirrors with wire grids) will select the required polarisation and coupling into fundamental waveguide by means of corrugated horn antennas will select the correct mode. After a converter-taper the radiation from two of the slave antennas is transmitted to the slave detection systems in the $TE_{1,1}$ mode in 27.8 mm smooth waveguide.

5.6 Detection

The super heterodyne detection system [17] measures the spectrum of scattered radiation between 134 and 146 GHz in 32 spectral channels. The bandwidths of the different channels are chosen to be proportional to their displacement from the central frequency (see fig 1). Fig 7 gives a schematic of the system. The 134-146 GHz spectral region is downconverted to 6-18 GHz. In order to correct for frequency drift of the gyrotron or local oscillator, which is important for the central portion of the frequency region, this part is downconverted again using a local oscillator which is derived from the frequency difference between first LO and gyrotron. The frequency discrimination is performed by 32 bandpass filters and the signals are detected by Schottky detectors.

To recover the scattered signal from the background a data acquisition system has been built to sample the scattered signal at up to 5 megasamples/s and perform coherent addition of the signal in real time. In standard operation it is expected that 10

or more pulses will be added (during 1 ms) to give a single pulse form, characterised by 20 points. Further pulse addition will then be done in hardware.

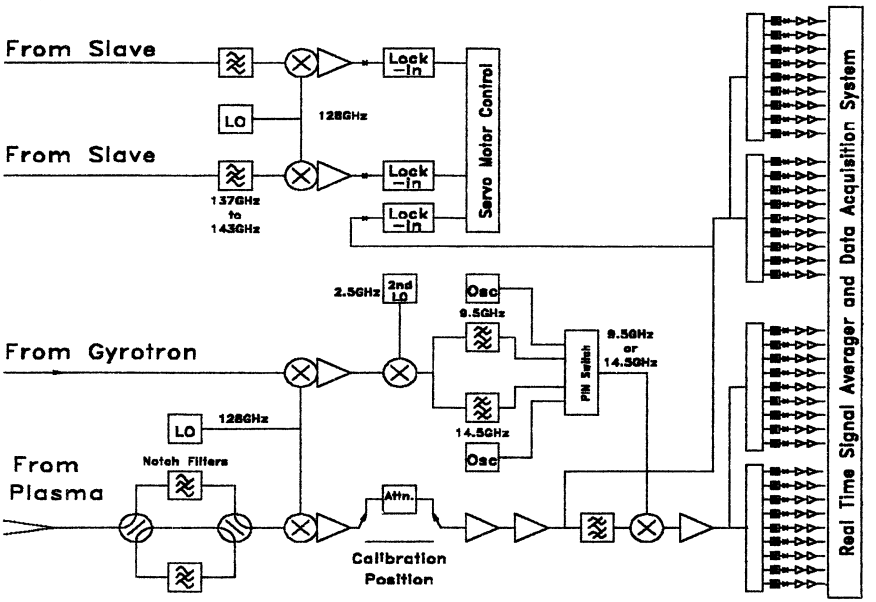

Fig 7: Schematic of the detection system

6 Status

During the last JET operational period the receiver system was used for passive measurements of the background radiation. These measurements confirmed expectations with respect to the background radiation level, which is important since statistical fluctuations on the background radiation are the main source of noise for the measurement. Transmission systems have been tested at low power, at which they perform satisfactorily. Presently, a prototype gyrotron, on loan from the US DoE, is being commissioned, while a commercial gyrotron is

now scheduled for delivery in early '94. New in-vessel components are being installed to make the diagnostic compatible with the new divertor geometry of JET. First plasma measurements are expected to be done after JET operation is resumed in '94 and will concentrate on measurements of the thermal ion feature and on fast ions created by the heating systems (mainly ICRH). There is a formal and important collaboration with the US DoE on this diagnostic, involving equipment and personnel from MIT and LLNL.

References

1. Costley AE et al, JET Report, JET-R(88)08,1988
2. Hughes TP and Smith SRP, J. Plasma Phys. 42,215 (1989)
3. Bindslev H, Plasma Phys. and Contr. Fusion 33,1775 (1991)
4. Bindslev H, Plasma Phys. and Contr. Fusion (in press) (1993)
5. Aamodt RE et al, Rev. Sci. Instr. 61,3211 (1990)
6. Aamodt RE et al, Nuclear Fusion 32,745 (1992)
7. Chiu SC, Phys. Fluids B3, 1374 (1991)
8. Bindslev H, Plasma Phys. and Contr. Fusion (in press) (1993)
9. Machuzak JS et al, Rev. Sci. Instr. 63,4648 (1992)
10. Costley AE et al, Proc. 7th Int. Workshop on ECE and ECRH (EC7), Hefei (1989)
11. Hoekzema JA et al, 16th Symp. on Fusion Technology, London, JET Report JET P(90)56 Vol 1, 61 (1990)
12. Thumm M et al, Report IPF Stuttgart (1988)
13. Hoekzema JA et al, 15th Symp. on Fusion Technology, Utrecht, Vol 1,314 (1988)
14. Birch JR et al, 18th Int. Conf. on IR an mm waves, Un. of Essex, Sept. 1993
15. Hughes TP et al, 18th Int. Conf. on IR an mm waves, Un. of Essex, Sept. 1993
16. Harvey AR, Int J. IR and mm Waves, Vol 14, no 1 (1993)
17. Fessey JA et al, 18th Int. Conf. on IR an mm waves, Un. of Essex, Sept. 1993

Peculiarities of the Strong Microwave-Plasma Interaction at the First Electron Cyclotron Harmonic in the FT-1 Tokamak

D.G Buliginsky, M.M. Larionov, V.V. Rozhdestvensky
Ioffe Physico-Technical Institute RAN,
St.-Petersburg, Russia

The strong MW-plasma interaction at the first EC harmonic, $f1$, under various densities have been studied in the FT-1 tokamak. MW-power of a gyrotron, $P_{mw} \simeq (60 - 100)$ kW, mode H_{02}, frequency $f_o = 30.6$ GHz, pulse duration $\tau_{MW} = 2$ ms, 80% P_{mw}—X-mode, was fed in the OH plasma through the Vlasov-type antenna placed from the high magnetic field side at 42° to the discharge chamber axis, [1]. Experiments were conducted in regimes with the toroidal magnetic field, $B_t = (8.7 - 11.6)$ kGs, discharge current, $I_p = 30$ kA,loop voltage $U_p = (2 - 2.5)$ V. The mean plasma density determined with a MW-interferometer was $\bar{n} = (5 - 7) \cdot 10^{12}$ cm^{-3}. Central electron temperature obtained from Thomson scattering and f_2 ECE measurements - $T_{eo} = (250 - 300)$ eV. Frequency dependencies of the radiation temperature , $T_r(f)$, in the f_2 magnetic broadening range, (44–67) GHz, were measured with a heterodyne radiometer, [2]. In the region near $2f_o$ a narrow band spectrum analyzer was used. The P_{mw} - signal, soft X-ray with quantum energy ≤ 10 keV, I_{sxr}, diamagnetic signal were registered also.

Basic experimental results are presented in Figs. 1-3.

Oscillograms, Fig. 1, obtained under $\bar{n} = 7 \cdot 10^{12}$ cm^{-3}, $B_t = 9.1$ kGs, $r_{ECR} = -8$ cm, show the following. Under MW-pumping,

(1), U_p, (2), goes down slowly from 2 V to 1.5 V, I_{sxr}, (3), and P_2, (4–6), grow essentially. At the same time during the MW-pumping with $P_{mw} \geq 20$ kW the more intensive emission near $2f_o$ arises, (7). After the MW-pumping U_p, (1), and P_2 from the central plasma region, (5), return to the initial level with the time constant appropriating the electron energy life time determined from diamagnetic measurements, $\tau_1 \simeq \tau_E \simeq 1$ ms.

However I_{sxr}, (3), and P_2 from the low B_t region, $r = +6$ cm, (4), go down with larger time constant, $\tau_2 = 3$ ms. P_2 from the high B_t region, $r = -12$ cm,(6), firstly falls down some what with $\tau_1 = 1$ ms, then increases, reaches the maximum value and diminishes again but with $\tau_2 = 3$ ms. The delay of the nonthermal component decrease relatively the MW-pumping end, $\Delta t = t_3 - t_2$, is of ~ 1 ms. Both τ_2, Δt increase together with $\bar{n}$ ramp down. It is possible to estimate the ECRH in the central plasma region where the f_2 optical thickness is larger then 1 on the thermal P_2 increase, (5), which is $\Delta T_{eo}/T_{eo} \simeq 30\%$ of the OH.

More complete data about the MW-pumping influence are in frequency, radial, dependencies T_r obtained under $B_t = 10.2$ kGs, $r = -2$ cm exhibited in Fig. 2.

Fig. 2 shows that in the OH plasma of $\bar{n} \simeq 5 \cdot 10^{12}$ cm^{-3} the profile $T_r(r)$ shape, (1.1, •), differs essentially from the T_e one,(⊗). The MW emission from the central plasma region, $r = \pm 2$ cm, is thermal, $T_r \simeq T_e$. The nonthermal emission character manifests in the plasma periphery. In the low B_t region, $r = -12$ cm, $f = 47$ GHz, there is the pike having $T_{rmax} \simeq 800$ eV, frequency broadening $\simeq 5$ GHz and shift $\Delta t = f - f_{2o} = 10$ GHz. The MW emission appears at frequencies for which the ECR-region is out the discharge chamber too.

Under MW pumping, $(1.2, t_2 - \Delta, t_{3-o})$, T_r increases essentially. The pike height reaches $T_r = 1.5$ keV. In regions: $r > 7$ cm $T_r(t_3) > T_r(t_2)$, $r < 7$ cm $T_r(t_3) \simeq T_r(t_2)$.

In the more dense OH plasma, $\bar{n} \simeq 7 \cdot 10^{12}$ cm^{-3}, (2.1, •), the MW emission from the high B_t region is thermal, $T_r(\bullet) \simeq T_r(x)$.

The T_r profile is asymmetrical. The small T_r pike in low B_t region

is at the same place. The MW emission at frequencies for which ECR region is out the chamber is remarkable yet. Under MW-pumping the T_r profile asymmetry increases, (2.2, ○). In the high B_t region, $r < +5$ cm, T_r is not changed practically. However the T_r pike height at $r = -12$ cm goes up to $T_{r\,max} \simeq 300$ eV. Such profile shape and behavior T_r, I_{sxr} in dependence of density and under MW-pumping are typical for the plasma with a beam of accelerated electrons.

They are synhrotron emission, SE, source and excite soft X-ray emission of heavy impurities like atoms Cr, Fe, Ni, [3]. It is possible in this case to evaluate the accelerated electron life time on $T_r(t)$ fall down, $\tau_b = 3$ ms, Fig. 1.4,6, and their full energy on the T_r pike relativistic shift, $W_o = W_{\parallel} + W_{\perp} = 100$ keV, Fig. 2.

Our experiments have shown MW-pumping is accompanied by effects analogous ones arising under density decrease in the OH plasma: the T_r profile asymmetry increases, pike T_r grows, but its place and broadening are not changed. On can explain the results obtained taking into account excitation of "pitch angle scattering" instability by the beam at abnormal Doppler effect, [4].

In the FT-1 tokamak with the relatively low Bt conditions for excitation of the instability in the OH-plasma are fulfilled under $\bar{n} = 5 \cdot 10^{12}$ cm^{-3} with a some storage, $\bar{n} = 7 \cdot 10^{12}$ cm^{-3}, at a limit. For the OH-plasma, $\bar{n} = 5 \cdot 10^{12}$ cm^{-3}, beam parameters are: $n_b/\bar{n} \sim 3 \cdot 10^{-4}$, $I_b/I_p \simeq 2\%$;$n_b \cdot W_b/\bar{n} \cdot \bar{T}e \simeq 0.1$.

The threshold meaning $W_{\parallel}$ is not high, $W^* \simeq 120$ keV. The time of electron acceleration up to the such energy and wave dumping are small. Therefore the "soft" continuous excitation of plasma waves occurs. In our case relaxation of plasma and beam parameters typical for the "hard" excitation regime in the high Bt tokamaks were not observed. Under plasma wave excitation decelerated beam component with $W_{\perp} \simeq W_{\parallel} \simeq W^*$ appears. Interaction with waves increases diffusion electron losses. Because of the B_t frillance, $\delta B_t/B_t \simeq 0.1\%$, $W_{\perp} \leq 30$ keV, as electrons of higher $W_{\perp}$ are locally trapped and drift very quickly to the chamber wall.

Owing to such diffusion and convective losses the full energy of accelerated electrons is the same as determined on the relativistic

shift of T_r pike one. The unchanged position of T_r pike under and without MW-pumping witnesses that Wo restriction mechanism is the same in both cases. Besides ECRH the MW-pumping increases the birth rate of runaways in the plasma. Fruitful conditions appear for the beam creation under larger plasma density and its density increase under lesser one. As the beam energy is frozen the T_r profile asymmetry increase and T_r pike growth may be produced by the beam density increase only. The more dense beam excites more intensive plasma waves. Therefore MW-pumping can increase both convective and diffusion electron losses.

Now consider the spectrum of the MW-emission near $2f_o$, Fig. 3. The spectrum contains the narrow maximum Tr appropriating the gyrotron emission at $2f_o$ and wings of different width: "red" $\simeq$ 2 GHz, "blue" $\simeq$ 1 Ghz. It seems the spectra at f_o, [5], and $2f_o$ are the same. As follows from [5], the such spectrum shape and threshold character of $2f_o$ emission can be produced by the parametric decay of pumping waves into electromagnetic and low hybrid ones, $t_{fo} \rightarrow t'_{fo} + l_{LH}$, in the upper hybrid resonance region, UHR. In this case broadening of the pumping wave spectrum may be of some LH-frequencies, $f_{LH} \simeq$ 300 GHz. What is the 2_{fo} emission nature? It is known in the UHR region not only the pumping wave parametric decay is possible but linear transformation into plasma waves too, $t'_{fo} \rightarrow l'_{fo}$. Under nonlinear interaction frequency of these waves can be twiced, $l'_{fo} \rightarrow l'_{2fo}$, [6]. During the their back transformation, $l'_{2fo} \rightarrow t'_{2fo}$, the powerful collective $2f_o$ emission arises. It was observed apparently in our experiments.

The obtained results let conclude that the high power MW-pumping together with ECRH can initiate in a plasma the beam of accelerated electrons exciting the Langmuir turbulence and produce the parametric generation of intensive plasma waves. As a result the plasma ECRH becomes unefficient due to increase of electron thermoconductivity together with convective and diffusion electron losses.

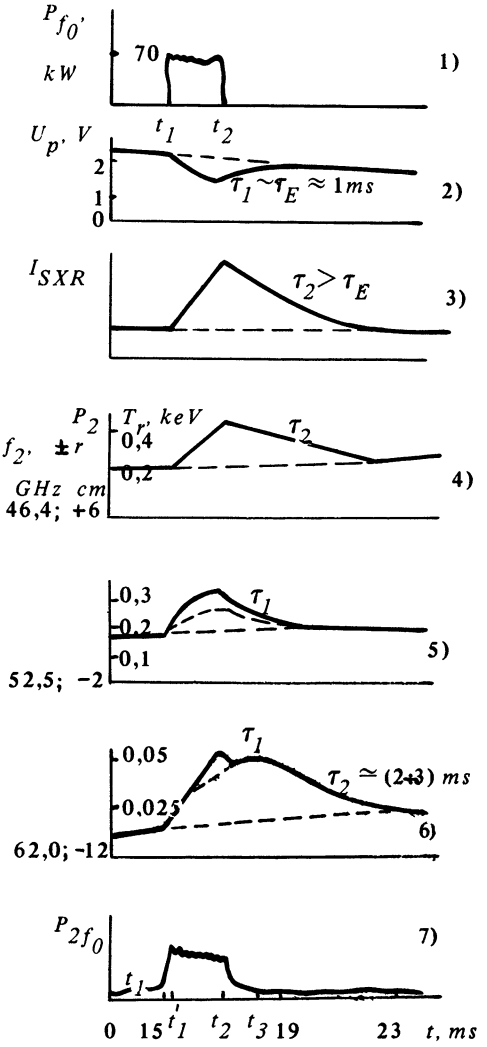
P_{f_0},
kW
70
1)
U_p, V
t_1
t_2
2
1
0
$\tau_1 \sim \tau_E \approx 1 ms$
2)
I_{SXR}
$\tau_2 > \tau_E$
3)
P_2
T_r, keV
f_2, ± r
0,4
0,2
τ_2
GHz cm
46,4; +6
4)
0,3
0,2
0,1
τ_1
5)
52,5; −2
τ_1
0,05
0,025
$\tau_2 \simeq (2+3)$ ms
6)
62,0; −12
P_{2f_0}
7)
t_1
0
15
t'_1
t_2
t_3
19
23
t, ms

Fig. 1.

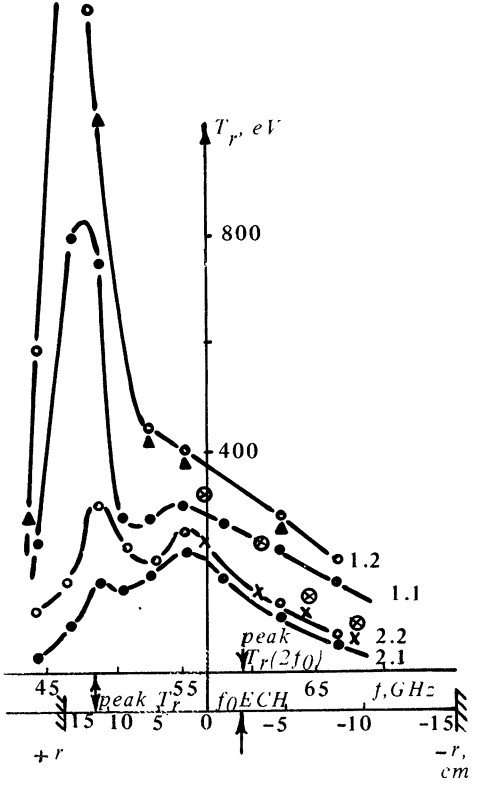
T_r, eV
800
400
1.2
1.1
2.2
2.1
peak
$T_r(2f_0)$
45
peak T_r
55
f_0ECH
65
f,GHz
15 10 5 0 -5 -10 -15
+r
-r, cm

Fig. 2.

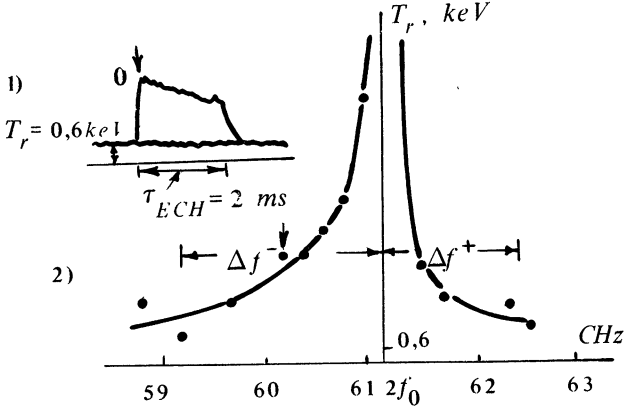
T_r, keV
1)
0
T_r = 0,6 keV
τ_{ECH} = 2 ms
2)
Δf^-
Δf^+
0,6
CHz
59
60
61
$2f_0$
62
63

Fig. 3.

REFERENCES

1. Baranov Yu.F., Buliginsky D.G., Golant V.E. et al. Fizika plasmi, 1982. v.8, p.682-693.
2. Buliginsky D.G.,Ivanov V.I., Larionov M.M. et al. Diagnostika plasmi, Issue 5, Edit. Pergament M.I., M. Energoatomizdat, 1986, p. 118-121.
3. Larionov M.M., Strong microwaves in plasmas Proc. of Int. Workshop, Suzdal, 18-23 September, 1990 Edit. Litvak A.G. Nizhniy Novgorod, v.1, p.252-257.
4. Parail V.V., Pogutze O.P., 1991 Voprosi teorii plasmi Edit. Leontovitch M.A. and Kadomtzev B.B, M. Energoizdat, 1982, n.11, p.5-55.
5. Buliginsky D.G., Djachenko V.V, Irzak M.A. et al. Fizika plasmi, 1986, v.12, p.138-142.
6. Hosea J., Arunasalam V., Cano P. Preprint, Prinston, 1977, PPP-1362.

CYCLOTRON RESONANCE HEATING OF ELECTRONS IN A SHORT MIRROR TRAP

V.D. Dugar-Zhabon, I.D. Mikhailov, D.V. Reznikov,
A.M. Umnov and V.I. Kushnarenko
Russian Friendship University, 117198, Moscow, Russia

1 Introduction

The analytical and numerical treatment of cyclotron resonance interaction of electrons with microwaves in mirror traps has been the objective of much research [1-3]. The upper limit of ECR heated electrons is a major goal of the theoretical analysis. This is because the energies observed experimentally [4,5] are usually greater essentially of one predicted. It should be noted that only longitudinal inhomogeneity of magnetic field has been taken into account in these theoretical and numerical studies. This method of attack is acceptable if magnetic field radial component such small that inequality

$$\rho \ll B/\nabla B \tag{1}$$

is satisfied. Here ρ is a Larmor radius of an electron, B is a magnetic field value, ∇B is a radial gradient of magnetic field. The inequality (1) can be valid for long mirror traps created by solenoidal type magnetic coils but short magnetic traps used especially as a basis for electron cyclotron resonance (ECR) ion sources are characterized by not only logitudinal inhomogeneity but also strong radial one. Magnetic mirror fields created by permanent magnets are of radial gradients that the inequality (1) is not satisfied. So an assumption of independence of electron heating on radial magnetic field profile is not correct.

This report is basically to atract attention to the fact that the ECR-phenomenon becomes more complicated due to strong tranverse imhomogeneity of magnetic field.

2 Experiment

To study the ECR heating in an inhomogeneous magnetic field, a mirror trap created by $Sm-Co$ disk type magnets is prepared. The dimensions of disks are: diameter $5.5cm$, thickness $3cm$, The separation between them is fixed at $8.4cm$. The hydrogen discharge is generated in an Aluminium TE_{111} cavity placed axisimmetrically between poles and supplied from a $2.45GHz$, $240W$ magnetron. The cavity is a cylinder of $13cm$ diameter and $8cm$ long. At magnetic field $3.4kG$ on the pole surfaces, the transversal gradient on a radius $R_c = 1.7cm$ in the mid-plane where value of magnetic field $B = 875G$ is equal to cyclotron resonance one $B_c = mc\omega/e$ is about $300G/cm$. So the inhomogeneity length scale $\lambda = 2.2cm$. The more detailed description of the device is done elsewhere [5].

To find the energies of ECR heated electrons we use a X-Ray telescope based on $NaJ(Tl)$ cristal connected with a storage-pulse- inheight 256-channel analyser. The electron energy distribution function can be deduced from experimentally found X-Ray spectrum taking into account the absorption in a Berillium window and the spectral sensivity of the cristal. Because of this, a Fredholm integral equation of the first kind as an unstable inverse ploblem is to be solved.

Localisation and geometrical sizes of the zone of accelerated electrons is determined by using the bremsstrahlung emission from a movable small ($1mm$ diameter) molibdenum target and taking X-Ray photographs through a pinhole.

The experimental data demonstrate that the effective heating takes place in a ring layer located practically in the mid-plane of the trap since the longitudinal size of rings is very small.

The energy and the fraction of ECR accelerated electrons are established to be function of gas pressure. Dependence on microwave power in the range from $75W$ to $240W$ is not clearly defind. To take an microwave power $220W$. as an example, the guiding center of the resonant heated electrons rests on the resonance surface in the mid-plane at a pressure 4×10^{-4} Torr and higher (see Fig.1a). The thicknesses of the ring, $(3-4)mm$, agree with the calculated electron

Larmor radius for observed middle electron energies of $(7-8)keV$ or less at these pressures. A negligible small Larmour radius in comparision with the inhomogeneity length scale,λ, allow to understand coincidence of the measured energy values with the calculated ones under assumption of homogeneous magnetic field [6]. Decreasing of pressure up to $1 \times 10^{-4} Torr$ is accompanied by a very sharp energy jump. At microwave power $220W$ the distribution function has a peak at energy about $310keV$. Simultaneously electron trajectories change drastically and an electron ring transforms into an electon vortex with the center on the magnetic field axis as shown in Fig.1b.

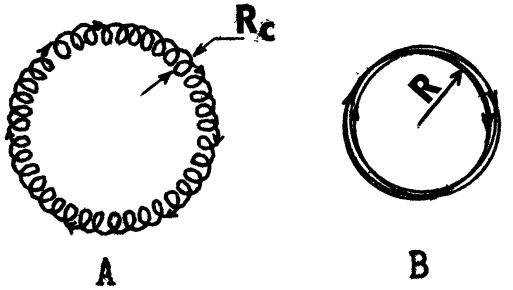

Fig.1

The fact that the radius of vortex is $1.1cm$ means localisation of the hot electrons in a magnetic field region where $B < B_c$. Radial stability of the vortex is provided by fulfilment of the expression for an relativistic equilibrium orbit [7]

$$\beta W = eBR, \tag{2}$$

where $\beta = v/c$; e, v and W are electron charge, velocity and energy, R is vortex radius. As for vortex stability along the magnetic field, the stability is maintained by the mirror configuration of magnetic field. The high longitudinal gradient of $250G/cm$ in the vicinity of a point $R = 1.1cm$ and compensation of interelectron repulsion due to magnetic field self-created by the electrons moving with a relativistic speed keep the vortex wideness within $(3-4)mm$. Cyclotron

resonance heating of electrons in the short mirror traps with strong transversal inhomogeneity and in the long ones with relatively weak inhomogeneity differs from each other not only by energy jumps under gas pressure change but ubnormal high energy to be observed in the case of a short trap. Because these effects are not explained analitically and numerically if it is taken into consideration the case of transversal homogeneity we try to examine some nonlinear effects arising from a transversal inhomogeneity of a magnetic field.

3 Orbital instability

It is well known that resonant absorption of microwaves by plasma electrons in magnetic field B takes place at coincidence of a microwave frequency ω to cyclotron frequency

$$\omega_c = eB/mc. \tag{3}$$

In our experiments there is some evidence for strong microwave energy absorption in a regeon where a microwave frequency significantly less the cyclotron one. It is clear that explanation is to associate with the nonlinear terms in an equation of motion.

From the theory of nonlinear oscilation follows that nonlinear terms bring into existence two crucially new effects: sccondary resonant frequencies lying above and below the main frequency are appeared; for another, jumps and hysteresis loops in an amplitude-frequency charactristic are originated. Such jumps result from nonlinear relativistic terms in dynamic equation at ECR were first demonstrated by Kaplan [8]. So we treat only the influence of a transversal inhomogeneity on the cyclotron resonance electron motion. Let the microwave field components are given by

$$\begin{aligned} \mathbf{E} &= E_0[\mathbf{i}\sin(\omega t - kz) + \mathbf{j}\cos(\omega t - kz)] \\ \mathbf{H} &= H_0[\mathbf{i}\sin(\omega t - kz - \pi/2) + \mathbf{j}\cos(\omega t - kz - \pi/2)] \\ H_0 &= E_0 k/\omega c \end{aligned} \tag{4}$$

Let restrict our considerstion of electron motion in XOY-plane. Then the equation of motion can be written as

$$m\frac{d\mathbf{v}}{dt} = \frac{e}{c}[\mathbf{v}(\mathbf{B}+\mathbf{H})] + e\mathbf{E} - \frac{m}{\tau}\mathbf{v}, \tag{5}$$

where τ^{-1} is frequency of electron collisions. Introducing notation φ for the angle between electric microwave component and the electron velocity direction we derive the expressions for normal and tangential components of eq.(5)

$$eE_0\cos\varphi - \frac{m\omega r}{\tau} = 0$$

$$m\omega^2 r - \frac{e}{c}\omega r B - eE\sin\varphi = 0. \tag{6}$$

To obtain the radius of electron rotation as a function of microwave frequency one can exclude φ

$$\frac{m\omega^2 r}{e^2E_0^2\tau^2} + \frac{(m\omega^2 rc - e\omega rB)^2}{e^2E_0^2c^2} = 1. \tag{7}$$

For axially inhomogeneous magnetic field $B = B_0\Theta(r)$, where B_0 is a magnetic field at the center of electron rotation so that $\Theta(0) = 1$. Putting dimensionless variables $\xi = \omega/\omega_0, \eta = r\omega/c$ eq.(7) can be rewritten in more simple form

$$\psi^2(\xi,\eta) + N^2[\psi(\xi,\eta)\xi - \Theta(\eta)]^2 = \frac{A^2}{\xi^2\eta^2}, \tag{8}$$

where $A = eE_0\tau/mc$, $N = \omega_c\tau$, $\Psi(\xi,\eta) = (1-\xi^2\eta^2)^{-1/2}$. The last equation gives in implicit form the dependence $\eta(\xi)$ which describes an amplitude-frequency characteristic $R(\omega/\omega_c)$ and due to its nonlinearity a jump of radius value is possibly to be observed. Then $\Psi(\xi,\eta) = 1$ and let $\Theta(\eta) = 1 + \alpha\eta^2$ one can derive an amplitude-frequency characteristic by solving a cubic equation

$$z^3 + az^2 + bz + c = 0, \tag{9}$$

where $z = \eta^2$, $a = -2(\xi - 1)\alpha^{-1}$, $b = 1 + N^2(\xi - 1)^2(N\alpha)^{-2}$, $c = -A(N\alpha\xi)^{-2}$. There are three solutions of Eq.(9) at the fulfilment of two requirements

$$3 - N^2(\xi - 1)^2 < 0 \tag{10}$$

and

$$\left[\frac{3 - N^2(\xi - 1)^2}{9N^2\alpha^2}\right]^3 + \left[\frac{(1 - \xi)[54 + 38(1 - \xi)^2]}{54N^2\alpha^3} + \frac{A}{2N^2\alpha^2\xi^2}\right]^2 < 0 \tag{11}$$

In Fig.2 we plot the grafs of electron rotation radius vs the ratio ω_r/ω for radially homogeneous (1) and inhomogeneous (2) magnetic field.

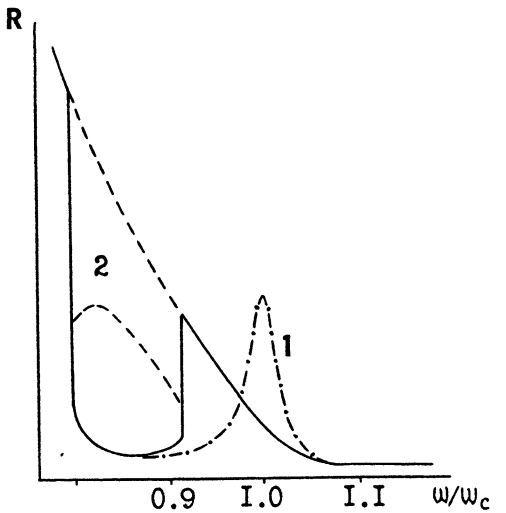

Fig.2

From this curves one can see that an usual resonance curve transforms into hysteretic one in the last case. It is obvious that the jump change of the radius depends on ω/ω_{c0}. At $\tau^{-1} = 2.5 \times 10^6 s^{-1}$ which corresponds in experiments to a pressure $(1 - 2) \times 10^{-4} Torr$ a radius of electron rotation can increase by a factor of three. The last is in good agreement with the experimental observations.

4 Calculation

In order to find mechanisms which lead to obtaining such high energy by electrons 3D - numerical model of the process has been applied. Relativistic equation of motion of electrons in "real" microwave electric and magnetic fields created in above mentioned installation are solved by means of leap-frog scheme. The influence of initial particle position, adiabatic effects and drifts on electron dynamics has been studied. The analysis of obtained calculating results show that sharp energy increase and jumps of electron ring location are possible in case of even very slight radial drift of Larmor orbit center of an electron. It is seen from Fig.3 that due to radial drift movement into the region of higher magnetic field value an electron gains energy till such a drift presents (Fig.3, curve 2).

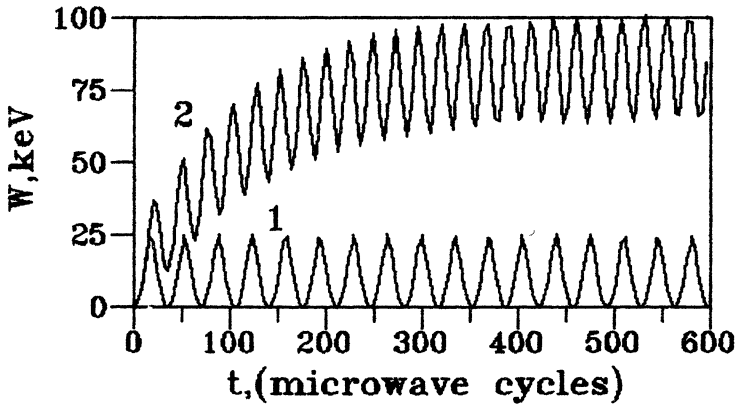

Fig. 3

In Fig.3, curve 1, the energy of electron not to be in drift movement is shown. The obtained results allow to propose that if this drift really exists it is the most probable reason for obtaining high electron energies. At the same time it should be pointed out that this calculations can not give the exostive explanation of electron acceleration (up to $310keV$ and above) mechanism. Thus we will examine the new effect of multiple resonances produced by transverse inhomogeneity of magnetic field.

5 Multiresonant effects

We consider electron gyrated in the XOY plane in magnetic field $\mathbf{B} = [0, 0, b(x)]$ at presence of microwave field $\mathbf{E} = (0, E_0 \cos \omega t, 0)$. Let the inhomogeneous is of parabolic along x-axis

$$b(x) = b_0 - b_1 x^2. \tag{12}$$

Here $b_1 d^2 \ll b_0$, d is characteristic length scale of electron trajectory. Taking into account that the cyclotron freqency is dependent on x position one can obtain the equation for v_x as follows

$$\ddot{v}_x + \frac{2}{\tau}\dot{v}_x + (\omega_{c0}^2 + \frac{1}{\tau^2})v_x = \frac{eE_0}{m}\omega_{c0} \cos \omega t -$$

$$\frac{b_1}{b_0}\left[x^2(\ddot{v}_x + \frac{2\dot{v}_x}{\tau}) + xv_x(\dot{v}_x + \frac{v_x}{\tau}) + \omega_{c0}^2 x^2 v_x(2 + \frac{1}{\omega_{c0}^2\tau^2})\right] \tag{13}$$

The eq.(13) is a nonlinear equation of forced oscilations in inhomogeneous magnetic field under microwave field action. The small parameter in the nonlinear term in the right side is the ratio b_1/b_0. We analyse here only resonant frequencies by the expantion method

$$v_x(t, \varepsilon) = v_0(t) + \varepsilon v_1(t).$$

The first term in the right side of the last relation is responsible for the main resonance $\omega^2 = \omega_{c0}^2 - \tau^{-2}$. An equation for $v_1(t)$ can be written as follows

$$\ddot{v}_1 + \frac{2}{\tau}\dot{v}_1 + (\omega_{c0}^2 t + \frac{1}{\tau^2})v_1 = \sum_{i=1}^{n} \frac{eE_0\omega_i}{m} \cos(\omega_i t + \delta_i) \tag{14}$$

The common solution of eq.(14) is

$$v_1(t) = a \exp(-t/\tau) \cos(t\sqrt{\omega_{c0}^2 + \tau^{-2}} + \alpha)$$

$$+ \frac{\sum_{i=1}^{n} eE_0\omega_i \cos(\omega_i t + \delta_i)}{m\sqrt{(\omega_{c0}^2 + \tau^{-2} - \omega_i^2)^2 + 4\omega_i^2\tau^{-2}}}, \tag{15}$$

where $tg\delta_i = 2\omega_i/\tau(\omega_{\omega}^2 + \tau^{-2} - \omega_i^2)$, a and α are time independent constants. The solution (15) evidences existence of many resonant frequences specified by type of nonlinearity in eq.(13). It should be noted that inclusion of relativism into consideration leads to the same effects.

6 Conclusion

Obtained results allow to conclude that in case of cyclotron resonance in short mirror traps with strong inhomogeneity there exist processes which lead to electron heating up to extremely high energies unlike cyclotron resonance heating in long mirror traps. Upper level of electron energy is determined by the magnetic field configuration, residual gas pressure and electric field strength. This gives a possibility to use such a phenomenon in some applications, for example, to design unexpensive simple constructed compact X-Ray source.

References

1. Jaeger F., Lichtenberg A.J. and Lieberman M.A., Plasma Phys.,197 14, 1073.
2. Sergeev A.A., Suvorov E.V. and Tokman M.D., preprint 172, Inst. of Applied Physics, Gorky (USSR), 1987.
3. Timofeev A.V. and Kharitonov K.Yu., preprint IAE-5084/6, Kurchatov Inst. of Atomic Energy, Moscow, 1990.
4. Fujiwara M. et al., Plasma Phys. and Contr. Nucl. Fus. Res.,1983. **2**, 197.
5. Dugar-Zhabon V.D.,Reznikov D.V. and R.Santos Mayorga, Proceed. XX Int.Conf.on Phenom Ion.Gases, Pisa, 1991, Italy, **5**, 1065.
6. Golovanivsky K.S., Dugar-Zhabon V.D. and Milantiev V.P., Fisika Plazmy, 1975, **1**, 655.
7. Ternov I.M., Mikhailin B.B. and Khalilov B.P., Synchrotron Radiation and its Application, 1985, Moscow Univ., 29.
8. Kaplan A.E., Phys. Rev. Letters, 1982, **48**, 138

EXPERIMENTS ON LOWER HYBRID WAVE EXCITATION IN FT-1 TOKAMAK

V.V.D'yachenko, M.M.Larionov, K.M.Novik, V.Yu.Shorikov
A.F.Ioffe Physical-Technical Institute,
St.Petersburg, Russia

The experiments on the excitation of powerful lower hybrid (LH) waves (ω = 300 MHz - 5 GHz) were realized in many tokamaks, FT-1 was one of the first of them [1,2,3,4]. Scalings with electron density ($\bar{n}_e$) and frequency (ω) were studied. In experiments with high ω and low $\bar{n}_e$ the regime of current drive and electron heating due to Landau damping of waves was found. In the opposite case, current drive effect turns off and generation of fast ions by LH waves was detected by the charge exchange (CX) diagnostics. In most experiments, fast ions have short life time. Probably, they are accelerated near the plasma periphery, whereas LH resonance conditions can be met in the central zone. In both regimes experimental results are found to be in some disagreement with theoretical predictions. These predictions are based on $N_{\parallel}$ spectrum of waves, calculated in assumption that the wave excitation structures (antennas, waveguide grills) are placed in a vacuum near the plasma boundary. The optimal $N_{\parallel}$ = 2-5 are used in experiments. To explain the experimental results, one can assume that more strongly slowered waves, $N_{\parallel} > 10$, $N_{\perp} > 10^3$, are really interacting with electrons and ions ($N_{\parallel}$, $N_{\perp}$ - refractive indexes in a magnetized plasma). There are some ideas about generation of high-$N_{\parallel}$ component during the wave propagation in a plasma (toroidal effects, parametric wave decay phenomena and so on). Besides, we propose another explanation. It is clear that any wave exciting structure is operating not in the vacuum, but it has a

contact with the rarefied peripheric plasma. This contact changes strongly the conditions of its operation and can lead to the excitation of strongly slowered waves. Corresponding phenomena are discussed in the theory of radiofrequency (RF) discharges between electrodes [5,6,7]. They present electrical polarization (generation of space charge layers) near surfaces carrying RF potentials. This Debye layer presents some electrical capacity and nonlinear conductivity. As RF current flows through it, plasma can increase its positive floating potential to the level of RF voltage amplitude at the antenna. This leads to the increase of thickness and to the decrease of capacity of Debye layer and to the redistribution of RF fields around the antenna. Small regions are formed near the antenna in which strong RF field is localized. This effect can provide excitation of strongly slowered waves, oblique Langmuir or ion Bernstein modes, with

$$N_{\perp} \cong \lambda/(10\ D) \cong 10^{3},\ N_{\parallel} = (\omega/\omega_{0})N_{\perp} = 10\text{-}10^{2}$$

(λ - vacuum wavelength, ω_o - local plasma frequency, D - Debye length). Plasma volume presents the inductive resistance at frequencies $\omega < \omega_o$. So the effect of polarization depends strongly on the ω and local density n_e. In the case of high ω and low n_e it is rather weak, and the excited spectrum of $N_{\parallel}$ coincides with the theoretically calculated one with some enhancement of strongly slowered component. This case corresponds to the current drive and electron heating regime. At low ω and high n_e, RF field is localized in the Debye layer and strongly slowered component becomes the main part of power spectrum. At the power level of tens of kW, RF field near the antenna or waveguide grill can reach 10^4 V/cm. The waves excited by this field can accelerate ions to the energy of some keV just near the antenna or grill, and can be absorbed by electrons through nonlinear processes. The increase of a positive floating potential of a plasma leads to the intensification of ion bombardment, accompanied by the reflection of fast neutral atoms and by the sputtering

of antenna material. This situation corresponds the regime of generation of fast ions by LH waves.

Resent experiments in FT-1 tokamak confirm the presented explanation of LH phenomena. FT-1 (R=62 cm, a=15 cm, B_o<1.2 T, I=30-50 kA) is supplied by two magnetron generators, 360 MHz and 920 MHz, 50-100kW in 5-10 ms pulses. As against of experiments using waveguide grills, in FT-1 the slow-wave structure is used, consisting of the number of ring limiters r=16 cm inside a discharge chamber. Active electrode (antenna) for electrostatic excitation of the waves is fed by a coaxial line [2]. Fig. 1A presents the scheme of antenna device and the position of diagnostic tools - soft X-rays (SXR) and charge exchange (CX) analyzers. The last was movable and allows to scan the discharge cross-section. Two versions of antenna position, symmetrical and asymmetrical, are shown in Fig. 1C,B.

Two different regimes of wave-plasma interaction were found, if different frequencies were applied to similar antenna devices. AT 360 MHz, 60 kW, the intensive generation of high energy ions was registered by charge exchange analyzer. The ohmic ion temperature was 100-120 eV. Under RF pulse the "tail" of ion distribution appears in the range of 0.5-5 keV. Main part of these particles have short life time, < 0.1 ms. In measurements with asymmetrical antenna position, strong dependence of "tail" intensity on the direction of toroidal drift of ions was found (Fig. 2). Chord measurements of CX fluxes in this experiment show that ions are accelerated by RF field nearby the antenna, but not in the zone of LH resonance in the central part of a discharge. RF pulse at 360 MHz also produces fast increase of $\bar{n}_e$ and corresponding increase of soft X-ray emission, without marked change its thermal spectrum. The ion temperature in ohmic discharge was 100-120 eV. In RF pulse, SXR measurements show $T_e \cong 500$ eV, as in ohmic heating (Fig. 4B,C)[3,4]. Quite different data are observed under 920 MHz pulse of the same power. The generation of high energy ions was strongly reduced. The increase of n also was not found. However, strong

flash of soft X-ray emission was detected (Fig. 4B,C). Its spectrum is of nonthermal nature and corresponds to the "tail" of electron distributions of effective $T_e \cong 5$ keV. So, well-known regimes of LH wave plasma interaction, generation of fast "tails" in electron or in ion energy distributions, are found in FT-1 experiment. These regimes are well studied in experiments using waveguide grills.

The construction of FT-1 antenna and its coaxial feeding line allows to make some measurements explaining the role of electrical polarization in LH experiments. Antenna rods are placed at 1 cm inside the limiter shadow, between the rings of slow wave structure. Probe measurements show the local density $n_e \leq 10^{11}$ cm^{-3} in this point, as $\bar{n}_e \geq 10^{13}$cm^{-3} was measured by interferometer. The dependence of antenna current on its constant potential relative to the liner of tokamak was measured (Fig. 3). It demonstrates the contact of antenna with the peripheric plasma. The V-A dependence is strongly nonlinear, electron and ion branches are well defined. At +300 V current reaches 40 A. In ohmic discharge, the floating potential of antenna is -3 - -5 V, its short circuit current is about 2 A. The construction allows to measure the rectified components of antenna voltage and current during RF pulse, generated due to nonlinear V-A dependence, Fig. 3. Constant antenna voltage presents a part of plasma floating potential around the antenna and it shows the level of polarization phenomena. Measurements show the strong difference between two frequencies. At 920 MHz, floating potential of antenna increases slightly to -8 - -10 V during RF pulse. In 360 MHz pulse the potential grows strongly to -450 V (Fig. 4D). Rectified components of antenna current are shown in Fig. 4E. Also, there is small increase under 920 MHz pulse, whereas at 360 MHz the current reaches 20 A. For comparison, in 60 kW RF pulse the amplitude of RF voltage at the antenna is about 2.5 kV and RF current in the feeding line is 35 A. Optical emission of a plasma surrounding the antenna is shown in Fig. 4F.

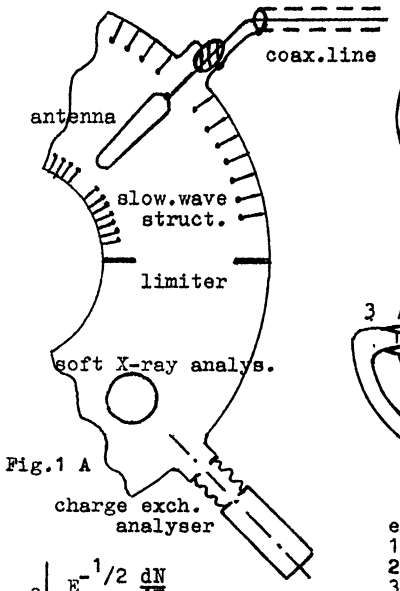

Fig.1 A

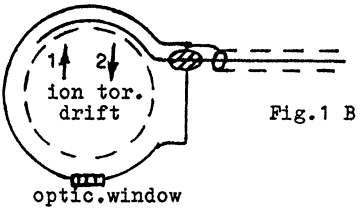

Fig.1 B

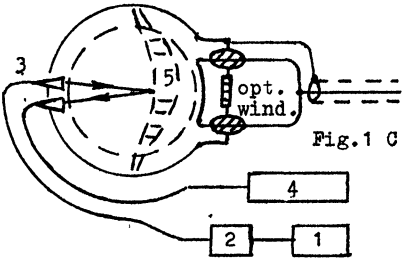

Fig.1 C

enhanced scattering exp-t:
1-generator 24 GHz
2-modulator 1 kHz
3-microwave horn antennas
4-spectr. analyser
5-upper hybrid res.zone

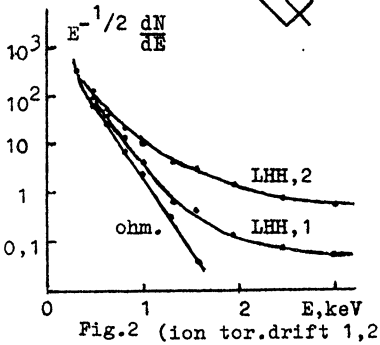

Fig.2 (ion tor.drift 1,2)

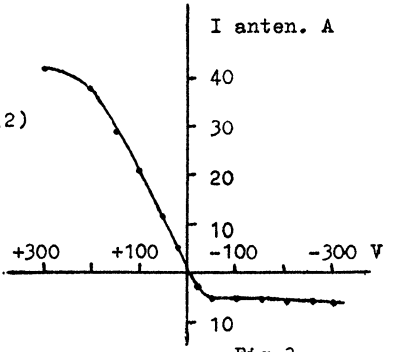

Fig.3

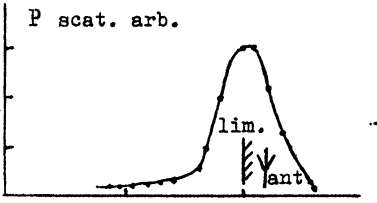

Fig.5 (position of upp.hybr.res.)

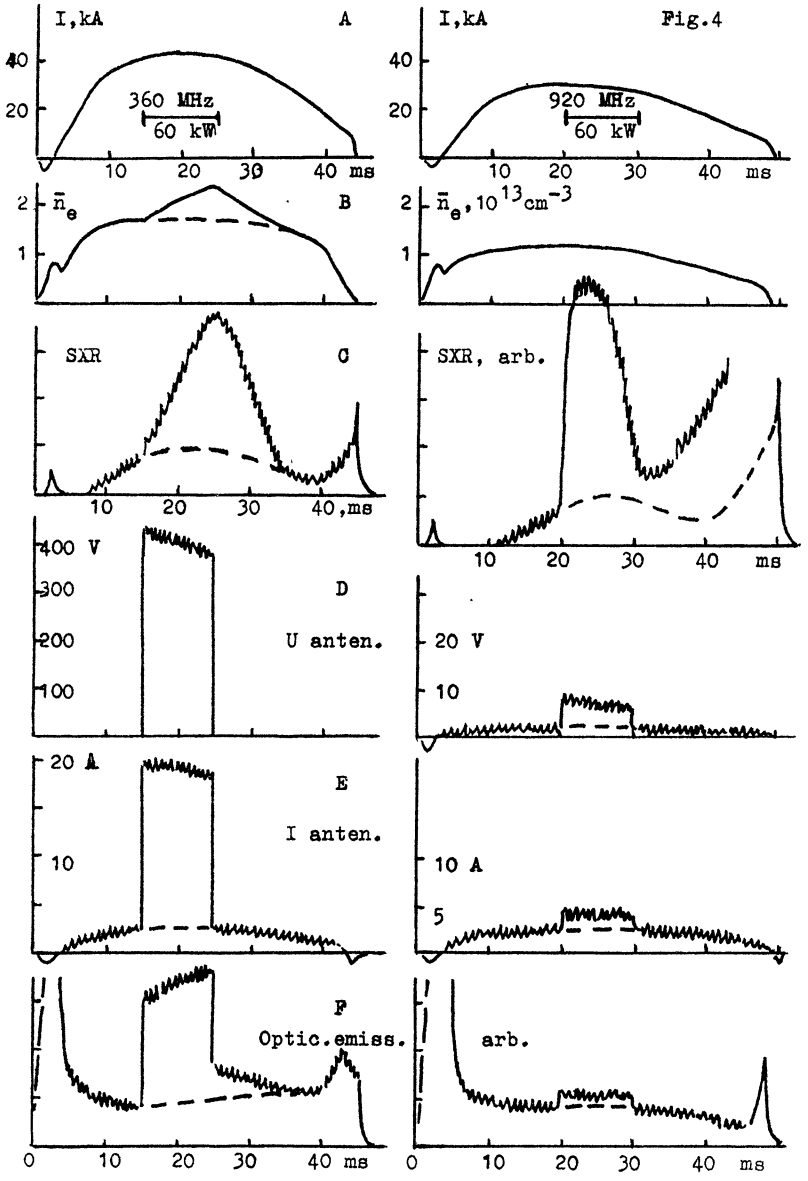
I,kA
A
40
20
360 MHz
60 kW
10
20
30
40 ms
I,kA
Fig.4
40
20
920 MHz
60 kW
10
20
30
40 ms
2
1
$\bar{n}_e$
B
2
1
$\bar{n}_e$, 10^{13}cm^{-3}
SXR
C
10
20
30
40,ms
SXR, arb.
10
20
30
40
ms
400 V
300
200
100
D
U anten.
20 V
10
20 A
10
E
I anten.
10 A
5
F
Optic.emiss.
arb.
0
10
20
30
40 ms
0
10
20
30
40
ms

Also, small effect is detected at 920 MHz, whereas a strong flash of light is observed during 360 MHz pulse, consisting of spectral lines of hydrogen and low ionized impurities. Extremely sharp increase of Fe I, Cr I lines demonstrates the results of strong ion bombardment and sputtering of antenna material under 360 MHz RF pulse.

So, at 360 MHz, 50-100 kW, the intensive generation of high energy ions in a tokamak plasma is accompanied by the phenomena presenting strong polarization of a plasma around the antenna. At similar pulse of 920 MHz ion acceleration is strongly reduced, but the generation of fast electrons is developed. In this case the polarization phenomena are much weaker. Probably, the difference in regimes of LH waves interaction with plasma particles at different frequencies depends on the level of polarization phenomena in peripheric plasma near the wave exciting structure. This level determines the relative intensity of strongly slowered component in $N_{||}$ spectrum of excited waves. The frequency dependence is consistent with the theory [5,6].

In the LH experiments at 920 MHz, the measurements of strongly slowered waves in a plasma volume and near the antenna were realized by the method of "enhanced scattering" of microwaves [8]. The backscattering of the probing signal of extraordinary mode near its upper hybrid resonance surface is extremely sensitive to the short wavelength (λ(osc) $\ll$ 1/2 λ(prob)) density oscillations in a plasma. The spectrum of scattered signal brings the information on the frequency spectrum of these oscillations. The scheme of FT-1 experiment is presented in Fig 1C. 24 GHz signal is used for probing Changing the magnetic field B_o, one can observe the scattering in a plasma at radial positions X = R+r, r=9-18 cm. Measurements were fulfilled only in the regime of weak polarization phenomena at the antenna, where no ion acceleration was detected by CX analyzer, but the interaction of LH wave with electrons was observed by SXR signal. In this case, only oscillations

of a pumping frequency, 920 MHz, were found, no oscillations at ω<920 MHz, generated by some wave decay processes,were detected. The radial distributions of scattered signal is shown in Fig. 5. Strongly slowered component of LH waves is observed at all accessible radial points, but the signal is extremely increased nearby the antenna position. Probably this component of a wave spectrum is generated not in the plasma volume, but by the space charge layer surrounding the antenna.

REFERENCES

1. Gladkovsky I.P., Golant V.E., D'yachenko V.V., Larionov M.M. et al. Zh. Techn. Fiz. 1973,18,1632.
2. Gladkovsky I.P., D'yachenko V.V.et al. Fiz. Plasmy 1979,5,512.
3. Bulyginsky D.G., Goncharov S.G., D'yachenko V.V. et al. Plasma Physics and Contr. Nucl. Fusion Research 1984,v.1,491.
4. Baranov Yu.F., D'yachenko V.V., Larionov M.M. et al. Proc 15th Europ. Conf. Contr. Fusion and Plasma Heating, Dubrovnik 1988, v.3, 908.
5. Godyak V.A., Kusovnikov A.A, Fiz. Plasmy 1975, 1, 496.
6. Godyak V.A., Fiz. Plasmy 1976,2,141.
7. Raizer Yu.P., Shneider M.N. Fiz. Plasmy 1987, 13, 471, Fiz. Plasmy 1988,14,226.
8. Novik K.M. Proc. Int. School of Plasma Physics Varenna, Italy, 1986, v.2, 517.

ON THE POSSIBILITY OF CURRENT DRIVE IN TOKAMAKS BY BERNSTEIN MODES

A.G. Litvak, E.V. Suvorov, M.D. Tokman
Institute of Applied Phys., Russian Academy of Science
46, Ulyanov st. 603600 Nizhny Novgorod, Russia

Inductionless current drive (CD) in tokamaks by rf radiation is being intensively studied both theoretically and experimentally [1]. The greatest success in rf CD was achieved using lower-hybrid (LH) waves. Nevertheless CD scheme by electron-cyclotron (EC) waves proposed by Fish & Boozer [2] also seems rather attractive (due to relative simplicity of the launching system and the possibility of fine localization of driven current). This scheme does not assume the injection of noticeable longitudinal momentum into plasma electrons. The concept of CD is based here on the preferrable heating of electrons with a fixed sign of longitudinal velocity $v_{\|}$ and producing in this way an anisotropic electron resistivity. This can be easily realized with oblique launch of EC waves into toroidal plasma with the optical depth $\tau > 1$.

Within the limit of strong Coulomb collisions efficiency of rf current-drive is determined by relation (the form of the expression for η is identical for the EC and LH methods when $v_R \gg v_T$ [1]):

$$\eta = \frac{I}{P} = k v_R^2 \qquad (1)$$

where P is radiation power , v_R is characteristic velocity of resonance particles (it is assumed that $v_R \gg v_T$, where v_T is thermal velocity

$(2T_e/m)^{1/2}$), and coefficient k depends on the dimensions and geometry of the tokamak and on the plasma parameters.

EC CD efficiency can achieve up to 75% of LH CD efficiency in the case of high collision frequency; with the strong quasi-linear modification of electron distribution function these two efficiencies become equal [3]. In experiments EC CD efficiency is usually essentially lower than the value obtained theoretically [4]. This is an effect of electron trapping into the local magnetic traps of the toroidal system [4, 5].

It may be seen from Eq. (1), that CD efficiency increases with the increase of resonance particle velocity; besides, the increase in the longitudinal velocity of resonance particles tends to diminish the toroidal trapping effect [5]. If microwave power is absorbed in the region $\omega_H < \omega$ (ω_H is electron gyrofrequency, and ω, wave frequency), the trapping effect can be reduced also due to the increase of the longitudinal refraction index $n_\parallel$ [6]. At present experiments have being performed [7] in which essential increase in the EC current drive efficiency was obtained due to injection of microwave power into the torus at small enough angles to the magnetic field ($n_\parallel \approx 0.7$) and its absorption by the "tail" of hot electrons previously formed by lower-hybrid waves.

In the present communication we would like to draw attention to the possibility of preventing electron trapping effects and significant raising the energy of resonance particles $mv_R^2/2$ by the mode conversion with the radiation reflection from the upper-hybrid resonance layer and subsequent absorption of radiation in the form of Bernstein wave.

1. Excitations and absorption of Bernstein waves in tori was considered in [8]. Radiation is injected into plasma from a high field side in the form of an extraordinary wave (X-mode), then it is transformed into a longitudinal wave by reflection from the upper-hybrid resonance zone, and further is absorbed in the region of cyclotron resonance.

Due to poloidal component of magnetic field B_θ the Bernstein wave can undergo singnificant slowing-down in the magnetic field di-

rection even with the quasi-transverse launch of X-mode. Maximal longitudinal refractive index $n_{\|}$ is determined by the following relation:

$$n_{\|} \simeq n_{\perp} B_{\theta} / B_{\varphi} \tag{2}$$

where $n_{\perp}$ is transverse refractive index, and B_{φ} is toroidal magnetic field. If the plasma temperature is not too high (nonrelativistic), and its density is of the order of magnitude of the critical one ($\omega_p^2 \sim \omega^2$), then in the dissipation zone of the Bernstein mode its refractive index $n_{\perp}$ may be estimated as:

$$n_{\perp} \simeq \beta_T^{-1} ; \tag{3}$$

here $\beta_T = v_T / c$.m Variations of the longitudinal and transverse momenta of particles $p_{\|}$, $p_{\perp}$ under the ECR conditions are related by the following equation [9]:

$$\alpha = dp_{\perp} / dp_{\|} = \omega_H c / \gamma v_{\perp} \omega n_{\|} \tag{4}$$

where ω_H is nonrelativistic gyrofrequency, γ is relativistic factor, and $v_{\perp} = p_{\perp} / m\gamma$ is transverse electron velocity. Untrapped particles in the toroidal system satisfy the condition:

$$v_{\perp} < |v_{\|}| A^{1/2} \tag{5}$$

where $A = R/r$ is the local aspect ratio (R is the major radius of a torus, r is the radius of the magnetic surface). If the inequality

$$|\alpha| < A^{1/2} \tag{6}$$

is valid at the boundary of trapping condition (5), then accellerated electrons will not be trapped; on the contrary, in this case ECRH stimulates detprapping of trapped particles. Equations (4–6) yield the condition

$$(n_{\|} \beta_{\|})^{-1} < A \tag{7}$$

(here $\beta_{\|} = v_{\|} / c$) with longitudinal velocity of particles being determined by the Doppler relation:

$$\beta_{\|} = \beta_{\|}^R = \frac{\omega - \omega_H}{\omega n_{\|}} \tag{8}$$

From Eqs. (7, 8) and (2, 3) we find the condition for absence of trapping due to ECRH in the following form:

$$\omega_H < \omega\,; \qquad Z > q \tag{9}$$

where $q = A^{-1}\frac{B_\varphi}{B_\theta}$ is the local safety factor, and

$$Z = \frac{-\omega_H + \omega}{\omega n_\parallel \beta_T} = \frac{\beta_\parallel^R}{\beta_T} \tag{10}$$

is the ratio of the longitudinal velocity of resonance particles to the thermal velocity. All the parameters are to be taken in the region of ECR absorption. In systems with large optical depth absorption of microwave energy takes place in the region, where $Z > 1$. The dispersion equation for longitudinal mode [9] easily yields the expression for the coefficient of power absorption μ_B

The region of absorption of the main part of microwave power is determined by estimation $\int\limits_{-\infty}^{Z} \mu_B dZ (n_\parallel \beta_T R) \lesssim 1$, wherefrom we obtain

$$Z \geq Z^R = \ln^{1/2}\left(\pi^{1/2}\frac{\omega R}{c} V\left(\frac{n_\parallel}{n_\perp}, \beta_T\right)\right) \tag{11}$$

where function V is a value of the order of unity for $T_e \simeq 5$ keV, and $n_\parallel / n_\perp \simeq B_\theta / B_\varphi = 0.1$.

In the tokamak with $R = 150$ cm and radiation wavelength $\lambda = 2\pi c/\omega = 3$ mm, Eq. (11) yields $Z^R \simeq 3$, so that condition (9) is easily satisfied.

2. Another specific feature of the scheme using the Bernstein mode is the fact that the coefficient of quasilinear diffusion of resonance particles over energies in plasma waves is about $\left(T_e/mc^2\right)^{-1}$ times higher than that in electromagnetic waves with the same radiation power (see, e.g.,[15]). In accord with today notions, quasilinear effects can increase efficiency of current drive [3].

For the scheme of current drive under discussion to be efficient, weak absorption of the X-mode in the ECR zone is, evidently, necessary, when power is transported to the UH resonance region. This

condition, apparently, is easy to satiafy with the quasi-transverse launching of rf power into devices of the T-10 and T-15 scale. As for the ITER scale tokamaks, realization of the scheme discussed seems to be problematical. At the same time, the preliminary estimation presented here give hope for successful demonstration at installations like TUMAN-2 or WT-3.

REFERENCES

[1]. V.V.Parail. Noninductive methods of current-drive in a tokamak, in High-Frequency Plasma Heating (Litvak, A.G., Ed.), Amer. Inst. of Phys., New York (1990)

[2]. N.J.Fish and A.M.Boozer, Phys. Rev. Lett., 21 (1980) 720

[3]. Y.N.Dnestrovskij et al., Nucl. Fusion, 28 (1988) 754

[4]. H.Tanaka et al., Phys. Rev. Lett., 60 (1988) 1033

[5]. T.Ohkawa. General Atomic Company Rep.,NA 13847 (1986)

[6]. C.F.F.Karney and N.J.Fish, Nucl. Fusion, 21 (1981) 1549

[7]. S.Tanaka et al., in Radiofrequency Heating and Current Drive of Fusion Devices. (Contr. Papers of Europhys. Topical Conf., Brussel, 1992). Vol.16E, Europ. Phys. Society (1992) 265

[8]. V.E.Golant, Physica Scripta, 2 (1982) 428

[9]. A.I.Akhiezer et al., Plasma Electrodynamics, Nauka, Moscow (1974)

QUASILINEAR DIFFUSION COEFFICIENT IN TOKAMAK AT ECR

A.Yu.KUJANOV, A.A.SKOVORODA, A.V.TIMOFEEV

RRC "Kurchatov Institute", Moscow, Russia

1.In [1,2] it was proposed to carry out ECR current drive (CD) in tokamaks at autoresonanse regime. Tentative evaluation show, that CD efficiency must be very high in this regime. For precise calculation of the efficiency it is required the quasilinear diffusion coefficient of the electron under microwave action at the most general conditions: arbitrary angle of the wave beam propagation to the magnetic field, complete account of the influence of the magnetic field inhomogeneity and of the finite dimension of the wave beam on ECR interaction and also complete account relativistic effects. Although the quasilinear diffusion coefficient was obtained in many papers, see for example [3–6], we did not find required expression. The aim of this paper is to fill this gap.

2.Let us propose, that the tokamak magnetic surfaces are to ruses with the circle cross sections. Let us consider the electrons placed on the surface with radius r. The magnetic axis radius is equal to R0. Let us suppose that the electromagnetic beam has the Gaussian intensity distribution with characteristic scale L at the transverse cross section. The Fig.1 make the problem geometry clear.

Under one run through the beam the electron obtain the energy increment

$$\Delta\gamma = \frac{1}{\gamma}\, q_\perp E\, \mathrm{Re}\left(G e^{i\Phi}\right),$$

$\gamma=\varepsilon/mc^2$– relativistic factor, $\mathbf{q} = \mathbf{p}/mc$, Φ –the phase which changed randomly at the successive runs through the beam,

$$E = \frac{J_{n-1}(\varkappa_e)E_- + 2(q_\parallel/q_\perp)J_n(\varkappa_e)E_\parallel + J_{n+1}(\varkappa_e)E_+}{2B_0},$$

J_n – Bessel function, $\varkappa_e = N_\perp q_\perp \omega/\gamma\omega_e$,

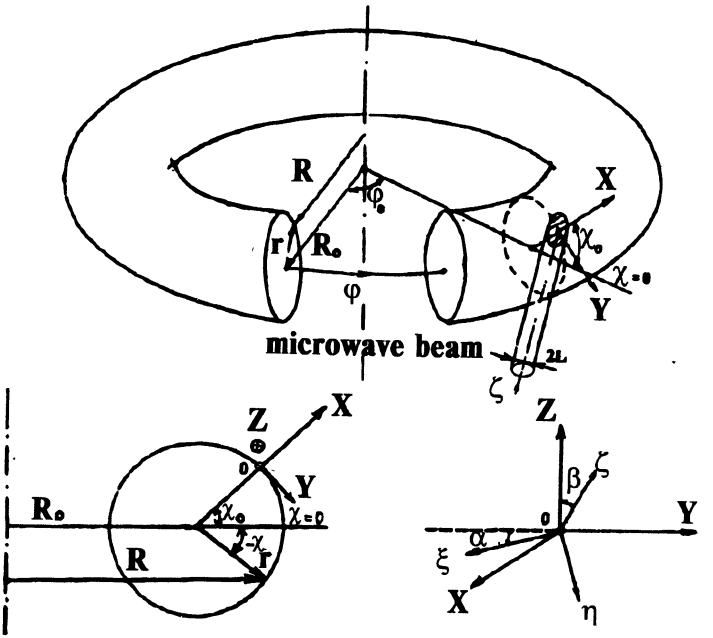

Fig.1.Microwave beam and tokamak geometries

$$E_{-,+,\|} = \left[\frac{8P}{cL^2\sqrt{Q(N^2Q-1)}} \right]^{1/2} e_{-,+,\|} \ ,$$

P(r) – microwave power on magnetic surface r,

$$e_{+,-} = N_\perp \left[1 - \frac{\omega_{pe}^2}{\omega(\omega \pm \omega_e)} - N^2 \right]^{-1};$$

$$e_\| = N_\| \left[1 - \frac{\omega_{pe}^2}{\omega^2} - N^2 \right]^{-1}.$$

G–nondimensional (at unites of ω_{e0}^{-1}) time of ECR interaction with electromagnetic wave beam

$$G = \omega_{e0} \int_{-\infty}^{\infty} dt \ \exp\left[-\frac{\xi^2+\eta^2}{2L^2} - i\omega t + i\int^{t} \Omega(t')dt' \right],$$

$\xi=x\sin\alpha - y\cos\alpha$, $\eta=(x\cos\alpha+y\sin\alpha)\cos\beta - z\sin\beta$,
$x=r(\cos(\chi-\chi_0)-1)$, $y=-r\sin(\chi-\chi_0)$, $z=R\sin(\varphi-\varphi_0)$,
$\Omega(t)=n\omega_e(\chi(t))+k_{||}v_{||}(\chi(t))$, $\varphi(t)\approx\varphi_0+\varphi' t, \varphi'=\chi'\iota$,

$$\chi(t)\simeq\chi_0+\chi^*+\chi' t+\chi'' t^2/2,\ \chi'=\frac{v_{||}}{\iota R}\left[1+\left(\frac{r}{\iota R}\right)^2\right]^{-1/2},$$

$$\chi''\approx\chi'\frac{2v_{||}r\ \sin\chi}{\iota R^2}\left[1-\frac{\sin^2\theta}{4\cos^2\theta+\varepsilon(\cos\chi-1)}\right],$$

ι–safety factor, θ–pitch angle. Integration lead to

$$|G|=\frac{\sqrt{\pi}\ \omega_{e0}}{(A_2^2+\alpha_2^2)^{1/4}}\exp-\left[A_0+\frac{A_1^2}{4A_2}+\frac{A_2\left[\alpha_1-\frac{A_1\alpha_2}{A_2}\right]^2}{4(A_2^2+\alpha_2^2)}\right],$$

$A_0=(x_0^2a + y_0^2b - x_0y_0c)/2L^2$, $x_0 = r(\cos\chi^*-1)$,
$A_1=(2x_0x_1a+2y_0y_1b-x_0y_1c+x_1y_0c-x_0z_1d-y_0z_1f)/2L^2$,
$A_2=[(x_1^2+2x_0x_2)a + (y_1^2+2y_0y_2)b - (x_1y_1+x_0y_2+x_2y_0)c+$
$+z_1^2\sin^2\beta - x_1z_1d - y_1z_1f]/2L^2$, $x_1= - r\chi'\sin\chi^*$,
$a = 1 - \sin^2\beta\cos^2\alpha$, $b = 1 - \sin^2\beta\sin^2\alpha$, $c=\sin^2\beta\sin2\alpha$,
$d = \sin2\beta\cos\alpha$, $f = \sin2\beta\sin\alpha$, $y_0 = -r\sin\chi^*, z_1 = R\varphi'$,
$x_2=-0.5r(\chi''\sin\chi^*+\chi'^2\cos\chi^*)$, $y_1=-r\chi'\cos\chi^*$, $\alpha_1=\omega-\Omega$,
$y_2 = -0.5r(\chi''\cos\chi^* - \chi'^2\sin\chi^*)$, $\alpha_2 = -0.5\chi'\partial\Omega/\partial\chi$,
quantities χ', χ'', φ' it is necessary to calculate at $\chi = \chi_0 + \chi^*$.

At the random phase Φ variation the electron resonance interaction lead to the diffusion on the phase plane with the diffusion coefficient

$$D(\chi) = \frac{\omega_b}{4}|\Delta\gamma|^2 = \frac{\omega_b}{4}\left(\frac{q_\perp}{\gamma}\right)^2 E^2|G|^2.$$

Where ω_b–the run through the beam (line $\varphi=\varphi_0$) frequency, it is expressed in terms of the bounce frequency

of the trapped electrons ω_b^t

$$\omega_b = \iota\chi_{max}\omega_b^t/\pi \approx \frac{\pi c q\sqrt{\varepsilon}}{2\sqrt{2(1+\varepsilon)}\ R_0\gamma\iota K\left(\frac{(1+\varepsilon)\cos^2\theta}{2\varepsilon}\right)}$$

and of the untrapped ω_b^u

$$\omega_b = \omega_b^u \approx \frac{\pi c q\ \cos\theta}{2R_0\gamma\ K\left(\frac{2\varepsilon}{(1+\varepsilon)\cos^2\theta}\right)},$$

where χ_{max} – the poloidal angle maximum on the trajectory of the trapped electron.

Due to motion along the magnetic field lines trajectories of the untrapped electrons cover the all magnetic surface and due to toroidal drift trajectories of the trapped electrons – some part of the magnetic surface. The averaging $D(\chi)$ on the electron motion give

$$D^u = \int_{-\pi}^{\pi} D(\chi)B_\varphi(\chi)d\chi \ / \int_{-\pi}^{\pi} B_\varphi(\chi)d\chi,$$

$$D^t = \int_{-\chi_{max}}^{\chi_{max}} D(\chi)B_\varphi(\chi)d\chi \ / \int_{-\chi_{max}}^{\chi_{max}} B_\varphi(\chi)d\chi.$$

3.At this time we fulfilled only preliminary job for the calculation of the current drive efficiency. We developed the code for the quasilinear diffusion calculation. We calculated also the diffusion coefficient for the T–10 condition at the two value parallel refraction index, see Fig.2. We considered extraordinary wave (first harmonic). The first value 0.3 is typical for the present experiments, the second 1.2 is close to the autoresonance condition (N=1). At the first case the diffusion coefficient have substantial value only at the small ($q \ll 1$). At the second case the equivalent region is elongate to relativistic values of

momentum (q≈1). As it known, at autoresonance regime the energy gain do not destroy resonance. Therefore electrons must form the stream which elongate along the resonance curve. It is naturally to expect that CD efficiency is more high at the second case.

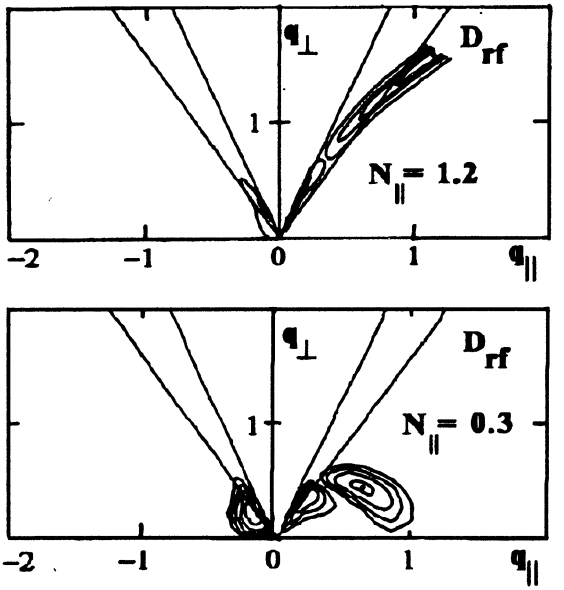

Fig.2.D for T10 conditions:n=1;74.6GHz X–wave;r=25cm; L=7cm;B_0=2.8T;$\chi_0=90^0$;$\alpha=0^0$;$\beta=33^0$(N||=1.2)/75^0

As we know the diffusion coefficient D, so we may to calculate the power density which the electrons absorb on the magnetic surface r

$$\frac{dP}{dV} = -\frac{2mc^3(1+\varepsilon)}{R_0 \iota \omega} < \frac{D}{\omega_b^*} \left(n\omega_e(0) \frac{\partial}{\partial(p_{\perp 0}^2)} + (\omega - n\omega_e(0)) \frac{\partial}{\partial(p_{\|0}^2)} \right) f >$$

where $\omega_b^*=\omega_b/\iota$ for the untrapped electrons and $\omega_b^*=\omega_b$ for the trapped, $\omega_e(0)=\omega_e(\chi)|_{\chi=0}$, < > denote the averaging over electron distribution.

This calculation method coupled with ray–tracing procedure represent more adequate the ECR process then

standard method which grounded on the using of dielectric constant of the infinite homogeneous plasma.

The result of the calculation for the T–10 condition is showed on the Fig.3. The electron distribution function is taken as Maxwellian. The second harmonic of the extraordinary wave is considered. Let us mark the coincidence theoretical and experimental results on the initial section of the trajectory. Later divergence is caused by the distribution function modification.

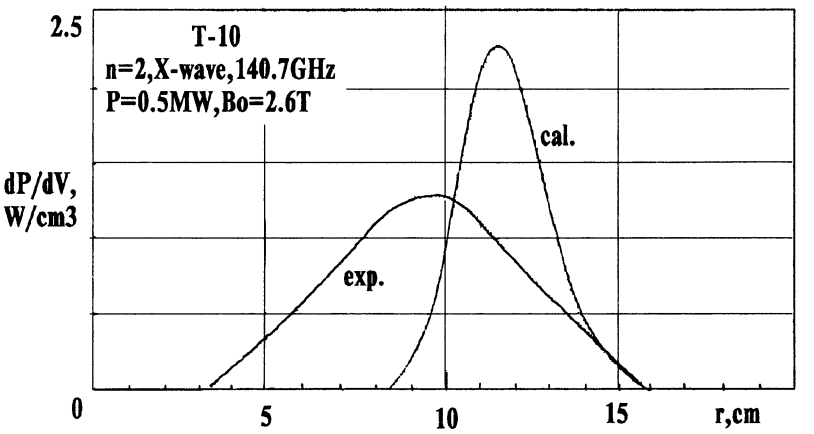

Fig.3.Absorbed power density distribution in T10.

References

1.Kuyanov A.Yu.,Skovoroda A.A.,Timofeev A.V.,Zvonkov A.V. Proc. **19** Eur. Conf. Contr. Fus. Pl. Phys. Innsbruck. 1992, 2, 1521

2.Kuyanov A.Yu.,Skovoroda A.A.,Timofeev A.V.,Zvonkov A.V. **14**th Int. Conf. Pl. Phys. Contr. Nucl. Fus. Res. Wurzburg 1992. Rep. E–3–5.

3.Fidone I.,Granata G.,Meyer R., Phys. Fl. 1982,**25,**2249.

4.O'Brien M.R.,Cox M.,Start D.F.H.,Nucl.Fus.1986,**26,**1625

5.Cairns R.A., Lasmore–Davis C.N. Plasma Phys. Contr. Fus. 1986, **28,** 1539.

6.Demeio L.,Engelman F. Pl. Phys. Contr. Fus. 1986,**28,**1851

HIGH-POWER RF HEATING AND CURRENT DRIVE EXPERIMENTS PLANNED FOR ITER

ITER Joint Central Team
presented by T. Nagashima
ITER Joint Work Site, c/o Max-Planck-Institut für Plasmaphysik
Boltzmannstraße 2, 85748 Garching bei München, FRG

1. Introduction

Based on the success of the large tokamaks JET, JT-60U and TFTR we have started an engineering design of the first thermonuclear experimental reactor and also intend its construction. The framework for this undertaking is ITER, the International Thermonuclear Experimental Reactor, which is just completing its first year of the Engineering Design Activities (EDA). Although a considerable part of this year has been spent in forming teams at the three joint sites in San Diego (USA), Garching (Germany) and Naka (Japan), work on the ITER design, and development of a supporting R&D program, are now progressing rapidly. The objective of this paper is to give a brief overview of the tokamak design concept and a planned high-power RF heating and, possibly, current drive experiments in ITER. Major engineering R&D items are described. Appropriate for this meeting, the requirements of a high-power gyrotron will be emphasized.

2. Guiding design philosophy in the EDA

The general principles guiding the EDA design, as developed by the Director [1] are:

(i) the flexibility associated with the long lead time before operation;
(ii) the reliability necessary for the operation of key systems without fault over a period of 30 years;

(iii) the safety required for the operation of a nuclear device;
(iv) the attempt to use wherever possible reactor-relevant technology;
(v) development of a design suggestive of an attractive fusion reactor.

These principles can be translated into the design by increasing wherever possible: safety and technical margins, the reliability and simplicity of each component and by lowering the tritium inventory and the activation of the overall structures.

For example, the main factors affecting the last point are economical and environmental.

Regarding economics, the cost of ITER is constrained by the cost estimated at the conclusion of the Conceptual Design Activities (CDA). The effective cost of electricity will however depend on other factors such as the level of power that can be produced and the operational availability that can be achieved. Thus the EDA design should permit, at least on a demonstrative basis, operation at high power and high availability. The cost of the device must be commensurate with the capital cost of the other energy sources.

Similarly, the environmental characteristics of ITER depend mainly on the materials chosen and the inventory of tritium. Thus, wherever possible, low activation materials should be used and the tritium inventory in the fuel processing system should be minimized.

In some cases, judgement must be exercised and another overriding principle invoked: above all, ITER must work.

3. Main Tokamak Parameters and Plasma Performance

3.1. Device Descriptions

As shown in Figure 1, the cross-sectional shape of the ITER device is that of a conventional modern tokamak with moderate aspect ratio and elongation, and a single null divertor. The basic engineering parameters were presented to and approved by the ITER Council in April 1993 and are given in Table 1. Small

changes in the values of some of these quantities may be expected to occur as the design progresses.

The aspect ratio of 2.8 is in the range of the large tokamaks from which most of the recent confinement scaling results were obtained. The elongation of $\kappa = 1.6$ represents a compromise between the competing requirements of higher current, favoured by high κ, and lower growth rate of the axisymmetric instability, favoured by lower κ.

The toroidal field magnet consists of 24 super conducting toroidal coils of size (11.5 x 17.3 m) and weight (400 tons for each coil). The field on axis is 6 T and the stored energy in the TF systems is approximately 100 GJ. The maximum ripple at the plasma boundary, which is important in determining the confinement of fast alpha particles, is $< \pm 2$ %.

Having set the aspect ratio, elongation and value of the toroidal field, the size is determined by the current required to ensure ignition. The key element determining the current capability is the transport model. Both the Rebut-Lallia model of the critical electron temperature gradient [3] and projections based on empirically determined scaling relations such as those developed and used during the CDA (the ITER CDA scaling law) [4] indicate that 25 MA is the minimum acceptable current capability. For $q_\psi > 3$, the corresponding major radius is then 7.75 m.

A single-null divertor has been chosen for exhausting the plasma heat and particles. The thermal power which is not exhausted to the divertor will be radiated to the first wall. An integrated first wall and blanket approach is being developed, in which the first wall is also the main structural element of the blanket. In the breeding phase, the blanket is filled with lithium and beryllium.

Beyond the blanket is the vacuum vessel, a double-walled structure made of inconel, or stainless steel, and typically has a thickness of 50 - 100 cm. Poloidal ribs provide mechanical strength and the voids are filled with stainless steel pebbles which are cooled, for example, by lithium, helium or water.

The poloidal field (PF) is being designed to provide sufficient volt-seconds for a 1000 s burn. During the initial charge,

the system provides 220 Vs, and for a plasma current of 25 MA and burn time of 1000 s, the total flux released is 570 Vs. The key component of the PF system is the central solenoid which has a maximum design field of 13 T, stores over 13 GJ, and weighs just under 1000 tons.

The more detailed description of the ITER device is found in reference [1], [2].

3.2. Plasma Performance

Performance of the EDA design has been evaluated using a variety of confinement models including the Rebut-Lallia model [3] and the ITER CDA scaling law [4]. The Rebut-Lallia model has been successfully used to predict the confinement performance of L-mode discharges. A set of steady-state operational parameters derived from 1.5 D time-dependent simulations using the Rebut-Lallia model are presented in Table 2. In these cases, 1 % of the plasma exhaust is pumped and the helium level builds to substantial, e.g., 24 %.

The performance can also be evaluated using the ITER CDA scaling law. An example is shown in Figure 2, which describes plasma operational contours using the 1989 ITER CDA scaling law. An "H-mode factor" of 2 was used and the helium level was set at approximately 15 %. Each contour represents the location in n-T space that is energetically possible with the auxiliary heating power indicated.

Also of interest in Figure 2 is the fusion power that can be produced within the allowable ß-limit. For estimation purposes, a Troyon factor of 3 (i.e., $ß \leq 3\ I\ (MA)/aB\ \%$) has been used. As seen from the figure, fusion power of over 3 GW is permitted using this simple estimate for ß. From this we conclude that the EDA device should be designed to accommodate a substantial number (10^4) of burning discharges at a fusion power level of 3 GW, with fewer (e.g. 100) excursions of up to 4 GW.

Another point of interest from Figure 2 is the relatively low auxiliary power required to reach the "Cordey pass". Depending on the transport model, and level of impurities, values in the range 5 - 25 MW are typical. A combination of ion and/or electron cyclotron heating totalling about 50 MW is presently foreseen for meeting the heating requirements. Detailed design of these heating systems, including the antennas has been deferred until the blanket

and first wall design have reached a more mature stage of development.

4. ICH System Description and Antenna

The Ion Cyclotron Heating (ICH) is considered to be the primary heating method. The ICH system will be modular with a basic module consisting of an antenna, a vacuum coaxial line to the vacuum vessel periphery, a vacuum feed-through, a tuning and matching system, a transmission line to the RF unit and the power supply.

The RF system should be capable of covering a wide frequency range, e.g., 20 - 90 MHz. The system would then be capable of minority heating of D, He^3 and H as well as the second harmonics of T (tritium). Possibilities for current drive with IC waves exist presently in low frequency windows, one around 20 MHz, below all frequencies for significant ion absorption, the other near 70 MHz, between the second and third harmonic resonance of T. In 1993 the design study will start to define the ITER RF systems (including the ECH system) as one of the design tasks.

RF generator and transmission technologies are well-established, and there exists a substantial data base and experience which can serve as a basis for antenna design.

On the other hand, the ITER environment poses new challenges to the design of an ICH system. All components, including the Faraday screen, must be steady-state cooled; the antenna materials must be tolerant of neutron irradiation effects; the insulators must be located remotely and well-shielded from neutrons; the entire apparatus inside the vessel must be maintained and repaired in a reasonably straightforward way by a remote handling system; and finally the antenna must not act as a significant source of impurities even while maintaining strong RF coupling to the plasma as the plasma shape changes during start-up and under different operating regimes.

The basic approach to the blanket and first wall design is illustrated schematically in Figure 3. The blanket is formed by a series of canisters distributed around the toroidal circumference of the machine. As indicated in the figure, the front surface of the

canisters also forms the first wall. Thus in this design the thermal power which is not removed by the divertor must flow through the first wall to the cooling system in the blanket. It is necessary to imbed the ICH antennas in the blanket structure, a difficult but not impossible configuration to realize. Further study will be needed to develop such a concept.

5. High-power Gyrotron and Window for ECH

An Electron Cyclotron Heating (ECH) system would offer a high degree of flexibility, especially to design the launching system: higher power density; no constraint on antenna-plasma distance. In addition to meeting basic heating needs, ECH power would be useful in the early start-up phase where the ohmic power may be insufficient to break through the radiation barrier. Also highly localized heating or current drive may be useful in stabilizing or optimizing certain plasma regimes.

The basic ECH module consist of an antenna, e.g. a simple horn which could be located in a port, a low-loss transmission line, e.g., corrugate waveguide or a quasi-optical system, a window, the gyrotron and associated power supplies.

The main barrier to committing to the ECH system for ITER is the technological uncertainty of efficiently producing power at around 160 GHz (TBD) in a unit of > 1 MW and a reasonable cost and with high reliability. Technical difficulties in developing gyrotrons have been the rule, rather than the exception.

However, as shown in Table 3 recent Russian gyrotron results, namely 140 GHz, 0.97 MW, with an efficiency of 34 % for 0.3 sec and 167 GHz, 0.5 MW, 30 % for 0.7 sec and also the successful operation of the Russian 140 GHz, 0.5 MW gyrotron at W7-AS in 1993 [5] are encouraging and a significant step towards the development of a gyrotron for ITER, but further R&D efforts will be required to realize an attractive advanced ECH system.

The first step should aim at the demonstration of high-power (1 MW or more) long pulse (10 sec to CW) operation at an ITER-relevant frequency (e.g. 160 GHz). To cope with the ICH (cheapest) as the primary heating method, as next step, further increases in efficiency of the ECH system should be pursued, as should the simplification of the power system and the reduction in

costs. The CPD (Collector Potential Depression) concept would be beneficial to reducing the cost of the high voltage power supply as well as to increasing the overall system efficiency. Multi-MW gyrotrons also would reduce the cost of the transmission line and the antenna, and lead to a more attractive system.

The development of a reliable vacuum and tritium barrier of windows is also an especially critical R&D task that needs immediate emphasis.

Developing an economical solution to gyrotron and window (finally advanced ECH system) is one of the most important tasks to be undertaken in the R&D supporting the EDA design. Further discussions will also be required to define the feasibility of the ITER gyrotron and window. In view of the intense effort now underway in all of the Parties, it seems quite likely that a satisfactory solution will be developed by an international collaboration.

Summary

(1) The ITER EDA design is based on conservative extrapolation of present-day physics and points in the direction of an attractive fusion power.
(2) A combination of ICH and/or ECH of about 50 MW is presently foreseen for meeting the heating requirements.
(3) The design of the ICH antenna which fits in the integrated first wall and blanket approach is a critical issue to be developed.
(4) Attractiveness of ECH warrants emphasized R&D efforts on gyrotron and window. Especially the cost of ECH system could be reduced by an appropriate R&D including increase in the system efficiency. Technological risks of R&D exist for these advanced requirements, but could be reduced to an acceptable level only by the real international collaboration.

References

1. ITER Joint Central Team presented by the ITER Director, ITER Preliminary Design Report to the ITER TAC 2, 15 - 16 March 1993.
2. ITER Joint Central Team presented by R.R. Parker, in Proc. of 20th EPS Conference on Controlled Fusion and Plasma Physics, Lisboa, 26 - 30 July 1993.
3. Rebut, P.-H,, Watkins, M.L. and Lallia, P.P., in Plasma Physics and Controlled Nuclear Fusion Research (Proc. of 12th Int. Conf., Nice, France, 1988) Vol.2, IAEA Vienna (1989).
4. Tomabechi, K. and the ITER Team, Nucl. Fusion, 31 (6) (1991) 1135.
5. Erckmann, V., Burhenn, R., Hartfuss, H.J., et al., in Proc. of 20th EPS Conf. on Controlled Fusion and Plasma Physics, Lisboa, 26 - 30 July 1993 (Vol .17c, PartI, p. 345).

Table 1. ITER EDA basic reference parameters.

Parameter	Design Value
Typical minor radius (at mid plane and separatrix)	2.8 m
Typical major radius	7.75 m
Typical elongation (95% flux surface)	1.6
Divertor configuration	Single null
Toroidal field at 7.75 m	6 T
Maximum toroidal field ripple at plasma edge	$< \pm 2\%$
Fusion power; Normal operation (10^5 cycles) Extended operation (10^4 cycles)	 ~ 1500 MW ~ 3000 MW
Burn time	1000 sec at 25 MA

Table 2. Performance of ITER design using the critical electron temperature gradient model.

		EDA			
Parameters		**Case 1**	**Case 2**	**Case 3**	**Case 4**
I_p	(MA)	25	←	←	←
q_ψ		3	←	←	←
P_{FUS}	(MW)	**1080**	**2135**	**3185**	**4250**
P_α	(MW)	216	427	637	850
$T_i(0)$	(keV)	19	23	21	26
$\langle n_e \rangle$	(10^{20} m^{-3})	1.1	1.6	2.1	2.1
n_{He}/n_e	(%)	**19**	**24**	**24**	**20**
g*-Troyon		1.40	2.34	2.86	2.97
I_{BS}	(MA)	2.7	4.8	6.6	7.1
V_{LOOP}	(Vs)	0.15	0.10	0.10	0.11
τ_E*	(s)	4.0	3.4	2.8	2.1

Note: $\tau_E^* = W_p/(P_\alpha + P_{OH})$

g*-Troyon = β_t(thermal)(%)/[I(MA)/a(m)B(T)]

n_{Be}/n_{DT} = 1% in all case

Table 3. Status of gyrotron development ($f \geq 100$ GHz, $P \geq 500$ kW).

Institution	Mode	Frequency	Power	Efficiency	Pulse Length
Thomson*	$TE_{9,3}$	110 GHz	410 kW		
KfK	$TE_{10,4}$	140 GHz	700 kW	26 %	5 ms
MIT	$TE_{16,2}$	149 GHz	1.3 MW	43 %	3 μs
MIT	$TE_{38,5}$	231 GHz	1.19 MW	20 %	3 μs
VARIAN	$TE_{15,2}$	140 GHz	330 kW		2.5 s
		140 GHz	1.04 MW	38 %	0.5 ms
	$TE_{22,2}$	100 GHz	1 MW	31 %	1 ms
		110 GHz	500 kW	35 %	2.5 s
VARIAN*	($TE_{22,2}$)	(110 GHz)	(1.0 MW)	(30 %)	(CW)
GYCOM (IAP,	$TE_{15,4}$, GB	110 GHz	1 MW	44%	0.1 ms
N. Novgorod;	$TE_{20,13}$, (coax)	100 GHz	2.1 MW	30 %	0.03 ms
TORIY, Moscow;	$TE_{22,5}$, GB	140 GHz	970 kW	34 %	300 ms
SALUT,	$TE_{22,5}$, GB	140 GHz	600 kW	34 %	2 s
N. Novgorod)	$TE_{24,6}$, GB	167 GHz	500 kW	30 %	700 ms
GYCOM*		(110 GHz)	(500 kW)	(40 %)	(500 ms)
TOSHIBA	$TE_{12.2}$, GB	120 GHz	548 kW	30 %	100 ms
	$TE_{22.2}$, GB	110 GHz	460 kW		100 ms
TOSHIBA*	($TE_{22.2}$), GB	(110 GHz)	(500 kW)		(1 s)
MITSUBISHI	$TE_{15.2}$	120 GHz	610 kW	31 %	1 ms
NRL (Q.O.)	TEM_{00q}	115 GHz	600 kW	9 %	~ 15 μs

* ( ): under development and the designed performances

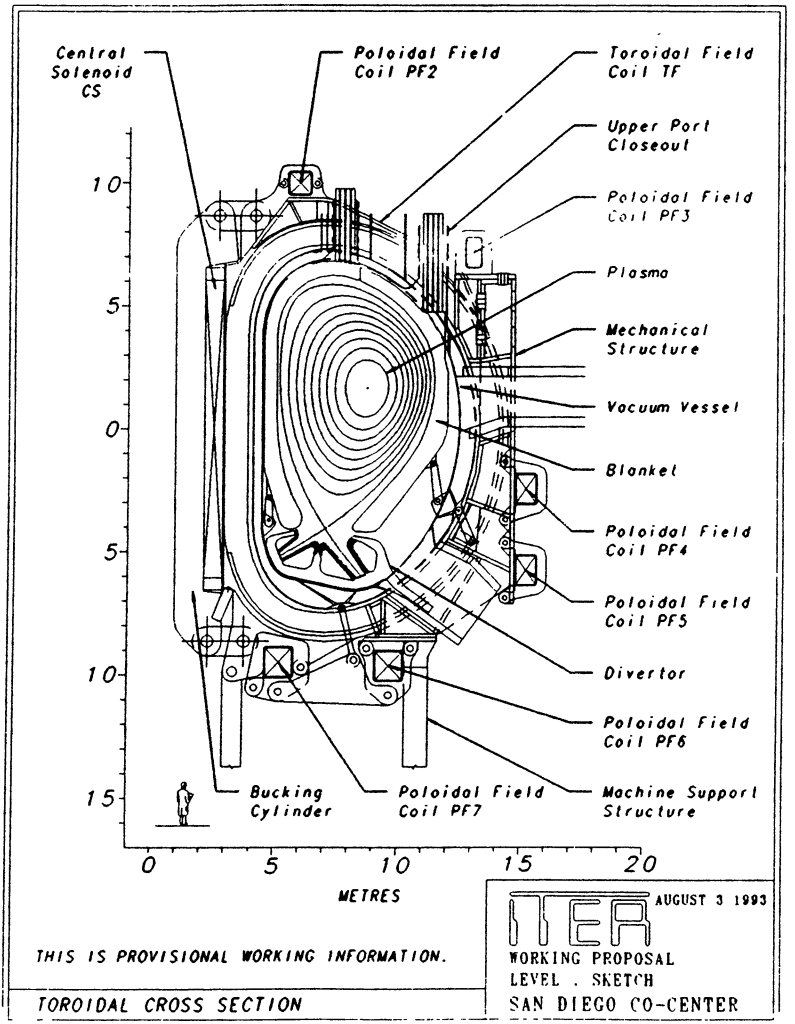

Figure 1. Cross-section of ITER device

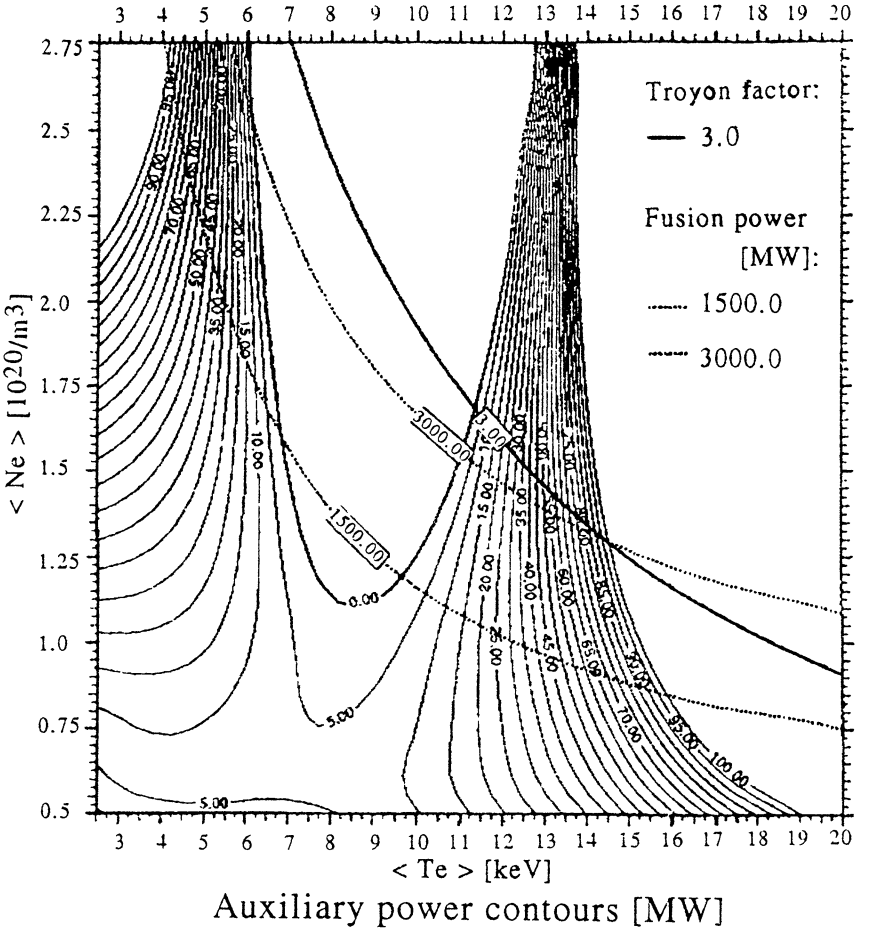

Figure 2. Plasma operational contours for $\tau_E = 2\ \tau_E$, ITER 89 P and $n_{He}/n \approx 10$ %.

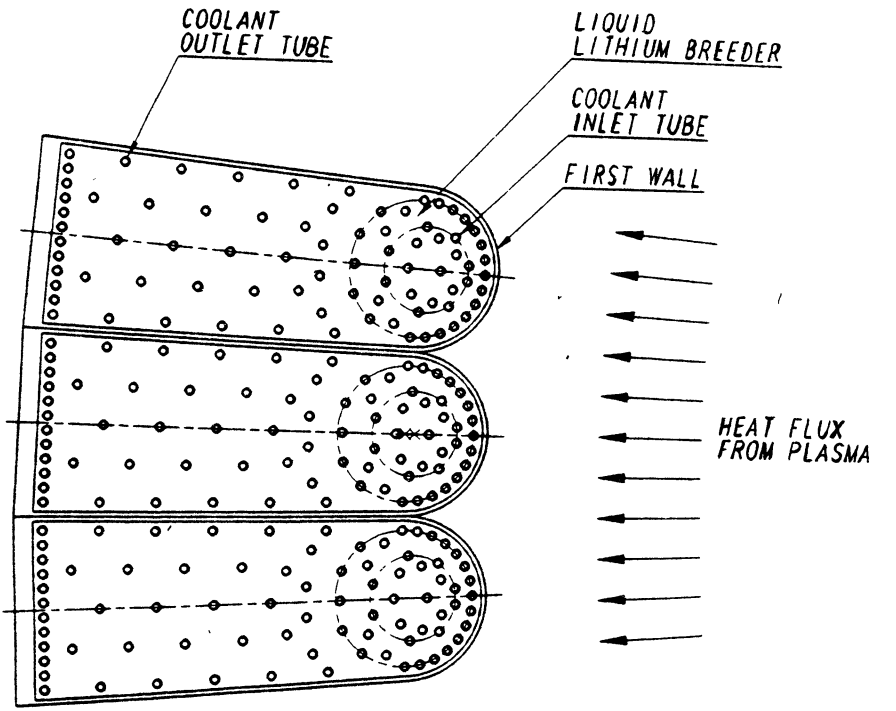

Figure 3. Schematic approach to the integrated first wall and blanket (also ICH antenna) design

ECRH AND ECCD WITH 70 AND 140 GHz AT THE W7-AS STELLARATOR

V. Erckmann, W7-AS Team, NBI Team
Max-Planck-Institut für Plasmaphysik, EURATOM Ass.,
D-85748 Garching, Germany

W. Kasparek, G.A. Müller, P.G. Schüller
Institut für Plasmaforschung, Universität Stuttgart, Germany

Borschegovsky, A.*, V.I.Il'in*, V.I. Kurbatov, S. Malygin**, V.I.Malygin***
* Kurchatov Inst., Moscow, Russia, ** SALUT, *** IAP, Nizhny Novgorod, Russia

ABSTRACT

ECRH is provided at W7-AS with two systems running at 70 GHz and 140 GHz. Experiments with 140 GHz focused on high density operation up to 1.1×10^{20} m^{-3}. The operational window for the Stellarator H-mode, the influence of gas puffing on the H-transitions and heat wave experiments are discussed. Density control is achieved in combined heating with NBI despite the beam particle fuelling, whereas with NBI alone a steady density rise is observed. The impact of combined heating on the impurity confinement was investigated. The influence of trapped particles on the ECCD efficiency was examined experimantally and compared to theory.

W7-AS TEAM: J. BALDZUHN, R. BRAKEL, R. BURHENN, G. CATTANEI, A. DODHY, D. DORST, A. ELSNER, M. ENDLER, K. ENGELHARDT, V. ERCKMANN, U. GASPARINO, S. GEIßLER, T. GEIST, L. GIANNONE, P. GRIGULL, H. HACKER, H.J. HARTFUSS, O. HEINRICH, G. HERRE, D. HILDEBRANDT, J.V. HOFMANN, R. JAENICKE, F. KARGER, M. KICK, H. KROISS, G. KUEHNER, H. MAASSBERG, C. MAHN, K. MCCORMICK, H. NIEDERMEYER, W. OHLENDORF, P. PECH, H. RINGLER, A. RUDYJ, N. RUHS, J. SAFFERT, F. SARDEI, S. SATTLER, F. SCHNEIDER, U. SCHNEIDER, G. SILLER, U. STROTH, M. TUTTER, E. UNGER, H. VERBEEK, F. WAGNER, A. WELLER, U. WENZEL, H. WOLFF, E. WÜRSCHING, D. ZIMMERMANN, M. ZIPPE, S. ZÖPFEL
NBI-TEAM: W. OTT, H. P. PENNINGSFELD, E. SPETH

1. INTRODUCTION

The ECRH capability for plasma start-up from the neutral gas and highly effective electron heating assigns a key role to ECRH in the field of stellarator research. Major drawbacks of presently running high power ECRH systems, however, were the density restrictions given by the cut-off density for the present day microwave frequencies and the limited power per microwave source (typically 0.2 MW). The application of 140 GHz ECRH overcomes this density restrictions and opens a new parameter window with respect to density and power for plasma physics investigations.

A brief description of the W7-AS experiment together with the 140 GHz gyrotron and transmission system is given in Section 2. First plasma experiments focussed on the investigation of high density plasmas, which could be generated up to now with NBI only. The comparatively low densities accessible with 70 GHz ECRH provided clear experimental conditions for the investigation of electron heat transport, because the ions are only weakly coupled to the electrons and do not play a significant role in the overall power balance. At high densities, however, the collisional electron-ion coupling becomes strong and the ion confinement becomes important in the power balance analysis. Under high density conditions, H-mode transitions, which are well known from tokamak experiments [1, 5-10] were observed for the first time in a stellarator. The operational window for these transitions and the correlated phenomena are discussed in Section 3. The basic features of the Stellarator H-mode were reported in previous papers [2,3] and are briefly reviewed. Here we concentrate on the discussion of the influence of gas puffing on the H-transitions and heat wave studies to determine the heat diffusivity before and after the H-transition.

Combined heating experiments with NBI, which is inherently related to high density operation are discussed in section 4 of this paper. Typical high-power NBI-heated plasmas in W7-AS are nonstationary, because the combined effect of beam particle fuelling and recycling causes a steady density rise [11]. Such discharges are usually terminated by a thermal collapse induced by the increase of the impurity radiation with increasing density. Quasistationary behaviour could only be achieved in some corners of the W7-AS parameter range, i.e. operation in poor confinement regimes selected by an apropriate choice of the external rotational transform or directly

after glow-discharge conditioning of the vessel walls. There was clear evidence from early experiments at W7-A [12,13] and W7-AS, that the density could be controlled by combining ECRH and NBI. These experiments suffered, however, from either short pulse lengths of ECRH and/or low density operation given by the 70 GHz cut-off constraints. Experiments with combined heating in long pulse operation and at high densities became now accessible with 140 GHz ECRH.

The influence of trapped particles on ECCD was investiagted in different magnetic field configurations, i.e. with different populations of trapped particles in the wave-particle interaction region and the experimental results are compared to a theoretical modelling in Sec.5.

2. EXPERIMENTAL ARRANGEMENT

W7-AS is a modular stellarator with 5 magnetic field periods, low vacuum magnetic shear and high aspect ratio, the average minor and major radii are ≤ 0.18 and 2.0 m, respectively. The plasma cross section changes from nearly triangular to nearly elliptical within half a magnetic field period, indicating the dominant Fourier components (l=2,3) of the magnetic configuration. Two movable instrumented limiters can be inserted to control the plasma edge or removed outside the last closed flux surface for sufficiently high rotational transform ($\iota > 0.5$) as shown in Fig. 1. The plasma is limited in this case by a natural separatrix, which is shaped by the relicts of 5/m natural magnetic islands originating from the non-axissymmetry of the configuration. For $\iota < 0.5$, the limiter always defines the last closed magnetic flux surface (even in the outermost position), because the poloidal cross section of the plasma increases.

Net current free plasma build-up and heating is achieved at W7-AS with up to 0.8 MW microwave power at 70 GHz in long pulse operation (< 3 s). The corresponding resonant magnetic induction is 2.5 T, with a cut-off density of $n_{e,crit} = 6.2 \times 10^{19}\ m^{-3}$ for 1st harmonic O-mode operation. This System was operated also at 1.25 T with the 2nd harmonic X-mode at a reduced cut-off density of $n_{e,crit} = 3.1 \times 10^{19}\ m^{-3}$. Four microwave beams (0.2 MW each) are combined at one poloidal plane and each beam can be

steered independently by movable launching mirrors inside the vacuum vessel.

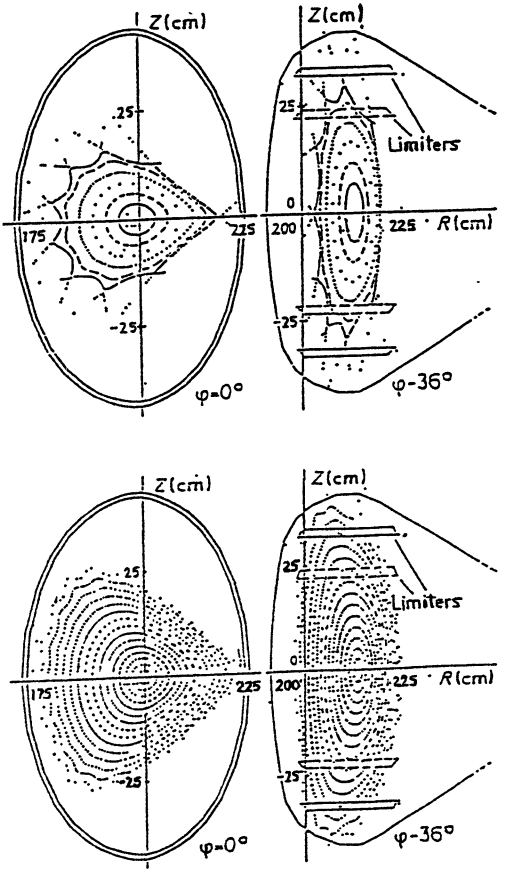

Fig.1: Poloidal cross sections for the magnetic configurations of W7-AS at $\iota > 0.5$ (top) and at $\iota \approx 0.3$ (bottom) and extremal positions for the movable instrumented limiter.

A separate 140 GHz prototype gyrotron from the development line at the IAP-Nizhny Novgorod generates 0.5 MW power with up to 1.1 s pulse duration or 0.9 MW for a pulse duration of up to 0.4 s. The linearly polarized Gaussian output beam

is transmitted to the plasma by an optical mirror system [14] with 10 mirrors. The overall transmission efficiency was measured calorimetrically at high power and is 80 %. The main losses (15 %) are coupling losses from the gyrotron output to the optical transmission system due to non-Gaussian emission (side lobes) from the gyrotron, because the internal mode converter is not yet fully optimized. Additional 5 % are transmission line losses such as spill-over and resistive losses. The transmission system allows for an arbitrary choice of the wave polarization. The microwaves are launched similar to the 70 GHz system by two movable mirrors inside the vacuum vessel from the low magnetic field side in the equatorial plane of the torus and can be steered with an arbitrary toroidal and poloidal launch angle, respectively. The experiments were performed with perpendicular launch in the X-mode polarization at the 2nd harmonic. The cut-off density for this mode is 1.2×10^{20} m^{-3}. At 2.5 T resonant magnetic field both the 70 and 140 GHz systems can be operated together. The microwave beams of both, the 70 and the 140 GHz systems are launched at equivalent poloidal planes with elliptical cross sections and an almost tokamak-like 1/R dependence of the magnetic induction. Thus the power deposition profile is narrow with a typical spatial width of 3 cm.

3. H-MODE TRANSITIONS

The experiments reported here were performed at the EC-resonant magnetic induction of B_0=2.5 T, with $\iota(a) \approx 0.5$. The plasma net current was feedback controlled by compensating the bootstrap current with the OH transformer (I_p=0). All experiments were performed with boronized vacuum vessel walls and graphite armour of exposed in-vessel components.

The plasma is generated and heated by a 70 GHz ECRH prepulse, which is followed by 140 GHz ECRH. The density is ramped up to a line integrated density of 4×10^{19} m^{-2} ($n_{e0} \approx 0.9 \times 10^{20}$ m^{-3}) as seen from Fig. 2. The H-mode transition to a moderately improved global confinement occurs in the flat top phase. The density starts to increase further after the transition with no external gas feed, which indicates an improved particle confinement. The H-mode transition phenomena are similar for

hydrogen and deuterium operation. The most pronounced signatures of the H-mode is as a drop of the H_α line emission signals from both limiters (only one signal is displayed) indicating a reduced particle recycling.

The edge value of the rotational transform, the density and the edge condition (limiter position) are leading parameters to achieve the H-mode. Below a line integrated density of 2×10^{19} m^{-2} ($n_{e0} \approx$ 4-5 $\times$ 10^{19} m^{-3}) no transitions were observed at 2.5 T operation. Recently, H-mode transitions were also found at 1.25 T operation with a lower density limit of 2-3 $\times$ 10^{19} m^{-3} ,which is close to the cur-off density for 2nd harmonic X-mode ECRH. This transitions occur already at about 0.2 MW heating power, which is about half the power needed to sustain the discharges, which show the transition at 2.5 T. In all cases investigated so far (limited available heating power), the H-mode transitions occur only in a narrow

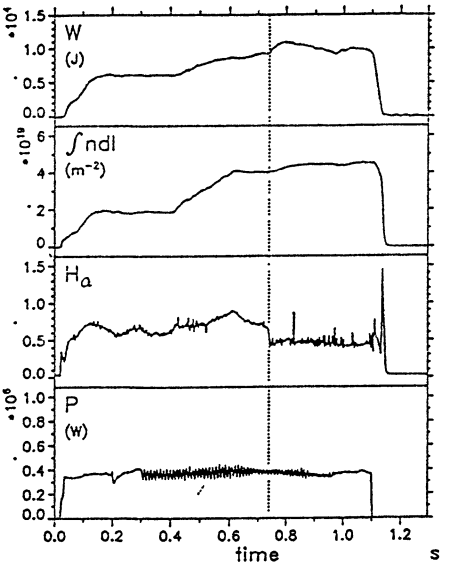

Fig. 2. Time evolution of the stored plasma energy W, the line integrated density ∫ndl, the H_α emission (top limiter) and the ECRH input power P. The dotted line marks the transition.for a hydrogen discharge

parameter window around $\iota = 0.52$. The choice of the rotational transform is closely interlinked with the magnetic topology at the plasma boundary. Magnetic islands have significant influence on the edge structure due to the low shear in W7-AS. The transition was suppressed, if the limiter was inserted about two centimetres from the last closed flux surface.

An unperturbed and separatrix dominated plasma boundary seems to play a significant role to establish the H-mode with the available heating power. Experiments around $\iota(a) \approx 0.3$, where the last closed flux surface is defined by the limiter position and no separatrix exists showed no H-transition even at higher ECRH-power of 0.75 MW and densities well above the H-mode threshold.

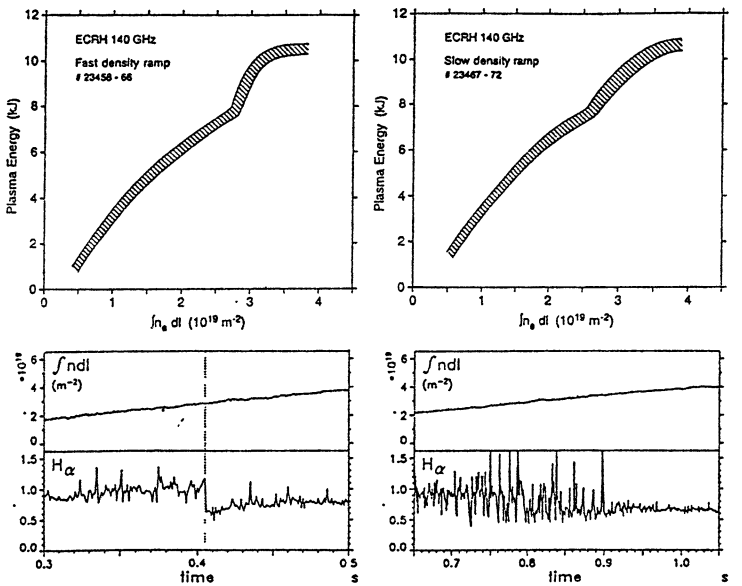

Fig. 3. Total stored plasma energy as a function of the line integrated density ∫ndl for fast (top left) and slow (top right) density ramp-up. The time development of ∫ndl and the H_α signal is given on bottom for both cases. Note, that the time intervals are different by a factor of two.

The smoothness of the transition is dependent on the strength of the gas puffing. Experiments with a slow (1×10^{20} m^{-3} s^{-1}) and fast (2×10^{20} m^{-3} s^{-1}) density ramp showed, that the transition occurs in both cases at approximately the same density of $n_{eo} = 5 \times 10^{19}$ m^{-3} as a lower limit for the transitions. With a slower density ramp, however, the transition is smoothed out by a series of ELM's as seen from Fig.3

Heat waves were exited by a modulation (typically 15%, 92 Hz) of the microwave power and measured by ECE diagnostics [15]. The phase delay and amplitude decay of the propagating heat wave is shown in Fig. 4 b as a function of the effective radius for a 200 ms quasi steady state time interval before and after the transition, respectively.

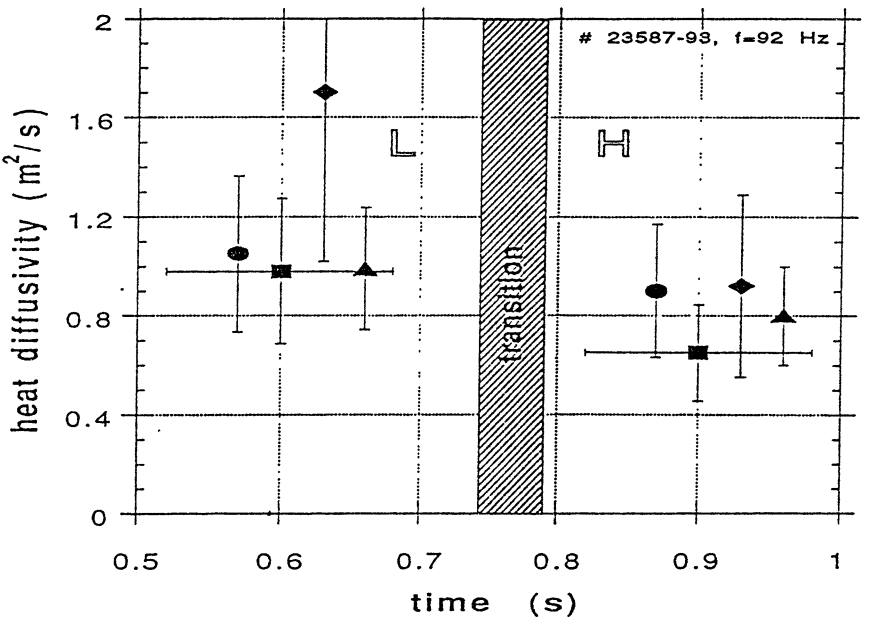

Fig. 4a: Heat diffusivity derived from the heat wave propagation before and after the transition for different simplifying assumptions (different symbols) and averaged over 0.2 s in both phases.

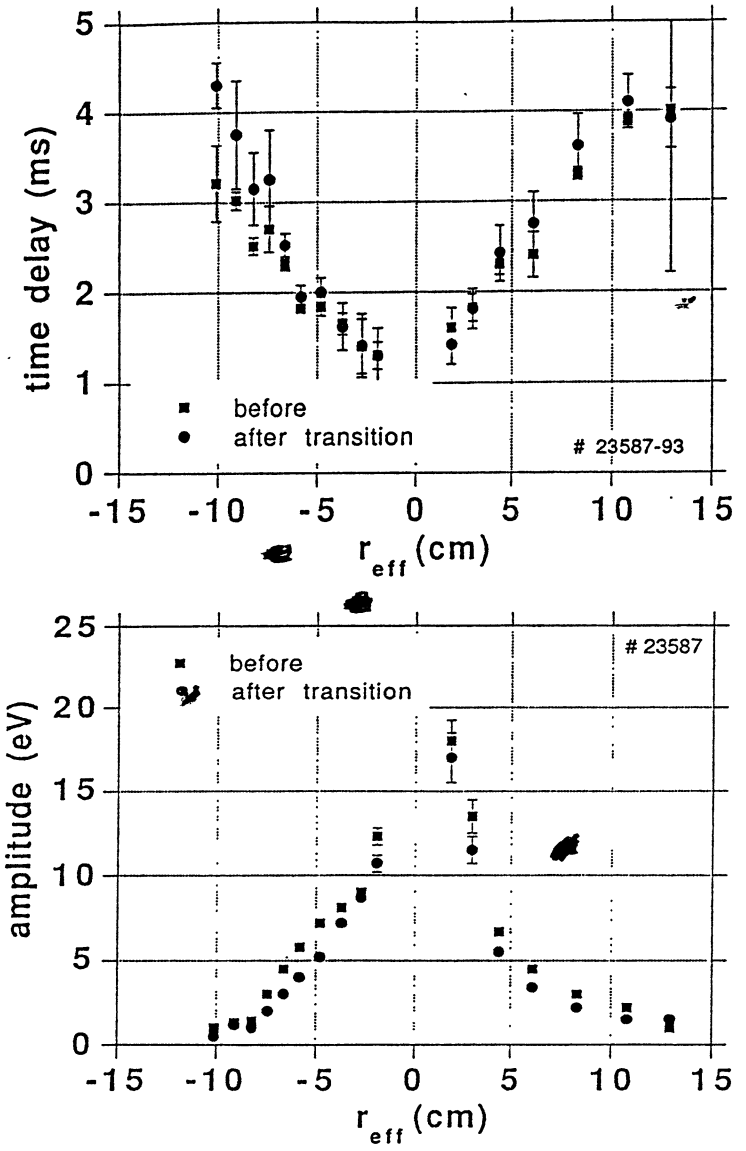

Fig.4 b: Time delay and phase decay of the stimulated heat wave before (squares) and after (dots) the H-mode transition as a function of the effective radius for the same discharge as Fig.4 a.

The heat wave is travelling slower in the H-mode phase of the discharge as compared to the pre-transition phase. The interpretation in terms of heat diffusivity is difficult, because of the strong electron-ion collisional coupling at the high densities of 0.9×10^{20} m^{-3}. Furthermore, the slight density increase after the transition would already lead to a small reduction of the heat diffusivity due to the favourable density scaling of the confinement in W7-AS and has to be taken into account. A simple analysis for different model assumptions and assuming constant χ in the analyzed radial interval is shown also in Fig.4 a. A trend for a reduction of the heat diffusivity from 1.0 m^2/s in the pre-transition phase to 0.8 m^2/s in the H-mode phase is indicated although the error bars are large. The change of the heat diffusivity from the steady state power balance analysis shows a similar reduction mainly in the gradient region of the electron temperature but is still within the experimental error bars. Please note, that for W7-AS the heat diffusivity derived from pertturbativ methods is in general agreement with the steady state results in contrast to the tokamak [15].

4. COMBINATION OF ECRH AND NBI

Experiments with combined heating were performed at densities around $n_{e0} \approx 5 \times 10^{19}$ m^{-3} and $n_{e0} \approx 1 \times 10^{20}$ m^{-3}, respectively, with both, on- and off-axis power deposition of ECRH. An example with on axis ECRH at $n_{e0} \approx 5 \times 10^{19}$ m^{-3} is seen in Fig. 5. The time sequence of the heating pulses is seen from the bottom trace in Fig. 5, the discharge is sustained in the final phase by NBI only. During the ECR-heated prephase and the combined heating phase density control is maintained by feedback controlled gas puffing, whereas after switch off of ECRH the density increases with the external gas feed turned off. The density increase with pure NBI heating is a well known feature at W7-AS [4], where beam fuelling (typically 1×10^{20} s^{-1} for 0.35 MW) and recycling fluxes have a comparable contribution to the overall density rise.
The density could be controlled also with off-axis ECRH power deposition at r/a = 0.5, at high plasma densities and with

combination of 0.75 MW ECRH and 0.7 MW NBI heating. As a rule, the density control could be maintained only, if the ECRH power was approximately equal or larger than the NBI power.

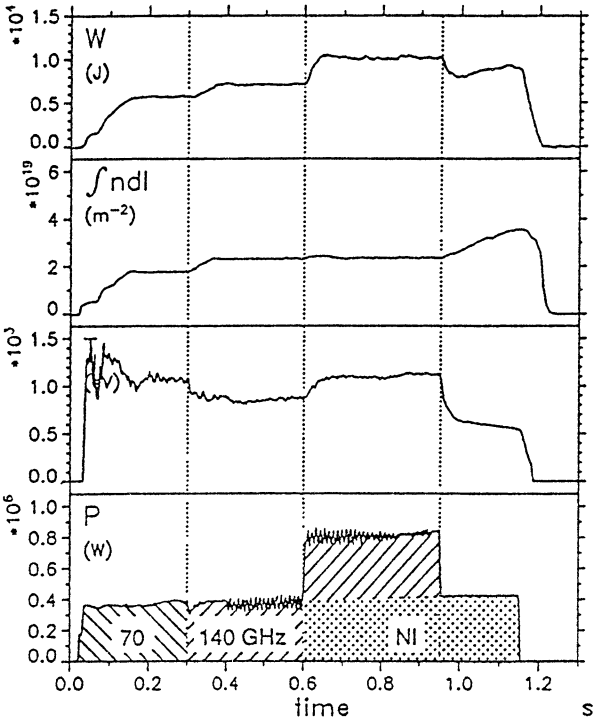

Fig. 5. Time evolution of the stored plasma energy W, the line integrated density ∫ndl, the central electron temperature (SX) and the input power P for combined heating with on-axis ECRH and NBI.

Evidence for degraded particle confinement in the bulk plasma comes from the profile development in the different heating cases as seen from Fig.6. The density profile for combined heating is flat and the T_e-profile is strongly peaked for on-axis ECRH. On the other hand, the density profile becomes peaked and the T_e-profile is flat in the plasma centre for off-axis ECRH. These results suggest, that the particle confinement is affected mainly by the temperature profile

changes inferred by the additional ECRH. This would also explain the empirical finding, that a certain ECRH-power is needed to provide the density control, which means that for the given high plasma densities sufficient ECRH power has to be added to shape the temperature profile.

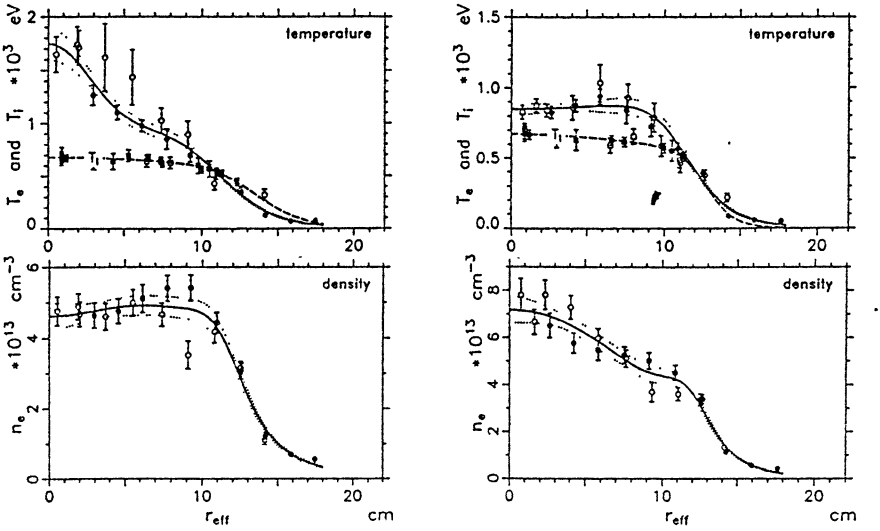

Fig. 6: Radial profiles of n_e, T_e (from Thomson scattering) and T_i (from active CX diagnostics) for combined heating with on-axis (left) and off-axis (right) ECRH + NBI

The impurity confinement was investigated by Al laser-blow off experiments as shown in Fig.7. The central impurity line emission from Al XII shows a decay time of typically 200 ms for the on axis combined heating case, whereas the decay time is much larger (and could not be quantified within the available discharge time) in the off-axis case. For both cases, the decay of the Al XII line emission is very similar in the ECRH prephase and in the combined heating phase. The degradation of the impurity confinement time with combined heating confirm the results from W7-A [12].

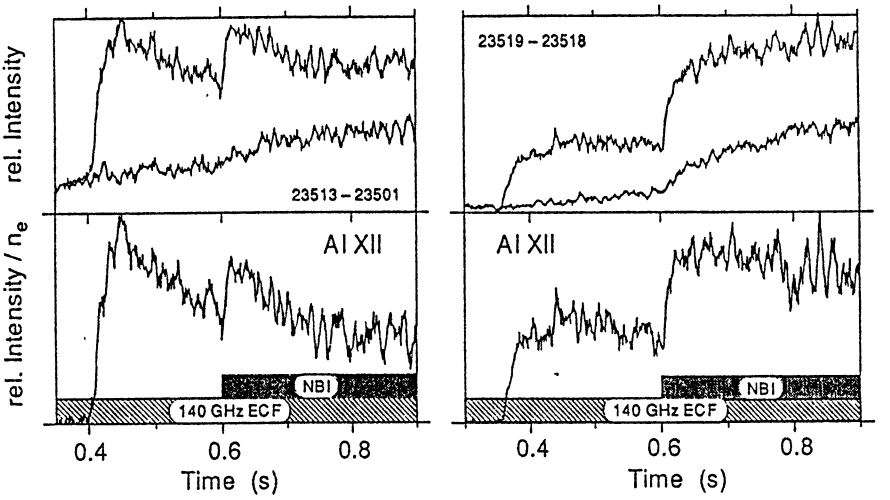

Fig. 7:Time behaviour of the Al XII intensity from laser blow-off for on-axis (left) and off-axis (right) ECRH in combination with NBI.

The understanding of the measured behaviour is of crucial importance and more detailled investigations are under way, because combined heating may provide tools for impurity control in steady state plasma operation.

5. ELECTRON CYCLOTRON CURRENT DRIVE

In stellarators the EC-driven current can be measured with high accuracy because of the absence of large "obscuring" inductive currents as in tokamaks. ECCD-experiments at W7-AS could be well described by linear theory [17], if trapped particle effects are taken into account. In stellarators plasma net currents of the order of 1-10 kA were measured in present day devices and identified as the neoclassical bootstrap current. Compensation of this small currents can be provided easily by ECCD to achieve net current free operation and maintain a particular ι-profile and/or control of the

edge iota, which may be of importance for future divertor concepts. The bootstrap current can be kept small also in large scale optimized stellarators. For W7-X small residual bootstrap currents of the order of 10 to 50 kA are expected and can be compensated, if necessary, by ECCD. The good understanding of the ECCD physics and the narrow driven current profiles have been used to investigate the influence of low order rational magnetic surfaces (islands) and different shear (i.e. different internal current density distributions) on the stellarator confinement [16].

The sensitivity of ECCD with respect to trapped particles was investigated by making use of the W7-AS flexibility to operate at different magnetic field configurations. In particular the magnetic mirror ratio and thus the population of trapped particles can be changed in a contolled way by changing the external coil currents. ECCD results are compared for the two cases with different magnetic field configurations shown in Fig.8.

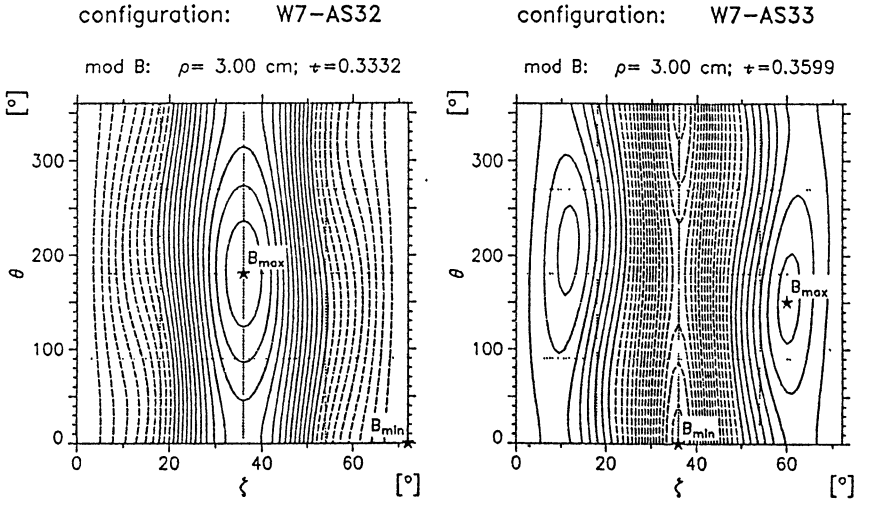

Fig. 8: Magnetic field configurations of W7-AS with the maximum (left) and minimum (right) of /B/ in the ECRH plane located at ζ=36 deg. θ and ζ are the poloidal and toroidal angular coordinate, respectively.

For case 1 the maximum of the magnetic field is located at the poloidal plane, where ECRH is launched, i.e. the trapped particles are mainly located outside the wave-particle interaction region and their impact on the ECCD efficiency is mainly due to friction with the current carrying passing particles (standard case). In case 2 the minimum of the magnetic field is placed in the plane, where ECRH is launched and consequently a considerable fraction of the injected ECRH power interacts directly with trapped particles, which do not contribute to ECCD. Both configurations have a comparable total trapped particle fraction of about 40 % on axis. The experiments were performed at 2nd harmonic X-mode with a resonant magnetic field of 1.25 T. The plasma is heated by 0.4 MW ECRH power and

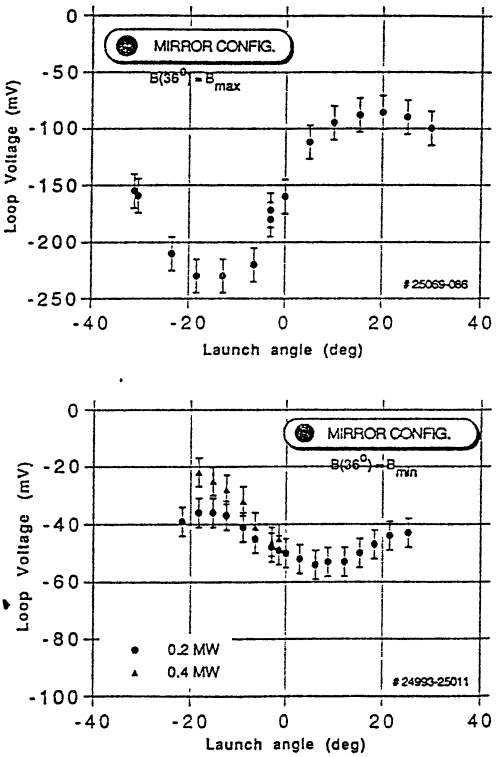

Fig. 9: Loop voltage response on a launch angle scan with plasma net-current I_p=0 for two magnetic field configurations. The discharges are heated with 0.4 MW ECRH, the launch angle scan is performed with 0.2 MW (dots) and 0.4 MW (triangles).

0.2 MW were used for current drive. In both cases the launch angle of the microwave beams was varied by means of internal movable mirrors in a wide angular range. Both current components, the EC-driven current and the bootstrap current were compensated by an inductively driven current (OH-transformer) in a feedback loop to keep the net current Ip = 0 with a high accuracy (± 0.2 kA). The required loop voltage is plotted at a function of the launch angle in Fig. 9 for both cases.

The loop voltage at perpendicular launch (φ = 0, no ECCD) is nonzero and indicates the compensation of the bootstrap current alone. Two effects are clearly seen, i.e. the loop voltage and thus the driven current is much smaller in the case where the trapped particles are located mainly in the ECRH-plane (note the different scales) and the ECCD-efficiency even changes sign. This is in agreement with theoretical predictions using linearized theory in the long mean free path[18]. For comparison the calculated ECCD efficiency for both configurations is seen from Fig. 10, which is in ecxellent agreement with the measurements.

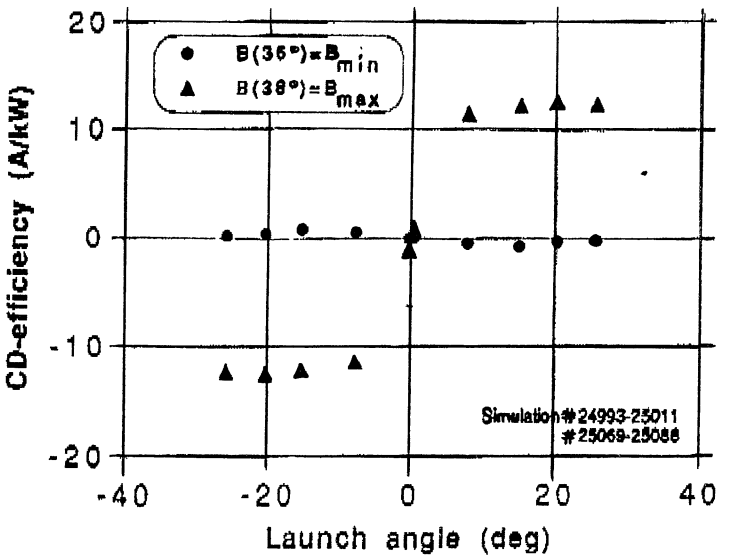

Fig. 10: Modelling of the current drive efficiency for the magnetic field configurations shown in Fig.8 as a function of the launch angle.

The degradation of the ECCD efficiency is mainly due to the large fraction of the injected ECRH-power, which is directly absorbed by trapped particles without contributing to current drive. The reversal of the sign as compared to the usual current drive mechanism is a consequence of the ECRH-induced trapping of otherwise barely passing particles.

6. SUMMARY AND CONCLUSION

A new 140 GHz ECRH system (0.5 MW, >1.1 s or 0.9 MW, 0.4 s) was operated at W7-AS. The parameter range for ECR-heated discharges was extended to densities up to 1.1×10^{20} m^{-3}.

H-mode transitions were observed at W7-AS, which behave similar for hydrogen and deuterium discharges and no pronounced isotope effect was seen. The H-mode transitions where observed at densities above 4-5 $\times$ 10^{19} m^{-3} (2.5 T) and under optimum confinement conditions in the vicinity of $\iota = 0.5$, where the plasma is separatrix dominated. At the same density and even higher power no transitions were observed in a limiter dominated case. The transition occurs independent of the density ramp rate at about the same threshold density. With lower gas puffing, the transition is smoothed out by a series of ELMs. The lower density limit for H-mode transitions is reduced to 2-3 $\times$ 10^{19} m^{-3} at 1.25 T operation and occurs at about half the heating power required at 2.5 T. Heat wave experiments showed a reduction of the heat diffusivity in the H-mode phase.

A strong effect on the particle confinement was measured in experiments with combined heating of ECRH and NBI. Whereas the density increases steadily in purely NBI heated discharges due to the beam fuelling and recycling, the density can be controlled in combined heating scenarios. There is experimental evidence, that the particle and impurity confinement is affected by the profile changes inferred by ECRH.

The influence of trapped particles on the ECCD efficiency was investigated. ECCD experiments in different magnetic configurations with different magnetic mirror ratios showed a strong dependence on the location and fraction of the trapped particle population. Direct heating of trapped particles leads to a significant reduction of the ECCD efficiency in excellent agreement with linear theory.

References:

[1] F. Wagner et al., Phys. Rev. Lett. 42 (1982) 1408

[2] V. Erckmann, et al., Phys. Rev. Lett.70, 14 (1993), 2086

[3] V. Erckmann, et al., Proc. 14th Intern. Conf. on Plasma Physics and Contr. Nucl. Fusion Research, 1992, Germany, post deadline paper.

[4] H. Renner, et al., Plasma Physics and Contr. Nucl. Fusion Research, 1990, Vol. 2, IAEA, Vienna (1991) p. 439

[5] K. Odajima et al., Plasma Physics and Contr. Nucl. Fusion Research 1986, Vol. 1, IAEA, Vienna (1987), p. 151

[6] S.M. Kaye, et al., J. Nucl. Mat. 121 (1984), 115

[7] C.E. Bush et al., Phys. Rev. Lett. 65, 4, (1990) 424

[8] JET-team, Plasma Physics and Contr. Nucl. Fusion Research 1988, Vol. 1, IAEA, Vienna (1989), p. 159

[9] G.L. Jackson et al., Phys. Rev. Lett. 67 (1991) 3098

[10] ASDEX-team, Nucl. Fusion, Vol. 29, No. 11, (1989), p. 1959

[11] H. Renner, et al. , Plasma Physics and Contr. Nucl. Fusion Research 1990, Vol. 2, IAEA, Vienna (1991) p. 439

[12] H.Ringler, et al., Plasma Physics and Contr. Nucl. Fusion Research 1986, Vol. 2, IAEA, Vienna (1987) p. 603

[13] V. Erckmann, et al., Plasma Physics and Controlled Fusion, Vol. 28, No.9A, p 1277, (1986)

[14] W.Kasparek, Proc. of the 8th Joint Workshop on Electron Cyclotron Emission and Electron Cyclotron Heating, Gut Ising, Germany, (1992), p. 423

[15] L. Giannone, et al., Nucl. Fusion, Vol. 32, No. 11 (1992)

[16] V. Erckmann, et al., Europhysics Topical Conference on RF Heating and Current Drive of Fusion Devices, Brussels, Vol. 16 E, (1991), p.297

[17] V. Erckmann, U. Gasparino, H. Maaßberg, M. Tutter, Europhys. Topical Conf.on RF Heating and Current Drive of Fusion Devices, Brussels, Vol. 16 E, (1991), p.301

[18] U. Gasparino, et al., Theory of Fusion Plasmas, Varenna 1990, p.195

COLLECTIVE SCATTERING OF POWERFUL GYROTRON RADIATION AT W7-AS

G.G.Denisov, A.A. Fraiman, V.A. Isaev, A.G. Litvak,
L.V. Lubyako, O.B. Smolyakova, E.V.Suvorov,
Institute of Applied Physics, Nizhny Novgorod, Russia
V. Erckmann, T. Geist
IPP, Garching
E. Holzhauer, W. Kasparek, G.A. Müller, P.G. Schüller
IPF, Stuttgart
N.V. Nickel, M. Thumm
KfK, Karlsruhe

Introduction

Collective Thomson scattering of microwave radiation may serve as a nondisturbing tool for measurements of ion temperature, or more general - the ion distribution function with sufficient spatial resolution. This technique has good prospects to be used in a reactor-scale tokamak for alpha-particle diagnostics [1,2].

The few present day experiments on the measurements of ion features in the scattered spectrum are based mainly on two sources of radiation, namely D_2O laser and gyrotrons . It was demonstrated experimentally that the scattering of D_2O laser radiation gives opportunity to measure ion temperature in middle-scale tokamaks [3,4]. The advantages of this technique are related to the possibility of very strong suppression of stray radiation by using viewing dumps which absorb an essential part of incident radiation and deep notch-filters based on gas cells (absorbing stray radiation in the main line which

which comes to the receiving antenna). A disadvantage is the rather complex D_2O laser which emits only pulses in themicroseconds range.

The main advantage of using the gyrotron radiation is the long pulse duration which gives opportunity to increase the signal-to-noise ratio by the factor $g = \sqrt{\Delta f \cdot \tau}$ (so called radiometric gain) due to integration. Here, τ is the integration time, and Δf is the bandwidth of the IF channel. Disadvantage is that in the case of using gyrotron radiation the problem of stray radiation is more serious. Longer wavelengths of radiation and long pulse duration make it difficult to use viewing dumps. It is more difficult to construct notch-filters with strong rejection of the gyrotron radiation in the center of the line; this also puts serious requirements to the frequency stability of the gyrotron. Nevertheless at present the only possibility to detect scattered signals from alpha-particles in JET-scale installations is to use a long-pulse gyrotronto obtain a large gain in signal-to-noise ratio.

The availability of 70 GHz and 140 GHz gyrotrons at the stellarator W7-AS makes it reasonable to use them for proof-of-principle experiments on collective Thomson scattering. Here we present the results of the first experimental attempt to detect ion features in the spectrum of scattered radiation at W7-AS using existing ECR heating systems based on 70 and 140 GHz gyrotrons.

1 ECRH systems

The 70 GHz ECRH system includes 4 gyrotrons with a unit power of about 200 kW in a pulse with up to 3 sec duration. The microwave radiation is transported from the gyrotrons to the stellarator in TE01 mode via closed circular oversized waveguides. After undergoing a mode conversion to the linearly polarized HE11 mode, it is launched into the plasma via steerable mirrors in the form of a quasi-optical Gaussian beam with circular cross-section. The waist diameter $(1/e)$ of the beam inside the plasma volume is about 4cm. The top view of two launching antennas is shown in Fig.1.

The 140 GHz ECRH system includes one gyrotron with a power

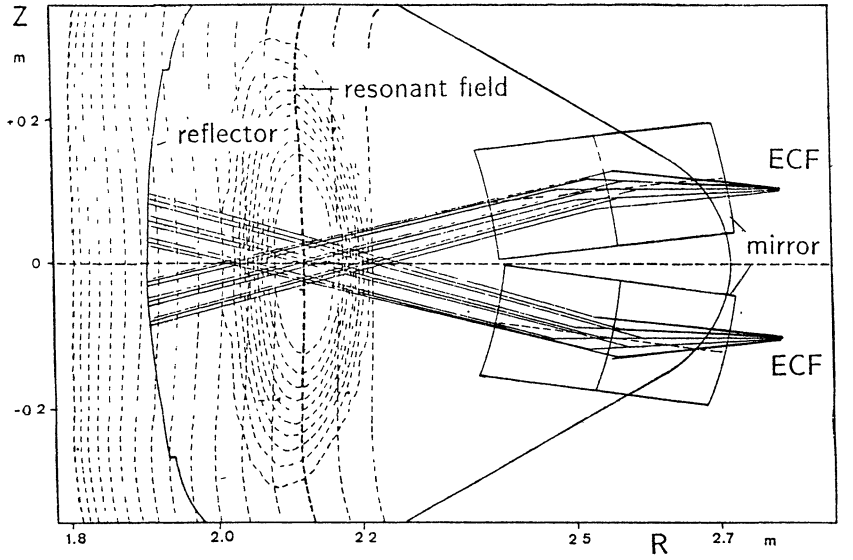

Figure 1: Scattering geometry at 70GHz

up to 500 kW in a pulse with up to 1 sec duration. Radiation is transported by a mirror transmission line and launched into the plasma by means of a steerable double-mirror antenna. Launched radiation is also in the form of a quasi-optical, vertically or horizontally polarized rf beam with circular cross-section and a waist diameter of about 4 cm in the plasma.

A very important point for CTS is the frequency stability of the source during the part of the pulse which is used for the scattering experiments. Measurements showed that the 140 GHz gyrotron had a continuous drop in frequency with a rate of about 100 MHz during 1 sec pulse; the frequency variation of the 70 GHz gyrotron was about 25 MHz/sec. As the (calculated) bandwidth of the thermal ion spectrum is several hundred MHz, no significant distortion of the spectra is expected if the duration of the probing pulse is of the order of 100 ms.

The first CTS experiments on W7-AS have been performed using existing ECRH antennas. In the 70 GHz CTS system one of the launching antennas was used as receiver, while the neighboring one was used as launcher. In the 140 GHz system, a receiving antenna consisting of a focusing mirror and a corrugated horn was placed outside the vacuum chamber; its receiving characteristics were matched to the probing radiation. In both cases the scattering geometry was close to back-scattering with practically no spatial resolution within the plasma column (see Figs. 1 and 2). The angle between scattering wavevector and magnetic field B was below 75 deg to avoid magnetic field effects in the spectra. With the plasma para meters given below, the scattering parameter lies in the range from 3 to 9.

2 Detection systems

Both detection systems include the same main components: notch-filter, heterodyne receiver with a fixed frequency local oscillator tuned to the gyrotron frequency, spectrum analyzer (filter banks at the intermediate frequency), analog-digital converter and software for data processing. The characteristics of detection system components are

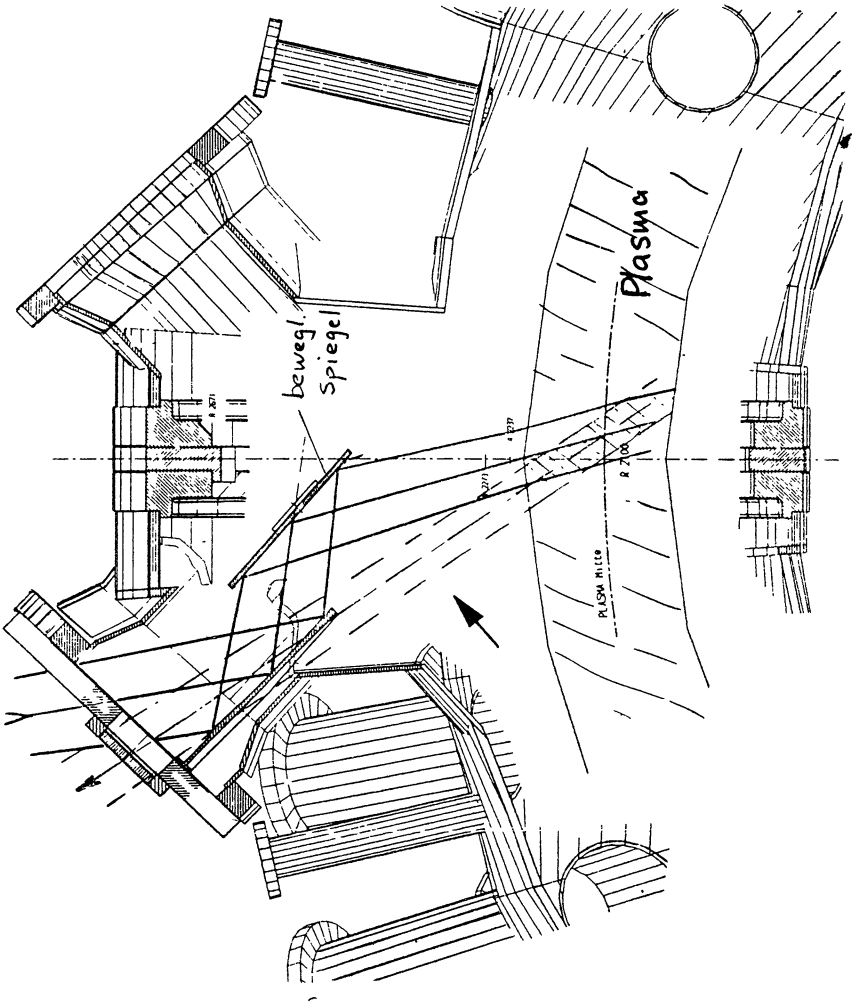

Figure 2: Scattering geometry at 140GHz

listed below.

70 GHz system:

- notch filter rejection : more than 50 dB within 50 MHz
- SSB noise temp of the mixing receiver: 4000 K
- bandwidth of the IF system: 20 - 420 MHz in 9 channels
- integration time 30 -100 ms for SNR of approx. 100
- synchronous detection for amplitude modulated gyrotron operation

140 GHz system:

- notch-filter provides rejection level more than 30 dB in the frequency band about 20 MHz;
- SSB noise temperature of superheterodyne receiver is within 2000-3000 deg;
- total band of frequency spectrum analysis is about 1.2 GHz;
- total number of frequency analyzer channels is 32, bandwidth of every channel is about 10% of its center frequency (frequency difference from the center of gyrotron line), minimum frequency is about 50 MHz;
- integration time of frequency analyzer about 5 ms should provide radiometric gain in SNR not less than 100;
- analog-digital converter can provide data acquisition from all channels during 3 sec with the sampling rate 10 kHz.

3 Experimental results

An overview on the operational regimes of W7 AS can be found in the paper by V.Erckmann et al (this conference). At the time of the scattering experiments, the stellarator needed the ECRH system (besides for heating) also for start-up; therefore, the scattering experiments had to be performed at magnetic fields, where the EC resonance is within the plasma. Most of the scattering experiments have been performed at B= 1.25 T: First, the plasma was ionized and heated by two 70 GHz gyrotrons in the X-mode at the second harmonic of

the cyclotron freqency. During this phase, the plasma density was kept at $2 \cdot 10^{13}$ cm^{-3}, the electron temp. Te_o was 1.5 keV, the ion temperature was approximately 250 eV. In this part of the discharge, the 70 GHz scattering experiments were performed. After 300 ms, the discharge was overtaken by neutral beam injection, the 70 GHz system was switched of, and the electron density was increased to 10^{14} cm^{-3}. Then, the electron and ion temperatures are nearly equal with Te = Ti = 0.5 keV. In this phase of the discharge, the 140 GHz gyrotron was fired to measure the scattered spectrum.

3.1 Collective scattering at 70 GHz

At 70 GHz, the probing frequency is equivalent to the second EC harmonic. Thus, the plasma is optically thick and the radiation temperature (ECE) is similar to the electron temperature, i.e. 1.5 keV. This radiation was used to test the characteristics of the receiver. The expected scattered power level for the plasma parameters given above was equivalent to a radiation temperature of only 50 eV; however, increase of scattered power by plasma refraction effects [7] had been ignored in this estimate. To discriminate the scattered signal from the ECE background, the gyrotron was amplitude modulated (40%) at a frequency of 10 kHz. For this case, the modulated ECE radiation was only 6 eV and thus one order of magnitude lower than the scattered signals. An additional suppression of the modulated ECE radiation could be obtained by optimizing the phase-setting of the lock-in amplifier which was used for the detection, as the ECE signal should be delayed in time compared to the scattered signal. In Fig. 3 a, b), a typical result of the experiments at 70 GHz is shown. For comparison, a thermal ion spectrum has been calculated using the plasma parameters given above and assuming 4% fully ionized carbon as the main plasma impurity; influences of plasma dielectric properties on the spectrum were ignored in the calculation. The following points can be seen: At frequencies above 300 MHz, the signal is very low which demonstrates the high suppression of the ECE radiation by the phase-coherent detection scheme. At scattered powers which are comparable with the thermal fluctuation level, the width of

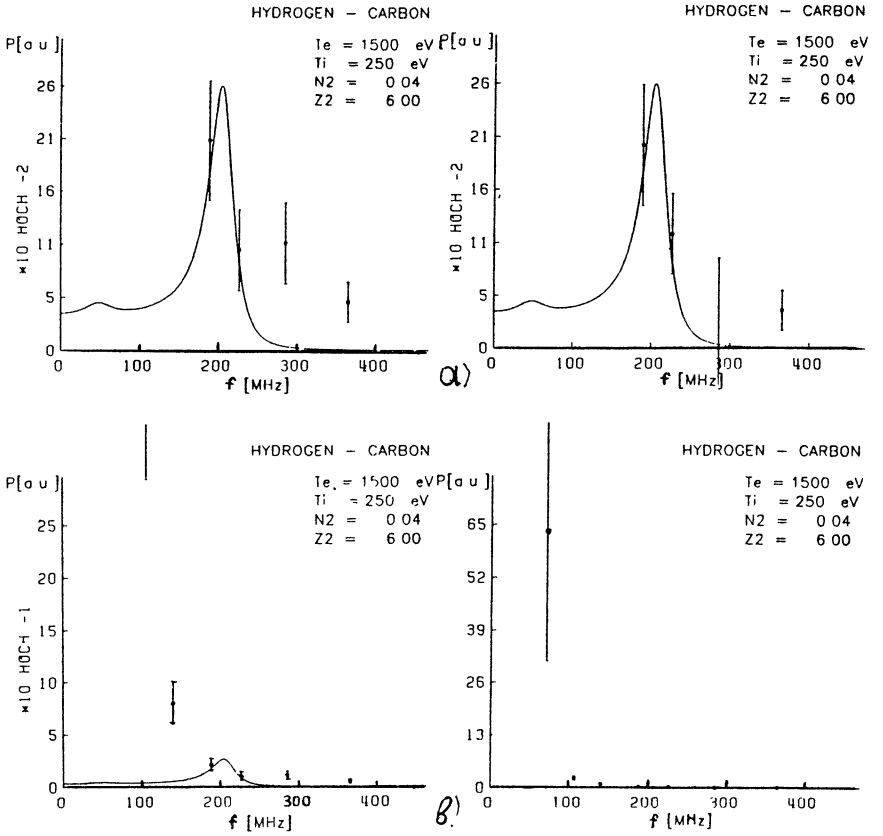

Figure 3: Typical result of the experiments at 70GHz

the measured spectra is comparable with the calculated spectrum. At lower frequencies, the signals are much higher than expected, which can be especially seen from Fig. 3b, where the same spectrum as Fig. 3a is plotted in a scale which is compressed by a factor of 250. This means, that in the lower frequency range strong suprathermal fluctuations are present in the plasma. By scanning of the scattering volume through the plasma, it was confirmed that these signal are indeed scattered signals and no spurious frequencies from the gyrotron; however, the present spatial resolution was not good enough to detect the location of these waves.

3.2 Collective scattering at 140 GHz

Examples of expected CTS spectra for back scattering geometry are shown in Fig. 4 for few sets of plasma parameters.

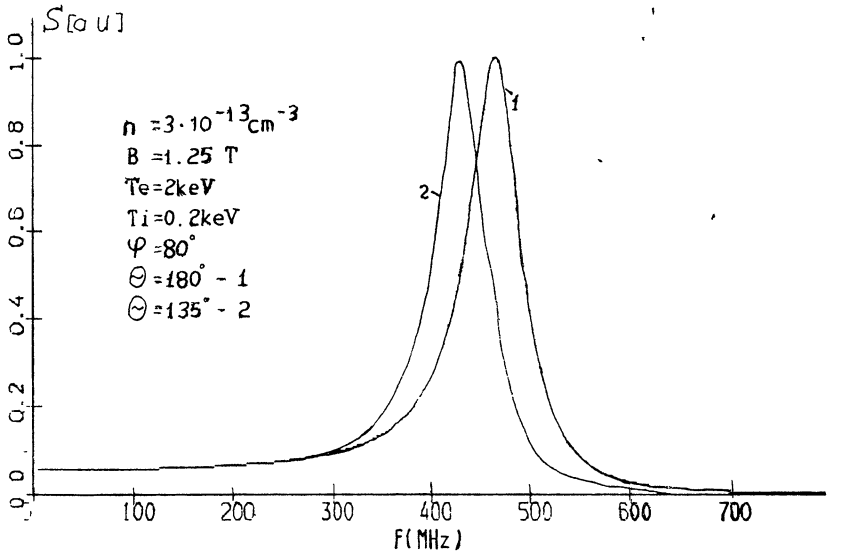

Figure 4: Expected spectra for back scattering geometry

The expected level of the CTS signal at 140 GHz is about 100 eV of equivalent noise temperature with 300 kW power of probing radiation. At 140 GHz the background radiation stems from 4th harmonic

ECE, which was measured to be below 2 eV. Taking into account the radiometric gain, the expected signal-to-noise ratio should be increased at least by two order of magnitude. This value should be just enough for CTS experiments both in 1.25 T and in 2.5 T regimes. In practice this ratio was less because of the unjustifiedly large losses in the antenna and input line.

The sensitivity of the 140 GHz detection system was determined by passive measurement of ECE from W7-AS plasma with different parameters and magnetic field values. For example, the variation of electron temperature from calibrated ECE system and plasma emission measured by CTS receiver at 140.9 GHz with fairly good agreement between each other (B = 2.5 T). More delicate test was performed with b = 1.25 T in which case ECE system is close to its sensitivity limit; there is also a correlation between ECE and the signal registered by the CTS receiver (Fig.5).

As described above, the scattering experiments were performed in dense plasma with a gyrotron pulse duration of 20 ms. The main difficulty which prevented successful measurement of CTS spectra was the stray radiation which was not rejected by narrow-band notch-filter. Most probably it is due to the fact that in the front of a short pulse used in CTS experiments gyrotron frequency undergoes fast variation which is outside the rejection band of notch-filter. This strong radiation overflows the registration system after which the signal decays with the characteristic integration time of the system (about 4 ms). The difference between registered signals with scattered volume inside the plasma and outside of it (see Fig.6) may serve as an indication of the presence of scattered radiation in the registered signal. Additional evidence for this statement is that the frequency band in which sthis difference is registered is of the same order as the expected bandwidth of CTS spectra.

4 Conclusions

Collective scattering of powerful gyrotron radiation at 70 GHz by thermal ions was registered in the back scattering geometry at W7-

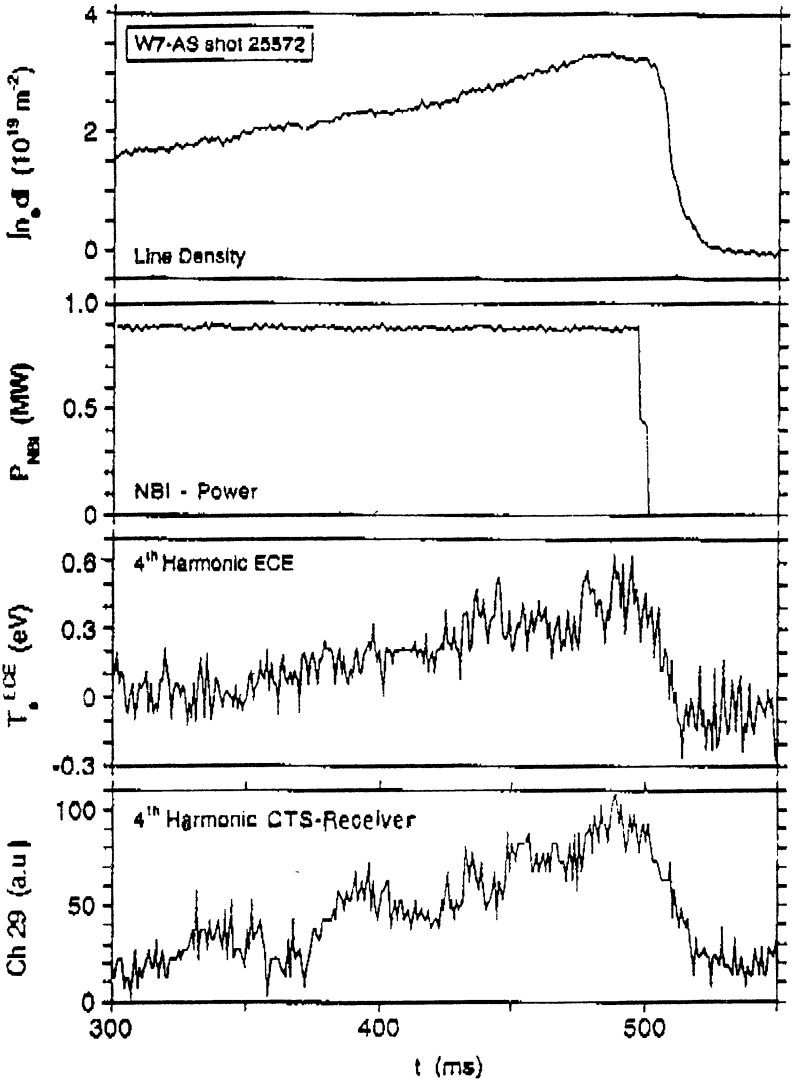

Figure 5: Line integral of the plasma density, neutrail-heating power, fourth harmonic ECE measured by ECE diagnostics and by 140GHz CTS receiver

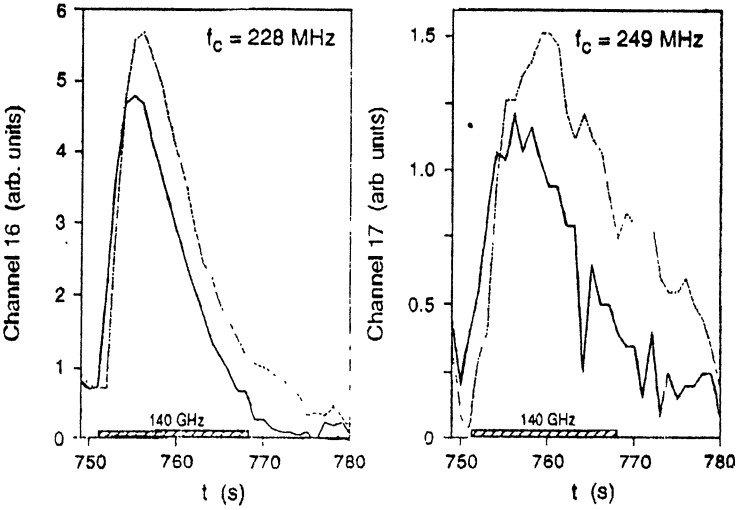

Figure 6: Time bihavior of measured signals at 2 typical frequency channels. Signal with (top) and withuot (bottom) scattering volume in plasma.

AS, nonthermal fluctuations being detected in lower frequency part of the scattered radiation spectrum. The CTS system at 140 GHz demonstrated its principle operating ability which evidently will be realized after solving the problem of stray radiation. After optimizing both systems, new experiments are planned, where a new ionization scheme for W7-AS will also allow non-resonant experiments, i.e. measurements where no EC resonance is present in the plasma.

References

1. J. A. Hoekzema, A. E. Costly, T. P. Hughes, J. A. Fessey, N. P. Stott, W. Swoeikropp. Collective mm-wave scattering to measure fust ion and alpha-paticle distributions in JET. IR & mm wave 18 conferens, 1993, Colchester.

2. A. E. Costly et. al. A Thomson scattering diagnostic to measure fast ion and alpha-particle distribution in JET. Report JET R(88)08 1988

3. R. Behn, D. Dicken, J. Hackmann, S. A. Salito, M. R. Siegrist, P. A. Krug, J. Kjelberg, B. Duval, B. Joye, A. Pochelon. Ion temperature measurement of tokamak by collective Thomson scattering of D_2O laser radiation. Phys. rev. v 62 N24, (1989)

4. M. Born, H.-D. Dichen, J. Hackmann, J. Uhlenbusch. Loca ion temperature measurements in the tocamak UNITOR by collective Thomson scattering. Plasma Phys. Cjntrol Fusion v 34, (1993), pp 391-396.

5.J. S. Machuzak, et. al. Rev. Sci. Instrum.,v57(8), pp.1983-1985, Aug. 1986.

6. J. A. Hoekzema, N. P. Hammond, E. F. Taylor, A. L. Stevens. Some key technical developments for the fast ion and alpha-particle diagnostic system on JET.

7. T. P. Hug hes, S. R. Smith. J. Plasma Physics,v 42, pp 215-240 (1989).

MICROWAVE DISCHARGE AND ITS APPLICATIONS

Nonequilibrium plasma produced by microwave nanosecond radiation: parameters, kinetics, practical applications

A.L.Vikharev, O.A.Ivanov, A.G.Litvak
Institute of Applied Physics, Nizhny Novgorod, Russia

1 Introduction

Creation of nonequilibrium plasma by microwave radiation is one of applications of microwave generators. Development of gyrotrons generating high-power pulses ($P \sim 10^5$ W) of long duration ($\tau \sim 10^{-5}$–10^{-3} s) made it possible to carry out investigations of a freely localized microwave discharge. The gas is ionized in the focus of a converging wave beam or in the region of intersection of two beams. Such a discharge is identical to a laser spark within the microwave range, but has some specific features connected with manifestation of nonlinear electrodynamic processes [1]. At microwave gas breakdown these processes of refraction, absorption, and reflection of electromagnetic waves limit the level of electron density lower than the critical density. As a result, there is no quick gas heating and the strong nonequilibrium condition of discharge plasma is retained for a long time. This type of the discharge was investigated in a set of experimental and theoretical works summarized in review [2]. It must be stressed that these investigations were stimulated by the creation and development of gyrotrons at the beginning of the 70ths [3,4].

At present the situation with generators on relativistic electron beams is similar. There is a great progress in their development [5].

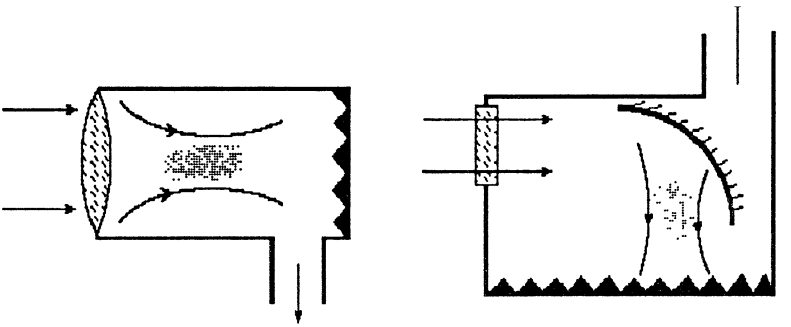

Fig. 1. Schematic diagrams of experiments

These generators have high peak power $P = (3-5) \cdot 10^9$ W at pulse duration $\tau = 10$–100 ns [6] and can work with a high repetition frequency up to $F = 100$ Hz [7]. They are widely used in laboratory experiments [8,9]. At present their application in radaring is being discussed [10]. These generators can be used also for creation of nonequilibrium plasma in a wave beam.

2 Experimental scheme

Investigations of a nanosecond microwave discharge were performed according to the following schemes (Fig. 1).

The discharge was created in the focal region of a wave beam formed with a lens or a parabolic mirror in the vacuum chamber. The chamber was pumped out and then filled with the investigated gases like argon, nitrogen, oxygen and the N_2:O_2 mixture. In the experiments a 3-cm microwave radiation was used, the pulse duration ranged from 10 to 100 ns. The power of the microwave beam was such that the root mean square of the electric field intensity in the beam focus varied from 10 to 60 kv/cm. In such fields for a wide range of pressures $p = 0,2$–760 Torr the oscillatory electron energy was

$$\epsilon_\sim = e^2 E^2 / 2m(\omega^2 + \nu^2) = 0.3 - 900 \text{ eV} \qquad (1)$$

3 Comparison of discharges in long and short pulse regimes

The conditions of creation of freely localized discharges in a wave beam by radiation of gyrotron and nanosecond microwave generator are as follows:

In the first case $E \sim 1-3$ kV/cm, $E/N \sim (8-10)\cdot 10^{-16}$ V·cm^2, $\tau \sim 10^{-5}$–10^{-4} s;

In the second case $E \sim$ 10–60 kV/cm, $E/N \sim (3-50)\cdot 10^{-15}$ V·cm^2, $\tau \sim 10^{-8}$–$5\cdot 10^{-8}$ s.

It should be noted that at one and the same scheme of experiment the discharge created by nanosecond microwave pulses differs greatly from the discharge created by gyrotrons (in the long pulse regime). It is primarily connected with the fact that a strong electric field is needed for gas breakdown by short nanosecond pulses. In such a strong field in the region of low and moderate gas pressures the oscillatory electron energy is equal to or more than the ionization potential: $\epsilon_\sim > I_i$.

Under these conditions the discharge development is accompanied by a number of effects [11,12] that are absent during the gas breakdown in moderate intensity fields, where $\epsilon_\sim << \bar{\epsilon} < I_i$ ($\bar{\epsilon}$ is the mean electron energy). Some effects are connected with a high ionization frequency by electron impact. Other effects are determined by high electron energies.

In a nanosecond discharge a great share of energy of microwave pules is spent on ionization, excitation of electronic states of molecules and their dissociation. As the result, plasma chemical reactions differ from those in a discharge of microsecond duration.

4 An artificial ionized layer (AIL)

Performed investigations of the nanosecond microwave discharge were stimulated by the idea of the creation of an AIL in the upper atmosphere [13,14]. The scheme of AIL creation in the region of intersecting wave beams is investigated in detail (Fig. 2).

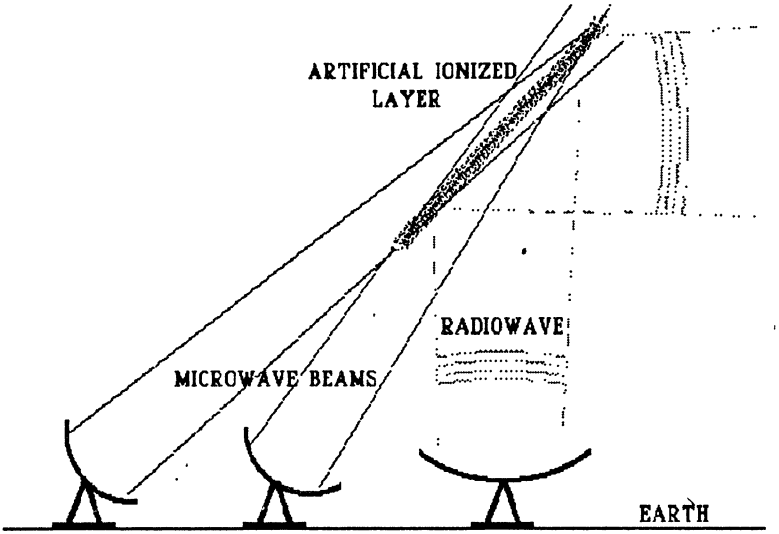

Fig. 2

The estimation shows that for formation of an AIL at the height of $H = 30$ km by transmitting antennas with diameter $d = 60$ m placed at the distance of 35 km, the pulse microwave power (radiation within the 3-cm band, pulse duration $\tau = 40$ ns) in every beam must exceed the level $P \approx 4$ GW. This level of microwave power has already been achieved by modern generators [6].

The AIL is supposed to be created at the heights $H = 30$–60 km by microwave radiation with wavelength $\lambda = 3$–100 cm and pulse duration $\tau = 10$–100 ns [15]. In the optimum energetical regime the wavelength and the level of microwave power must satisfy the following condition:

$$\omega = \nu \quad \text{and} \qquad E/E_c = 5 - 7\,, \tag{2}$$

where ω is the angular frequency of the microwave radiation, ν is effective collisson frequency of electrons and molecules, $E = 30 \cdot p \cdot (1 + \omega^2/\nu^2)^{1/2}$ (V/cm) is the critical field satisfying the condition of equality of ionization frequency by electron impact ν_i and the frequency of

attachment of electrons to the oxygen molecules ν_a: $\nu_i = \nu_a$, and p is air pressure in Torr. Condition (2) means that the maximum share of microwave pulse energy will be used for ionization (formation of electron-ion pairs) [15]. For example, at the chosen microwave radiation within the 3-cm band ($\lambda = 3$ cm) the optimum height of AIL creation is $H = 30$ km (that corresponds to gas pressure $p = 10$ Torr). When pulse duration is $\tau = 10$ ns, the gas breakdown takes place at root mean square electric field intensity $E/E_c = 5$. In this field satisfying the optimum condition for ionization, the oscillatory electron energy is $\epsilon_\sim = e^2 \cdot E^2/2 \cdot m(\omega^2 + \nu^2) \simeq 0.2$ eV. For gas breakdown at larger heights more powerful microwave pulses are needed. Thus, at the height of $H = 50$ km (the corresponding gas pressure $p \simeq 0.7 Torr$) the breakdown field is $E = 50 \cdot E_c$, where the oscillatory energy of electrons is $\epsilon \sim 35$ eV is larger than the energy of molecule ionization I_i.

Thus, the conditions of gas ionization in the strong microwave field ($\epsilon > I_i$) appear when the radiation of one frequency band is used for AIL creation at various heights. Specific features of the discharge development in such conditions were already described and the effects that appear during the gas breakdown by microwave radiation of nanosecond duration were mentioned. Some of these effects will appear during the open air breakdown.

5 AIL application

The interest to the AIL is explained by the variety of tasks which can be solved with the help of AILs. Thus, at present there are suggestions to use AIL for:

1) distant radio- and television communication [16],
2) generation of ozone [17],
3) diagnostics of atmosphere [18], and
4) clearing of atmosphere from pollution [19]. Let us consider each of these suggestions.

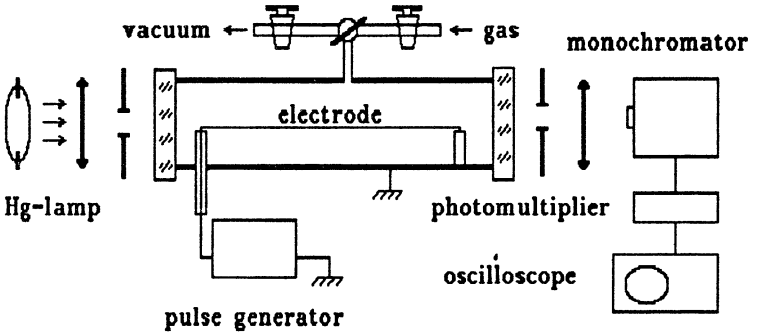

Fig. 3 Scheme of the experimental set-up for studying plasma chemical processes in a nanosecond corona discharge

5.1 Radioreflection

Application of AIL for radioreflection is analyzed in book [16] (see Fig. 2). So, there is no need to discuss it in detail. It should be only noted that the AIL in the form of a thin plasma layer can reflect radiowaves with the frequency less than 1-2 GHz. It is two orders of magnitude higher than the maximum frequency of radiowaves reflected from the ionosphere.

5.2 Generation of ozone

Laboratory experiments and numerical calculations of plasma chemical kinetics show that the nanosecond microwave discharge can be used for the predominant generation of ozone. For AIL maintenance it is necessary to use high-power nanosecond microwave pulses with high repetition frequency $F = 10^3$–10^4 Hz. Since at present microwave generators on relativistic electron beams do not produce the required high-repetition rate, the above mentioned regime of AIL maintenance was modeled using a nanosecond corona discharge in air [17].

The scheme of the experimental set-up is shown in Fig. 3. The discharge chamber was made as a section of a metal cylinder 3 cm

in diameter and 40 cm long; this cylinder worked also as the outer electrode. The chamber was vacuumed at the butt-ends with quartz windows. The second electrode 0.7 mm in diameter was placed along the cylinder axis; to this electrode pulses with positive polarity were delivered from a pulse voltage generator. The amplitude of voltage was 30-40 kV, pulse duration was $\tau = 50$ ns and the rise time of the pulse did not exceed 5 ns. The pulse repetition rate F was up to 200 Hz. The experiments were performed without gas pumping in the pressure range 10–760 Torr. The value of reduced electric field in the discharge region varied in the range $E/N = (1-10)\cdot 10^{-15}\text{V}\cdot\text{cm}^2$.

Thus, the conditions realized in the corona discharge were the same as in the microwave discharge. The gas was ionized by electrons that were born and stored their energy in the electric field within the reactor volume. There was no electron emission from the central electrode (wire), since it was given the positive potential.

The experiment studied the dynamics of O_3, NO_2, NO_3, N_2O_5 in the discharge. Production of ozone is weakly dependent on the distance from the central electrode. This means that the value of the reduced electric field E/N is high in the whole region of the discharge, when the value of the oxygen dissociation constant k_0 is close to saturation.

Figure 4 shows the dependence of reduced ozone density $[O_3]/p$ produced in one high voltage pulse under various air pressures. It is seen that the density of ozone grows linearly with the increase of pressure p. At the same time the density of oxygen atoms produced in saturation region k increases in proportion to the gas pressure:

$$d[\text{O}]/dt = 2 \cdot k_0 N_e \cdot [\text{O}_2]\,, \tag{3}$$

$$[\text{O}_3] = [\text{O}] = 2 \cdot k_0 \cdot N_e \cdot [\text{O}] \cdot \tau\,. \tag{4}$$

Thus the production of ozone is the main reason of destruction of oxygen atoms after the pulse. Characteristic time of ozone production measured in the experiment indicates that the main channel of the production of ozone is reaction

$$\text{O} + \text{O} + \text{M} \rightarrow \text{O}_3 + \text{M} + 1.08\,\text{eV}\,, \tag{5}$$

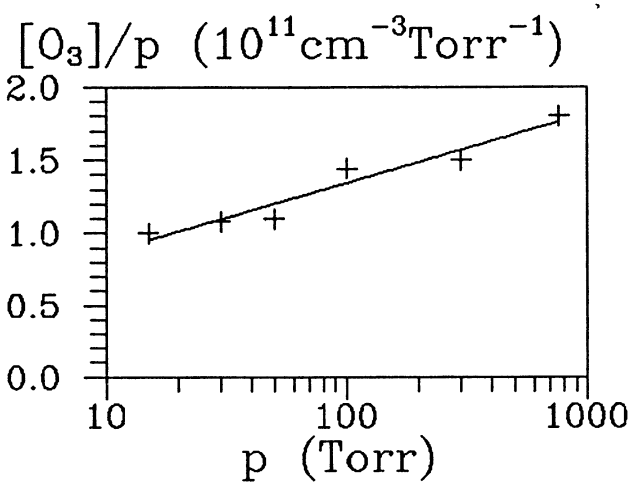

Fig. 4. Dependence of the density of reduced ozone in the discharge on air pressure

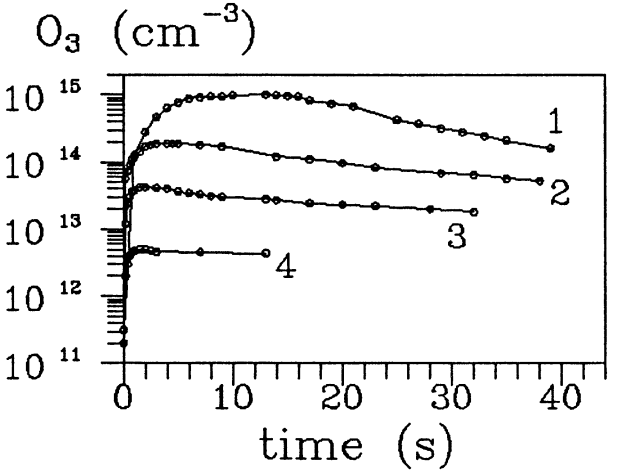

Fig. 5. Dependence of ozone concentration on time under various air pressures: 1–100 Torr, 2–50 Torr, 3–30 Torr, 4–15 Torr

the constant of which at $T_g = 350°$ C is $k_5 = 3.7 \cdot 10^{-34}$ cm^6/c.

Study of ozone synthesis in the multipulse regime showed that at the initial stage each pulse produces one and the same number of O_3 molecules; this leads to ozone accumulation in the discharge region. As the result, the ozone density reached quickly the stationary level, Fig. 5. Figure 5 represents the time dependence of ozone concentration under different pressures. Then with gas heating and formation of nitrogen dioxides, ozone density growth becomes slower, and even decreases, as shown in Fig. 6. However, the overall production of NO_2 is not great and occurrs mainly at times when the absorbed specific energy reaches great values. Figure 6 presents the dynamics of O_3 and NO_2 at pressure $p = 50$ Torr. The pulse repetition frequency in this case was $F = 50$ Hz.

The experiments showed also that when nitrogen dioxide was added to the gas as a minor admixture ($\sim 10^{15}$ cm^{-3}), the switching-on of the discharge led to NO_2 destruction, Fig. 7. The process of decrease in NO_2 density in the discharge is caused, evidently, by dissociation of nitrogen molecules at large values of E/N and high rate of reactions regenerating nitrogen:

$$N + NO \rightarrow N_2 + O\,, \tag{6}$$

$$N + NO_2 \rightarrow N_2 + O_2\,. \tag{7}$$

Efficiency of plasma chemical reactions was determined on the basis of measuring the energy absorbed in the discharge and on the basis of direct measurements of the charge entering the discharge gap, and voltage on the latter. Thus, efficiency of ozone generation was $\sim$ 15 eV per O_3 molecule, and energy losses on the removal of one NO_2 molecule $\sim$ 35 eV.

At nanosecond microwave pulses (as in corona discharge) the effective dissociation of molecules of O_2 and N_2 in AILs will naturally take place. Figure 8 presents the results of the calculation of the dynamics of O and N atoms for the discharge in converging cylindrical wave at pressure $p = 10$ Torr for the pulse duration $\tau = 40$ ns.

When making calculations we took into account the fact that atomic oxygen appears during the processes of dissociative electron

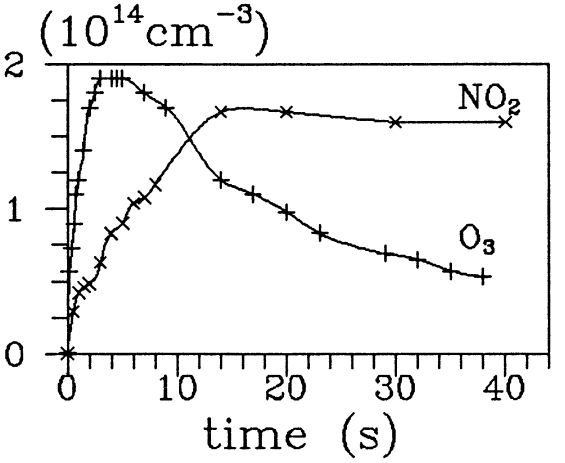

Fig. 6. Time dependence of the densities of ozone and nitrogen dioxide at pressure $p = 50$ Torr.

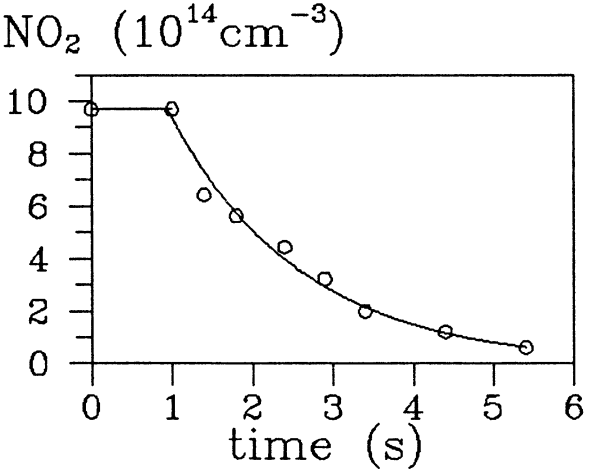

Fig. 7. Variation of nitrogen dioxide density after the discharge was switched on at time $t = 1$ s, air pressure $p = 10$ Torr.

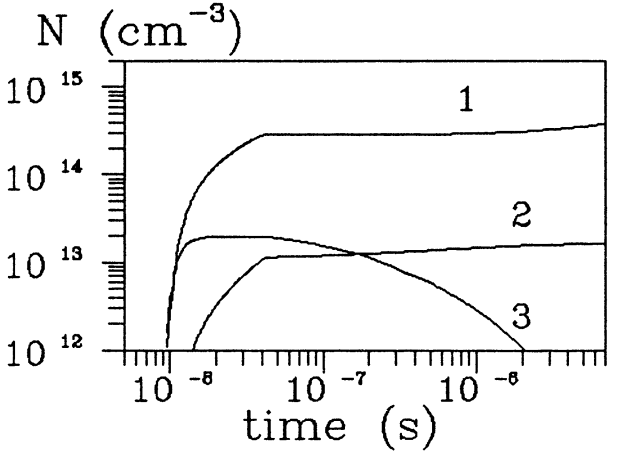

Fig. 8. Time dependence of air dissociation products (1–oxygen atoms, 2–nitrogen atoms, 3–electrons). Parameters of calculation: nondisturbed field $E = 3$ kv/cm, $p = 10$ Torr, $\tau = 40$ ns

attachment:

$$e + O_2 \rightarrow O^- + O\,, \tag{8}$$

electron impact dissociation of oxygen molecules

$$e + O_2 \rightarrow O_2^* \rightarrow O + O + e \tag{9}$$

and at the collision of O_2 with the metastable N_2 molecules

$$O_2 + N_2^* \left(A^3\textstyle\sum_U^+\right) \rightarrow O + O + N_2 \tag{10}$$

The rate constants of the processes are defined by the electron energy distribution function and depend on electric field intensity in the discharge. The calculations showed that for the chosen parameters of microwave radiation the processes (9) and (10) are the main ones for creation of atomic oxygen in the discharge.

The values of the rate constants for oxygen dissociation process for the direct current discharge are well known [20]. Using them we

can evaluate the expenditure of energy for production of one ozone molecule in a microwave discharge. Assuming that all atomic oxygen formed in the process of dissociation (9) takes part in the reaction of ozone synthesis (5), then we can evaluate the ozone density produced by one pulse from formulas (3 and 4). The expenditure of energy for generation of one ozone molecule is [21]

$$\delta = \sigma \cdot E^2 \cdot \tau / [O_3] = 2.5 \cdot (e^2/m) \cdot (E_e/N)^2 \cdot (N/k_0 \cdot \nu), \qquad (11)$$

where $[O_2] = N/5$, $\sigma = e^2 N_e \nu / m(\omega^2 + \nu^2)$ is plasma specific conductivity.

At characteristic parameters of microwave radiation for AIL creation at the height of $H = 30$ km [15]: $E_e/N = 3 \cdot 10^{-15}$ V·cm^2, $N = 3.7 \cdot 10^{17}$ cm^{-3}, according to [20], the value of $k_0 = (8 - 10) \cdot 10^{-9}$ cm^3/s. From (11) we calculate the value of $\delta = 25$–30 eV/molecule. Thus the low expenditure of energy for O_3 production can be achieved in a nanosecond microwave discharge (as well as in a corona discharge) due to the high oxygen dissociation rate, compared to the rate of dissociative attachment. Taking into account process (10), the rate of which in a strong field is also high (coefficient $\sim 10^{-8}$ cm^3/s, [22]) decreases the expenditure of energy for ozone molecule production.

Basing on the results obtained for the corona discharge, one can predict the efficiency of ozone generation in an artificial ionized layer. Let us assume that the AIL is produced at the crossing of wave beams at the height $H = 30$ km by microwave radiation (of the 3-cm wavelength band) with power $P = 4 \cdot 10^9$ W and pulse duration $\tau = 40$ ns by aid of transmitting antennas 60 m in diameter distanced to 35 km from each other. Assuming that 1) microwave power is totally absorbed in the discharge region, and 2) expenditure of energy for generation of one ozone molecule in a nanosecond microwave discharge are equally low, as in the corona discharge, then the density of O_3 molecules generated by one pulse in the region of wave beams crossing (with volume $\sim 10^7$ cm^3) will be about $2 \cdot 10^{12}$ cm^{-3}. Such value of density coincides by the order of magnitude with the maximum of O_3 density at such heights. By scanning with the wave beams,

the volume of region of ozone generation can be essentially increased. For example, at repetition frequency of microwave pulses $F = 1$ kHz the ozone loss in the volume ~ 1 km^3 will be replenished in one day, and the expenditure of energy will be ~ 5 MW·h. Such low expenditures of energy make it possible to suggest using AILs for ozone replenishment in the regions of local "ozone holes" that appear during launching Shuttle spacecrafts [23,24].

It is known that along the trajectory of the rockets "Energy" and "Shuttle" the ozone is totally destroyed at all heights in the diameter of several hundred metres. Some hours later, as calculations show [23,24], the filling of ozone hole due to turbulent diffusion takes place. Figure 9 shows the time dependence of the radius of the ozone hole. Then the slow recreation of ozone takes place. Figure 10 shows the local ozone change evolution at different heights. It is seen that the characteristic time of ozone regeneration is equal to one day and night.

5.3 Diagnostics of the minority species of the atmosphere

The AIL can be successfully used also for the measurement of the minority species of the atmosphere such as Cl, NO, H. The increase of these active particles in the atmosphere influences greatly changing of the climate. First of all it is connected with the fact that these particles are catalysts in the reactions of ozone destruction:

$$\mathrm{Cl} + \mathrm{O_3} \rightarrow \mathrm{ClO} + \mathrm{O_2} \tag{12}$$

$$\mathrm{ClO} + \mathrm{O} \rightarrow \mathrm{Cl} + \mathrm{O_2} \tag{13}$$

or

$$\mathrm{NO} + \mathrm{O_3} \rightarrow \mathrm{NO_2} + \mathrm{O_2} \tag{14}$$

$$\mathrm{NO_2} + \mathrm{O} \rightarrow \mathrm{NO} + \mathrm{O_2}\,. \tag{15}$$

Therefore, the AIL can be applied for continuous monitoring of the stratosphere (at 25–60 km altitudes). This problem was discussed in paper [18].

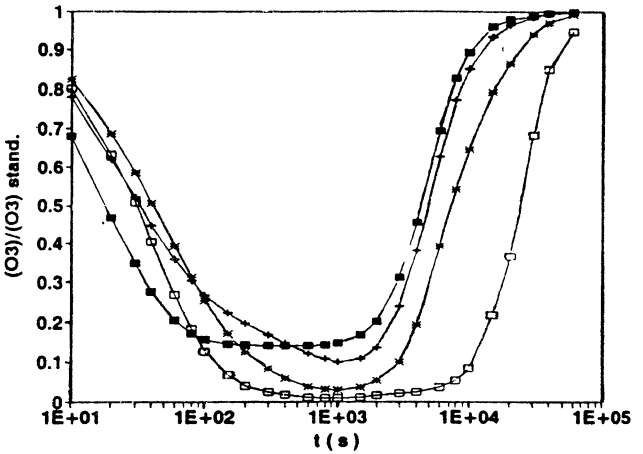

Fig. 9. Local ozone change evolution by Shuttle launch at the different altitudes: $\square$–$z = 16$ km; $+$–$z = 24$ km; $*$–$z = 32$ km; $\square$–$z = 40$ km.

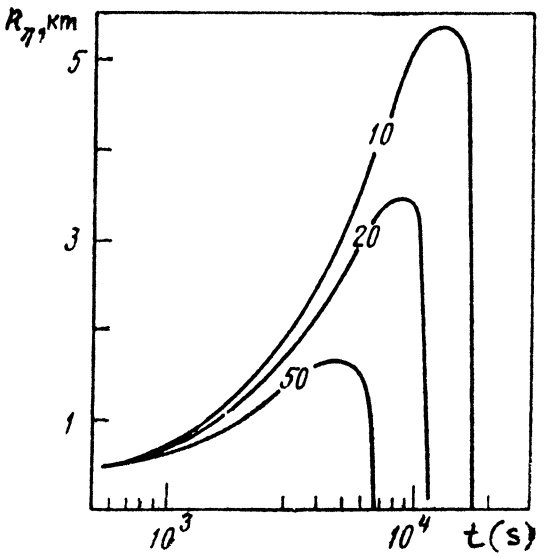

Fig. 10. Time variation of the radius of the ozone tunnel R_η at the height 24 km (decrease in ozone concentration within the tunnel is 50, 20, and 10% of the background one)

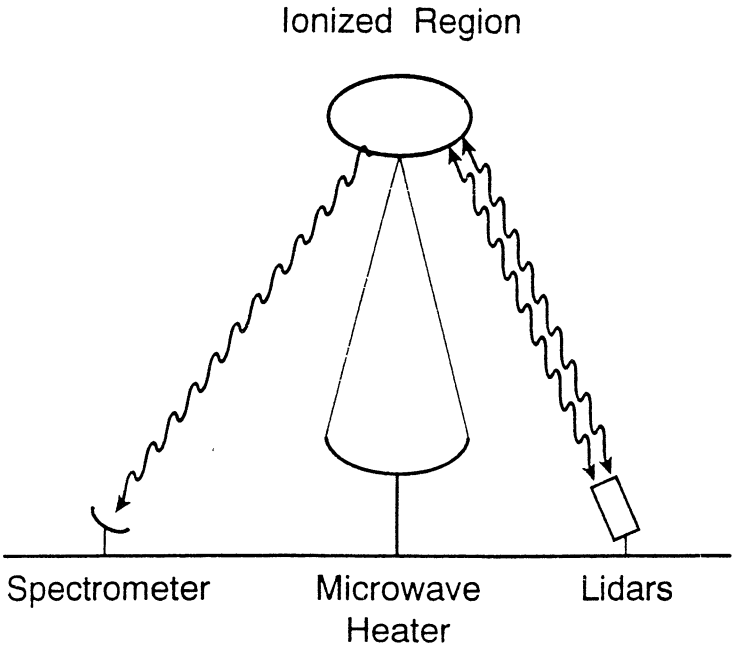

Fig. 11

The measuring technique is illustrated in Fig. 11. It relies on atmospheric breakdown by using a ground-based microwave transmitter. The wave beam is focused at the desired altitude. The ratio of the density of these active particles to the gas density can be measured by passive or active spectroscopy.

The ionization process in the breakdown region is accompanied by excitation of atoms by an electron impact. The density of the atoms in the excited j electronic state can be defined from the following ratios:

$$dN_{js}/dt = k_{js}N_e(t)N_e - N_{js}/\tau_{js} \tag{16}$$

$$N_e(t) = N_{eo} \cdot \exp(\nu_i t)\,, \tag{17}$$

where k_{js} is the excitation rate of the corresponding atom

$(k_{js} = f[f(v), \omega, P])$, τ_{js} is lifetime of the excited electronic state and $\nu_i = k_i \cdot N$ is ionization frequency. On the basis of these equations we find the number of photons P_{js}, connected with the excited electronic state. They are received by a telescope with area S located at distance H from the breakdown during microwave pulse τ.

$$P_{js}(\tau_U) = (k_{js}/k_i) \cdot (N_s/N) \cdot (S/4\pi H^2) \cdot (N_{em} \cdot V) \qquad (18)$$

where $N_{em} = N_e(t = \tau)$ is electron density created during the microwave pulse, V is volume of the AIL. This equation can be used for definig the value of (N_s/N) because the ratio (k_{js}/k_i) for $\omega > \nu$ is an easily defined value depending only on the oscillatory electron energy $\epsilon_\sim$ and the ratio of cross-sections for the excitation and ionization of molecules by an electron impact σ_{js}/σ_i [16,18,25].

Two different techniques for defining the particle density were considered in [18]. The first method is based on passive spectroscopy. It can be applied for the particles which allowed transitions in the atmospheric window. This method is based on the measurement the intensity of optical emission. By this method we can measure the density of molecules of Cl, ClO, CO, NO, H, N, O, F.

The second method is based on active lidar spectroscopy. It can be applied to particles having metastable states excited by electron impact. The number of metastables is measured by using two laser pulses with slightly different wavelength and comparing their attenuation (DIAL). The wavelength of the first laser is chosen to coincide with the strong absorption feature between metastable and allowed transition, located above the metastable electronic level. The wavelength of the second laser is detuned in the wing of the feature. This method can be applied for measuring the molecule density of CO, NO, OH, H.

The calculations made in [18] show that for the microwave radiation with $\lambda = 3$ cm, $P = 4$ GW, $\tau = 100$ ns, $F = 1$ kHz by a 34 m antenna the ratio N_s/N on the altitude $H = 50$ km can be defined:
1) for the first method $N_e/N \sim 10^{-11}$ would require $\sim 10^3$ pulses, which at $F = 10^3$ kHz corresponds to integration times of 1 s;
2) for the second method $N_s/N \sim 10^{-11}$ would require $\sim 10^4$–10^5

pulses, which at $F = 10^3$ kHz corresponds to integration times of 10–100 s.

5.4 The purification of the atmosphere

It is a well known fact that pollution of the atmosphere by chlorofluorocarbons (freons) leads to destruction of the ozone layer. So development of methods of air purification is very actual. In paper [19] the authors suggest the method of destruction of freons with the help of an AIL (of a freely localized discharge in the upper atmosphere). At present investigations of this problem have only started. Nevertheless, some results of the model experiments are quite interesting.

The suggested method of air purification is based on the process of dissociative attachment of electrons to molecules of freons, that leads to the destruction of freons.

$$CFCl_3 + e \rightarrow Cl^- + CFCl_2 \tag{19}$$

$$CF_2Cl_2 + e \rightarrow Cl^- + CF_2Cl \tag{20}$$

With a high probability the destruction of the molecules of freons in these processes is achieved by cold electrons.

The reason is that the cross-section of dissociative attachment of electrons to freons is maximum at low energies $\epsilon \sim 0,006$ eV. For an O_2 molecule it is not so, the cross-section of dissociative attachment has some energy threshold. Thus the AIL is used for creation of sufficiently high electron density in the atmosphere. And purification takes place in the decaying plasma after the microwave pulse. Evidently, the efficiency of purification is determined by the rate of plasma decay and is greater the longer the plasma lasts. In some model experiments the relaxation processes in the discharge plasma created by nanosecond microwave pulses were investigated.

5.4.1 Effect of slow plasma decay in nitrogen-oxygen mixture

The plasma decay of the nanosecond microwave discharge has interesting feature. Figure 12 represents the time dependence of the in-

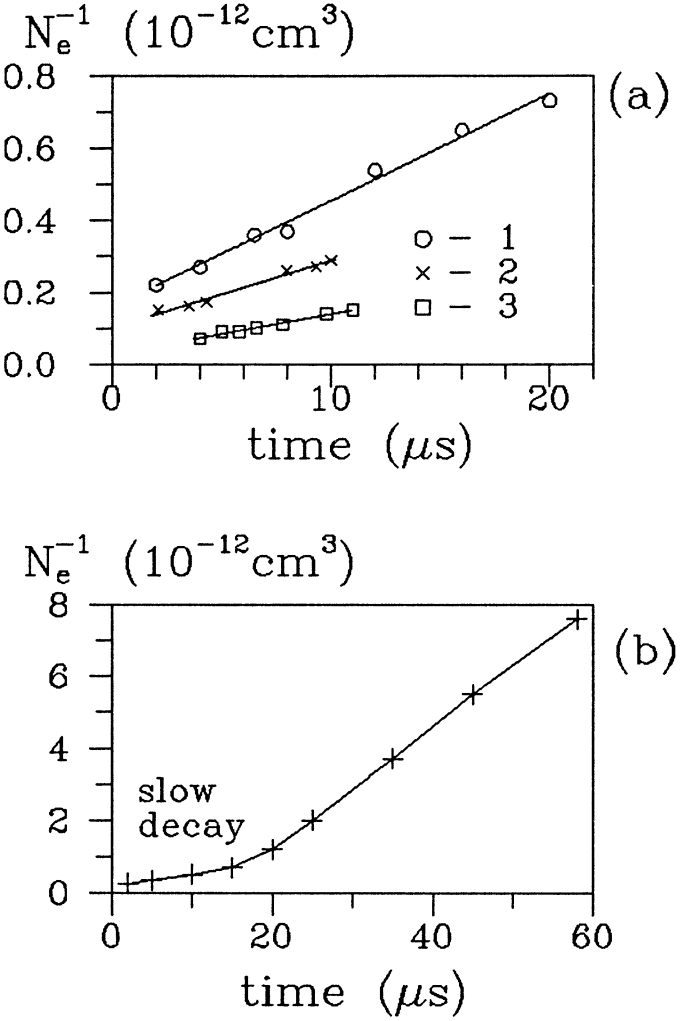

Fig. 12. Dependence of the inverse electron density N_e^{-1} on time at nitrogen pressures: a) 1–$p = 5 \cdot 10^{-2}$ Torr; 2–$p = 3 \cdot 10^{-1}$ Torr, 3–$6 \cdot 10^{-1}$ Torr; b) $p = 6 \cdot 10^{-1}$ Torr; •–experiment, curve 1–calculated data.

verse electron density at nitrogen pressure $p = 0,6$ Torr. The linear time of dependence N_e^{-1} testifies recombination plasma decay with low effective recombination coefficient $\alpha = 2 \cdot 10^{-8}$ cm^3/s. At longer times $t > 20$ μs the rate of decay changes and recombination coefficient equals $\alpha = 1,6 \cdot 10^{-7}$ cm^3/s. During the first ten microseconds after the pulse plasma decay is slow due to slow relaxation of high electron temperature. In their turn the basic factors determining the high temperature of electrons after the microwave pulse are:
1) energy transfer to electrons in their collisions with electronic excited metastable nitrogen molecules $N_2(A^3 \sum_U^+)$ and 2) electron-electron collisions. These processes are essential due to a large part of electronic excited nitrogen molecules and high level of gas ionization 10^{-4}–10^{-3}.

This conclusion is confirmed by the results of calculations. Numerical calculations of the Boltzmann equation for the electron energy distribution function in nitrogen plasma decay for the experimental conditions are carried out in paper [26]. They have shown that the electron energy distribution function has maximums at energies proportional to energy of excitation of the nitrogen electron level $A^3 \sum_U^+$ (6,17 ev). Thus, the rate of plasma decay after nanosecond microwave pulse is influenced by great share of fast electrons.

This experiment shows that the share of the electronic excited molecules in nanosecond discharge is great. The processes where excited molecules take part should be taken into account when calculating the regimes of AIL maintaining. It should be noted, however, that these experiments were performed at the specific energy depositions to the discharge equal to $\sim 10^{-2}$–10^{-1} J/cm^3, while at the creation of AIL they will be equal to $\sim 10^{-5}$–10^{-4} J/cm^3.

6 Conclusion

It is seen that AIL attracts our attention because of the number of problems which can be solved with its help. Therefore, at present the laboratory modeling of plasma chemical processes in microwave discharge created by nanosecond pulses with a high repetition frequency $F = 10^3$–10^4 Hz is actual.

Acknowledgements

This report is partially based on the project supported by the Russian Fund for Fundamental Investigations under contract No. 93-02-846.

References

1. Litvak A.G.,Proc.Intern.Workshop: Strong Microwave in Plasmas, Ed.A.G.Litvak, N.Novgorod: Inst.Applied Phys., 1991, 1, 267.
2. Vikharev A.L.,Gildenburg V.B.,Kim A.V.,Litvak A.G.,Semenov V.E In: High-Frequency Discharge in Wave Fields, Ed.A.G.Litvak, Gorky: Inst.Applied Phys., 1988, 41.
3. Gaponov A.V. et al.,Radiophys.Quantum Electron., 1967, 16, 794
4. Flyagin V.A. et al., IEEE Trans. Microwave Theory and Techn., 1977, 25, 514.
5. Gaponov-Grekhov A.V., Petelin M.I., Vestnik Akad. Nauk SSSR, 1979, 4, 11.
6. Bugaev S.P. et al., Radioengineering and Electronic, 1990, 35, 2346; Dokl. Akad. Nauk SSSR, 1988, 298, 92.
7. Belousov V.I., Bunkin B.V., Gaponov-Grekhov A.V. et al., Pis'ma v Zh.Tech.Fiz., 1978, 4, 1443.
8. Vikharev A.L.,Gildenburg V.B.,Ivanov O.A. et al., Fiz. Plazmy, 1986, 12, 1503 (Sov.J. Plasma Phys., 1986, 12, 870).
9. Sullivan C.A.,Destler W.W.,Rodgers J. et al., J.Applied Phys., 1988, 63, 5228.
10. Bunkin B.V., Gaponov-Grekhov A.V., Elchaninov A.S. et al., Pis'ma v Zh. Tech. Fiz., 1992, 18, 61.

11. Brizhinev M.P., Vikharev A.L., Golubyatnikov G.Yu. et al., Sov.Phys.JETF, Engl.Transl., 1990, 71, 242.
12. Vikharev A.L.., Proc. Intern. Workshop: Strong Microwave in Plasmas, Ed.A.G.Litvak, Nizhny Novgorod: Inst.Applied Phys., 1991, 1, 306.
13. Gildenburg V.B., Litvak A.G., In: Modification of Ionosphere by Powerful Radio Waves, USSR, Apatity, 1979, 65.
14. Gurevich A.V., Geomagnetizm and Aeronomy, 1979, 19, 633.
15. Gurevich A.V., Sov. Phys. Usp., Engl.Transl., 1980, 23, 862.
16. Gurevich A.V., Borisov N.D., Milikh G.M., Artificially ionized region in the atmosphere, Consultants Press, Boston, Mass., 1992, in press.
17. Vikharev A.L.,Gorbachev A.M.,Ivanov O.A. et al., Physics Letters A, 1993, 179, 122.
18. Papadopolous K., Milikh G.M., Ali A.W. et al., Remote spectroscopy of the atmosphere using microwave breakdown, in press.
19. Askaryan G.A.,Kossyi I.A. et al., Sov. J Plasma Phys., Engl. Transl., 1992, 18, 625.
20. Eliasson B. et.al., J. Phys.B: At.Mol.Phys., 1986, 19, 1241; J. Phys.D: Appl.Phys., 1987, 20, 1421.
21. Bykov Yu.V., Khimiya Vysokikh Energiy, 1984, 18, 347.
22. Aleksandrov N.L.et al.,Pis'ma v Zh.Tech.Fiz.,1990, 16, N4, 4.
23. Burdakov V.P., Elanskii N.F., Falin V.M., Vestn. Akad. Nauk SSSR, 1990, 12, 72.
24. Karol I.L., Ozolin Y.E., Rozanov E.V., Ann. Geophys. 1992, 10, 810.
25. Tsang K., Papadopoulos K., Drobot A. et al., Radio Science, 1991, 26, 1345.
26. Dyatko N.A., Kochetov I.V., Napartovich A.P., In: High-Frequency Discharge in Wave Fields, Ed.A.G.Litvak, Gorky: Inst.Applied Phys., 1988, 9.

MICROWAVE OR DC PLASMA CHEMICAL REACTOR?
State-of-the art.

Yu. A. Lebedev

Institute of Petrochem. Synthesis, Russian Acad. Sciences,
Moscow, 117071, RUSSIA

Introduction.

Last few decades are characterized by increased interest to the nonequilibrium low temperature gas discharge plasma which due to it's unique properties can be effectively used for generation of the active medium in the gas discharge lasers, light sources, and in plasma chemistry (see e.g. [1-7]). Different types of electrical discharges have been used as plasma sources covering a wide frequency spectrum of the external plasma producing electric fields from DC up to the laser frequency, namely DC, low, radio, microwave and laser frequency discharges. Moreover, at any chosen frequency of external electric field it is possible to design, and by now exist, variety of plasma devices realized different principles of external field-plasma interaction. For instance the capacitive and inductive coupled plasmas or surface wave produced plasma are used in RF region. Waveguide, resonator, slow wave or surface wave produced plasma sources are known in microwave region.

All these give rise the questions: How does the properties of nonequilibrium plasma depend on the frequency of external electric field? What are the advantages or disadvantages of one method of plasma producing over the others for a certain application? Unfortunately the answers are not yet clear now and additional efforts are still necessary to solve these problems.

Here we will present our point of view on these problems based on the experience in the field of experimental and theoretical investigations of nonequilibrium plasma properties in different types of electrical discharges at reduced pressures. Our intention will be emphasized on the properties of self-sustained microwave

and DC plasmas.

This choosing can be explained by the next reasons.

First, why did we choose microwave plasma? The microwave induced plasma (MIP) is the youngest and the less investigated type of plasma. It is interesting to know the correlations of their properties and those of the other plasmas. Moreover, at present time one can see an increasing interest to the application of MIP due to some of it's attractive features which will be described later.

Secondly, why did we choose the direct current plasma (DCP)? It is clear, that now this type of plasma is the most investigated. For example, the most of the known rate constants for plasma processes were measured or calculated under the condition of direct current plasma. It is important to know: is it possible to use these data in the other type of plasmas? If it is so, how can one do it?

We will consider the plasmas generated by the electric fields with frequencies lying in the opposite parts of the frequency scale: the frequency equal to zero and that which is much grater than the frequency of electron-heavy particle collisions. This is why we can propose the both type of plasmas as time independent and thus we avoid the difficulties of time averaging of plasma parameters, as it is necessary for comparing with RF plasma properties.

This paper will be organized as follows. First we will give the brief review on the problem of comparative study of plasma chemical activities of different plasmas. Then we will consider: the principles of plasmas comparison; the main differences in plasma quantities which can influence on the chemical activity of plasmas; the properties which are close the same in different plasmas and which define the chemical activity of nonequilibrium plasmas. For the end, the factors will be presented which must by taken into account before the choosing of plasma generator.

Plasma Chemical Activity.

Plasma chemical activity is the ability of plasmas for the purposeful influence on the initial chemical composition or on the treated substrates. The comparative characterization of different plasmas have been considered in a numerous publications (see, e.g. [3-6]) and here we will review the several of them only. Up to now the highest chemical activity of MIP is the most widespread point

of view.

Apparently, the paper of McCarthy [8] was the first, where this statement was formulated. The concentrations of atoms and radicals in MIP have been measured in MIP in different gases. From the comparison with the known literature data it was concluded that concentrations of these chemical active particles in MIP much more (more than the order of magnitude) than that in the other plasmas.

The next step on this way was made in [9] where on the basis of the analysis of literature data on the deposition processes was supported the highest efficiency of MIP. The results of calculations [10] was used for the physical explanation of this conclusion. Calculations was fulfilled for the argon gas and have shown that the high energy tail of the electron distribution function (EDF) increases with increasing the external electric field frequency ω keeping the same mean electron energy. This leads to the increased value of the rate constants of the electron impact processes and, hence, to the higher chemical activity.

The highest chemical activity of MIP was supported in [11] on the basis of experiments with the microwave slow wave discharge device and capacitive coupled RF discharge.

The recent results obtained with the surface wave produced plasmas [12] have shown that the optimal frequency of external electric field ranged between 50 and 100MHz for the processes of plasma deposition and etching.

Anticipating the following consideration, our point of view can be formulated as follows: the chemical activity of different plasmas slightly depends on the method of plasma generation (or on the type of discharge) if one keep the same specific plasma absorbed power.

To solve the problem of chemical activity of different plasmas it is necessary to analyze the plasma properties which can influence on the chemical activity. The first question to be answered: what is the most convenient principle of different plasmas comparison?

Principles of plasmas comparison.

By the present time there has been a vast literature concerning the comparison of plasmas and choosing of invariant group of parameters (see e.g. [13-19]). It is clear, that any of plasma characteristics (the electron and excited particles concentrations, the intensities of excited particles emission, the

mean electron energy, the energy absorbed by the unit of plasma volume, or the energy absorbed per electron or per heavy particle, the rates of excitations, etching, polymerizations, etc) can be used as the invariants of comparison. Correlations between properties of different plasmas directly related with the invariant chosen (see e.g.[6,17,18]).

Similarity theory could be considered as the basis of invariants choosing, if were not a serious limitations of its application. The characteristic feature of similar discharges is the same velocity distributions of particles in the similar spots of plasmas. This means the same internal structures of compared plasmas, the same gas and wall temperatures. The discharge vessels must have the same shape and must be manufactured from the same material [14,15]. The wall temperature is a very important factor because it defines both the gas temperature (and temperature profile [19]) and the physico-chemical characteristics of the wall surface. The latter define the coefficients of recombinations, attachment, and accommodation of plasma particles.

If there are neither limiting factors one must prefer the set of known similarity parameters such as E\N, ω\N etc (there E is the external electric field strength, ω is the frequency of this field, N is the heavy particle concentration) which must generalize and simplify the description of discharges. The reduced electric field E\N are widely used for parameterization of DC plasma both in theoretical and experimental studies.

There are the serious limitations of the similarity theory. The main limiting factor for the gas discharge of one type (in this case the similarity theory transforms to the scaling of discharge is the presence of the forbidden plasma processes which disturb the similar transformation of the collision integrals of the electron Boltzmann equation [13-15]. The analysis fulfilled in [14] for the electron-heavy particle collisions can be extended to the general case of plasmas with chemical reactions [20] and resulted list of the forbidden and permitted processes are shown below.

It can be seen that the forbidden processes include the interactions which always exist in the real plasma. The main of them are the superelastic collisions, the electron-electron interactions, reactions of the particles generated in plasma (reactions of excited atoms and molecules, radicals, atoms, ions, ion-radicals, formation of complex ions, etc). This means that the

application of the similarity theory must be substantiated in each case even for the discharge of the chosen type (DC, RF, or MIP).

Table 1.Permitted and forbidden plasma processes for the scaling

a) gas phase processes

permitted processes	forbidden processes
- direct interactions of electrons with the initial ground state atoms/molecules (direct ionization, excitation, dissociation, etc)	- stepwise processes with the exception of the electron collisions with the excited particles being in the equilibrium with electrons (saturation)
- radiative and dissociative attachment of electrons	- three particles electron attachment
- electron detachment under the collision of the negative ion with neutral particles	- electron detachment initiated by the electron impact - photo detachment
- ion-ion recombination under the high pressures	- ion-ion recombination with the exception of recombination under the high pressures
- drift and diffusion of the charged particles formed in the direct processes	- drift and diffusion of the charged particles formed in the stepwise processes
- stepwise processes of electrons with particles being in equilibrium with electrons (concentration of saturation)	- dielectron collisions - superelastic collisions - electron-ion recombination
- charge transfer in the collisions of the fast ions with the slow neutrals	- charge transfer in the collisions of the slow ions with the fast neutrals
- charge transfer between different particles if ionization potential of neutrals is less than the energy released in this process	- charge transfer between different particles if ionization potential of neutrals is higher than the energy released in this process
- Penning processes	- photo processes

a) gas phase processes (continue)

permitted processes	forbidden processes
- reactions of primary ions, radicals, atoms with the initial reagents, and reactions of metastables being in the equilibrium with electrons (concentration of saturation) - diffusion of the reaction products formed by the electron impact and disappeared in the interactions with molecules or through diffusion - three particle reactions of the initial reagents stimulated by the gas heating	- two-particle reactions of reagents if both of them are formed in plasma with the exception of metastables being in equilibrium with electrons (concentration of saturation) - three-particle reactions of the plasma products

b) surface processes

permitted processes	forbidden processes
- secondary electron emission under the electron impact, nonresonant photons, fast neutrals and ions, and metastables being the product of the primary reactions	- electron emission under the action of fast ions formed in the charge transfer and under the action of the self-absorbed photons
- processes of etching, polymerization, modification, rates of which are proportional to the flux of primary reactions	- chemical processes depending on the flux of the secondary plasma products (the complex ions, macroparticles, etc)
-chemical reactions initiated by the nonresonant photons	-chemical reactions initiated by radiation with self-absorbtion

Another limiting factors appeared if one compare discharges of different types. First of them is the known differences in the spatial structures of discharges (see e.g.[18]). This fact was illustrated, for example, by the optical measurements in DC and slow wave produced discharges [21]. It was shown that in DC plasma the radial distributions of the emission intensity have a maximum in the axis while in RF plasma that distribution more flatter or depleted in the axial region in MIP. In the latter cases the shape of distributions depends on the gas pressure, the frequency of electric field, and the discharge radius.

The spatial distributions of MIP parameters depend also on the electrodynamic characteristics of the plasma device used. Fig.1 shows the radial dependencies of emission intensity of argon line in MIP produced in adjustable length rectangular microwave cavity [22]. It can be seen that the radial profile of emissivity can be effectively varied by the changing of the cavity length.

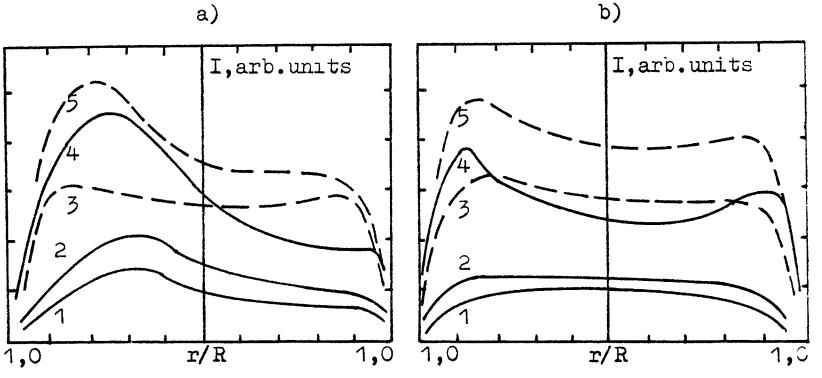

Fig.1. The radial distributions of emission intensity of Ar(6965Å) in MIP in the mixture Ar+1%CH_4 in the direction if the incident power (Fig 1a) and in the transversal direction (Fig.1b). Gas pressure 2,8Torr. Plasma absorbed power, W: 0,85 (curve 1), 1,35 (curve 2) 6,45 (curve 3), 5,2 (curve 4), 9,0 (curve 5). Cavity length, cm: 7 (curves 1,2,4), 12 (curves 3,5).

The next limiting factor is the differences in the equations describing the plasmas (e.g. the Boltzmann equations for DC and microwave fields, etc).

All these make it difficult to apply the similarity theory to the problem of comparative investigation of different discharges. Owing to limitations of the similarity theory, the similarity parameters do not posses any priority over the other ones.

Following the tradition and by analogy with DC plasma, reduced electric field E\N is used for parameterization of RF and microwave plasmas, where E value is substituted by the known effective electric field E_{ef}. The term "effective" have not a single meaning up to now (see e.g [20]). In contrast to DC case, it includes the effective electron-heavy particle collision frequency in addition to electric field strength. This effective frequencies be defined by the different manners. So to compare the results of different authors using effective reduced field, it is necessary to know the rules of E_{ef} calculations. Note that E_{ef} value can not be measured directly, as distinct from the electric field in DC case.

Some advantages have the energetic parameterization of plasmas using the absorbed power per unit of volume P_{ab}, or the absorbed power per one electron $\theta=P_{ab}/n_e$:

-P_{ab} and θ have a single physical interpretation;

-P_{ab} and θ can be measured or calculated for any type of gas discharge plasmas.

The next set of external discharge parameters is, to our opinion, the most convenient for the purposes of plasmas comparison [17-19]:

-the absorbed powers per unit of volume (P_{ab});

-the gas pressure (p) and initial gas composition;

-the wall temperature (T_w);

-the dimensions of plasma container (e.g. tube radius).

General approach to the differences in the DC plasma and MIP.

To analyze the properties of different plasmas first we will examine the electron distribution functions in DCP and MIP. This is necessitated by the role of the electron gas in the initiating of plasma processes (ionization, dissociation, etc) and in the redistribution of the external energy between the internal degrees of freedom of the heavy particles.

At present it is possible to formulate the general conformity to natural laws describing the differences of EDFs in DCP and MIP.

Self- consistent modelling, the numerical and analytical solutions of the electron Boltzmann equation [17-19, 23-25] have shown that there are the major parameter defining the characteristic feature of EDFs in both plasmas. This parameter is the shape (the energetic dependence) of the electron-heavy particle momentum transfer cross-section $\sigma_{tr}(\varepsilon)$. Another factor determining the correlation between parameters of different plasmas is a chosen invariant of comparison.

Some results of self-consistent modelling of DCP and MIP in the model gases differed in $\sigma_{tr}(\varepsilon)$ are shown in Fig.2. The ratio of EDF in MIP to that in DCP are drawn under the same mean electron energies. The case $\sigma_{tr}(\varepsilon)=\text{const}\ \varepsilon^{-1/2}$ corresponds to the known condition of the "direct-current analogy". It is the only case when EDFs in both plasmas are equal.

For $\sigma_{tr}(\varepsilon)$ varied with ε slowly than $\varepsilon^{-1/2}$, EDF in MIP is enriched in fast electrons compared with DCP, while for the rapid dependence of $\sigma_{tr}(\varepsilon)$ on ε it is depleted in fast electrons. These differences are decreased by the superelastic collisions in the high energy region of EDFs (curves 1,3).

All these are in a good agreement with results of the analytical approach [17,25]. The high energy tails of EDFs can be expressed as:

$$\text{MIP:}\quad f(\varepsilon) \to \exp\left[-\int_{u_\alpha^j}^{\varepsilon}\left(\frac{3m\omega^2}{eE^2}\,\frac{1}{\varepsilon}\,\frac{\sigma_\Sigma}{\sigma_{tr}(\varepsilon)}\right)^{1/2}d\varepsilon\right], \qquad (1)$$

$$\text{DCP:}\quad f(\varepsilon) \to \exp\left[-\int_{u_\alpha^j}^{\varepsilon}\left(\frac{3N^2}{E^2}\,\sigma_\Sigma\sigma_{tr}(\varepsilon)\right)^{1/2}d\varepsilon\right], \qquad (2)$$

where σ_Σ is the total inelastic cross-section.

If we neglect the dependence of σ_Σ on ε, the ratio of EDF in MIP to that in DCP can be written as

$$f^{MIP}(\varepsilon)/f^{DCP}(\varepsilon) = \exp\left[\pm\text{const}\cdot\varepsilon/U_j\right], \qquad (3)$$

where the plus sign refers to $\sigma_{tr}(\varepsilon)=\text{const}$ and the minus sign to $\sigma_{tr}(\varepsilon)=\text{const}\cdot\varepsilon^{-1}$. This agrees qualitative with the curves drawn in Fig.2.

The considered condition of the equal mean electron energies in different plasmas is a case of a special interest. Actually,

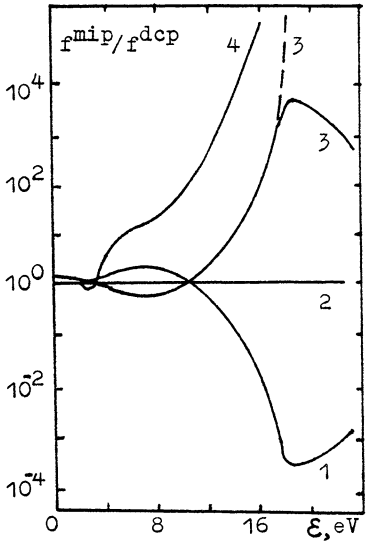

Fig.2. The ratio of EDFs in MIP and DCP at equal values of the mean electron energies. $\sigma_{tr}(\varepsilon), 10^{-16}$ cm^2: ε^{-1} (curve 1), $\varepsilon^{-1/2}$ (curve 2), const (curve 3,3'), CO_2 (curve 4). Curve 4 calculated neglecting the superelastic collisions.

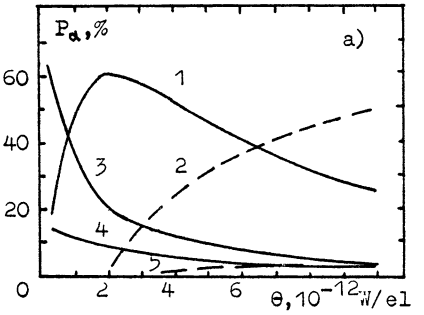

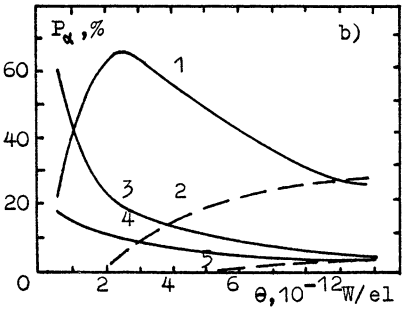

Fig.3. The fractional energy losses of electrons, transmitted to the vibration excitation of CO_2 molecule in DCP (a) and MIP (b) at pressure 1Torr, T_g=1000K. Curve 1 - $CO_2(00^01)$, 2 - $CO_2(\Sigma n1^10, n>2)$, 3 - $CO_2(01^10)$, 4 - $CO_2(10^00 + 02^20)$, 5 - $CO_2(10^00)$.

this means the close similarity of the compared EDFs in the low energy part (Fig.2). For the atomic gas plasma, as a zero approximation (see below), this fact leads to the differences in the EDF's in the energetic region of inelastic collision and, hence, to the differences in P_{ab}.

For the molecular gas, where the main energy losses of electrons concentrated in the low energy part of EDF (vibration excitation), this condition is similar to the condition of the equal absorbed powers. Hence Fig.2 describes the behavior of EDFs in molecular gases under $P_{ab}^{DCP}=P_{ab}^{MIP}$. This is illustrated by the results of calculations for CO_2 plasmas [23] (curve 4 in Fig.2). The fractional losses of the electron energy in the processes of vibration and electronic excitations of CO_2 molecule in DCP and MIP are drawn in Fig 3,4.

It must be noted that the term "plasma of atomic gases" proposes the existence of the wide region of pure elastic scattering of electrons up to the threshold energy of the first excitation of atom. But in real plasma it is not the case. Large densities of excited atoms increase the role of stepwise processes having the threshold energy in the region of atomic elastic scattering of electrons (the fractional losses of the energy in this processes can exceed 20% of the total absorbed powers). This means that plasma of atomic gases shows the properties of molecular gases. It must be taken into account before the using of the calculation results, especially of the numerical solution of Boltzmann equation, in the analysis of experiments.

The knowledge of $\sigma_{tr}(\varepsilon)$ allows not only define the comparative behavior of EDFs in MIP and DCP but also imagine the character of influence of elementary processes on such a behavior.

Let us analyze the role of electron-electron collisions which are very important for the atomic gas plasmas especially for the gases having the Ramsauer minimum in $\sigma_{tr}(\varepsilon)$. Fig.5 presents the typical plot of EDFs in the cases $\omega=0$ and $\omega>\nu_{tr}$ (where ν_{tr} is the momentum transfer electron-heavy particles collision frequency). Assuming the power law energy dependence of $\sigma_{tr}(\varepsilon)\sim\varepsilon^{-n}$, the curve 1 corresponds to the case $\omega>\nu_{tr}$ for $n<1/2$ or to the case $\omega=0$ for $n>1/2$; curve 2 corresponds to the case $\omega=0$ for $n<1/2$ or to the case $\omega>\nu_{tr}$ for $n>1/2$ [17]. Supposing the electron-electron collisions as a main process of energy transfer, it is possible to consider the changing in EDFs in general case.

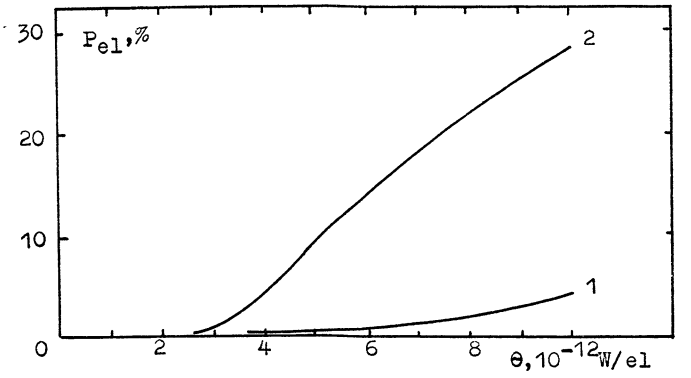

Fig.4. The total fractional energy losses of electrons transmitted to the electronic excitation of CO_2 in DCP (curve 1) and MIP (curve 2).

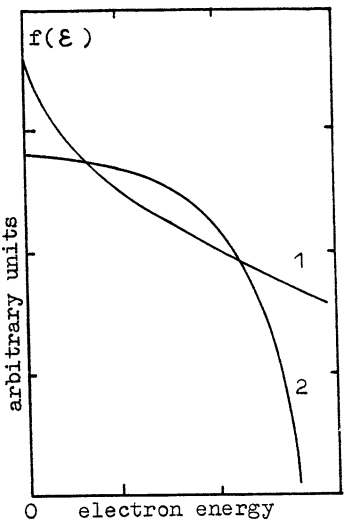

Fig.5. The typical plot of EDFs in nonequilibrium plasmas for different shapes of momentum transfer cross-sections $\sigma_{tr}(\varepsilon) \sim \varepsilon^{-n}$. Curve 1 corresponds to the cases $\omega > \nu_{tr}$ and $n < 1/2$ or $\omega = 0$ and $n > 1/2$. Curve 2 corresponds to the cases $\omega > \nu_{tr}$ and $n > 1/2$ or $\omega = 0$ and $n < 1/2$.

The curves in Fig.5 can be presented as a superposition of Maxwellian EDFs with the electron temperature $T_e=-(d\ln f(\varepsilon)/d\varepsilon)^{-1}$ corresponding to each group of electrons with energy in the interval $(\varepsilon, \varepsilon+d\varepsilon)$. It can be seen what for the curve 1 the temperature rises with increasing ε, whereas for the curve 2 it falls. Thus the interaction of different groups of electrons produces the average energy flux from the high- to low-energy region for the curve 1, but from the low- to high-energy region for the curve 2. This means the increase of mean electron energy with increasing the degree of ionization for curve 1, while for the curve 2 it decreases. These are in a qualitative agreement with the results of numerical calculations for argon [24] where curve 1 and curve 2 corresponds to the MIP and DCP, correspondingly.

This analysis can be easily extended to the changing in the high energy region of EDFs and for the superelastic collisions.

All parameters of self-sustained plasmas are self- consistent. Hence the changing of one of them leads to the changing of the other ones. This fact as well as the role of the invariant of comparison chosen is clear from the Tables 2,3,4 [30].

Table 2. Comparison of MIP and DCP properties for the same $\bar{\varepsilon}$

σ_{tr}, $10^{-16}cm^2$	$\bar{\varepsilon}$, eV		$n_e, 10^{11}cm^{-3}$		$N^*, 10^{11}cm^{-3}$		$P_{ab}, W/cm^3$	
	DCP	MIP	DCP	MIP	DCP	MIP	DCP	MIP
2.0	4.6	4.5	0.02	7.9	1.4	2.0	0.001	1.6
$2\cdot\varepsilon^{-1/2}$	4.6	4.7	2.8	1.2	2.7	2.8	0.3	0.3
$100\cdot\varepsilon^{-1}$	4.3	4.25	25	0.064	1.8	2.0	2.0	0.01

Table 3.Comparison of MIP and DCP properties for the same n_e.

σ_{tr}, $10^{-16}cm^2$	$\bar{\varepsilon}$, eV		$n_e, 10^{11}cm^{-3}$		$N^*, 10^{11}cm^{-3}$		$P_{ab}, W/cm^3$	
	DCP	MIP	DCP	MIP	DCP	MIP	DCP	MIP
2.0	5.1	4.0	1.1	1.07	3.5	2.4	0.15	0.2
$20\cdot\varepsilon^{-1}$	3.8	5.2	0.97	1.0	2.5	3.2	0.075	0.3
$200\cdot\varepsilon^{-2}$	2.8	5.9	1.0	1.05	1.7	3.5	0.04	0.35

Table 4. Comparison of MIP and DCP parameters for the same $P_{ab}=0.3W/cm^{-3}$.

σ_{tr}, $10^{-16}cm^2$	$\bar{\varepsilon}$, eV		n_e, $10^{11}cm^{-3}$		N^*, $10^{11}cm^{-3}$	
	DCP	MIP	DCP	MIP	DCP	MIP
2.0	5.2	4.1	1.4	2.5	4.7	1.8
$20\cdot\varepsilon^{-1}$	4.0	5.2	3.7	1.0	2.2	3.2
$200\cdot\varepsilon^{-2}$	3.2	5.9	6.6	0.85	1.5	3.7
argon	6.0	3.1	1.4	2.5	4.7	1.8

The results described above on the role of the momentum transfer cross-section on the differences in EDFs in MIP and DCP are in a good agreement with the results of measurements of EDFs using Langmuir probe method [26-29].

On the similar behavior of different plasmas.

Let us now analyze the following question. Are there any plasma quantities which are equal in MIP and DCP?

Although follow the previous consideration one must make a conclusion that each of individual parameters of MIP and DCP are different in general case, we can give an affirmative answer on the question. Such quantities are the power consumptions of the power-capacious processes P_α (the processes occurring with high fraction of the total absorbed power) at the same P_{ab}, gas pressure, radius and wall temperature [18,19]. This result was substantiated by the self-consistent calculations for different model gases, covering the atomic and molecular plasmas.

Neglecting the superelastic collisions, the power consumption P_α can be determined by the expression

$$P_\alpha=n_e N_M k_\alpha u_\alpha, \qquad (4)$$

where u_α is the threshold energy of the α-th inelastic process. k_α is the rate constant of this process, N_M is the density of heavy particles taking part in the process. The first three parameters depends on the plasma conditions. The product of these parameters is just the rate of the α-th process. Thus the above statement about P_α can be reformulated as follows: the rates of the power-capacious processes are nearly equal in MIP and DCP for equal P_{ab}, p, R, T_w.

Plasma chemical activity does not defined by the individual

plasma parameters separately such as EDF, or the electron density, etc. It does not depends on the rate constants only but on the rates of the processes which are related with the partial power consumption on the certain processes (see eq.4). This means that we can reformulate the above statement again as follows: the plasma chemical activity of MIP and DCP are nearly equal for the power-capacious processes and for the chosen here principle of plasmas comparison.

Following the equality of the rates of the power-capacious processes in MIP and DCP, the rules can be defined that allow one to calculate the rate constants of such processes under the electron impact in plasmas of one type if these are known for another type. These rules for direct and stepwise processes are

$$k_\alpha^{MIP}(\text{dir.}) \simeq k_\alpha^{DCP}(\text{dir.})\left[n_e^{DCP}/n_e^{MIP}\right], \qquad (5)$$

$$k_\alpha^{MIP}(\text{step.}) \simeq k_\alpha^{DCP}(\text{step.})\left[n_e^{DCP}/n_e^{MIP}\right]\left[N_M^{DCP}/N_M^{MIP}\right]. \qquad (6)$$

The similar chemical behavior of nonequilibrium MIP and DCP was experimentally shown in [31]. Experiments were fulfilled with rectangular cavity type of microwave plasma device and positive column of DC discharge at pressures ranged between 2 and 10Torr in the mixtures of Ar and Ne with CH_4. The total absorbed powers were less than 10W. The plasma lengths and discharge tube radius were the same in both devices.

Gas chromatographic analysis of the gaseous components of the discharged mixtures have shown that the composition of the gaseous products were the same in DCP and MIP, as well as the dependencies of the product concentrations on the absorbed power and pressure, and the distributions of the products in the order of decreasing concentrations. Some examples are shown in Fig.6. The observed differences in the absolute values of some products can be attributed to the differences in the spatial structures of compared plasmas. This fact can be taken into account by the form-factor the which does not exceeds value of 3.

Conclusion.

The main results of this paper can be summarized as follows.

-All separately considered parameters of different plasmas (EDF, n_e, etc) are different in general case and the real display of this differences depends on the fundamental characteristic of plasma gas, namely on the shape of the momentum transfer electron-heavy

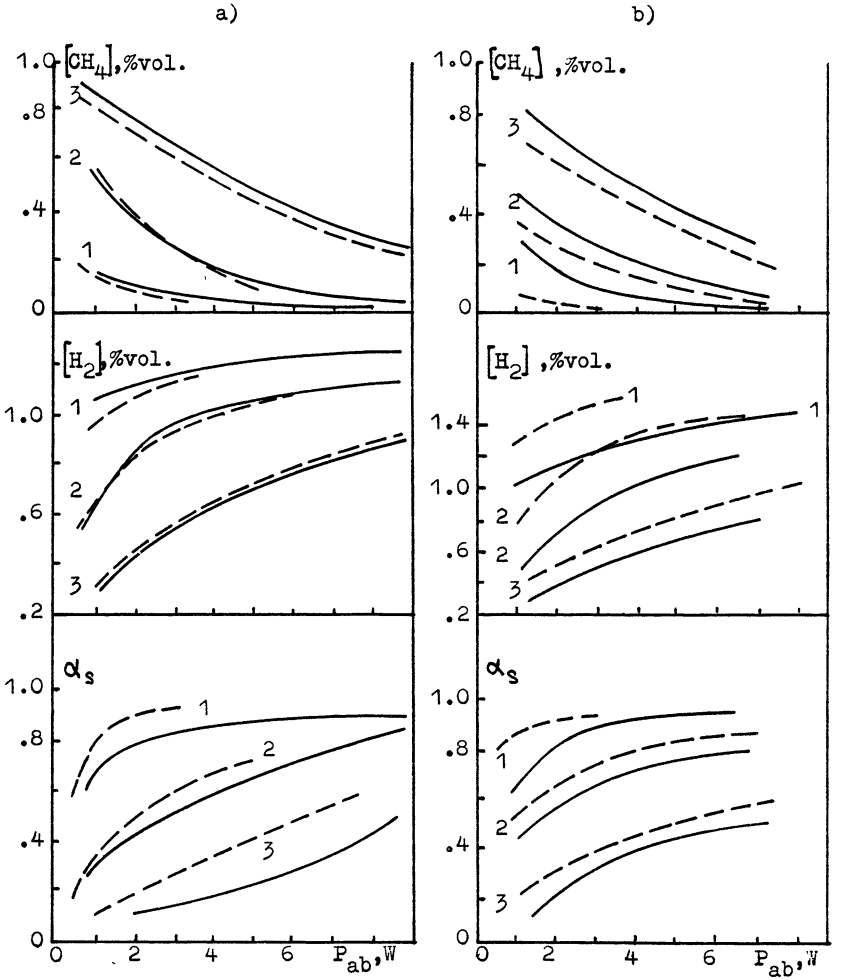

Fig.6. The concentrations of the main gaseous components (CH_4 and H_2) and extent of methane conversion in condensed phase (α_s) in MIP (solids) and DCP (dotted lines) in the initial mixtures Ar+1vol.%CH_4 (Fig.1a) and Ne+1vol.%CH_4 (Fig.1b). The gas pressures 2,8Torr (curves 1), 4,9Torr (curves 2), 8,4Torr (curves 3).

particle cross-section $\sigma_{tr}(\varepsilon)$. This gives the possibility to predict those differences a priori.

-The chemical activity of self-sustained quasi homogeneous DC and microwave plasmas slightly depends on the discharge used (i) under the same absorbed powers per unit of volume and (ii) if the energy capacious processes define the plasma chemical activity.

These conclusions were substantiated exactly for DC plasma and MIP. Analysis of the nature of the latter result (the law of the conservation of the energy) gives hope that it can be extended to the other self-sustained discharge plasmas (e.g., for the time averaged properties of RF plasma).

All our results can be attributed to the plasma region of discharges only. Before the choosing of the plasma generator it is necessary to analyze the secondary factors which are inherent to the different discharges (or to the construction of plasma devices) and can influence on their chemical activity. These factors are: the electrode (or substrate)-plasma sheaths, the double electrical layers near the jumps of the discharge tube dimensions, etc.

Moreover it is necessary to take into account the distinctive features of each discharges. For example, MIP gives evidence of some attractive properties:

-the simplicity of plasmas generation with the high levels of absorbed power ($>1 W/cm^3$);

-the wide region of operating pressures (from 10^{-5}Torr up to atmospheric pressure);

-the simplicity of control the internal structure of plasmas by means the changing of electrodynamic characteristics of microwave-plasma applicators;

-the possibility of plasmas generation both in the low and large volumes including the free space plasma;

-the developed family of the high effective MIP devices (waveguide, cavity, and slow wave plasma generators, surface wave produced plasmas, wave beam plasmas, microwave magnetized plasmas) permits to chose the necessary construction for any application.

References

1.Principles of Laser Plasma. Ed. by G. Bekefi. John Wiley & Sons Inc. N.Y., 1976.

2.The Applications of Plasmas to Chemical Processing. Ed. by R.F.Baddour and R.S.Timmins. MIT Press, Cambridge, Mass.,1967.

3.Technique and Applications of Plasma Chemistry. Ed. by J.R.Hollahan and A.T.Bell. A. Willey-Interscience Publ. N.Y., 1974.
4.Lebedev Yu.A., Polak L.S. High Energy Chem., 1979, 13, 331.
5.Rusanov V.D., Fridman A.A. Physics of Chemically Active Plasmas. Moscow, Publ.Comp."Nauka", 1984 (in Russian)
6.Chemistry of Plasmas. Ed. by L.S.Polak and Yu.A.Lebedev. Novosibirsk, Publ. Comp."Nauka", 199[illegible] (in Russian).
7. Wightman J.P. Proc. IEEE, 1974, 62, 4.
8. McCarthy R.L. J.Chem. Phys., 1954, 22, 1360.
9. Wertheimer M.R., Moisan M. J.Vac. Sci. Technol., 1985, 2643.
10. Ferreira C.M., Loureiro J. J.Phys.D: Appl.Phys., 1984, 17, 1175.
11. Wrobel A.M., Lamontagne B., Wertheumer M.R. Plasma Chem.& Plasma Proc., 1988, 8, 315.
12. Moisan M., Barbeau C., Claude R., et al. J. Vac. Sci. Technol., 1991, B9, 8.
13.Engel A. Ionized Gases. Oxford, Clarendon Press, 1955.
14.Fransis G. Handbuch der Physic. V.22, p.53, 1956.
15.Granovsky V.L. Electric Current in Gases. GITTL, p.298, 1952 (in Russian).
16.Ferreira C.M., Moisan M. Physica Scripta, 1988, 38. 382.
17.Karoulina E.V.,Lebedev Yu.A. J.Phys.D: Appl.Phys., 1988, 21,411.
18.Lebedev Yu.A. In "High Frequency Discharge in the Wave Fields" Ed. by E.Kogan, Samara, p.25, 1990 (in Russian).
19.Karoulina E.V., Lebedev Yu.A. J.Phys.D: Appl.Phys.,1992, 25, 401.
20.Lebedev Yu.A. Nonequilibrium plasmas of DC and microwave discharges: comparative aspects and similarity. Thesis D.Sc. 993. (Moscow).
21.Margot J., Moisan M., Ricard A. Appl.Spectroscopy, 1991, 45,260.
22.Lebedev Yu.A. Proc. VI Allunion Conf. on Low Temp. Plasma Phys., Leningrad, USSR, 1983, 2, 125.
23.Karoulina E.V., Lebedev Yu.A. Plasma Phys., 1988, 14, 1238.
24.Alexandrov D.I., Lebedev Yu.A. In "Physicochemical Processes in a Low-Temperature Plasma, ed. L.S.Polak. Moscow, Inst. of Petrochem. Synth., Acad. Sci. USSR. p.115 (1985) (in Russian)
25.Ivanov Yu.A., Lebedev Yu.A., Polak L.S. Plasma Phys.(Rus.). 1980, 6, 178.
26.Ivanov Yu.A., Lebedev Yu.A., Polak L.S. J.Techn. Phys., 1976, 46, 1459 (in Russian).

27.Ivanov Yu.A., Lebedev Yu.A., Polak L.S. Methods of Contact Diagnostics in Nonequilibrium Plasmachemistry. Moscow, "Nauka", 1981 (in Russian)
28.Ivanov Yu.A., Lebedev Yu.A., Polak L.S. Plasma Phys., 1976, 1, 871 (in Russian).
29.Ivanov Yu.A., Lebedev Yu.A., Polak L.S. Plasma Phys., 1977, 3, 146 (in Russian).
30.Karoulina E.V., Lebedev Yu.A. Proc. Seminar "Creation, investigation and application of plasma in microwave fields" 9-10 Sept.1987, p.6 (in Russian)
31.Gerasimov Yu.A., Gratchova T.A., Lebedev Yu.A. High Energy Chem. 1983, 17, 270; 1984, 18, 363.

GAS-DISCHARGE CLEANING OF ATMOSPHERE FROM CHLOROFLUOROCARBONS (CFC's) CONTAMINATIONS

G.A.ASKARYAN, G.M.BATANOV, S.I.GRITSININ,
E.G.KORCHAGINA, I.A.KOSSYI, A.A.MATVEYEV
A.V.SAPOZHNIKOV, V.P.SILAKOV, N.M.TARASOVA
General Physics Institute
Vavilova Street 38
117942, Moscow, Russia

I. Introduction

One of the most disastrous for the ozone layer effects resulting from the practical activities of mankind is a throw out of such chlorofluorocarbons as CF_2Cl_2, $CFCl_3$ and some others in the atmosphere. CFC's being chemically inert, pass through the troposphere and reach the altitudes of the ozone layer (H > 15-20km). At these altitudes CFC's molecules are destroyed by the solar ultraviolet radiation, forming chlorine radicals which annihilate ozone in multiple (up to 10^5 cycles) catalytic reactions of the type: $Cl + O_3 \Rightarrow ClO + O$; $ClO + O_2 \Rightarrow Cl + O$ (see, e.g. [1,2]).

CFC's can also essentially influence the heat balance of the Earth enhancing the greenhouse effect. Since one $CFCl_3$ or CF_2Cl_2-molecule acts as 10^4 CO_2-molecules in the nearest future the role of CFC's in the greenhouse effect is likely to be comparable with the carbon dioxide.

In discussing ways of ecological safety the basic measure is thought to be, as a rule, an absolute abandoning of CFC's utilized in technologies and everyday life (Montreal protocol 1987). However, even if complete stoppage of CFC's production is gained, that is unreal in itself, large amount of it were already thrown out into the atmosphere and they exist for many decades, slowly diffusing from the Earth surface to the stratosphere and polluting it (according to literature CFC-11 lifetime in the atmosphere is 75 years, CFC-12 lives for 111 years and CFC-13 for 90 years).

Mankind could escape the danger only it would succeed in finding and realizing ways of the environment cleaning from CFC's (a complete CFC content in the atmosphere amounts now to ~ 1 M tonne).

II. State of the problem

Two proposals on atmosphere cleaning and ozone-layer protection from CFC's are made by T.Stix [3,4] and A.Wong [5-7]. The first proposal is based on the resonance step-by-step CFC's-molecules excitation by CO_2-laser. It admits that the optical affect on CFC's should lead to the transition of vibrational excitation up the energy axis and result in molecule dissociation. In order to irradiate efficiently the atmosphere, the Earth pass of CO_2-laser rays is supposed to be prolonged thus producing a system of facing one another mirrors placed on the neighbor tops in mountains. The selectivity, i.e. ability to influence only CFC's without actually touching other air components, is an evident advantage of this method.

The concept of A.Wong involves realizing in the stratosphere or ionosphere the conditions in which atomic chlorine is efficiently converted into negatively charged ions (Cl^-) which do not actually take part in catalytic reactions of ozone destruction. Some particular schemes are considered. In the early paper [6] it is proposed to use a fairly weak microwave radiation which is to heat an electron component of a ionosphere plasma, the charge equilibrium being shifted towards the increase in Cl^- content. In the papers [5,7] the methods are considered of plasma production either by microwave radiation or by using corona discharge on board the plane or photo ionization on the surfaces placed in the atmosphere. The electrons in the plasma produced by any of these methods supposed to attach efficiently to Cl, removing it thus from the reactions destroying the ozone.

The above methods of environment cleaning from CFC's and their radicals are the first and apparently not completed attempts to solve a very complex problem. In e.g. laser method by T.Stix only those atmosphere regions may be cleaned which are located at relatively low altitudes and particular places on the Earth surface (valleys between the mountains, etc.). CO_2 -laser radiation losses via multiple mirrors are likely to cause essential difficulties. Also in a thorough and well elaborated method by A.Wong a number of problems arise. The ionosphere electrons are e.g. supposed to be heated at high altitudes ($H > 40$km) where the content of both ozone and CFC's is very small so that even a complete Cl conversion into Cl^- in this region practically does not influence neither the state of the ozone layer nor the CFC's diffusing from the low altitudes. It should be also noted that the authors of a recent paper [8] opposed the idea to shift the charge equilibrium of the plasma towards the increase in Cl^- density during the electron heating. Plasma production in the stratosphere or ionosphere is known to be very likely accompanied by production of the nitrogen oxides, which destroy

ozone in catalytic reactions [9-12].

It is thus evident that the problem of global environment cleaning from CFC's contaminations cannot be treated as finally solved new ways of removal either CFC's or products of their photo dissociation from the atmosphere are to be sought. Our paper is devoted to such a way which has not been discussed earlier before the appearance of our papers [13,14]. A new - gas discharge - method of atmosphere cleaning from CFC's is analyzed which together with a selective action on molecules (like in the papers by T.Stix) has an advantage of possible application at any given altitudes including the ozone layer itself and the lower regions of the atmosphere.

III. Gas-discharge method of atmosphere cleaning from CFC's

The method of atmosphere cleaning analyzed in the present paper is based on the gas-discharge decomposition of CFC's at low altitudes, in the troposphere (H < 10-15km), i.e. before they reach the ozone layer. A gas discharge excited by one or another method in a chosen free-space region efficiently destructs CFC's in the air region covered by the discharge, and the produced radicals are separated by the bulk particles and thrown down by rains. A step-by-step displacement of the discharge region involves the treating of large volumes of the atmosphere and can provide a global atmosphere cleaning.

This method differs from that considered by A.Wong et al sincethe discharge region is placed at low altitudes. It also differs from the method by T.Stix since it allows us to treat the entire troposphere region (from the sea level up to 10-15km) and thus to overcome completely the consequences of antropogenic activities.

Let us consider in detail the mentioned properties of the gas discharge freely localized in the atmosphere and analyze the engineering aspects of its realization.

Located in the gas-discharge region CFC's molecules, which are fairly chemically-stable, may be destroyed due to collisions with the electrons whose energy exceeds the energy of atomic coupling in the molecule (more than 3eV). The dissociation by direct electron impact occurs according to the scheme:

$$CF_2Cl_2 + e \Rightarrow CF_2Cl + Cl + e \quad (1)$$

$$CFCl_3 + e \Rightarrow CFCl_2 + Cl + e \quad (2)$$

etc. Since there are no literature data on the rate constants (k_d) for the processes (1) and (2) we shall give the upper limit of their values. With this aim in view let us use the data from Ref.[15] on the cross-sections of

fluorocarbon-compound dissociation (C_2F_6, CF_4, C_3F_8, ...) by an electron impact. The proposed principle of the upper limit estimation is governed by the behavior of such cross-sections depending on the electron energy and is based on the choice of the most high growth rates in the over the threshold region and the most large values of the maxima of the cross-sections. The calculations show that when $E_{eff}/n_m \leq 10^{-15}$ V cm^2 the values of k_{d1} and k_{d2} should not exceed the value 5.10^{-9} cm^3/s (E_{eff} is the effective electric field, n_m is the neutral density in air, k_{d1} and k_{d2} are rate constants for the processes (1) and (2) respectively).

Dissociation due to bombarding by fast electrons is the most evident but not a single and not the most efficient channel of CFC's destruction. According to analysis the process of dissociativeattachment may turn out to be a dominant process of CFC's decomposition. It occurs according to the scheme:

$$CF_2Cl_2 + e \Rightarrow CF_2Cl + Cl^- \quad (3)$$

$$CFCl_3 + e \Rightarrow CFCl_2 + Cl^- \quad (4)$$

etc. Note that CFC's behavior in reactions (3) and (4) is not trivial.Actually, according to [16,17] CFC-11 and CFC-12 being the most stable against chemical processes are at the same time the most "fragile" against the interaction with slow electrons. Fig.1 taken from [17] presents the $\sigma_D(\varepsilon_e)$ dependencies of the total cross-section of electron attachment to CFC's on the electron energy. Taking into consideration that the electron attachment to CFC's is mainly dissociative, we find for the maxwellian distribution:

1. At $T_e = 0{,}0207$eV (240K)
   $k_3 \equiv k_D^{(CFC\text{-}12)} = \langle \sigma_D^{(CFC\text{-}12)} v_e \rangle \cong 2{,}05.10^{-9}$ cm^3/s;
   $k_4 \equiv k_D^{(CFC\text{-}11)} = \langle \sigma_D^{(CFC\text{-}11)} v_e \rangle \cong 8{,}86.10^{-8}$ cm^3/s;
2. At $T = 0{,}25$eV
   $k_3 \equiv k_D^{(CFC\text{-}12)} \cong 1{,}85.10^{-9}$ cm^3/s;
   $k_4 \equiv k_D^{(CFC\text{-}11)} \cong 2{,}87.10^{-8}$ cm^3/s.

Such high rate constants of the processes, the electron energies being extremely low, are due to the fact that the energy of the electron-chlorine atom coupling exceeds the energy of CFC-molecule dissociation. This relationshipis converse for all the other molecules in the atmosphere and there exists an energy threshold for the cross-sections of the dissociative attachment [18]. This fact provides the selectivity of the processes of CFC-molecule dissociation in a cold and decaying gas discharge plasma.

In the gas discharges together with the above direct mechanisms for CFC's destruction the channels of indirect affects can also occur. CFC's destruction can be e.g. a result of the excitation of the metastable states of

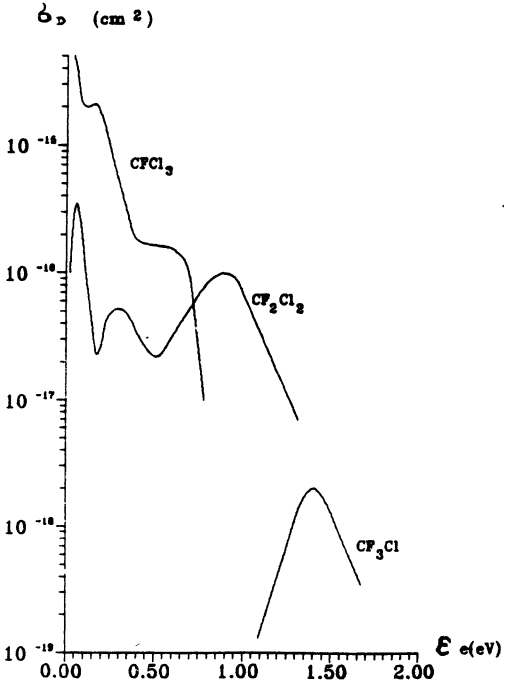

Fig.1.
The dependence of electron-CFC's attachment cross-section on the electron energy.

nitrogen and oxygen molecules and atoms followed by their interaction with CFC-molecules. And these channels of destruction may be fairly efficient. That is evident from the CFC-11 and CFC-12 interaction with the metastable states of oxygen atoms $O(^1D)$. In this case the rate constant of CFC's destruction is determined by gas-kinetic values: $(1\text{-}2).10^{-10}$ cm^3/s [19]. But the high rates of the excited O* suppression by N_2 and O_2 molecules prevents them from competition with the cold electrons of the plasma (as the estimates show it is so even in the case of the most stable atomic states $O(^1S)$). In connection with the above-said the electron excited molecules of O_2 ($a^1\Delta_g$, $v \geq 1$) and O_2 ($b^1\Sigma_g^+$) draw a special attention. The energy balance permits a possibility of CFC's destruction reactions with these molecules (e.g. the reaction $CF_2Cl_2 + O_2$ ($a^1\Delta_g$, $v \geq 1$; $b^1\Sigma_g^+$) $\Rightarrow CF_2Cl + ClO_2$). They are the most stable molecular excitations of the air [20] (this statement concerns first of all the state of O_2 ($a^1\Delta_g$)).

Unfortunately the building of a developed model describing the effect of a gas discharge on the CFC-component is complicated by the lack of literature data on the elementary processes which can contribute to the destruction of CFC's. Table 1 presents some reactions which are of interest but are not studied enough (or are not studied at all). One of the urgent physical problems for our purpose is to determine rate constants for the processes presented in the Table.

Table 1

Reactions №	Possible reactions of CFC's destruction in a low-temperature air plasma.
1	$CFCl_3 + e \Rightarrow CFCl_2 + Cl + e$
2	$CFCl_3^* + e \Rightarrow CFCl_2 + Cl + e$
3	$CFCl_3^* + e \Rightarrow CFCl_2 + Cl^-$
4	$CFCl_3 + O(^1S) \Rightarrow CFCl_2 + ClO$ $\Rightarrow COFCl + Cl2$ $\Rightarrow COCl2 + FCl$
5	$CFCl_3^* + O(^3P) \Rightarrow CFCl_2 + ClO$ $\Rightarrow COFCl + Cl2$ $\Rightarrow COCl2 + FCl$
6	$CFCl_3 + O_2$ (a, v > 1) $\Rightarrow CFCl_2 + ClO_2$
7	$CFCl_3 + O_2$(b) $\Rightarrow CFCl_2 + ClO_2$
8	$CFCl_3^* + O_2(X) \Rightarrow CFCl_2 + ClO_2$
9	$CF_2Cl_2 + e \Rightarrow CF_2Cl + Cl + e$
10	$CF_2Cl_2^* + e \Rightarrow CF_2Cl + Cl + e$
11	$CF_2Cl_2^* + e \Rightarrow CF_2Cl + Cl^-$
12	$CF_2Cl_2 + O(^1S) \Rightarrow CF_2Cl + ClO$ $\Rightarrow COF2 + Cl2$ $\Rightarrow COFCl + FCl$
13	$CF_2Cl_2^* + O(^3P) \Rightarrow CF_2Cl + ClO$ $\Rightarrow COF2 + Cl2$ $\Rightarrow COFCl + FCl$
14	$CF_2Cl_2 + O_2$(a, v > 1) $\Rightarrow CF_2Cl + ClO_2$
15	$CF_2Cl_2 + O_2$(b) $\Rightarrow CF_2Cl + ClO_2$
16	$CF_2Cl_2^* + O_2(X) \Rightarrow CF_2Cl + ClO_2$

It should be, however, noted that even several investigated channels of CFC-destruction may turn out to be enough to provide efficient (with the low energy cost) cleaning of the air treated by a gas discharge. And, as has been already mentioned, a primary attention is drawn to the dissociative electron attachment to CFC's. Taking into account that the cold electrons are the most likely to destroy CFC-molecules in the processes (3) and (4), the only role played by the source of electric fields generating a discharge may be the following: to produce a fairly high electron density in air and, possibly, to maintain a fairly low temperature of this plasma component between the ionizing pulses. CFC-dissociation occur mainly at the plasma decay stages

just between the discharges. It is evident that the efficiency of the air cleaning is the higher, the longer is the ionized state of the medium when it is not sustained by the electric fields.

Let us assume that the electron density in the ionizing pulse amounts to the value n_{em} which satisfies the relationship:

$$n_{em} >> n_{Fo} \qquad (5)$$

where n_{Fo} is the initial density of CFC-molecules. Let us also assume that the plasma decay occurs according to the recombination low (later on we shall consider the validity of such strong assumption). It is then easy to estimate the fraction of CFC's molecules destroyed through dissociative attachment after the ionizing pulse:

$$\eta_F \simeq 1 - (1 + \alpha_r n_{em} t)^{-\gamma}, \qquad (6)$$

where

$$\eta_F \equiv n_F / n_{Fo};\ n_F = n_{Fo} - n_F(t);\ \gamma = k_D^{(F)} / \alpha_r,$$

α_r - is the recombination coefficient of the electrons and positive ions of the plasma.

In the case when $n_{em} = 10^{12}$ cm^3 and $T_e = T_g = 240$ K (i.e. plasma decay occurs on the absence of the electric field and $\alpha_r \leq 2.10^{-7}$ cm^3 /s it turns out that in 100μs more than 70% of $CFCl_3$ molecules dissociate. For CFC-12 molecules such an effect is achievable in the regime of multi pulse discharge action on the medium. In the considered situation the number of discharge pulses repeating every 100μs should be equal to approximately 40. In the latter variant it is important that the number of ionizing pulses may be essential shortened by a slight heating of the electron component of the decaying plasma by an electric field with a very small amplitude. Actually, when e.g. $T_e \simeq 0{,}25$eV less than 10 pulses are required to destroy 70% of CF_2Cl_2 molecules (we assume in estimates that $\alpha_r \leq 3.10^{-8}$ cm^3/s).

The estimation of the energy costs during the gas-discharge atmosphere cleaning can be made in terms of the evident relationship:

$$q \geq 0{,}5\, \sigma \omega\, E_o^2\, \tau_E \ (J/cm^3), \qquad (7)$$

where s is the high-frequency conductivity of a gas-discharge plasma, E is the amplitude of the electric field providing the gas breakdown and confining the plasma during the time t required to destroy CFC's molecules. In the assumption of a decisive role played by a direct electron impact:

$$\tau_E \cong \tau_d \approx 1/k_d n_{em} \qquad (8)$$

And if the assumption turn out to be valid that the process of dissociative attachment is the main channel of CFC's destruction, then:

$$\tau_E \approx \tau_i, \qquad (9)$$

where τ_i is the characteristic time of the gas ionization.

It is easy to see that in the conditions of proposed realization of the

atmosphere gas discharge:

$$\tau_d >> \tau_i \qquad (10)$$

and, consequently, the energy costs for the air cleaning may be essentially lower than in the case when we assumed a decisive role of the dissociation by a direct electron impact.

Let us now consider again the problem of plasma decay after the pulsed gas discharge in air. It seems to consider naturally that in the case of air discharge plasma decay should be governed by the processes of electron attachment to the oxygen molecules. The attachment time [21]:

$$\tau_a \simeq 10^{31} / n_m^2 \qquad (11)$$

is fairly small (for $H \simeq 10$km $\tau_a \simeq 0{,}1\mu$s) and that limits the number of events of CFC molecule dissociation after each gas discharge. The recent experimental studies show, however, that actually the gas-discharge plasma decay in air is recombination in nature and occurs in the times exceeding essentially τ_a. According to [22-24] the efficient recombination constant amounts in this case to $\alpha_r \approx 10^{-7}$ cm^3. According to [25] the phenomenon of "non attachment" decay in the discharge is associated with the production of singlet oxygen participating actively in reactions of associative electron detachment from negative ions and thus providing compensation of the attachment mechanism for free-electron losses. It follows from the experiments on non-self-sustained microwave discharges in air [26] that the electron detachment from oxygen becomes already noticeable at the energy inputs of $\approx 10^{-3}$ J/cm^3. Hence the assumption is very likely that in the conditions of realization of the considered discharges freely localized in the troposphere the plasma is to decay according to the recombination (and not attachment) law.

IV. Scheme of realization of the gas-discharge method of global (local) troposphere cleaning from CFC's

Fig.2 presents some of the possible schemes of realization of discharges freely localized in the atmosphere. A gas discharge may be excited by high-power CO_2-lasers (see fig.2a). In this case the volume of a gas-discharge region is not large. But the efficiency of the method may be fairly high if a photo-ionized gas volume near the laser spark (so-called "halo") is cleaned. The occurrence and anomaly long lifetime of this halo was first observed in [27,28]. However, a detailed study of the structure and properties of a laser-produced discharge from the standpoint of gas-discharge air cleaning is to be done.

It is also possible to use various types of electrode discharges starting from

glow, brushing, strimer discharges up to the igh-current discharges in constant, pulsed or HF fields produced by the systems placed on the platforms attached to the balloons or situated on the flying vehicles (see Fig.2a). In the latter case the flying vehicle may be supplied by intense microwave beams for the sake of ecological purity.

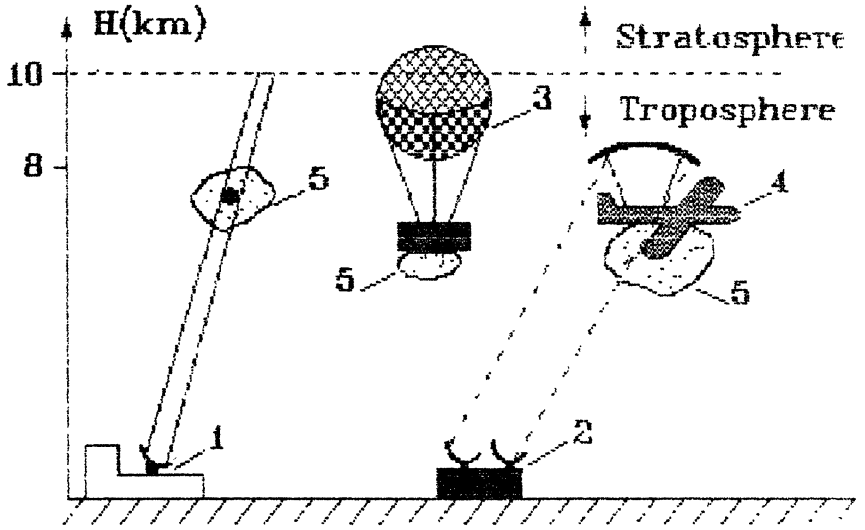

Fig.2.
The schemes of an environment cleaning by discharges localized in the troposphere.
a) 1 - powerful laser; 2 - microwave antennas; 3 - balloon; 4 - aircraft with microwave receiving antenna; 5 - gas-discharge.

However, the most promising of all the gas-discharge cleaning techniques seems to be the method based on the excitation of a freely localized discharge by intense microwave beams. Let us consider in detail this variant and mark two possible ways involving the Earth and space location of a microwave generator. The first one is presented in Fig.2b. Two (or more) Earth antennas produce inter crossing intense pulsed microwave beams focused at a given altitudes H. The radiation intensity in the intersection region should exceed the threshold intensity I for the microwave breakdown in air. An irradiation regime is possible in which a fixed space volume is treated while natural winds change continuously the air volumes treated by microwave discharge. Another scheme is also possible according to which the region of

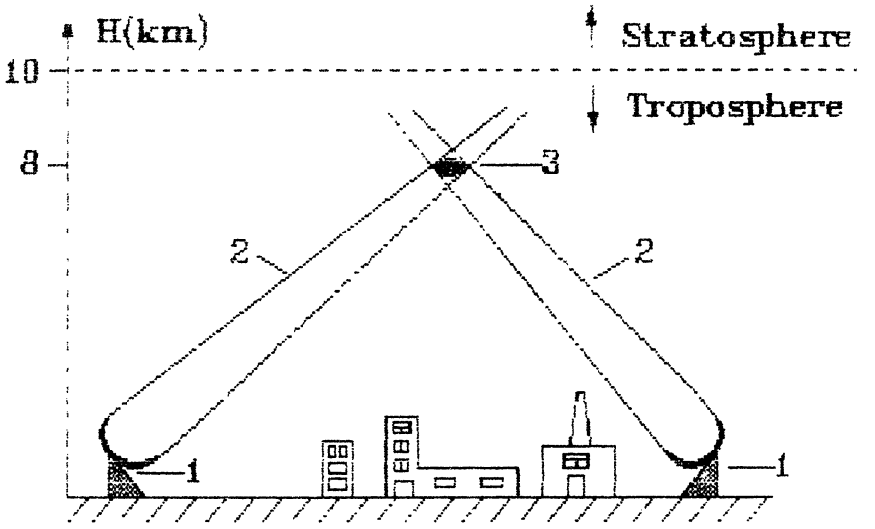

Fig.2.
b) 1 - ground-based microwave antennas; 2 - microwave beams; 3 - microwave discharge.

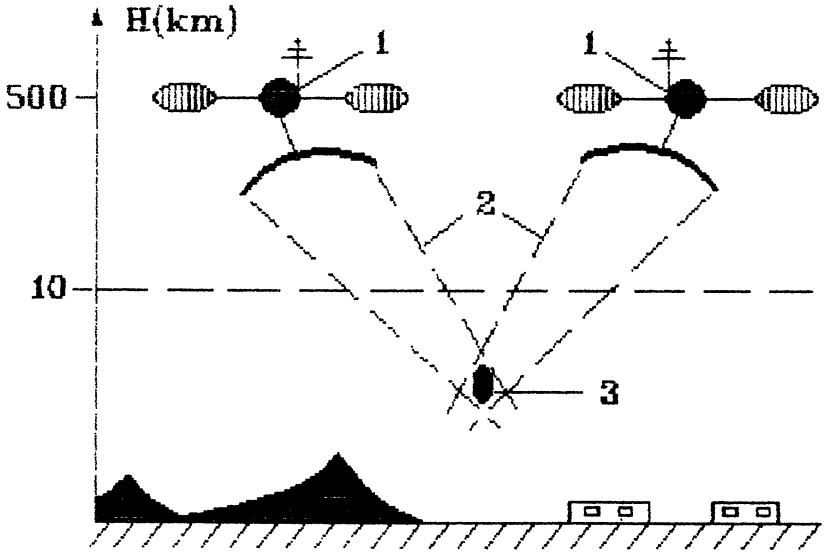

Fig.2.
c) 1 - satellites with microwave generators and antennas; 2 - microwave beams; 3 - microwave discharge.

beams intersection moves in space covering new and new gas volumes.

This system may be also based on the use of microwave beams generated and formed on space stations (see Fig.2c) [29]. One of the advantages of the space system is the possibility to include the problem of gas-discharge cleaning in the scope of space solar power stations [30] utilizing a "free of charge" energy of solar radiation. Furthermore the irradiation from top to bottom may turn out to be convenient providing the possibility to reveal simultaneously the atmosphere regions with an extra CFC's content (or with a low ozone content).

For both variants (from "top to bottom" and from "bottom to top") the problem of the thresholds for microwave breakdown in air is the primary one. The following relationship may be used to determine the thresholds:

$$E_{th} \simeq 32\ (n_m/2{,}67.10^{19})\ [2\ (1+\omega^2/\nu^2_{eff})\ ]^{1/2}\ V/cm \quad (12)$$

Here E_{th} is the amplitude of microwave electric field from the onset of which the air breakdown can be expected (the breakdown threshold); n_m is the molecule density at a given altitude H; ω is a cycle frequency of microwave radiation, ν_{eff} is the efficient frequency of electron-neutral collisions:

$$\nu_{eff} \cong 1{,}7.10^{-7}\ n_m \quad (13)$$

Expression like (12) is often used to estimate the amplitude of the threshold electric field. However, in a number of cases (see e.g. [21]) the multiplier (2) is omitted in this expression. The lack of this multiplier does not allow us to get a known value of the efficient threshold field: $E_{eff}^{(th)} \equiv E_{th} / [2\ (1 + \omega^2/\nu^2_{eff})\ ]^{1/2} \simeq 32$kV/cm, in particular in the case of an atmospheric pressure of the air.

Table 2 presents the results of calculations according to (12) of the threshold fields and corresponding intensities of microwave radiation with different wavelength and for different altitudes.

Table 2

H, km	n_m, 10^{19} cm^{-3}	$\lambda_f = 0{,}2$ cm		$\lambda_f = 0{,}8$ cm		$\lambda_f = 2$ cm		$\lambda_f = 5$ cm	
		E_{th} (kv/cm)	I_{th} (W/cm2)	E_{th}	I_{th}	E_{th}	I_{th}	E_{th}	I_{th}
5	1,52	27,42	10^6	25,87	$0{,}89.10^6$	25,78	$0{,}88.10^6$	25,77	$0{,}88.10^6$
10	0,86	17,34	4.10^5	14,76	$2{,}89.10^5$	14,61	$2{,}83.10^5$	14,58	$2{,}82.10^5$
15	0,4	11,59	$1{,}8.10^5$	7,17	$6{,}83.10^4$	6,84	$6{,}21.10^4$	6,79	$6{,}11.10^4$

The values of the quantities E_{th} and I_{th} correspond to quasi stationary microwave irradiation. In the case of pulse radiation (or fast beam scanning) the calculation of the threshold field incorporated the necessity to satisfy the

relationship:

$$\tau_f \geq \tau_i \ln (n_{em} / n_{e\,o}), \qquad (14)$$

where τ_f - is the microwave pulse duration and τ_i - is the characteristic ionization time determined from the relationship [21]:

$$\tau_i \simeq 2{,}0.10^{11} / n_m (E_o / E_{th})^{5,3} \qquad (15)$$

The electric fields required to initiate the discharge by microwave pulse are determined from condition (14) and may exceed by several-fold the threshold for the stationary breakdown.

Assuming the diameter of the Earth antenna to be d_a and the Gaussian beam to be axisymmetric we can find the beams diameter in the focus region using the estimation formula:

$$d_f \simeq 2\lambda_f H / \pi d_a \qquad (16)$$

and the caustic length l:

$$l_f \simeq \pi d_f^2 / \lambda_f \qquad (17)$$

When the radiating antenna is based in space at the altitude H_s and $H_s >> H$, the formulas (16) and (17) can be also used for determining d_f and l_f, then H should be changed for H_s.

If we choose $\lambda_f = 0{,}8$cm then, according to [16,17] at the altitude H = 10km the characteristic radius of the Gaussian beam in center is ≈ 100 cm and the caustic extent $l_f \simeq 400$m, the diameter of the Earth antenna being $d_a \simeq 50$m. In this case, according to Table 2 and relationship: $P_f = I_f \pi d_f^2/4$, (where I_f is the radiation intensity in the beam focus), the total pulse power of the microwave radiation required for an air breakdown at the altitude H = 10km should exceed 2,4GW. This power can be well provided by modern systems such as gyrotrons [31] and coaxial turned magnetrons in a centimeter range like МИ-389 [32], and also by relativistic microwaves generators [33].

Let us now estimate the energy costs (specific energy input) required for microwave gas-discharge cleaning of the medium. Assume that the wave discharge is maintained so that the electromagnetic energy coming to the intersection region is completely absorbed (to do this it is necessary, in addition to matching the parameters of separate beams, to provide the rate of discharge-region transportation in space). Let us take the assumption that the plasma decay mechanism is "recombination" in nature. The gas-discharge method was shown to provide practically complete CFC-11 destruction in a single-pulse irradiation regime. In this case the specific energy input is estimated from (7) with account for the relationship (9). Then using the equality (15) it is easy to get:

$$q \simeq 4{,}75.10^{-16} n_e (E_o / E_{th})^{-3,3} \ (J/cm^3) \qquad (18)$$

Assuming that the altitude, at which the microwave discharge is excited,

H = 10km we find for $E_o/E_{th} = 4$ and $n_{em} = 10^{12}\,cm^{-3}$:

$q \approx 5.10^{-6}\ J/cm^3$

(the multi-beam method of discharge initiation in air is likely to be the most reasonable variant for realization of these conditions).

The energy cost of destruction of one CFC molecule is:

$$\Delta\varepsilon = q / n_{Fo} \qquad (19)$$

In the considered case the value is: $\Delta\varepsilon_{CFC\text{-}11} \simeq 24keV/molec$ ($n_{Fo} \approx 1{,}3.10^9\,cm^{-3}$ [34]).

Assume that the total average power of microwave radiation applied for air cleaning amounts to p = 15,5GW. Then the productivity of irradiating system (i.e. the mass of CFC-11 decomposed in a time unit) is determined by the relationship:

$$dM / dt \simeq m_{CFC\text{-}11}\, n_{Fo}\, p / q \qquad (20)$$

($m_{CFC\text{-}11}$ - is the mass $CFCl_3$ molecule) and is equal:

$$dM/dt \simeq 30k\ tonne/year$$

In the case of air cleaning above the Europe the CFC-11 contamination may be removed completely from the atmosphere in a year (assuming that CFC-11 content above the Europe is ≈30k tonne).

The most important conclusions from the above analysis are the following:

i) the energy problem of the global troposphere cleaning from CFC's by microwave discharges may turn out to be far from unsolvable and ii) the modern engineering is able if not to realize the project but surely to provide long-scale natural experiments.

In discussing the usefulness of these experiments it should be kept in mind that together with the purely physical problems which can be solved with model laboratory setups and in terms of mathematical simulation, there are the problems associated with aerology, ecology and economy and their solution is required to take decision about the possibility of realizing the project of microwave cleaning. Among them there are e.g. the following problems:

— To draw a charts of CFC's distribution in the atmosphere and to find the "stagnant" regions, the channels of overflow from one region to another (e.g. from the above Antarctic region to that above the Australia, etc). This charts allow us to make more real estimations concerning the prospects of this method to be a global one;

— To estimate the admission - from the standpoint of ecology - of powerful sources of microwave radiation, especially in the case of space location;

— To study of channels of removal of the CFC's destruction products from the atmosphere in real conditions, etc.

Among the most urgent problems there is a problem of ecological safety of the products of plasma-chemical reactions in microwave discharges. It is necessary e.g. to take into account that while cleaning the atmosphere from CFC's, the microwave discharge may at the same time be a source of NO_x-contamination. Reaching the stratosphere the nitrogen oxides can also destroy the ozone layer (the same as chlorine but less efficiently). Some papers [9-12, 35-39] show the dangerous consequences of microwave discharges excited directly in the stratosphere. When, however, the discharge is initiated in the troposphere and the air irradiation time is short the ecological danger is much lower. That is e.g. illustrated by calculations carried out in terms of mathematical model described in [40]. Fig.3 presents the characteristic calculation results for the discharge initiated at the altitude H = 10km with a wavelength $\lambda_f = 0{,}8$cm, pulse duration $\tau_f = 1{,}7.10^{-8}$ s and $E_o/E_{th} = 2$. The calculations show that the cost of nitrogen oxide production in the discharge amounts to approximately 100eV/molec. In this case it is easy to see that the number of NO_x (NO_2, NO, etc.) molecules occurring in the atmosphere as a result of the discharge amount to approximately 10% of the antropogenic income related to the fuel burning, effluent from the powerful electric stations, air transport and cars, etc.

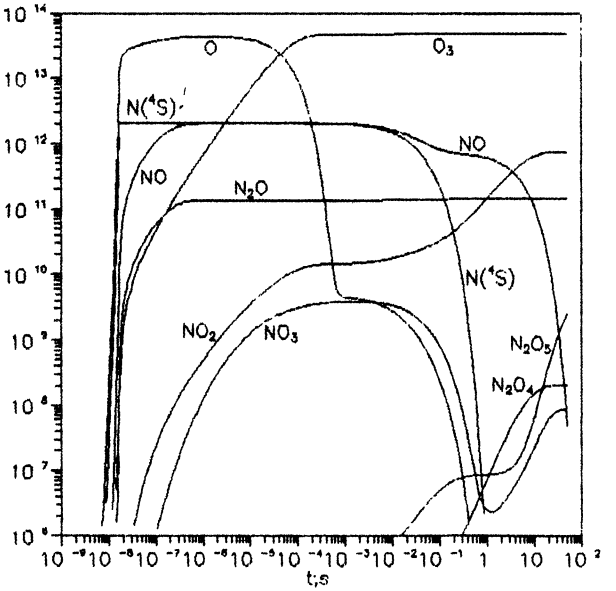

Fig.3.
Plasma chemical consequences of the microwave discharge freely localized in the troposphere. H=10 km; λ_f=0,8 cm; τ_f=1,7.10^{-8} s

At the same time it is important to note that it is just nitrogen monoxide N_2O which, having the lifetime in the troposphere up to hundred years, is able to penetrate in the stratosphere transforming there into the NO_x molecules which destroy the ozone in catalytic reactions. As for excess NO_x molecules produced directly in the troposphere they, having a fairly small lifetimes (for 2 weeks), are removed by rains on the Earth just increasing the rain acidity. According to calculations (see Fig.3) a small number of N_2O molecules (by an order of magnitude less than the natural content) is formed in short microwave pulses producing the discharges freely localized in the troposphere.

V. Experimental modelling of the influence of the discharges freely localized in the atmosphere on CFC's contamination

In experiments with General Physics Institute setups attempts are made for laboratory modelling of freely localized discharges excited by powerful microwave beams. The modelling of the air cleaning from CFC's contaminations was done according to the scheme presented in Fig.4 and

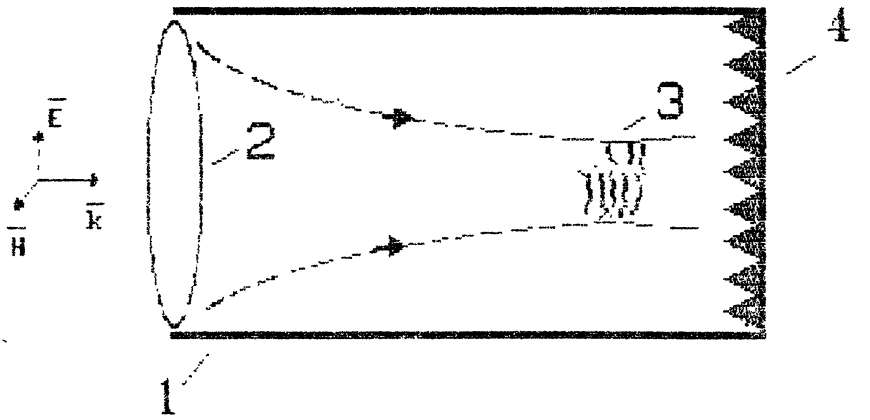

Fig.4
Scheme of the experiment. 1 - metallic vacuum chamber; 2 - lens preparing the converging microwave beam; 3 - microwave discharge; 4 - microwave absorbing load.

described in detail in some previous papers (see e.g. [35,41,42]). In some cases the experiments were carried out with generators yielding a radiation with the wavelength λ_f = 0,8cm and in others with generators yielding a radiation with the wavelength λ_f = 2,5cm. The characteristic parameters of these generators are given in Table 3.

Table 3

λ_f (cm)	τ_f (μs)	P(kW)	I_f (kW/cm^2)	f(Hz)
0,8	20-200	60-100	2,5-4,5	0,5-2
2,5	10-30	300-500	< 30	2

Microwave radiation is focused into $\Phi_k \simeq$ 350mm diameter metal chamber. The transverse size of the focal spot is $d_f \simeq \lambda_f << \Phi_k$. and the microwave radiation intensity in the focus is: $I_f \cong 4P / \pi d_f^2$. In some cases, a gas-filled flash of glass or quartz ($\Phi \cong 140$ mm >> d_f) is placed in the focal region of a beam. A discharge initiator including a system of metal points or metal-dielectric target is also situated in the flash.

The chamber (or the flash) is evacuated up to deep vacuum and feeled with air-CFC-12 or CFC-11 mixture (in some experiments a nitrogen or argon-CFC's mixture is used). The working pressure of the mixture ranged as $100 \leq p \leq 500$ Torr.

A discharge initiated by a microwave beam in high-pressure gases is described in several papers [26,43,44]. This discharge is characterized by a strong space inhomogeneity, i.e. by the presence of contraction regions ("filaments" or "channels") with an extremely high electron density ($n_e \geq 10^{16} - 10^{17}$ cm^{-3}) and relatively high electron ($T_e \geq$ 5eV) and gas ($T_g \leq$ 3000K) temperatures and by the presence of a cold ($T_e \simeq$ 0,5-0,7eV) and low-density ($n_e \leq 10^{12}$ cm^{-3}) plasma ("halo"). Such a high electron density in the contraction regions follows also from the theory of freely localized microwave discharge in igh-pressure gases (see, e.g. [45]).

Fig.5 presents the typical photographs of the microwave discharges.

In experiments with an air-CFC's mixture the CFC's content wasmeasured from the absorption of the diagnostic IR-radiation at the wavelength λ = 9mkm before and after the gas irradiation by a sequence of pulses producing a discharge in the focus of a microwave beam.

Fig.6 presents a typical dependence of CFC's content on the radiation time t. Experiments with discharges in argon and nitrogen mixtures have shown that when these gases are taken the efficiency of CFC's decomposition

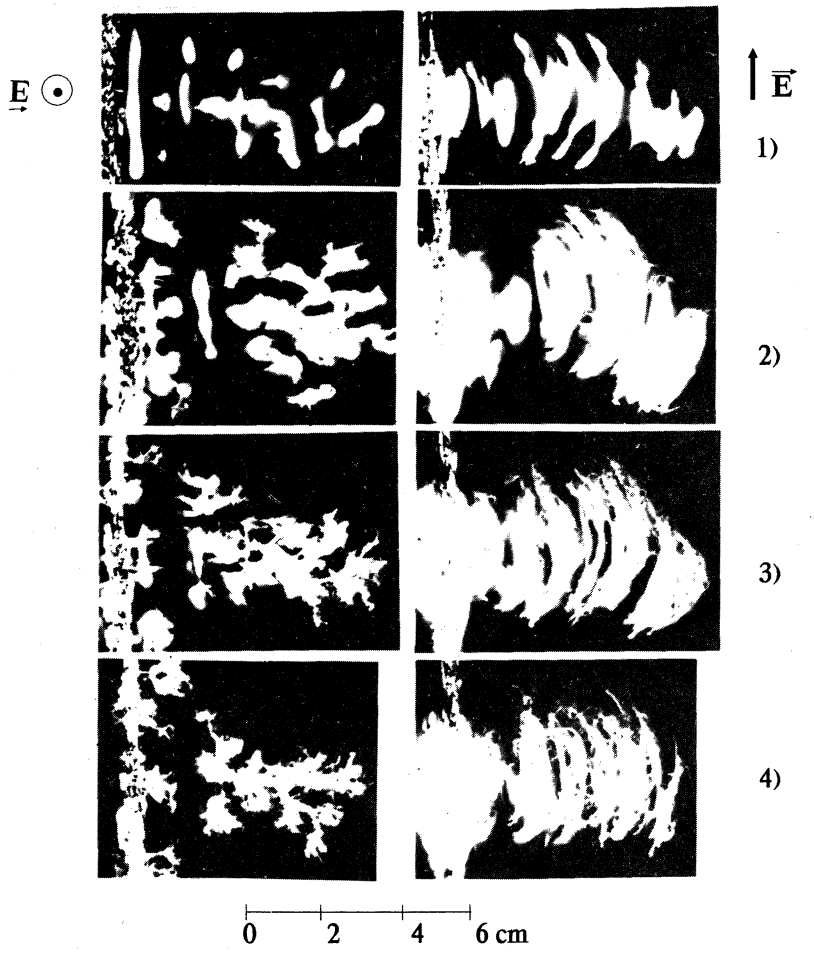

Fig.5. Typical photographs of microwave discharge in the air.
1) Simultaneous photographs along and orthogonal to the direction of microwave electric field.
λ_f *=2,5 cm;* I_f *=35 kW/cm²;* τ_f *=30 μs*
1) p=60 Torr; 2) - 90 Torr; 3) - 120 Torr; 4) - 150 Torr.

either does not change or even slightly increases (see Fig.6b).

Fig.7 presents the dependence of the energy cost of CFC-molecule (CFC-1 and CFC-12) decomposition reaction on its initial content in air. The energy cost is found for a small time of irradiation from the relationship:

$$\Delta\varepsilon \simeq P f \Delta t_c \tau_f / \Delta N_F, \qquad (21)$$

where ΔN_F is the number CFC-molecules dissociated during the time Δt_c

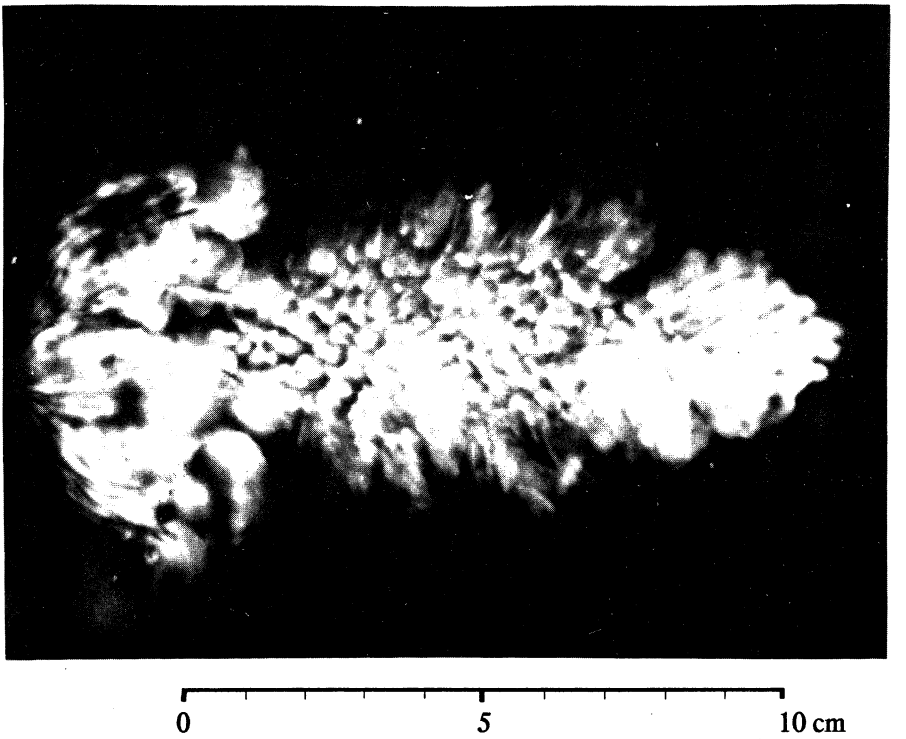

Fig.5.
b) λ_f =0,8 cm; If = 16 kW/cm ; τ_f = 200 μs; p = 100 *Torr.*

of gas irradiation by microwave pulses of the power P, pulse duration τ_f with a repetition frequency f.

For the considered cleaning technique the study is also urgent of the content of the gas medium after the discharge and the determination of the products of CFC's transformation in air. The content was preliminary measured with a chromatographic analyzer DANI-3000 connected to a mass-spectrometer VG-7070E and also with a IR-spectrograph from the absorption spectrum of a gas volume before and after its irradiation by powerful microwaves. Table 4 presents the stable products resulting from CFC decomposition which were recorded and identified during the measurements.

Table 4

Starting substances	Identified products of plasma chemical reactions								Method of measurements
CFC-12 + + air (75Torr + 75Torr)	CF_4	CO_2	C_2F_6	CF_3Cl	CF_2Cl_2	COF_2	SiF_4	$(CH_3)_2SiF_2$	Chromatograph+ mass analyzer (arbit. units)
	0,4	1	0,03	1,61	0,05	-	-	0,16	
	+	-	-	+	+	+	+	-	IR-spectrograph. (+) - -identified substances

It follows from the above analysis that for the considered cleaning technique one of the main physical problems is the following: is the nature of a gas-discharge plasma relaxation "attachment" or "recombination"? To answer this question special measurements of the electron density dynamics were made during the described model experiments. Electron density n_e was measured by two diagnostic microwave techniques: translucence of a gas-

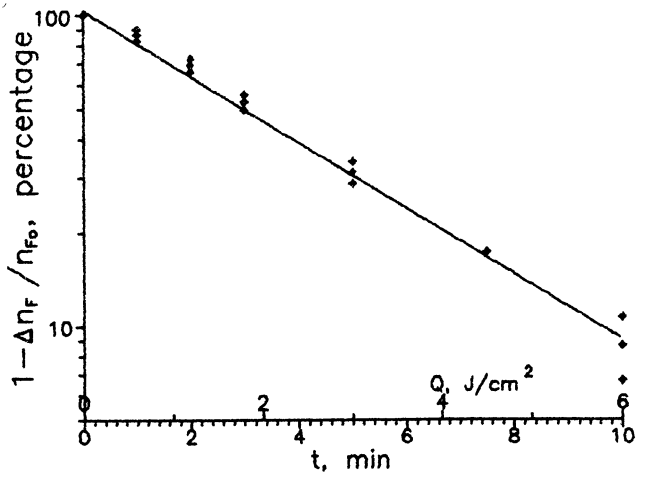

Fig.6. The dependence of CFC-12 content on the time of gas irradiation by means of sequence of microwave pulses.
a) λ_f *=2,5 cm;* I_f*=10kW/cm*^{2}*;* τ_f*=30 μs; f=2 Hz.*

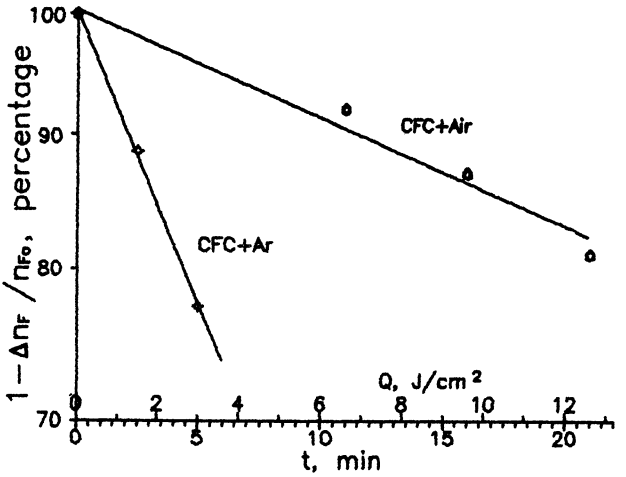

Fig.6.
b) Argon-CFC-12 and air-CFC-12 mixtures; p=250 Torr; p_{F_0} =1,7 Torr.
Q - the total energy containing in the microwave pulses have irradiated gas target.

discharge region by a microwave diagnostic beam (with $\lambda \simeq$ 0,8cm) or using Lekcher line crossing the gas-discharge region and supplied also by microwave with the same wavelength (see Fig.8). The data from both methods agree fairly well.

Figs.9,10 and 11 present the density time evolution in a decaying after-the-discharge plasma (the discharge being in air and in air-CFC mixture). Fig.12 presents a typical dependence of the gas-discharge plasma decay time on a relative CFC content in air.

In discussing the results we should first note that the localization of the microwave discharge, the content of a gas medium and its pressure are fairly well simulated in the considered experiments. At the same time the phenomenon studied in laboratory conditions differs in some parameters from that expected in the atmosphere. That concerns in particular the partial pressure of CFC. In the experimental conditions CFC-11 and CFC-12 content is by many orders higher than in natural conditions that is first of all due to the difficulties in recording small content of contaminations. Special studies have, however, shown that relatively high CFC's density, with which we concerned, does not noticeably changes such discharge properties as its dynamics, space structure, plasma parameters.

Let us put a special attention to the plasma decay in air. Fig.9 shows well

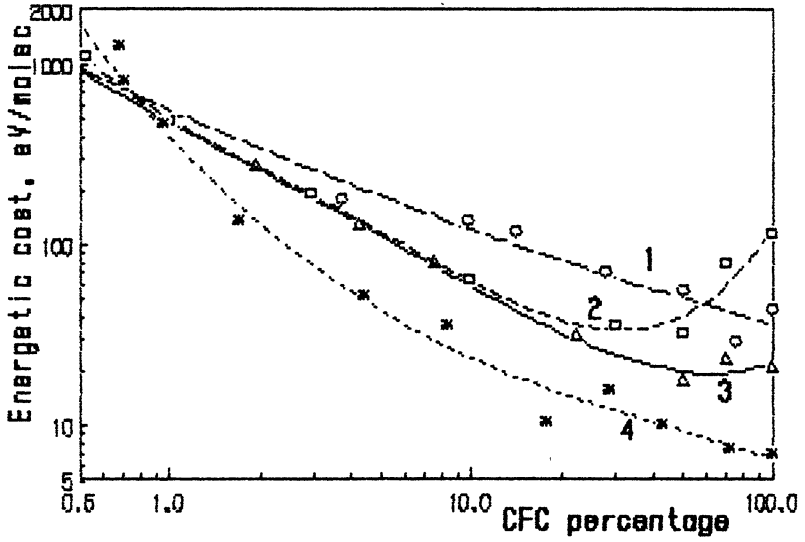

Fig.7. Dependence of energetic cost of the CFC molecule destruction upon the content of CFC-11 and CFC-12 in a CFC-air mixture.
1 - p=30 Torr; t=30 μs; f=2 Hz; P=100 kW; λ=0,8 cm; CFC-12.
2 - p=100 Torr; t=30 μs; f=2 Hz; P=365 kW; λ=2,5 cm; CFC-12.
3 - p=100 Torr; t=200 μs; f=0,5 Hz; P=100 kW; λ=0,8 cm; CFC-12.
4 - p=100 Torr; t=55 μs; f=0,1-1 Hz; P=300 kW; λ=2,5 cm; CFC-11.

that after the end of the microwave pulse the relaxation of the plasma formation is not only essentially slower than in the case of attachment ($\tau_a \leq$ 1 μs) but also tends to the quasi stationary state (the lifetime becomes anomaly long). Fig.9 presents the calculation curves describing the dynamics of CFC-11 and CFC-12 molecules decomposition under the assumption that a small admixture of these molecules is thrown in the discharge region relaxing according to the law given by the experiment and that the main mechanism for CFC destruction is dissociative attachment. According to the Figure, practically omplete decomposition of CFC-11 component and 50% decomposition of CFC-12 component may be expected by ~ 10μs. Hence an actual velocity of CFC's contamination in an after-the-discharge air may turn out to be essentially higher then even in assumption of completely "recombinative" plasma decay. It should be, however, noted that from the standpoint of the considered cleaning technique, the plasma behavior after the discharge remains one of the urgent physical problems. First of all it is not clear whether an anomaly long life of an electron component observed in

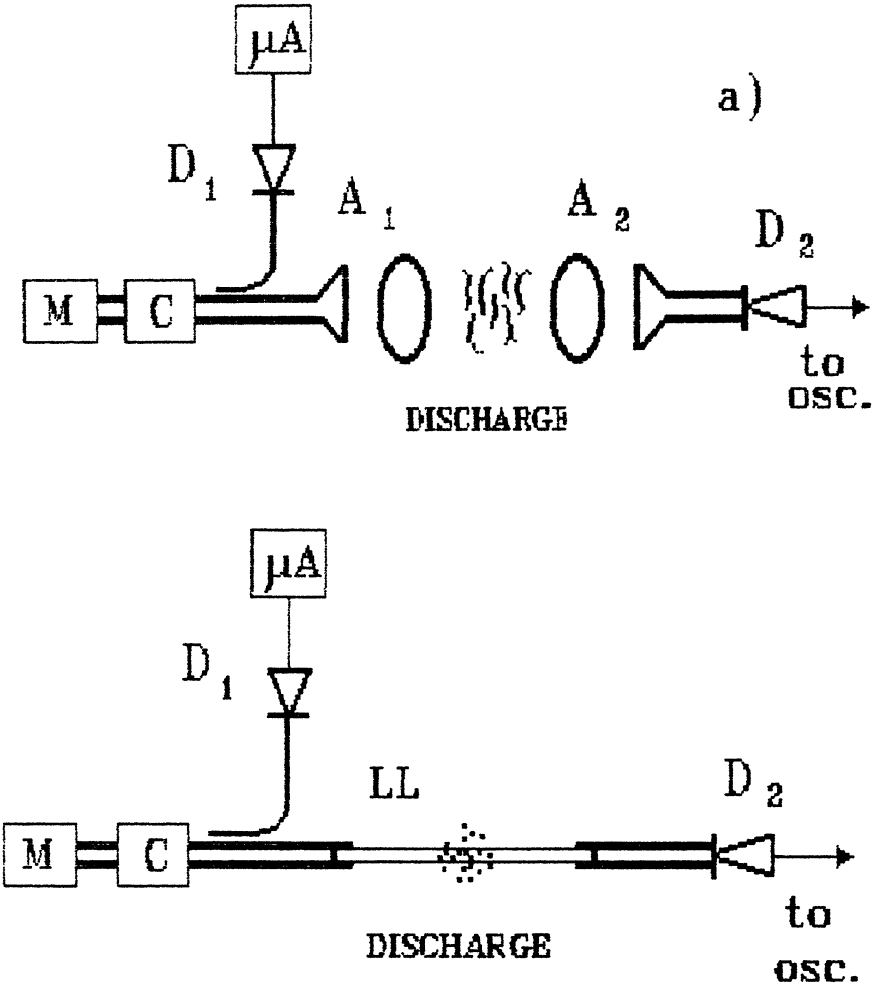

Fig.8. Scheme of electron density measurements.
a) System with diagnostic microwave beam (λ=0,8 cm).
b) System with Leckher Line (λ=0,8 cm).
D_1 , D_2 - microwave detectors; M - microwave generator; C - microwave circulator; A_1 , A_2 - horn-lens antennas; LL - Leckher Line

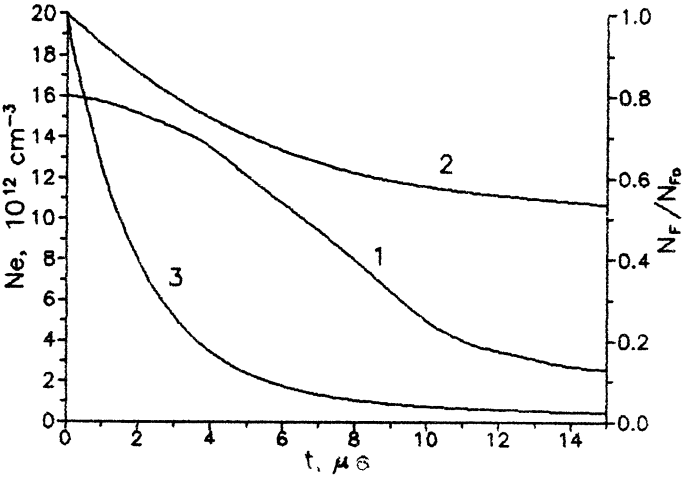

Fig.9. Time-variation of electron density in the decaying microwave gas-discharge in the air.
λ_f =2,5 cm; I_f =35 kW/cm^2; τ_f =30μs; p=150 Torr.
1 - measured time-variation; 2 - calculated content of CFC-12 in the after-the-discharge medium; 3 - calculated content of CFC-11 in the after-the-discharge medium.

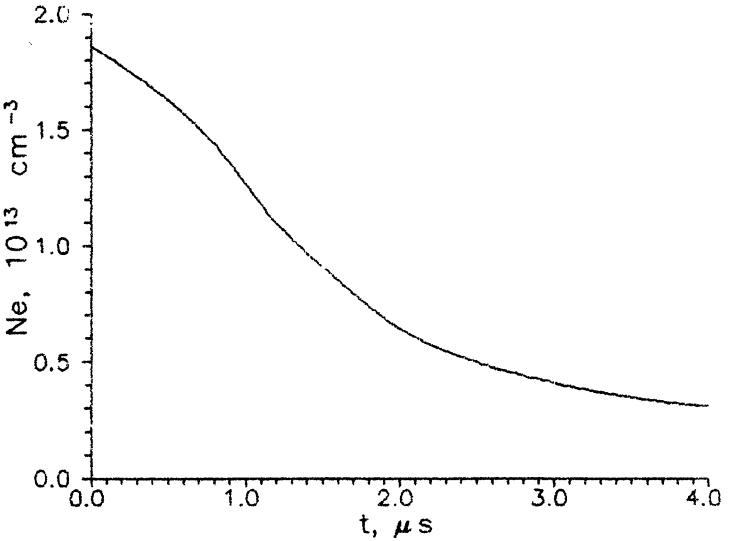

Fig.10. Time-variation of electron density in the decaying microwave gas-discharge in the air-CFC-12 mixture.
λ_f =2,5 cm; I_f =35 kW/cm^2; τ_f =30μs; p=180 Torr; p_f =3,6 Torr.

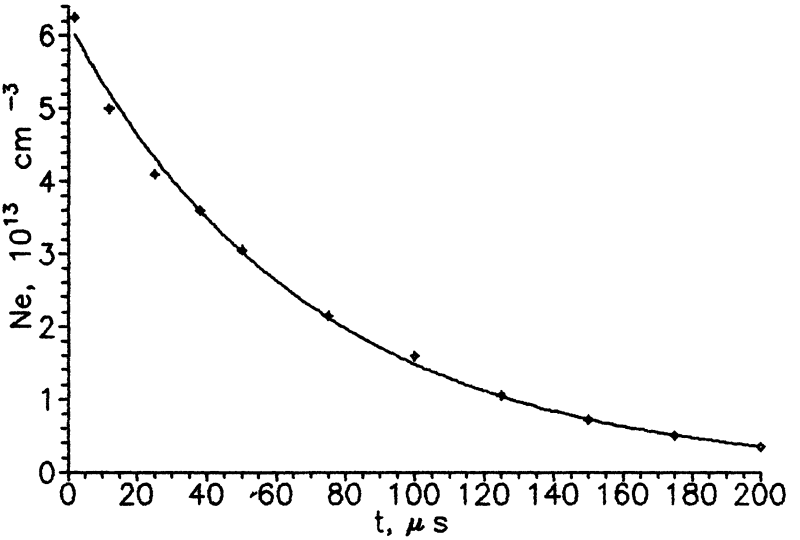

Fig.11. Time-variation of electron density in the decaying microwave gas-discharge in the air.
λ_f=0,8cm; I_f=10kW/cm^2; τ_f=200 μs; p=130 Torr.

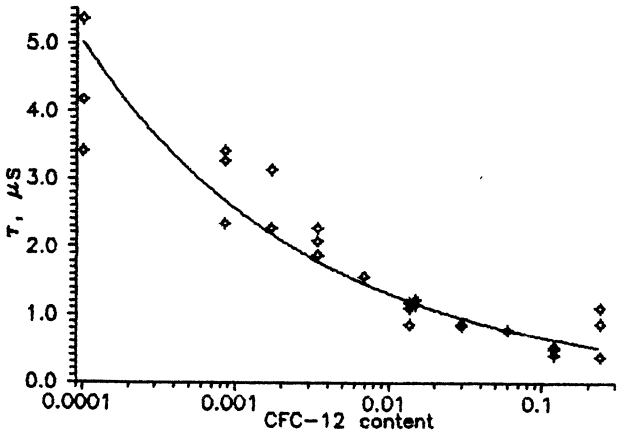

Fig.12. The dependence of the gas-discharge plasma decay time on a initial relative CFC-12 content in air.
λ_f =2,5 cm; I_f =30 kW/cm^2; τ_f =30 μs; p=120 Torr

our and in previous experiments presents in the conditions of low energy input in gas medium ($\leq 10^{-5}$ J/cm^3) expected in natural realization. The situation is the more uncertain since no convincing explanation is found of a slow recombinative decay even in the case of fairly high energy inputs ($\geq 10^{-2}$ J/cm^3) typical for concerned experiment. In order to build an adequate physical model it is evidently necessary to find the reason for which the coefficient of electron attachment to oxygen is essentially lower. The calculations carried out for the conditions of our experiment in terms of a scheme described in [40] have shown that the discovered lower attachment coefficient cannot be neither due to the onset of an atomic oxygen nor due to the production of metastable electron-excited states of oxygen and nitrogen. The problem is also complicated by the fact that even if we find the detachment channels the problem will be not get solved since according to calculations done in terms of [40] a noticeable contribution to the charge content in a gas-discharge plasma should come from the complex ions with a high recombination coefficient ($\geq 10^{-6}$ cm^3 s^{-1}) and which accordingly lead to the plasma relaxation which is much more rapid than it follows from the experiments described in the present work. The future studies should be thus aimed at determining the nature of both the processes resulting in the complex-ion destruction.

The above experimental results shows that the discharge contraction regions ("brightly shining filament" structures in Fig.5) are likely to be the place where CFC's molecules are efficiently treated. That follows in particular from the dependencies $\Delta\varepsilon$ (p_{F_0}/p_F) shown in Fig.7.

Really, assuming that the mechanism of dissociative attachment is responsible for CFC's decomposition, the fall in the energy cost with the increase in the relative CFC content may occur only when $n_{em} > n_{F_0}$. Since in experiments $n_{F_0} \simeq 10^{17} - 10^{18}$ cm^{-3}, it is worth to consider that just the channels in which the electron density (according to [46,47]) exceeds $10^{16} - 10^{17}$ cm^{-3} are the place of CFC's destruction (and not the regions between the channels where $n_{em} \simeq 10^{12}$ cm^{-3}).

The falling $\Delta\varepsilon$ dependence on p_{F_0}/p_F is also possible in the case of dominant role played by reactions (1) and (2). It is, however, easy to show that this process requiring fairly high electron energy and igh electron density may also occur only in the regions of contractions.

The conclusion on localization of the processes of CFC-destruction in the "channel" structures is proved by the results of the study of plasma decay during the discharge in air containing CFC contaminations (see Figs.10 and 12). Extremely high values of the cross-section of dissociative attachment (Fig.1) should lead to the fast disappearance of an electron component in the

after-the-discharge period. Really even in the case of such a low partial CFC pressure as $\approx$ 1 Torr the lifetime of the plasma governed by the two processes (3) and (4) should amount to: $\tau_p \approx 1/k_D\, n_{F_0} \simeq 10^{-9}$ s that is much shorter than that observed in experiments ($\geq$ 2-4.10^{-6} s).

The measurements results can be explained by the fact that almost all the CFC-molecules dissociate in the discharge region during one microwave pulse. As has been already mentioned such a fast CFC's destruction could occur only in the filaments, i.e. the regions with igh electron densities.

Taking an assumption of complete CFC decomposition in the discharge "filaments" we find a characteristic time of CFC decomposition all over the reactor (flash):

$$\tau_c \approx (V/V_k)\ 1/f \qquad (22)$$

where V and V_k are the volumes of the flash field with a gas mixture and of the region of gas-discharge channels, respectively. From (22) it follows that at $V/V_k \simeq 400$ $\tau_c \cong$ 200s that is close to the experimental results (see Fig.6).

One of the main problems involved in the considered research is associated with the content of the products of CFC's decomposition during the gas discharge and their possible influence on the ecological situation. Accordingly in analyzing the experiments a special attention should be drown to the promising results of the measurements made after the irradiation of an air containing CFC's by series of microwave pulses forming the discharges (see Table 4). According to the literature data [34] on photo dissociative decay of CFC's decomposition products with the increasing altitude above the Earth all the identified products are not actually dangerous for the ozone layer. The Fig.13 shows an extremely low probability of dissociation of chlorine- and fluorine-containing matters resulting from the discharge at the stratospheric altitudes (it is much less than that for the initial CFC's). Hence it follow that even in the case when after-the-discharge products are not removed by rains from the air volume irradiated by microwave beams and reach the stratosphere, their action on the state of the ozone layer may turn out to be negligible.

Thus the preliminary experimental results do not contradict neither the assumption that the microwave discharge freely localized in the troposphere destroys efficiently CFC contamination nor the assumption that the decomposition products are not practically dangerous for the ozone layer.

The experimental studies are certainly to be continued. And the change for super-power and super-short over-threshold microwave pulses, at which a gas-discharge plasma is accompanied by a low ($\leq 10^{-5}$ J/cm^3) specific energy input in air, seems to be the most useful. It is also necessary to reduce

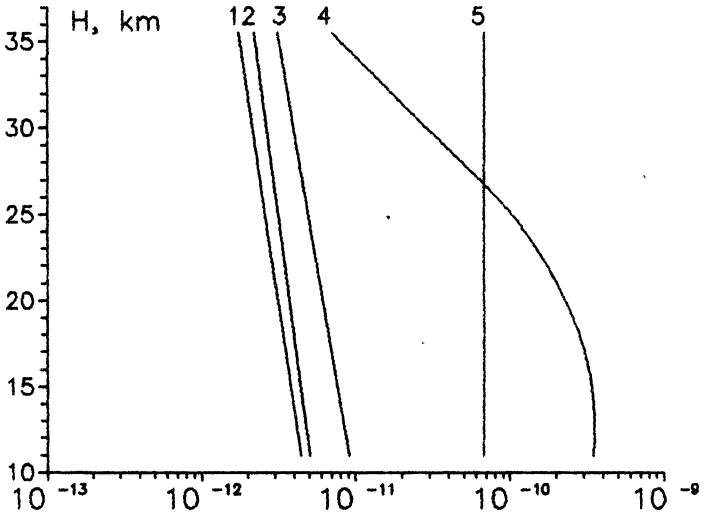

Fig. 13. The generalized data on a vertical distribution of the halocarbons in the stratosphere.
1 - CF_3CL; 2 - C_2F_6; 3 - $C_2Cl_2F_4$; 4 - CF_2Cl_2; 5 - CF_4.

CFC content up to the level, at which $n_{Fo} < n_{em}$ (n_{em} is the discharge-averaged electron density) attaining partial pressures typical for the natural conditions.

VI. Conclusion

Hence we propose the method of environment cleaning from CFC's by excitation of a freely localized discharge in the given air region. A possibility is thorough studied of using intense pulsed microwave beams producing a gas-discharge in the point of their intersection above the Earth. Application of beams scanning make it possible to treat noticeable atmosphere volumes by means of fairly small energy inputs in a volume unit (10^{-3} - 10^{-5} J/cm^3). The dissociation products are supposed to be removed from the atmosphere by the rains.

The main channel via which the CFC destruction occurs is dissociative attachment of cold electrons of a decay plasma to the molecules of this matter. This method is selective because only CFC's of all the air components have such a high cross-section of dissociative attachment and the energy threshold for them practically does not exist. It cannot be excluded that a noticeable

contribution to CFC's destruction comes from active electron-excited atoms and molecules of oxygen and nitrogen occurring in the discharge. Microwave radiation is considered only as a convenient and economical technique for energy transport in the treated atmosphere region. That is why it evidently is of interest to study other possible ways of pulsed discharge excitation, in particular, high-voltage breakdown between the electrodes, laser sparks, flares, etc.

The experiments modelling freely localized microwave discharges in the atmosphere and carried out with General Physics Institute devices do not contradict neither the assumption of high efficiency of gas-discharge method nor the ecological purity of the latter.

In the case the further studies confirm the economical worth of the proposed method of environment cleaning from CFC's contaminations, the mankind will find a means to prevent the oncoming ecological disaster.

Acknowledgments

This work was partially supported by the Grant of Russian Fund for Fundamental Investigations under contract 93-02-1698.

The authors would like to thank Prof.L.G.Christophorou (Oak Ridge National Laboratory, USA) for useful advice and Dr. J.N.Benford (Physic. Internat. Company, USA), Prof. T.Consoli (France), Prof. N.L.Aleksandrov and Prof. A.P.Napartovich for fruitful discusions.

References

1. Richard S. Stolarski, The Ozone Hole Over Antarctic, Scientific American, 258, No 1, (1988).
2. J.G.Anderson, D.W.Toohey, and W.H.Brune, Free Radicals Within the Antarctic Vortex. The Role of CFC's in Antarctic Ozone Loss, Science, 251, 4989, 39-46, (1980).
3. T.H.Stix, Processing the Earth's Atmosphere, ISPP-7 "Piero Caldirola", Control Active Global Experiments (CAGE), E.Sindoni, and A.Y.Wong (Eds), SIF, Bologna, 281-288, (1991).
4. T.H.Stix, Removal of Chlorofluorocarbons from the Earth's Atmosphere, J. Appl. Phys., 66, 11, 5622-5626, (1989).
5. K.T.Tsang, D.D.Ho, A.Y.Wong, R.J.Siverson, Stratospheric Ozone Conservation by Electron Attachment to Chlorine Atoms, ISPP-7 "Piero Caldirola", Control Active Global Experiments (CAGE), E.Sindoni and A.Y.Wong (Eds), SIF, Bologna, 143-157, (1991).

6. A.Y.Wong, J.Steinhauer, R.Close, and T.Fukuchi, Conservation of Ozone in the Upper Atmosphere by Selective Ion Removal, Comments on Plasma Phys. Controlled. Fusion, 12, 5, 223-234, (1989).
7. A.Y.Wong, R.W.Wuerker, J.Sabutis, R.Suchannek, C.D.Hendricks and P.Gottlieb, Ion Dynamics and Ozone, ISPP-7 "Piero Caldirola", Control Active Global Experiments (CAGE), E.Sindoni and A.Y.Wong (Eds), SIF, Bologna, 129-142, (1991).
8. N.L.Aleksandrov, A.M.Konchakov, I.V.Kochetov, A.P.Napartovich, Effect of Electromagnetic Wave on the Upper Atmosphere Plasmas with Halocarbons, Proc. Int. Workshop, Strong Microwaves in Plasmas, Suzdal, Nizhny Novgorod, v.1, 458-464, (1991).
9. I.A.Kossyi, A.Y.Kostinsky, A.A.Matveyev, and V.P.Silakov, Microwave Discharge Action on the Ozone Layer, Comments Plasma Phys. Controlled Fusion, 14, 2, 73-87, (1991).
10. G.A.Askaryan, G.M.Batanov, D.F.Bykov, S.I.Gritsinin, I.A.Kossyi, A.Yu.Kostinskii, A.A.Matveyev, V.P.Silakov, Microwave Discharges in the Stratosphere and their Effect upon the State of the Ozone Layer, ISPP-7 "Piero Caldirola", Controlled Active Global xperiments (CAGE), E.Sindoni and A.Y.Wong (Eds), SIF, Bologna, 239-259, (1991).
11. G.A.Askaryan, G.M.Batanov, I.A.Kossyi and A.Yu.Kostinskii, Possibility of Destruction and Restoration of the Ozone Layer by Microwave Discharges. ISPP-10 "Piero Caldirola", High Power Microwave Generation and Applications, E.Sindoni and C.Warton (Eds), SIF, Bologna, 207-227, (1992).
12. G.A.Askaryan, G.M.Batanov, A.E.Barkhudarov, D.F.Bykov, S.I.Gritsinin, I.A.Kossyi, E.K.Korchagina, A.Yu.Kostinskii, A.A.Matveyev, V.P.Silakov, Microwave Discharges in the Stratosphere and their Effect on the Ozone Layer, XX ICPIG, Invited Papers, Pisa, Italy, 100-108, (1991).
13. G.A.Askaryan, G.M.Batanov, A.E.Barkhudarov, S.I.Gritsinin, E.G.Korchagina, I.A.Kossyi, V.P.Silakov and N.M.Tarasova, Fizika Plazmy (in Russian), 18, 9, 1198-1210, (1992).
14. G.A.Askaryan, G.M.Batanov, A.E.Barkhudarov, S.I.Gritsinin, E.G.Korchagina, I.A.Kossyi, V.P.Silakov and N.M.Tarasova, Pis'ma v Zhurnal Eksperimental'noi i Teoreticheskoi Fiziki (in Russian), 55, 9, 500-504, (1992).
15. G.F.Reinking, L.G.Christophorou and S.R.Hunter, Study of Total Ionization in Gases/Mixtures of Interest to Pulsed Power Applications, J. Appl., Phys., 60, 2, 499-508, (1986).
16. L.G.Christophorou (Ed), Electron-Molecule Interactions and Their

Applications, Orlando: Academic Press, v. 1,2, (1984).
17. D.L.Mc Corkle, A.A.Christodoulides, L.G.Christophorou, J.Szamrej, Electron Attachment to Chlorofluorocarbons Using the Electron-Swarm Method, J. Chem. Phys., 72, 4049-4057, (1980).
18. A.V.Eletskii and B.M.Smirnov, Uspekhi Fizicheskikh Nauk, 147, 3, 459-484, (1985).
19. V.A.Isidorov, Organic Chemistry of the Atmosphere (in Russian), Leningrad: Khimiya, (1985).
20. D.I.Slovetskii, Chemical Reactions Mechanisms in a Nonequilibrium Plasmas, Moscow: Nauka, (1980).
21. N.D.Borisov, A.V.Gurevich, G.M.Milikh, Artificial ionized region in the Atmosphere (in Russian), Moscow: IZMIRAN, (1986).
22. A.L.Vikharev, O.A.Ivanov and A.N.Stepanov, Zhurnal Tekhnicheskoi Fiziki (in Russian), 54, 1617-1625, (1984).
23. A.L.Vikharev, O.A.Ivanov and A.N.Stepanov, Fizika Plazmy (in Russian), 10, 792-796, (1984).
24. A.L.Vikharev, O.A.Ivanov, A.N.Stepanov, Radiofizika (in Russian), 28, 36-42, (1985).
25. V.N.Kulikov, V.E.Mitsuk, Radiotekhnika i Elektronika (in Russian), XXXIV, 10, 2129-2134, (1989).
26. S.V.Golubev, S.I.Gritsinin, V.G.Zorin et al, High-Frequency Discharge in the Wave Fields (in Russian), Gor'kii: IPF AN USSR, (1988).
27. G.A.Askaryan, M.S.Rabinovich, M.M.Savchenko, A.D.Smirnova, Pis'ma v Zhurnal Eksperimental'noi i Teoreticheskoi Fiziki (in Russian), 1, 6, 18-21, (1965).
28. G.A.Askaryan, M.S.Rabinovich, M.M.Savchenko, V.K.Stepanov, Pis'ma v Zhurnal Eksperimental'noi i Teoreticheskoi Fiziki (in Russian), 3, 12, 465-468, (1966).
29. T.Consoli, On a Contribution of Fusion Plasma Research to Space Physics, ISPP-7 "Piero Caldirola", Controlled Active Global Experiments (CAGE), E.Sindoni and A.Y.Wong (Eds), SIF, Bologna, (1991).
30. V.A.Vanke, V.M.Lopukhin, V.A.Savin, Uspekhi Fizicheskikh Nauk (in Russian), 123, 4, 633-655, (1977).
31. N.I.Zaitsev and M.I.Petelin, Radiotekhnika i Electronika (in Russian), 19, 1056-1058, (1974).
32. Magnetron МИ-389, Moscow, 107120, "Pluton".
33. J.Benford, J.Swegle, High-Power Microwaves, Artech House, Boston, MA.
34. E.L.Aleksandrov, Yu.A.Izrael, I.L.Karol, A.Kh.Khrgian. Ozone Layer and its Change (in Russian), St. Petersburg: Gidrometeoizdat, (1992).

35. G.A.Askaryan, G.M.Batanov, I.A.Kossyi, A.Yu.Kostinskii, Doklady Academii Nauk SSSR (in Russian), 302, 3, 566-569, (1988).
36. G.A.Askaryan, G.M.Batanov, I.A.Kossyi, Chemical and Optical Changes in the Air During Microwave Discharges, Nonlinear World, Proc. IV Intern. Workshop on Nonlinear and Turbulent Processes in Physics, Kiev: Naukova Dumka, v.2, 65-68, (1989).
37. G.A.Askaryan, G.M.Batanov, I.A.Kossyi and A.Yu.Kostinskii, Problemy Fizicheskoi Electroniki (in Russian), Leningrad: AN SSSR, 147-158, (1990)
38. G.A.Askaryan, G.M.Batanov, I.A.Kossyi, A.Yu.Kostinskii, Fizika Plasmy (in Russian), 17, 1, 85-96, (1991).
39. I.A.Kossyi, A.Yu.Kostinskii, A.A.Matveyev, V.P.Silakov, Pis'ma v Zhurnal Tekhnicheskoi Fiziki (in Russian), 16, 12, 57-61, (1990).
40. I.A.Kossyi, A.Yu.Kostinsky, A.A.Matveyev, V.P.Silakov, Kinetic Scheme of the Non-Equilibrium Discharge in Nitrogen-Oxygen Mixtures, Plasma Sources Sci. Technol., 1, 3, 207-220, (1992).
41. G.A.Askaryan, G.M.Batanov, S.I.Gritsinin, I.A.Kossyi and A.Yu.Kostinskii, Zhurnal Tekhnicheskoi Fiziki (in Russian), 60, 11, 77-84, (1990).
42. S.I.Gritsinin, L.V.Kolik, I.A.Kossyi, A.Yu.Kostinskii, A.V.Sapozhnikov, N.M.Tarasova, V.E.Terekhin, Zhurnal Tekhnicheskoi Fiziki (in Russian), 58, 12, 2293-2301, (1988).
43. G.M.Batanov, S.I.Gritsinin, I.A.Kossyi, A.N.Magunov, V.P.Silakov and N.M.Tarasova, Trudy FIAN (in Russian), 160, 174-202, (1985).
44. S.I.Gritsinin, I.A.Kossyi, V.P.Silakov and N.M.Tarasova, High-Pressure Discharges in Electromagnetic Wave Beams, XVIII ICPIG, Swansea, Invited Papers, 232-240, (1987).
45. I.V.Bezmenov, V.V.Rusanov, V.P.Silakov, Preprint of IPM RAN, No 30, (1992).
46. V.G.Avetisov, S.I.Gritsinin, A.V.Kim, I.A.Kossyi, A.Yu.Kostinskii, M.A.Misakyan, A.I.Nadezhdinskii, N.M.Tarasova and A.N.Khusnutdinov, Pis'ma v Zhurnal Eksperimental'noi i Teoreticheskoi Fiziki (in Russian), 51, 6, 306-309, (1990).
47. S.I.Gritsinin, A.A.Dorofeyuk, I.A.Kossyi, A.N.Magunov, Teplofizika Vysokikh Temperature (in Russian), 25, 6, 1068-1071, (1987).

Halocarbon decomposition in microwave post-discharge

N.L. Aleksandrov, S.V. Dobkin,
A.M. Konchakov, D.A. Novitskii

Moscow Institute of Physics and Technology,
141700 Dolgoprudny, Russia

Atmospheric pollution by halocarbons (freons) has many serious environmental impacts: ozone layer destruction, greenhouse effect, etc. This raises the necessity to develop methods for the removal of halocarbons from an ambient air. The initial halocarbon density may be both high (an emergency exhaust, the wastes of process cycles) and low (the atmosphere).

It has been proposed to clean the environment from halocarbons using a freely localized microwave discharge [1]. This method has been supported by the laboratory experiment [1] and computer simulation of atmospheric chemical kinetics [2]. One of the main mechanisms for halocarbon decomposition is supposed to be dissociative attachment of thermal electrons in post-discharge to form Cl^- ions. For freon-10 it can be written in the form

$$e + CCl_4 \rightarrow Cl^- + CCl_3 \qquad (1)$$

It has been shown [3] that the higher efficiency of halocarbon decomposition can be obtained through a negatively charged particle catalytic cycle. In that case electron detached from Cl^- ion due to collisional associative process attaches to another halocarbon molecule

and the cycle is repeated without electron loss. This takes place under certain conditions, among them [3]

$$K_a n_F >> K_{ei} n_p, \tag{2}$$

$$K_d n^* >> K_{ii} n_p, \tag{3}$$

where K_a, K_d, K_{ei} and K_{ii} are the attachment, detachment, electron-ion, and ion-ion recombination rate coefficients, respectively; n_F, n_p and n^* are the densities of halocarbon molecules, positive ions and active particles having the property of detaching electron from Cl^- ion. Failure to satisfy conditions (2) and (3) results in the terminating of catalytic cycle through the charged-particle recombination. Thus the cycle takes place at sufficiently high density of halocarbon and active particles only.

In this paper we carry out the computer simulation of chemical, charged-particle and excited-particle kinetics in microwave post-discharge stage in the humid air with halocarbon traces. The aim of the present work is to investigate the effect of catalytic cycle on the halocarbon decomposition in actual practice. The electron detachment is supposed to be due to the fast reaction

$$Cl^- + H \rightarrow e + HCl. \tag{4}$$

The high power pulsed microwave discharge is considered. For the sake of simplicity the pulse is assumed so narrow that at the active stage the loss of particles formed by electron-molecule collisions may be neglected. Therefore, the densities of particles formed in one pulse are in the same ratio as the rate coefficients of respective electron processes.

Simulation of charged- and active-particle kinetics at the post-discharge stage is carried out using a numerical solution of balance equations. A total of 200 reactions and 40 species, including Cl^-, O_2^-, $Cl^- \cdot H_2O$, $O_2^- \cdot H_2O$, O_2^+, N_2^+, N_4^+, $O_2^+ \cdot H_2O$, H_3O^+ ions, and electrons, are involved in the calculation. Input parameters are the pressure (P) and the temperature (T) of air, the initial volume fraction of water vapor (δ), the initial halocarbon density (n_{F0}), the density of electrons formed in one pulse (n_{e0}), and the interpulse period (τ).

The electron rate coefficients at the active stage of the microwave discharge are calculated using a numerical solving of the Boltzmann equation for the electron energy distribution function. The processes considered are the elastic scattering, the excitation of the rotational, vibrational and electronic levels of molecules, and the ionization. The self-consistent set of the electron cross-sections and the method of solving of the Boltzmann equation are taken from [4]. Calculations are carried out at the reduced electric field E/N=(1-2)$\times 10^{-15}$ V·cm^2, where N is the gas number density. The rate coefficients of the ternary ion-ion recombination are calculated by the method given by Flannery [5]. The rate coefficients of the other collisional processes are taken from literature [6-8].

Fig. 1 shows the results of calculation of the CCl_4 (1,2) and H (3) densities in the humid air versus the pulse number (N_p) for P=10 Torr, T=273 K, δ=0.02, $n_{Fo}=10^{13}$ cm^{-3}, $n_{e0}=10^{11}$ cm^{-3}, and $\tau = 0.5 \cdot 10^{-3}$s. Curve 1 represents the calculation without the catalytic cycle (without the electron detachment from Cl^- ion), whereas curve 2 represents the calculation involving this cycle. For a low pulse

number, the H component is present in minor amounts. Here, the cycle has a slight effect because of the failure to satisfy condition (3). The H density tends to increase with increase in the pulse number. Then the catalytic cycle can result in a tenfold decrease of the halocarbon density.

The effect of the cycle considered becomes less pronounced as the gas pressure increases. This is due to the difficulty to satisfy condition (3). On the one hand, the rate coefficient of the ternary ion-ion recombination increases, on the other the H density decreases through the fast ternary process

$$H + O_2 + M \rightarrow HO_2 + M$$

The H density can increase with increasing pulsed density power (increasing n_{e0} or decreasing τ). Fig. 2 gives the results of calculation for P=100 Torr, T=273 K, δ=0.02, $n_{F0}=10^{14}$ cm^{-3}, $n_{e0}=10^{13}$ cm^{-3}, and $\tau=10^{-5}$ s. The above mentioned notation is used. In this case the catalytic cycle tends to cause a fivefold decrease of the halocarbon density as the H density increases.

Although the calculations are carried out for freon-10, the data plotted in Figs. 1 and 2 are also adequate for other similar freons but with other initial densities. These quantities can be obtained from the condition $K_\alpha n_{F0}=const$, where K_α is the rate coefficient of electron attachment to a molecule of respective halocarbon.

In summary, the computer simulation of active-particle kinetics in microwave post-discharge in the humid air with halocarbon traces shows that the catalytic effect proposed by Aleksandrov et al. [3] has the beneficial effect on the halocarbon decomposition.

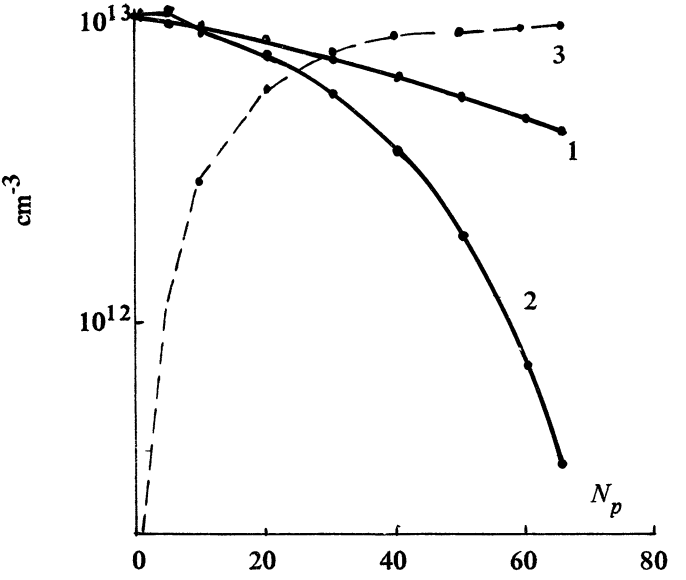
10^{13}
10^{12}
cm^{-3}
3
1
2
N_p
0
20
40
60
80

Fig. 1

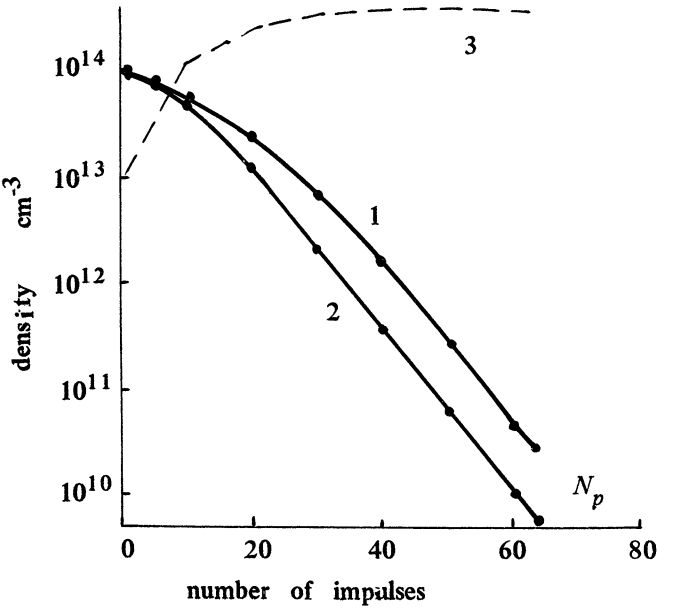
10^{14}
10^{13}
10^{12}
10^{11}
10^{10}
density cm^{-3}
3
1
2
N_p
0
20
40
60
80
number of impulses

Fig. 2

References

1. Askaryan G.A., Batanov G.M., Barkhudarov A.E. et al. Pis'ma v Zh. Eksp. Teor. Fiz., 1992, 55, 500; Fiz. Plazmy, 1992, 18, 1198.
2. Kolesnichenko Yu.S., Khmara D.V. Pis'ma v Zh. Tekhn. Fiz., 1993, 19, 36.
3. Aleksandrov N.L., Vakhrameev K.A., Dobkin S.V., and Son E.E., Ibid., 1992, 18, 73.
4. Aleksandrov N.L., Vysikailo F.I., Islamov R.Sh. et al. Teplofiz. Vys. Temp., 1981, 19, 22.
5. Flannery M.R., Chem. Phys. Lett., 1978, 56, 143.
6. Person J.C. and Ham D.O. Radiat. Phys. Chem., 1988, 31, 1.
7. Christophorou L.G., McCorkle D.L., Christodoulides A.A. Electron-Molecule Interaction and Their Applications, Ed. L.G. Christophorou, N.Y.:Acad. Press, 1984, 1, 477.
8. Atkinson R., Baulch D.L., Cox R.A. et al. J. Phys. Chem. Ref. Data, 1989, 18, 881.

FREON DESTRUCTION IN SHF DISCHARGE: MECHANISMS AND EFFICIENCY

V.G.Brovkin, Yu.F.Kolesnitchenko, D.V.Khmara
Moscow Radiotechnical
Institute of Russia Academy of Sciences
Moscow, Russia

1 Introduction

At present an active explorations of several perspective methods of local and distant air purification from harmful gaseous industry throwout are carrying out [1]. One of them consists in using microwave discharge which produces in a purified gas mixture radicals, charged and excited particles. Further these species react with harmful admixtures and decontaminate them [1].

Special attention is paid now to the problem of freon neutralisation [2,3,4], as these compounds pass feely through the atmosphere and may be destroyed only by UV radiation of the sun. As a result there occur active chlorine-containing radicals destroying the ozone layer. The specific content of freon impurities in the atmosphere may vary widely: from $\eta \sim 10^{-9}$ which corresponds to the content of freons dissipated in the atmosphere up to $\eta \sim 10^{-2}$ in local effluent, production cycles, etc.

Our research group has carried out a series of experiments in studying the effect provided by microwave discharge on freon and freon-containing gas mixtures. Also the numerical simulation of kinetics mechanisms of freon destruction in air in decaying microwave breakdown plasma has been carried out.

2 Experiments

The main purpose of the experiments consists in defining the levels of freon non-reversible decomposition obtained within the above process and in estimating the energetic cost of such decomposition.

Experiments were made in a linear polarized convergent at an angle 60° beam 7 GHz radiation with caustic diameter 4 cm and depth 20 cm, microwave pulse duration (100..740) μs, energy flux density up to $40 \frac{kW}{cm^2}$.

As a impurity we used one of widespread halo carbons: CF_2Cl_2 (freon−12), $C_2F_3Cl_3$ (freon-113) or $C_2F_4Cl_2$ (freon-114). Freon molecular concentration was determined by measuring the absorbtion in infra-red range. A double-ray IR spectrometer IKS-29 has been used for these measurements.

The main results of experiments concerning the effect provided by microwave discharge on freon-containing mixtures with $\eta = 0.037$ are presented in fig. 1 (freon content decrease $(1-\alpha)$ vs the number of microwave pulses n, where α is the freon decomposition degree) and in fig. 2 (energetic cost of freon decomposition ϵ vs α). Fig. 2 gives also results obtained in a similar conditions, but at microwave frequency $\simeq$ 15 GHz [2].

It may be seen that microwave discharge treatment reduces freon concentration in the mixture by a value order with the energetic cost of decomposition process of the order of several keV.

The character of freon concentration falling down $\ln(1-\alpha) \simeq -C \cdot n$ allow one to make the assumption that freon destruction takes place in first order reactions. According to $1-\alpha$ dependence one can also estimate the number of molecules which are destroyed during one microwave pulse: $N_F^{destr} \simeq N_F \cdot (1-e^{-C}) \simeq 5 \cdot 10^{14}\ cm^{-3}$ ($C \simeq 7 \cdot 10^{-3}$ for freon-114 and $C \simeq 4 \cdot 10^{-3}$ for freon-12).

The streamer type of stimulated microwave discharge was realized in this experimental series: the discharge looked like a totality of great number of filaments (streamers), i.e. was an extremely unhomogeneous object. The assumption that the complete freon destruction takes place in the streamer volume leads to the estimation which is consistent with the experimental data.

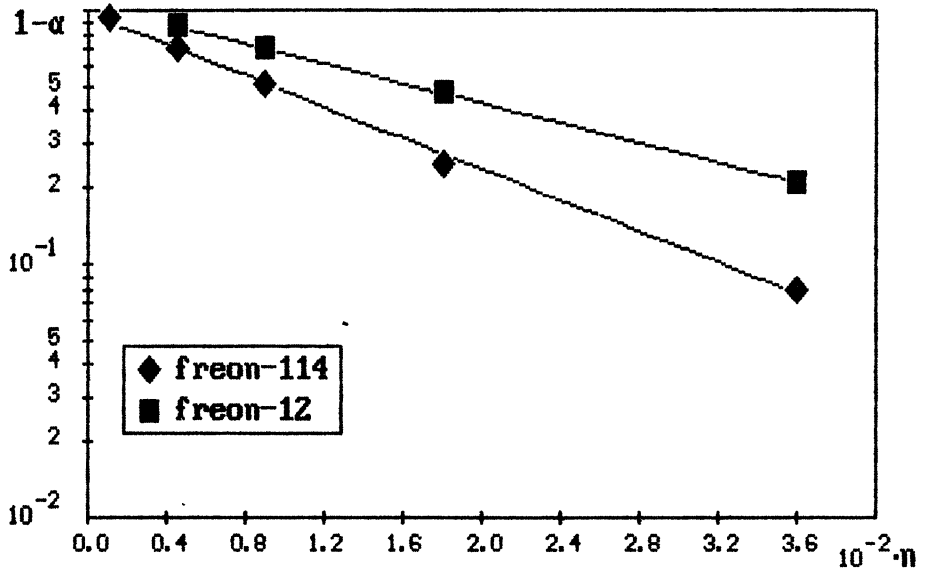
1-α
5
4
3
2
10^-1
5
4
3
2
10^-2
freon-114
freon-12
0.0
0.4
0.8
1.2
1.6
2.0
2.4
2.8
3.2
3.6
10^-2·n

fig. 1

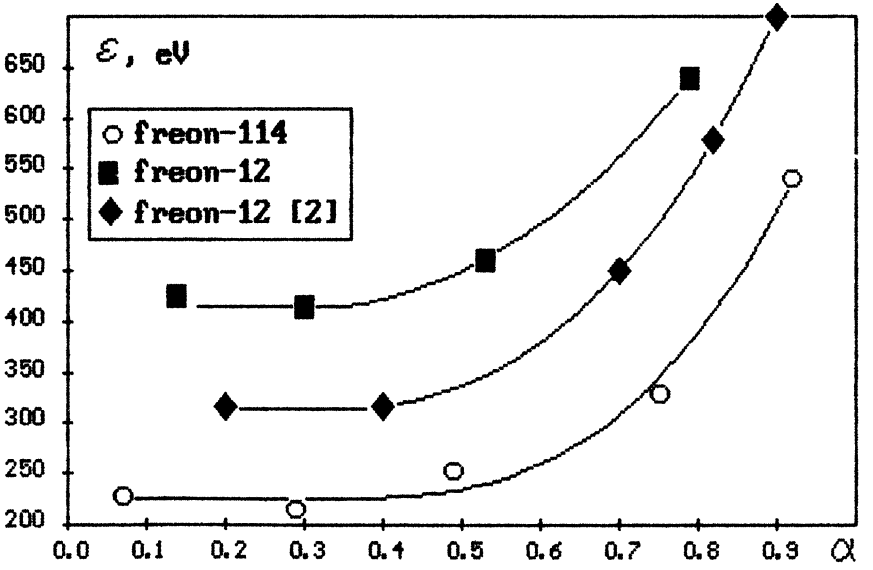
ℰ, eV
650
600
550
500
450
400
350
300
250
200
freon-114
freon-12
freon-12 [2]
0.0
0.1
0.2
0.3
0.4
0.5
0.6
0.7
0.8
0.9
α

fig. 2

Because of the high energetic cost obtained in these experiments, we've carried out experiments with another (low energetical) type of stimulated microwave discharge.

The scheme of experiment and the method of freon concentration measurements were the same as in the previous case.

Fig. 3 gives the main results of the experiments carried out, i.e. α vs η (its content in a mixture with air). One can see the high (up to 90%) freon decomposition level, especially in the mixtures with freon low content. The fact that discharge causes high freon decomposition level is proved indirectly by occurring of a discharge green light characteristic of atomic Cl, and by erosure of the reactor quartz walls witnessing the presence of F_2 in the products of decomposition.

Fig. 4 shows the energetic cost of freon molecule decomposition ϵ vs η. To calculate ϵ we've used not an absorbed energy, but an applied one, determined as energy applied through the reactor cross-section. The validity of using of such a value was checked in a special test experiments.

Thus, it is absolutely clear that the energetic cost of freon molecule decomposition turns out rather low and the energy efficiency of the process - rather high. In some cases the energetic cost of freon molecule decomposition gets similar to the binding energy in Cl molecule. The reduction of freon percent content in a mixture results in the increase of the energetic cost of freon molecule decomposition. For 3% freon-air mixture this value makes $\simeq$ 20 eV/molecule at 90% freon decomposition.

3 Numerical simulation

The results obtained in experiments show the possibility of freon decomposition in mixtures with specific freon content $\eta \sim 10^{-2}$. Till now the possibility of effective destruction of less freon impurities ($\eta \ll 10^{-2}$) has not been proved experimentally because of great difficulties connected with carrying out of quantity measurements of small concentrations (we discovered a simple method for small freon impurity diagnostics used microwave discharge since this paper was

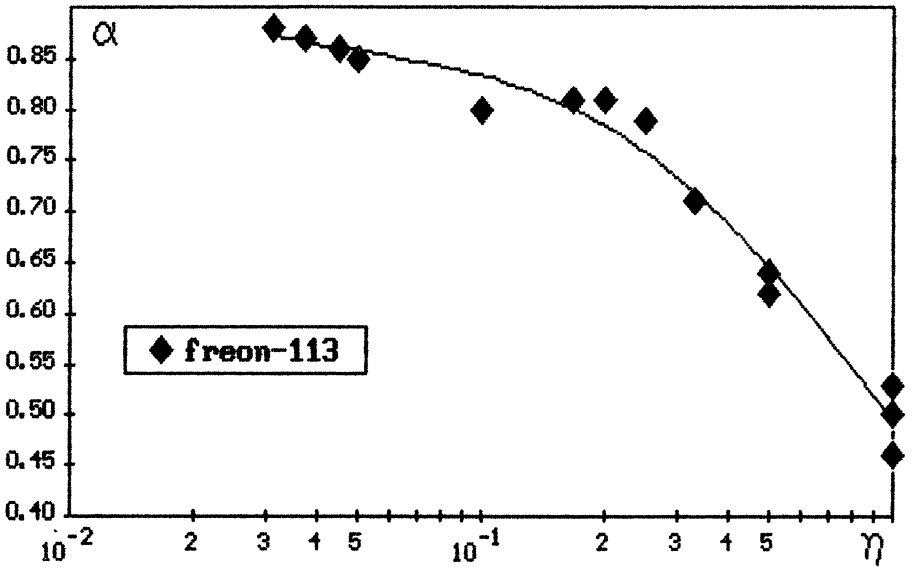
α
0.85
0.80
0.75
0.70
0.65
0.60
0.55
0.50
0.45
0.40
freon-113
10^-2
2
3
4
5
10^-1
2
3
4
5
η

fig. 3

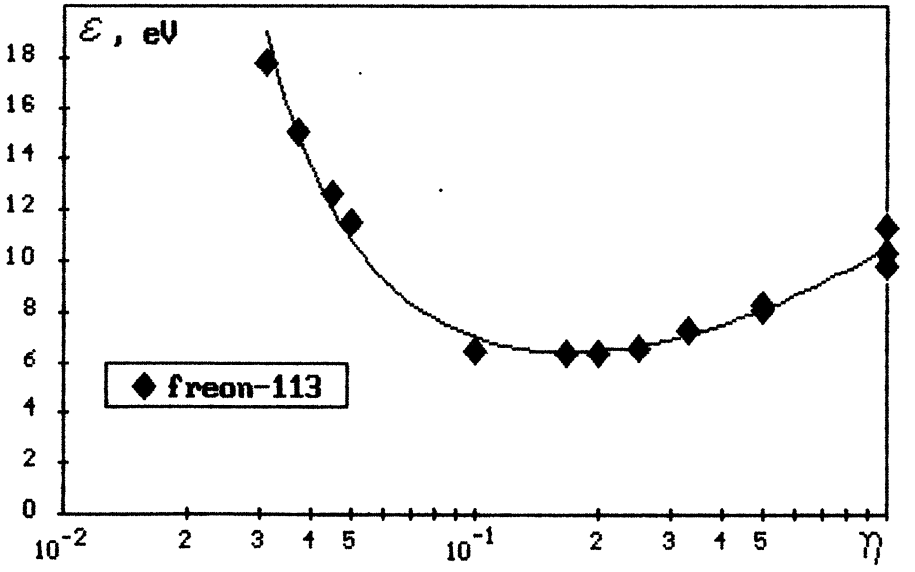
ε, eV
18
16
14
12
10
8
6
4
2
0
freon-113
10^-2
2
3
4
5
10^-1
2
3
4
5
η

fig. 4

written). To estimate energy required for destroying freon impurities in minute amount we have simulated the kinetics of freon destruction in the plasma of the atmosphere microwave breakdown.

We considered [4] two kinetics mechanisms of freon destruction in air: mechanism by way of dissociative attachment of electron to freon molecule (further – DA mechanism) $e + C_mCl_nF_k \rightarrow Cl^- + C_mCl_{n-1}F_k$ and mechanism through resonant transfer of vibrational excitation of nitrogen molecule to autodissociative levels of freon (further - AD mechanism) $N_2(v) + C_mCl_nF_k \rightarrow N_2 + (C_mCl_nF_k)^* \rightarrow Cl + C_mCl_{n-1}F_k$.

The freon destruction modeling was carried out at the example of CCl_4 and CF_2Cl_2 molecules. Each of these compounds is typical for one of two groups of freons. For CCl_4, $C_2F_3Cl_3$, etc. (group I) reaction DA passes rather intensive ($K \sim 10^{-7}\ \frac{cm^3}{s}$ at the thermal electron energies); for CF_2Cl_2, $C_2F_4Cl_2$, etc. (group II) this reaction passes "moderately" (K in the same conditions is $\sim 10^{-10}..10^{-9}\ \frac{cm^3}{s}$).

Kinetics models and assumptions we made described in detail in [4]. The results of DA and AD mechanisms modeling shown that the energetic cost of decomposition freon molecules mixed in minute amounts ($\eta \sim 10^{-9}$) with air in both mechanisms is rather large ~ 1 MeV/molecule. Energetic cost diminishes with increasing η and reaches minimum at $\epsilon > 10$ keV for the DA mechanism and at $\epsilon \sim 0.1$ keV for the AD mechanism. The degree of decomposition for DA mechanism is $\alpha \sim 10^{-4} \ldots 10^{-3}$ in the whole η range, for the AD mechanism it diminishes from $\alpha \sim 10^{-1}$ at $\eta = 10^{-9}$ to $\alpha \sim 10^{-2}$ at $\eta = 10^{-3}$. With increasing η up to $\sim 10^{-3}$ the reaction of dissociative attachment begins to delay the breakdown development, the fact that leads to energy absorbtion increase. For the DA mechanism this leads to ϵ increase. For the AD mechanism the increase of energy absorbtion (i.e. the increase of the number of excited molecules) "works" at freon decomposition: $N_2^* + O_2 \rightarrow O + O + N_2(v)$ (or $O_2^* + N_2(v)$). However, the similtaneous atomic oxygen production, taking place both at the discharge stage and afterglow period, impeds freon decomposition: $N_2(v) + O \rightarrow NO + N$. These contradictive tendencies confine from below the energetic cost in the AD

mechanism in it's present realization.

It is necessary to note that the variation of the electron concentration, produced during breakdown pulse, from 10^{13} cm^{-3} to 10^{12} cm^{-3} decrease energetic cost about two times, but the degree of decomposition under such conditions decrease in order of the value.

4 Conclusions

1. The results obtained in experiments show that repeated microwave discharge treatment reduces freon concentration in the mixture from initial specific content $\eta \sim 10^{-2}$ approximately by a value order with energy cost of decomposition $\epsilon \geq 0.5$ keV. Freon decomposition in a mixtures with high freon content takes place, probably, only in stimulated microwave discharge streamers, there being ratter effective.
2. The type of stimulated microwave discharge we used has ensured a wide energy efficiency of decomposition process (3.5 – 20 eV/molecule) within the range of freon percent content in mixtures.
3. The modeling of decomposition small freon admixtures kinetics in a single breakdown microwave impulse has shown that the energetic cost of decomposition of dissipated in the atmosphere freon impurities ($\eta \sim 10^{-9}$) turns out to be rather large - more than 1 MeV/molecule.

References

1. Radiation and Plasmachemical Methods in Ecology, Moscow Radiotechnical Institute, 1989, 104 pages
2. G.A.Askarian, G.M.Batanov et al. Letters to JETPh, v.55, ed.9, pp.500-504, 1992; Plasma Physics (Russian), v.18, 9, 1992, pp.1198-1210
3. N.L.Alexandrov, K.A.Vakhrameev, et al. Letters to JTPh, v.18, 23, 1992, pp.73-77
4. Yu.F.Kolesnitchenko, D.V.Khmara, Letters to JTPh, v.19, 10, 1993, pp.36-41.

STRUCTURE AND DYNAMICS OF STIMULATED DISCHARGE IN NARROW AND WIDE SHF BEAMS

V.G.Brovkin, Yu.F.Kolesnitchenko
Moscow Radiotechnical
Institute of Russia Academy of Sciences,
Moscow, Russia

Study of the stimulated gas discharges creating by microwave EM beams in the free space has become one of the most important trend in physics of gas discharge at the last ten years. Investigations made by different groups allowed to advance essentially in understanding of this unique object.

However up to the present time all investigations of the microwave discharges were made in the narrow beams with diameter of the order of the wavelength. Study of the microwave discharges in the wide beams with diameter more over than the wavelength is restrained by the deficient power of the existing experimental set-up and it is only possible in a few gases among which the argon is the most widespread. In this work we've aimed to compare the discharge structure and dynamics in narrow and wide SHF beams, because all the previous experiments were made in a narrow beams.

Exploration of stimulated discharge in electromagnetic beams with linear and circular polarization of radiation gave us foundation to formulate the concept of SHF discharge structure formation. It claims, that there is a base element which serves as a basis for forming the structure of the discharge and which is for our opinion a self-organizing plasma running-wave antenna. The antenna type is determined by radiation polarization, the electric field intensity of electro-

magnetic wave, the gas pressure and doesn't change at the variation of two last parameters in some region of values, which we've named a structural zone. The region of stimulated discharge existence is divided into several structural zones (SZ). These zones may be presented as universal, in other words, independent of the type of gas [1]. The most interesting from the point of view of discharge physics seems the wave structural zone with the base element in the form of sinusoid or spiral dependent on the radiation polarization and a streamer-like discharge.

In molecular gases and helium, tested earlier [1], the lowest electric fields of SHF wave, E_* , at which the discharge becomes a streamer-like, turned out rather large, $E_* > 1\frac{kV}{cm}$. Therefore, we've made experiments with argon. Experiments were made at the same conditions as in the case of earlier mentioned gases, i.e. in a linear polarized convergent at an angle 60° beam 7 GHz frequency SHF radiation. The caustic diameter was of the order of wavelength, its depth - about 20 cm. The pressure of argon in a chamber altered from 10 $Torr$ to 760 $Torr$, the SHF pulse duration - from 1 μs to 740 μs, energy flux density - from $10^2\ \frac{W}{cm^2}$ to $2 \cdot 10^4\ \frac{W}{cm^2}$ .The time-space dynamics of formation of the discharge glow picture has been studied with the use of the integral and high-speed methods of photo registration in the visible radiation range.

The conducted experiments showed, that SHF discharge in argon demonstrates the same behavior as the discharges in other gases. The existence of two SZ - the wave and the dipole - was confirmed. the transition from the wave SZ to the dipole SZ takes place at $\frac{E}{p} = (6-7)\frac{V}{cm \cdot Torr}$, the breakdown - at $\frac{E}{p} = (12-13)\frac{V}{cm \cdot Torr}$, where p is the pressure, E - the wave field intensity.

In the mentioned above ranges of pressure and energy flux density the discharge propagation velocity was measured. The results are presented in fig.1.

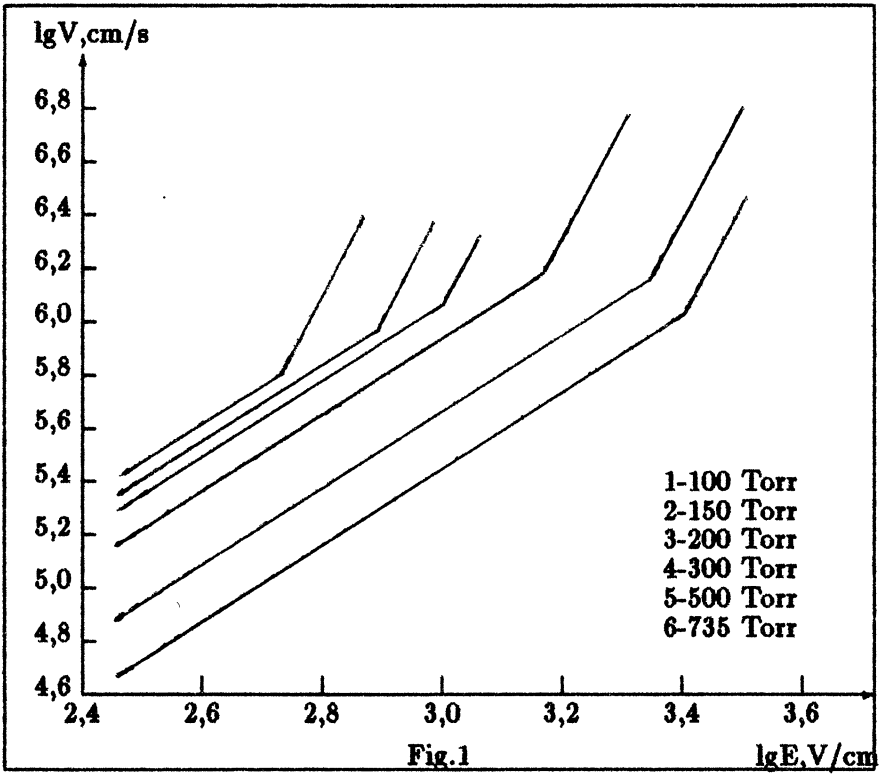

Fig.1

The breaks of the discharge velocity on the plot correspond to transition from wave to dipole SZ. The discharge propagation velocity in wave SZ may be presented in the form $V \sim E^{\mu} \cdot \rho^{-\nu}$, where $\mu = 1,7$, $\nu = 0,7$. The value of μ and ν in dipole SZ are two and four times as much correspondingly to the value μ and ν in wave SZ and have tendency to decrease with pressure increasing from 70 to $200 Torr$. So the values difference of μ and ν becomes small and it may be approved with the definite approximation that the discharge velocity in dipole SZ is a fuction of parameter $\frac{E}{p}$ in the form $V \sim \left(\frac{E}{p}\right)^k$, where $k \simeq 3...4$. The discharge velocity in the points of break is increasing

approximatly from $5 \cdot 10^5 \frac{cm}{s}$ to $3 \cdot 10^6 \frac{cm}{s}$ with pressure increasing from 70 to $300 Torr$. The argon peculiarity is that the spatial size of base element in wave SZ is turning out to be two time smaller. So it is equal to $\sim \frac{\lambda}{8}$. The observing streamers quantity per unit of discharge volume is more larger then in the early investigated gases. The diameter of the streamers in argon are more thiner than in other gases and they are of the order of $0,1 m.m.$ The discharge structure along vector E has the treelike (as fractal) character. Moreover the discharge was streamer-like at the lowest SHF energy flux density, that was available at a given regime of set up operation, i.e. from $100 \frac{W}{cm^2}$. Thus, it became clear, that the magnitude of electric field strength E in argon is less than $200 \frac{V}{cm}$. With receiving this result the opportunity to investigate SHF discharge in a wide beam was opened. The technical possibilities of the set up are such that give opportunity to diminish the convergent angle 5 times only. Correspondingly, the diameter of SHF beam increases at the same scale. In this regime of set up operation the SHF flux density altered from several $\frac{W}{cm^2}$ to $300 \frac{W}{cm^2}$. Experiments were made in a pressure range from $10 Torr$ to $300 Torr$. The critical electric field intensity was determined as $E = 60 \frac{V}{cm}$ and critical pressure $10 Torr$. The discharge structure in a wide beam looks like a structure "gathered" from the discharge structures in a narrow beams. Thus, the wide beam doesn't change the base element of SHF discharge structure. The comparison of the discharge velocity propagation in wide and narrow beams at the same pressure and energy flux density demonstrates their coincidence within the bounds of accuracy of measurements. To our opinion, these facts are the complementary evidence in favor of idea that the base element is a self-organizing reception antenna.

References

1. V.G.Brovkin, Yu.F.Kolesnitchenko. In: Proceedings of XX International Conference on Phenomena in Ionized Gases, Pisa, Italy, 1991

LOCALIZATION OF ABSORPTION OF MICROWAVE ENERGY ACCOMPANYING COMBINED ACTION OF MICROWAVE AND LASER RADIATION IN GAS

A. M. Akhmeteli

M. V. Lomonosov Moscow State University, Physics Department, 119899 Moscow, Russian Federation

1. Introduction. For many applications of gas discharge in wave fields it is necessary to inject considerable energy into small volume of matter in short time, thus achieving high specific power input. Diffraction sets lower limits to the transverse dimensions of the electromagnetic beam and represents a fundamental obstacle in the way to this end. A standard method to circumvent diffraction constraints by use of shorter wavelengths is connected usually with serious technical difficulties and lower efficiency. Multi-pass heating of small conducting regions, e.g., in resonators or waveguides, is unacceptably slow for many applications and it is practically impossible to use it to heat distant or inaccessible regions. Nonlinear effects, e.g., self-focusing, are very useful for some applications, but they often demand electron density minimum in the heated region and/or very high beam intensity.

In this context author's recent papers [1,2] seem to be of considerable interest, as they point out conditions of efficient absorption of energy of an electromagnetic beam in a conducting cylinder with transverse dimensions much less than those of the beam. These results were obtained in the frames of the linear electrodynamics and open a possibility of one-pass efficient heating of the region with two dimensions out of three several orders less than those of the beam, which are determined by the diffraction constraints. This allows one to

achieve very high specific power input in many applications and, as a result, high temperatures.

The above-mentioned results, when applied to the electromagnetic discharge in a dense gas, may be used as follows. As combined action of microwave and laser radiation in gas may be accompanied by considerable decrease of discharge thresholds for both kinds of radiation [3], for proper choice of intensities of the microwave and laser beams the discharge will be localized in a thin region where the waist's regions of these beams overlap. Dimensions of this region will be determined by the diffraction constraints for the laser beam, which are relatively weak. If conditions of papers [1,2] are satisfied, the discharge region is heated efficiently by relatively inexpensive energy of the microwave beam.

2. The conditions of efficient absorption of a broad electromagnetic beam in a thin conducting cylinder. Let the axes of a gaussian electromagnetic beam (frequency ω_1) and of the cylinder coincide, the focal waist's region's radius be r_1, the cylinder's radius be r_2, cylinder overlaps completely the length of the waist's region, dielectric and magnetic permittivities of the cylinder are $\varepsilon_2=\varepsilon=\varepsilon'+i\varepsilon''$ and $\mu_2=1$, those of free space are $\varepsilon_1=1$ and $\mu_1=1$. To estimate a share of the beam's energy, absorbed in the cylinder, we assume that skin-depth δ_s is roughly equal to the diameter of the cylinder: $4r_2^2=c^2/(4\pi\omega_1\sigma)=\delta_s^2$, where σ is the cylinder's conductivity ($\varepsilon''=4\pi\sigma/\omega_1$). If we assume that the electric field's modulus inside the overlap of the cylinder and the waist's region is of the same order as that in the focus in the incident wave (this assumption is far from being always true, but it helps to un-

derstand the scaling of this problem), then it may be shown [1] that $\eta=W^a/W$ - the share of complete beam's power that is absorbed in the cylinder, is equal to 1 up to the order of magnitude. Qualitative explanation: due to absorption in the cylinder a fall on the axis in the fields distribution occurs. This fall causes axis directed diffractive diffusion of the field from the whole waist's region. In a more rigorous semiquantitative calculation we consider an incident cylindrical wave of TM or TE type (z-component of the electric or magnetic Hertz vector is equal to $\exp(i(\gamma z+n\phi-\omega_i t))\cdot J_n(\varkappa_i r)$, $\gamma^2+\varkappa_i^2=k_i^2=\varepsilon_i\mu_i k_o^2$, $k_o=\omega_i/c$, $J_n(x)$ is Bessel function). Diffraction on an infinite cylinder generates two refracted waves - of TM and TE type (z-components of the electric (magnetic) Hertz vector are equal to a_2F and b_2F correspondingly, where $F=\exp(i(\gamma z+n\phi-\omega_i t))\cdot J_n(\varkappa_2 r)$, $\gamma^2+\varkappa_2^2=k_2^2=\varepsilon_2\mu_2 k_o^2$). Calculating the amplitudes a_2 and b_2, one may calculate the linear power of energy absorption. We assume that if the cylinder is irradiated by a coaxial gaussian beam with the same intensity and field structure in the focus as on the axis of the cylindrical wave and the waist's diameter is roughly equal to the width of the first maximum of the cylindrical wave with n=1 ($r_1\approx 2/\varkappa_1$), then over the length of the beam's waist's region the same linear power is absorbed. In the frames of the semiquantitative method direct calculation was performed and also for the case of long beams ($l_1\gg r_1$) and thin cylinders ($r_2\ll r_1$) an analytical estimate of the share of the power absorbed in the cylinder was obtained [2]:

$$\eta=\frac{W^a}{W}\approx 4\mathrm{Im}\left(\left(p_2\frac{J_o(p_2)}{J_1(p_2)}\left(p_2^{-2}+\tfrac{i}{2}a^{-2}\right)+\ln p_1\right)^{-1}\right).$$

Let us describe most important domains of parameters that correspond to the efficient absorption of beam's power (typi-

cally $\eta=(2\div5)/L$, where $L=|\ln p_1|$): 1). $|p_2|\ll 1$, $x=a^{-2}L^{-1}<1$, $|x-1|\gg L^{-1}$, $\varepsilon''\simeq \max(|y+2x/(x-1)|, 2x(x-1)^{-2}L^{-1})$, $|y|\lesssim 2x(1-x)^{-2}$. Here $y=\varepsilon'-1$. 2). $p_2''\gtrsim 1$ ($p_2=p_2'+ip_2''$), $4L\lesssim\varepsilon''\lesssim 8a^2L^2$, $y\simeq 4a^2L^2$. 3). $p_2''\gtrsim 1$, $|y|\lesssim 4a^2L^2$, $\varepsilon''\simeq 8a^2L^2$, $a^2\gtrsim 1/(2L)$. The domain 1) may be roughly defined by the condition: the skin-depth, the cylinder's diameter and the wavelength are of the same order of magnitude. In the domain 3) cylinder's diameter is of the same order or greater then the skin-depth and the wavelength, and $2r_2/\delta_s\simeq\sigma/\omega_1$. It should be noted, that the above-mentioned domains have non-resonant character, and inside them the value of conductivity may vary by several times (and in the second domain - by several orders) without loss of efficiency of absorption. As the transfer of the results from the cylindrical wave upon a wave with finite power may cause doubts about such an approach, a control quantitative calculation has been performed. In a transverse section far from the focus a limited in the transverse direction distribution of the fields in the incident wave was fixed, with the help of numerical Fourier - Bessel transform the incident field in full space was presented as a linear combination of cylindrical waves, for each of them a problem of diffraction on an infinite cylinder was solved exactly [4]; after that reflected and refracted fields were calculated with the help of back Fourier - Bessel transform. The control calculation in the semiquantitative and quantitative methods gave values $\eta=27\%$ and $\eta=18\%$, correspondingly. So the semiquantitative method is satisfactory enough.

The analysis of the above-mentioned domains shows that they do not allow to heat efficiently cylinders with diameter much less than the wavelength. Such possibility has been found

in another ("transverse") geometry, where a converging axisymmetrical cylindrical wave with the direction of electric field vector along the axis (z-component of the electric Hertz vector has the form $\exp(-i\omega_1 t)\cdot H_0^{(2)}(k_0 r)$, where $H_0^{(2)}(x)$ is Hankel function) falls upon a cylinder. If $a=k_0 r_2 \ll 1$ (radius of the cylinder is much less than the wavelength), $|\ln a| \gg 1$, $\varepsilon'' \gtrsim |\varepsilon'|$, $\varepsilon'' \simeq 2a^{-2}|\ln a|^{-1}$ (roughly speaking, skin-depth is of the order of the cylinder's diameter), then the share of power of the incident wave, that is absorbed in the cylinder, is equal to $\simeq \pi|\ln a|^{-1}$ and is quite considerable.

3. Applications to the discharge in a dense gas under the combined action of the microwave and laser radiation. The achieved results may have numerous applications. Here we discuss only their realization in a discharge in a dense gas under the combined action of microwave and laser radiation. It is known that their combined action may cause considerable decrease of gas discharge threshold for both types of radiation [3]. For proper choice of intensities the discharge will take place only in the zone of overlap of the focal waist's regions of the microwave and laser radiations. The dimensions of the resulting ionized region will be determined by relatively weak diffractive constraints for the laser radiation. This zone may play the role of the conducting cylinder, where a considerable part of power of a much broader microwave beam will be absorbed. The electron density in the zone of discharge will be above the critical one for the microwave radiation (the microwave energy will be supplied to this zone sideways) and well below critical for the laser radiation, so the latter will pass the length of the zone without significant losses. Thus, the ionization will

be much more uniform, than, e.g., in a long laser spark. Optimal conductivity of the zone may be provided by proper choice of intensities. This scheme may be used to form long ionized or low density channels in the atmosphere or for plasma chemistry, especially if high sterility of reactions is necessary.

In a numerical example let the wavelength of the microwave radiation be λ_1=8mm and that of the laser radiation be λ_2=0.25mkm. Then for laser radiation intensity $\simeq 10^8 Wt \cdot cm^{-2}$ the microwave discharge threshold in air for normal conditions ($\simeq 10^6 Wt \cdot cm^{-2}$) will decrease 1.5÷2 times (cf. [5]). Let the diameter of the ionized zone be $\approx$ 2.5mm and the resulting electron density $10^{14} \div 10^{15} cm^{-3}$. Then $\omega_1 < \omega_p < \nu$, where ω_p is the plasma frequency, ν is the collision frequency. For optimal electron density conditions of domain 1) are satisfied, and in the ionized zone 20÷35% of the energy of the microwave beam (with transverse dimensions 2÷3 orders more than those of the zone) is absorbed. In this way a long ionized channel ($\simeq$ 100m) may be heated by the microwave energy. In transverse geometry one can heat intensively in a laboratory an extremely thin highly conducting channel with the length of the order of the microwave length.

References

1. Akhmeteli A.M., Pis'ma v ZhTF, 1991, **17**, #11, 21 (in Russian).
2. Akhmeteli A.M., submitted to Pis'ma v ZhTF, 1993 (in Russian).
3. Darmanyan A.P., Mitsuk V.E., Chernikov V.A., Pis'ma v ZhETF, 1968, **8**, 117 (in Russian).
4. Wait J.R. Electromagnetic radiation from cylindrical structures. London: Pergamon, 1959.
5. Akmanov A.G., Rivlin L.A., Shil'dyaev V.S., Pis'ma v ZhTF, 1968, **8**, 417 (in Russian).

Kinetics of charged and neutral components in a non-equilibrium plasma of a free localized microwave discharge in air

A.F. Aleksandrov, A.A. Kuzovnikov,
V.M. Shibkov, A.S. Zarin

Dept. of Physics, Moscow State University,
119899 Moscow, Russia

In many plasma applications it's necessary to use the energy supply systems without electrodes. One of possible ways to supply energy without electrodes is to use the free localized microwave discharge in the focused beam of electromagnetic energy. The successful use of the microwave discharge in many applications make it necessary to research the physics of a new kind of discharge - the electrodeless microwave discharge in the focused beam in the free space and search for ways to optimize this discharge parameters. The different channels of energy transmission into translational degrees of freedom of molecular gas which lead to fast gas heating are investigated in this work. The time evolution of the electron energy distribution $f(\varepsilon)$

$$\frac{\partial n(\varepsilon,t)}{\partial t} = -\frac{\partial J_f}{\partial t} - \frac{\partial J_L}{\partial t} + \mathrm{In} + \mathrm{Sup} + \mathrm{Rot},$$

the vibrational distribution function $f(v)$ of N_2 molecules in the electronic ground state

$$\frac{\partial n_V}{\partial t} = \left(\frac{\partial n_V}{\partial t}\right)_{eV} + \left(\frac{\partial n_V}{\partial t}\right)_{VV} + \left(\frac{\partial n_V}{\partial t}\right)_{VT} + \left(\frac{\partial n_V}{\partial t}\right)_{eD} + \left(\frac{\partial n_V}{\partial t}\right)_{VD} + \left(\frac{\partial n_V}{\partial t}\right)_{XV}$$

the molecules concentrations of N_2 and O_2 in the $A^3\Sigma_u^+$, $B^3\pi_g$, $C^3\pi_u$, $a'^1\Sigma_u^-$, $a^1\pi_g$, $a^1\Delta_g$, $b^1\Sigma_g^+$ states

$$\frac{\partial n_X}{\partial t} = \left(\frac{\partial n_X}{\partial t}\right)_{eX} + \left(\frac{\partial n_X}{\partial t}\right)_{XX} + \left(\frac{\partial n_X}{\partial t}\right)_{XY} + \left(\frac{\partial n_X}{\partial t}\right)_{XV} + \left(\frac{\partial n_X}{\partial t}\right)_{XR},$$

the concentrations of the N, O, O_3, NO, NO_2, N_2O

$$\frac{\partial n_Y}{\partial t} = \left(\frac{\partial n_Y}{\partial t}\right)_{Yi} + \left(\frac{\partial n_Y}{\partial t}\right)_{YX} + \left(\frac{\partial n_Y}{\partial t}\right)_{YY},$$

the concentrations of the n_e, O^-, O_2^-, O_3^-, O_4^-, NO^-, NO_2^-, N_2O^-, n^+

$$\frac{\partial n_i}{\partial t} = \left(\frac{\partial n_i}{\partial t}\right)_{ii} + \left(\frac{\partial n_i}{\partial t}\right)_{iX} + \left(\frac{\partial n_i}{\partial t}\right)_{iY} + \left(\frac{\partial n_i}{\partial t}\right)_{iV}$$

and the gas heating

$$cn_0 \frac{\partial T_g}{\partial t} = \left(\frac{\partial T_g}{\partial t}\right)_{el} + \left(\frac{\partial T_g}{\partial t}\right)_{VT} + \left(\frac{\partial T_g}{\partial t}\right)_{VV} + \left(\frac{\partial T_g}{\partial t}\right)_{XT} - Q_{losses}$$

were calculated for conditions of the free localized microwave discharge in air. The comparison of experimental and calculated data are carried out (see Fig. 1-10).

The data obtained let us conclude that for high values of reduced electric field quenching of electronically excited states of nitrogen molecules is one of the main mechanisms resulting in gas heating in the pulse discharge in air.

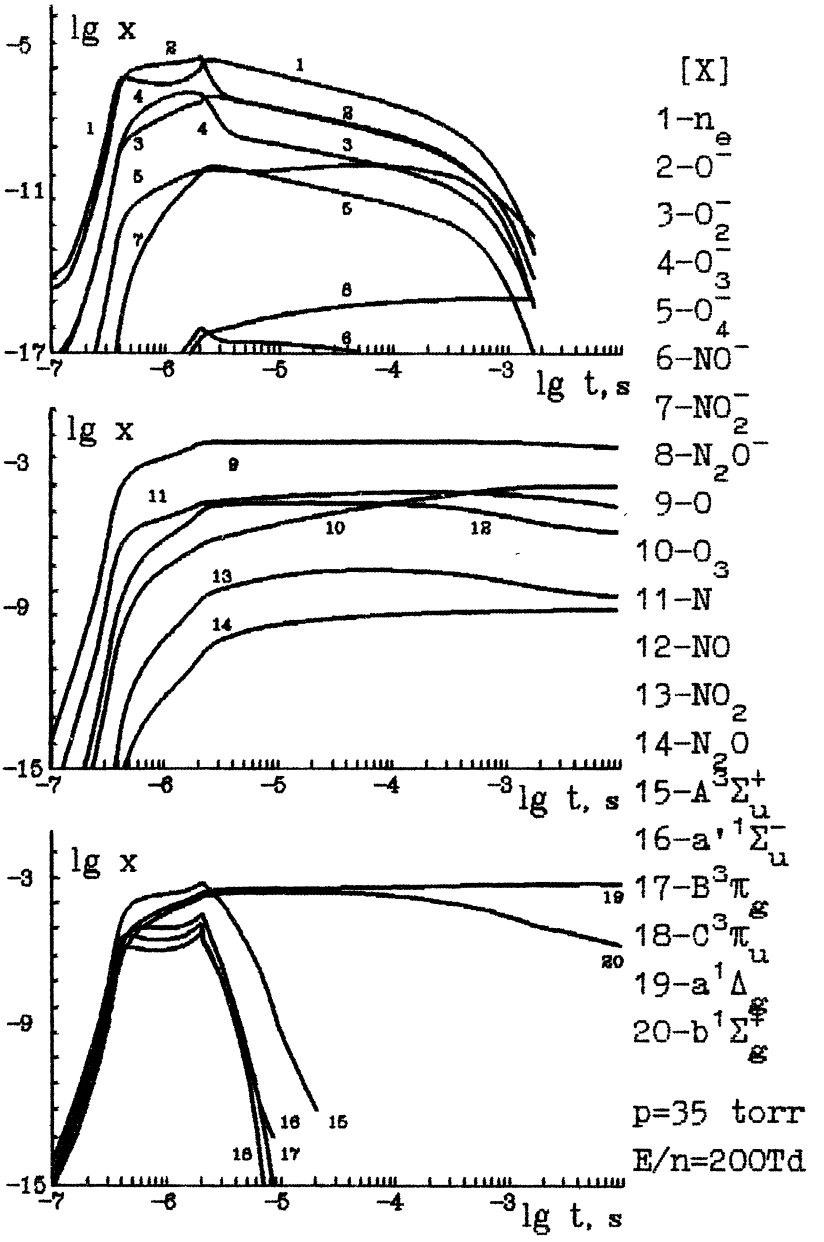
lg x
lg t, s
[X]
1-n_e
2-O^-
3-O_2^-
4-O_3^-
5-O_4^-
6-NO^-
7-NO_2^-
8-N_2O^-
9-O
10-O_3
11-N
12-NO
13-NO_2
14-N_2O
15-$A^3\Sigma_u^+$
16-$a'^1\Sigma_u^-$
17-$B^3\pi_g$
18-$C^3\pi_u$
19-$a^1\Delta_g$
20-$b^1\Sigma_g^+$
p=35 torr
E/n=200Td

Fig. 1.

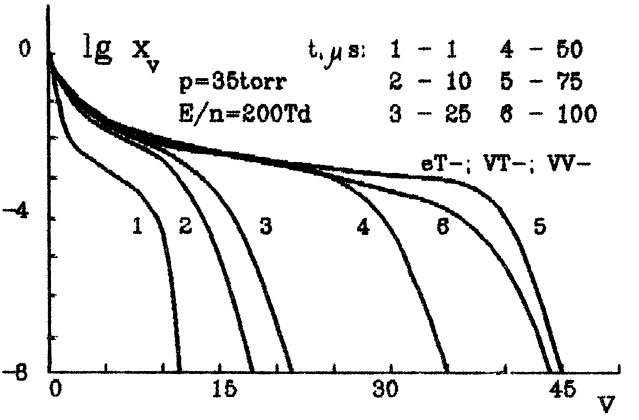

Fig. 2.

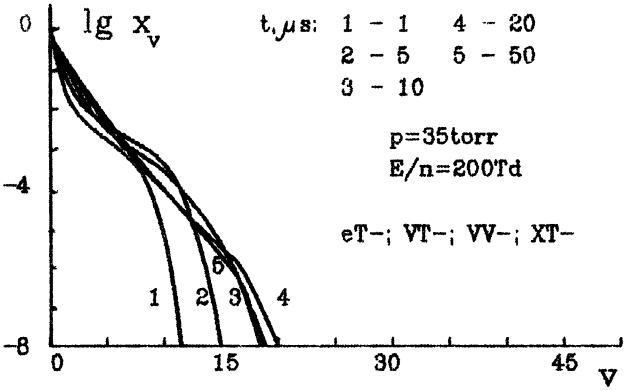

Fig. 3.

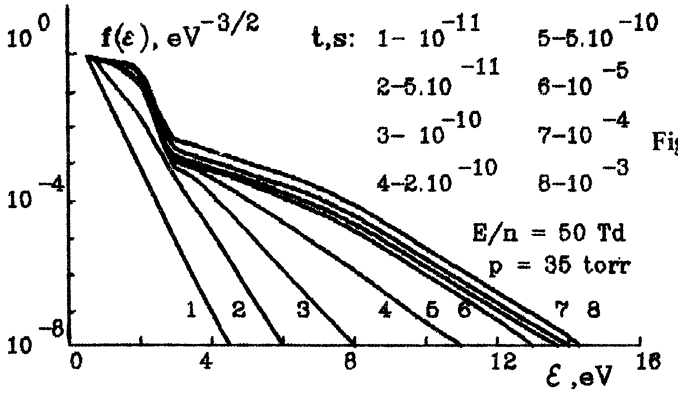

Fig. 4.

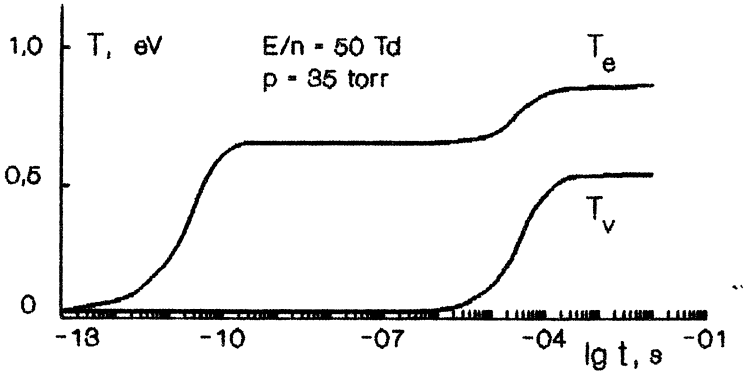

Fig. 5.

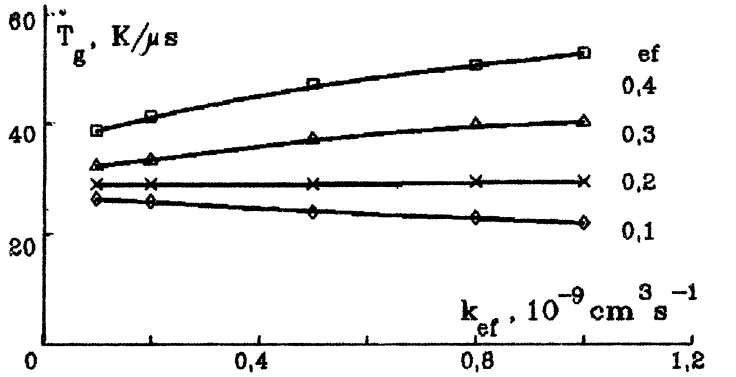

Fig. 6.

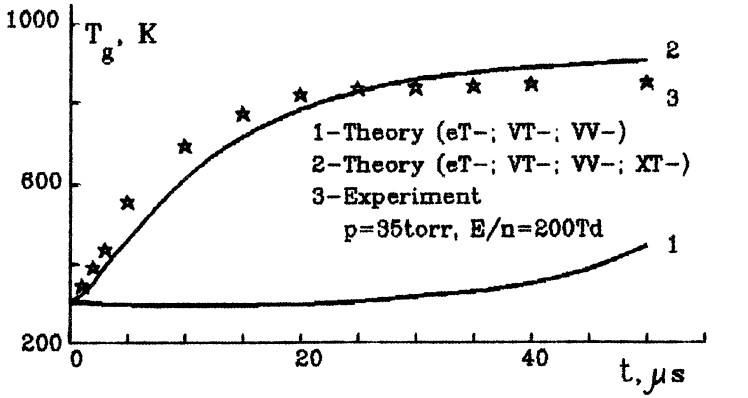

Fig. 7.

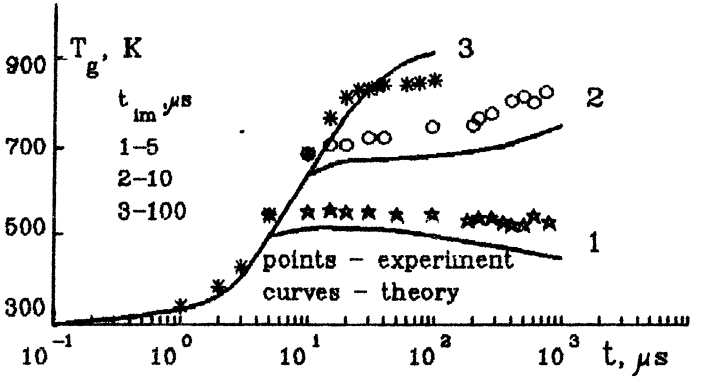

Fig. 8.

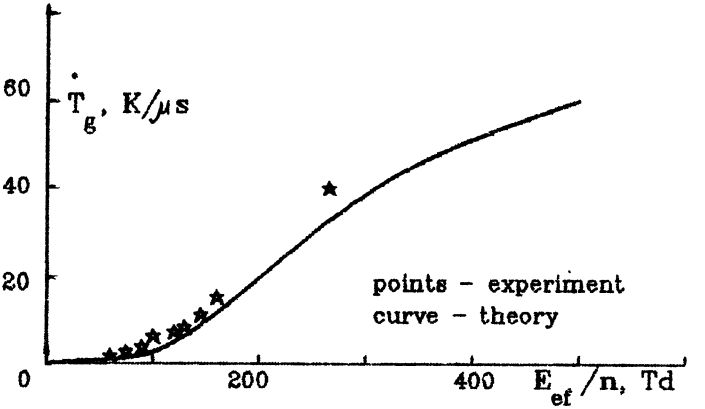

Fig. 9.

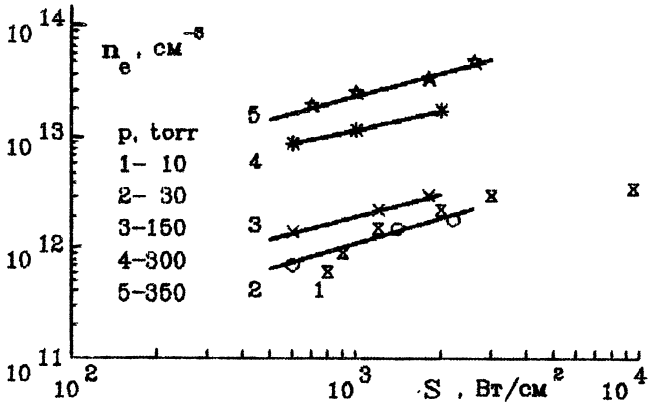

Fig. 10.

THE DECAY OF STRONG MICROWAVE DISCHARGE PLASMA IN AIR

N.A.Popov

Computing Center of Russian Academy of Sciences, Moscow

Recently various applications of the high power $\mu\omega$ discharges such as the generation of the artificially ionized layers, the destruction of freons in the stratosphere [1] et al. have been actively investigated.

Currently the significant volume of the experimental data concerning the kinetics of nitrogen-oxygen mixtures, excited by the strong discharges have been accumulated. The analysis of the available data allows to indicate a number of basic problems without adequate theoretical justification. These include the rapid gas heating in the discharges with the high reduced electric field number as well as the delay (as compared to the recombination time) of the high power $\mu\omega$ discharge plasma decay. The following discussion is devoted to the mentioned aspects.

The matching feature of the nitrogen-oxygen mixtures excited by strong discharge consist in the high efficiency of the oxygen molecules dissociation (as it follows from [2,3], the dissociation degree may be up to 30%). The oxygen atoms and the vibrationally-excited nitrogen molecules, being the basic long-lived components, can be involved in the associative ionization processes during the afterglow.

The oxygen atoms recombination occurs in the three-body process leading to the ozone molecules production. However, if the O_2 dissociation degree is high (which is the case under conditions being discussed), the reactions with the $O(^1S)$ productions:

$$O(^3P) + O(^3P) + O(^3P) \rightarrow O(^1S) + O_2(\upsilon), \quad 2\cdot10^{-32}\,cm^6/s, \quad (1)$$

$$O(^3P) + O(^3P) + M \rightarrow O_2^* + M, \quad 4.7\cdot10^{-34}\,cm^6/s, \quad (2)$$

$$O_2^* + O(^3P) \rightarrow O_2(\upsilon) + O(^1S), \quad 4.5\cdot10^{-11}\,cm^3/s, \quad (3)$$

become important.

To find out the main channels of the $O(^1S)$ generation in the stratosphere these processes have been investigated in aeronomia for a long time. In the [4] the data indicating the key role of the reactions (2,3) with $O_2^* = O_2(A^3\Sigma_u, v\geq5)$ in the $O(^1S)$ formation processes have been obtained.

Here for the first time the reactions of the associative ionization involving the excited $O(^1S)$ atoms are included in the model for simulation of the discharge plasma decay:

$$O(^1S) + O(^1S) \rightarrow e + O_2^+, \quad (4)$$

$$O(^1S) + N(^4S) \rightarrow e + NO^+. \quad (5)$$

These reactions proceed without the activation barrier and under given conditions their rates are about $3\cdot10^{-11}\,cm^3/s$.

In general the $O(^1S)$ quenching occurs due to the reactions:

$$O(^1S) + O_2 \rightarrow O(^3P, ^1D) + O_2, \quad 4\cdot10^{-12}\exp(-870/T)\ cm^3/s, \quad (6)$$

$$O(^1S) + O(^3P) \rightarrow 2\cdot O(^3P, ^1D), \quad 5\cdot10^{-11}\exp(-310/T)\ cm^3/s. \quad (7)$$

The reaction:

$$O(^3P) + N_2(\upsilon) \rightarrow N(^4S) + NO \quad (8)$$

is the dominant nitrogen atom source during the afterglow. This reaction rate is essentially dependent on the vibrational excitation of the nitrogen molecules. The rate value was used in this calculation procedure according to [6].

The distinctive feature of the present model in the part concerning the gas heating is the account of the metastable $O(^1D)$ atom quenching by the nitrogen molecules:

$$O(^1D) + N_2 \rightarrow O(^3P) + N_2(v) + \Delta T.$$

On the basis of the results [6] et al., the 67% of the $O(^1D)$ excition energy was supposed to be spent on the gas heating.

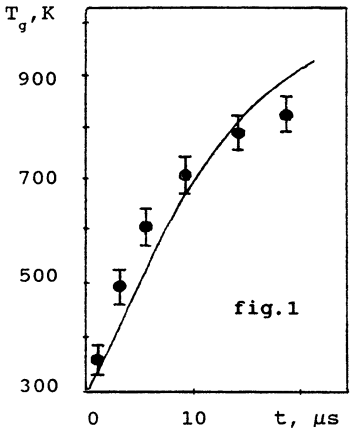

The results of our gas heating calculations (curves) and the experimental data [7] (points) are shown in **fig.1**. The decreasing of the gas heating rate at $t \geq 10$ μs is related to the discharge propagation towards the radiation source and to the electric field amplitude reduction in the region under consideration.

The calculation results and the experimental data [8] concerning the gas heating dynamics during the afterglow are presented in **fig.2**. In this case the VT- relaxation of the N_2 vibrational excitation on the oxygen atoms is the main heating channel.

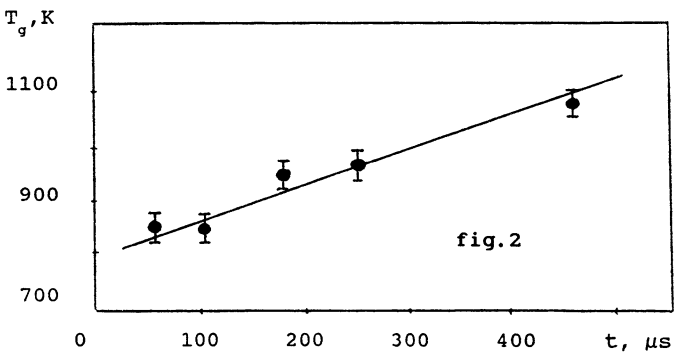

$N_e = 2 \cdot 10^{12}$ cm^{-3}, E/N= 100 Td, τ= 30 μs, P= 30 Torr.

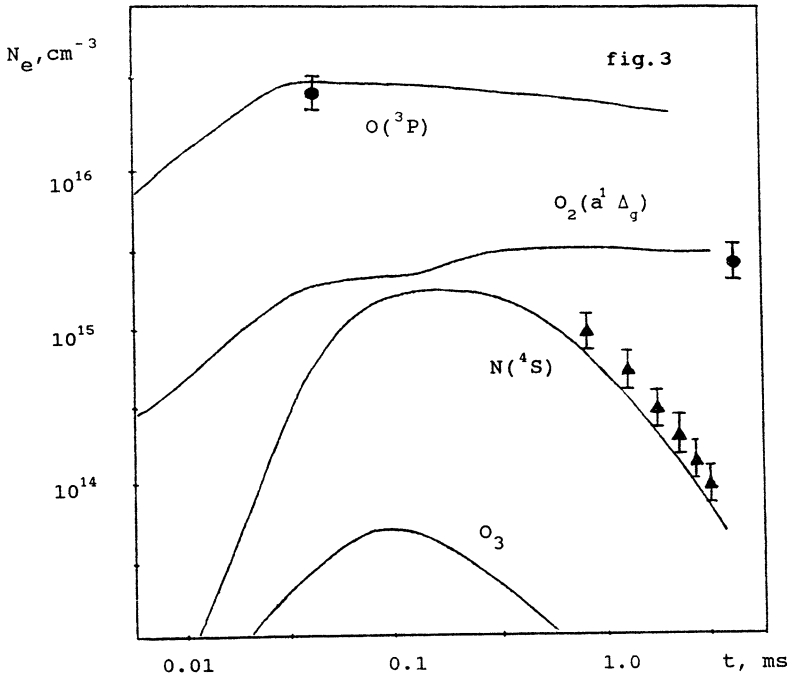

The calculation results and experimental data on evolution of the nitrogen-oxygen mixture (N_2:O_2=4:1) are illustrated in **fig.3** for the following conditions: N_e= $5\cdot10^{11}$ cm^{-3}, E/N= 140 Td τ= 30 μs, P= 30 Torr [2]. As it can be seen, after the $\mu\omega$ discharge pulse the nitrogen atom concentration grows due to the reaction (8) initiated by the vibrational N_2 excitation. It should be noted that the nitrogen atoms are involved in the associative ionization reaction (5) and so the $N(^4S)$ atom destruction explicitly affects the characteristic plasma decay times.

In a series of the experiments (for example [1,9-10]) the significant increase of the decay times (in comparison with the recombination times) for the plasma induced by the strong pulse $\mu\omega$ discharge, has been detected. In these cases the decay was of the recombination but not of the attachment character.

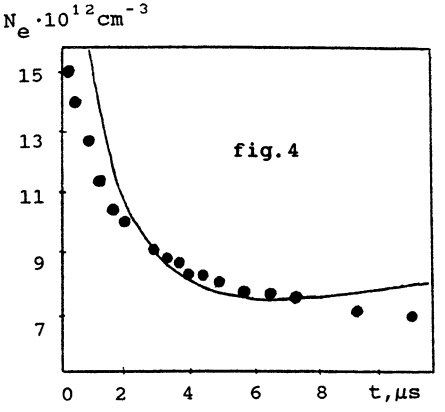

fig.4

The results of the calculation of the $N_2:O_2$=4:1 mixture dynamics under the action of the μω discharge with the parameters considered in the paper [1] are shown in **fig.4**. (E/N= 170 Td, τ= 6 μs, P= 54 Torr). In the kinetic process simulation the electric field has been represented as:

$$E = E_o / |1- \omega_e^2 / \omega \cdot (\omega - i \cdot \upsilon_m)|$$

where ω_e is the plasma frequency, ω is the μω radiation frequency, υ_m is the effective electron collision frequency. Under the conditions of the experiment [1] the field begins to vary after $N_e \geq 10^{13} cm^{-3}$.

The $O(^1S)$ and $N(^4S)$ atoms are the main particles controlling the associative ionization processes. During the afterglow the $O(^1S)$ atoms are generated as a result of $O(^3P)$ atom recombination reactions (1-3), while the nitrogen atoms are produced in the reaction (8), stimulated by the vibrational excitation of N_2. The $N(^4S)$ atoms actively participate in the associative ionization processes, and this fact leads to the NO^+ ion formation. These ions are responsible for the ion mixture content and hence for the recombination rate during the afterglow.

The data indicating the slow decay of the μω discharge plasma has been also obtained in [10]. To interprete such data the authors had to suppose the thermal ionization in the discharge region as well as the temperature about 7000 K. The present model

allows to account for these results by means of including the associative ionization reactions. In this case the gas heating does not exceed 600K that agrees with the measured in [7] value.

Thus in this work the model simulating the kinetic processes in the nitrogen-oxygen mixtures excited by the strong pulse discharge has been developed. The gas heating in the discharge is treated with account of the metastable $O(^1D)$ atom quenching by the nitrogen molecules. The effective proceeding of the associative ionization reactions, involving excited atoms has been shown possible. The reactions taking into account allow to understand the increase of the induced plasma life time.

The calculation results adequately represent the available experimental data on the air heating dynamics during the discharge pulse, as well as the electron, nitrogen and oxygen atom concentration evolution during the afterglow.

References

1. Askaryan G.A., Batanov G.M., Barhudarov A.E. et al. // Sov.Plasma Phys. **18**, 1198, 1992.
2. Kulikov V.N., Mitsuk V.E. // Sov. JTF Lett. **14**, 233, 1988.
3. Aleksandrov N.L., Konchakov A.M.// Sov.JTF Lett. **16**, 1, 1990.
4. Stott I.P., Thrush B.A. // Proc.R.Soc.Lond. 1989. A 424. P.1.
5. Popov N.A. // Sov. JTF Lett. **19**, 89, 1993.
6. Dmitrieva I.K. et al.// Preprint № 24. Minsk, 1985. (in Russ.)
7. Aleksandrov A.F., Devjatov A.M., Kuzovnikov A.A. et al. // Proc. X-th ESCAMPIG. France, 1990. P.179.
8. Berdyshev A.V., Vikharev A.L., Gytlin M.S. et al. // Sov. Tepl. Vys. Temp. **26**, 661, 1988.
9. Vikharev A.L., Ivanov O.A., Stepanov A.N. // Sov.Plasma Phys. **10**, 792, 1984.
10. Grachev L.P. et al. // Sov. JTF. **59**, 149, 1988.

NITROGEN LASER EXCITED BY A NANOSECOND MICROWAVE DISCHARGE IN THE FIELD OF A CYLINDRICAL TE MODE

A.L. Vikharev, A.M. Gorbachev, O.A. Ivanov, A.L. Kolisko
Inst.Applied.Phys.,N.Novgorod,Russia
L.S.Ivanova
Inst.Water Transp.Engin.,N.Novgorod

1. Pumping of a gas laser by a microwave gischarge is a relatively new method. The interest in it was aroused by recent intense progress in high-frequency electronics and physics of the gas discharge in microwave field. At present a number of successful experiments has been performed on excitation of gas laser by a microwave discharge [1-4]. The main advantages of this method are simplicity of energy input to a laser device, absence of instabilities initiated by electrodes in electric-discharge lasers, long-term preservation of purity of the working mixture due to the absence of electrodes, non-critically to pre-ionization and high homogeneity of the discharge.

The most traditional scheme that was used in experiments is pumping by a longitudinal microwave discharge in a single-mode waveguide [2,3]. A considerable drawback of waveguide structures is the limitation to the value of microwave power transported through the waveguide; this limitation is connected with breakdowns of the microwave line. On the other hand, advances in microwave electronics is to a great extend due to use multi-mode, rather than single-mode, and oversized electrodynamic systems [5]. Energy output from such

devices is usually a wave beam,and it is transported by means mirror line.

High energetic characteristics of modern relativistic generators makes them rather attractive for pumping of excimer laser and lasers on electron transitions of molecules, i.e., those lasers that require high energy contribution in a short time. The results of first experiments using relativistic microwave generators are presented in [3,6]. It should be noted, however, that these papers describes mainly the design versions of lasers and parameters of their generation, but pay little attention to the analysis of the work of the lasers associated with electrodynamics and kinetics of the microwave discharge.

This paper presents the results of numerically modeling a nitrogen laser excited by a nanosecond microwave discharge in the cylindrical TE mode in a tube and in free space. Self-consistent dynamics of the microwave discharge is analyzed with that of laser generation. Comparison with the experimental results is made.

2. In accord with the geometry of the experiment performed [4] we will consider a discharge in the cylindrical TE mode (vector of the electric field is $E\exp(i\omega t)$ is directed along the discharge axis). When describing field evolution in the discharge with electron density varying slowly (on the scale $1/\omega$) due to ionization we will base upon the scalar Helmholtz equation for the complex amplitude of the field $E(r,t)$:

$$\frac{l}{r}\cdot\frac{\partial}{\partial r}\left(r\cdot\frac{\partial E}{r}\right)+\epsilon\cdot k^2\cdot E=0\,,\ c=1-\frac{N_e}{N_c}\left(1+i\cdot\frac{\nu}{\omega}\right)\,, \qquad (1)$$

where ϵ is complex dielectric permitivity of plasma, and $k = w/c = 2\pi/\lambda$. Electron density was determined by the following equation:

$$\frac{\partial N_e}{\partial t}=D_a\cdot\frac{l}{r}\cdot\frac{\partial}{\partial r}\left(r\cdot\frac{\partial N_e}{\partial r}\right)+\left(\nu_i\left(\frac{|E|}{p}\right)-\nu_a\right)\cdot N_e-\alpha\cdot N_e^2\,, \quad (2)$$

where ν_i and ν_a are frequencies of ionization by an electron impact and dissociative attachment, D_a is coefficient of ambipolar diffusion,and α is coefficient of dissociate electron-ion recombination.

Power of induced radiation per volume unit was calculated within the frames of the simplified kinetic model [7]. For this, equations (1) and (2) were supplemented with the balance equations for population of the upper $N_c(v=0)$ and lower $N_b(v=0)$ laser levels and photon density N_{ph}:

$$\begin{aligned}
\frac{\partial N_c}{\partial t} &= k_c\, N\, N_e - \frac{N_c}{\tau_c} - \sigma\, c\, (N_c - N_b)\, N_{ph} - k_{cn}\, N_c\, N - k_{ec}\, N_c\, N_e \\
\frac{\partial N_b}{\partial t} &= k_b\, N\, N_e - \frac{N_b}{\tau_b} + \sigma\, c\, (N_c - N_b)\, N_{ph} - k_{bn}\, N_b\, N - k_{eb}\, N_b\, N_e \\
\frac{\partial N_{ph}}{\partial t} &= \frac{N_c}{\tau_c} + \sigma\, c\, (N_c - N_b)\, N_{ph},
\end{aligned} \tag{3}$$

where N is gas density; τ_c, τ_b, τ_{ph} are radiation life-times of laser levels and photons in the discharge; k_{cn}, k_{bn}, k_{ec}, k_{eb} are constants of quenching of these levels when they collide with molecules and electrons, respectively; and σ is cross-section of induced absorption. The values of the constants in the equations were chosen basing on [8,9].

System of equations (1) and (2) was supplemented with boundary conditions $dE/dr = 0$ and $dN_e/dr = 0$ at $r = 0$; at the tube boundary at $r > R$, where $N_e = 0$ (the tube thickness is neglected) we set the conditions of matching for the fields of the incident (converging) $E_p = A \cdot H_0^{(1)}(r)$ and reflected (diverging) $E - E_p \sim H_0^{(2)}(r)$ waves:

$$\begin{aligned}
E(R) &= A \cdot H_0^{(1)}(kR) + G_{\text{ref}} \cdot A \cdot H_0^{(2)}(kR) \\
\frac{\partial E}{\partial r}\Big|_{r=R} &= A \cdot \frac{\partial H_0^{(1)}}{\partial t}\Big|_{r=R} + G_{\text{ref}} \cdot A \cdot \frac{\partial H_0^{(2)}}{\partial t}\Big|_{r=R},
\end{aligned} \tag{4}$$

where $H_0^{(1)}(r)$ and $H_0^{(2)}(r)$ are the Hancel functions of the first and second kind that describe the converging and diverging cylindrical modes, and G_{ref} is complex reflection index. The amplitude A of the incident wave was assumed to be preset.

In the case of a freely localized discharge the boundary conditions were set at the distance $R \gg \lambda/2$. The pulse had no time to propagate from the axis to that distance during the effect of the microwave

pulse. Initial density of electrons was assumed to be homogeneous in space $N_e(r,0) = N_0 \sim 10^8 \text{cm}^{-3}$. Having solved system (1-4) numerically, we analyzed self-consistent temporal and spatial evolution the electromagnetic field, of electron density, populations of laser levels, as well as of spontaneous and induced radiation. Calculations showed that the dynamics of the discharge and laser radiation depend essentially on the value of the reduced electric fields E_e/p in the incident wave. Figure 1 shows the dynamics of spatial distributions of the electron density and electric field at various time moments under pressure $p = 1$ atm and $E_e = 80$ V/cm·Torr for a freely-localized discharge. Electron density is close to the critical one at the center of the discharge and decreases gradually towards its periphery. The field at the discharge axis decreases with time due to absorption and reflection of microwave power and increases to a certain extent at the boundary of the discharge. That leads to wider distribution of electron density. Such dynamics causes induced UV radiation to appear initially also at the discharge axis, and then to shift along the radius. It should be noted that a freely-localized discharge under high ($\nu > \omega$) pressures matches very well with the incident power, and, therefore, a greater part of the microwave wave (more than 95%) can be absorbed in the discharge plasma. When the power of microwave radiation is sharply increased, the breakdown occurs at several antinodes of the standing cylindrical wave; that causes the volume of the discharge plasma to become greater, and,hence, impairs the conditions for laser generation due to screening of the field.

Calculations for tubes show that at low values of E_e/p ,as well as for large-diameter tubes the parameters and dynamics of the discharge probe to be close to those for the case of the discharge in free space. It should be noted that such a discharge also matches relatively well with the incident radiation. Laser generation in this case begins at the center of the tube, and then is shifted along the radius towards its wall. Figure 2 shows spatial distribution of laser generation at various time moments for pressure $p = 100$ Torr and $E_e/p = 200$ V/cm·Torr. Due to this effect the long pulse generation was achieved. Figure 3 represents the shape of the laser pulse ob-

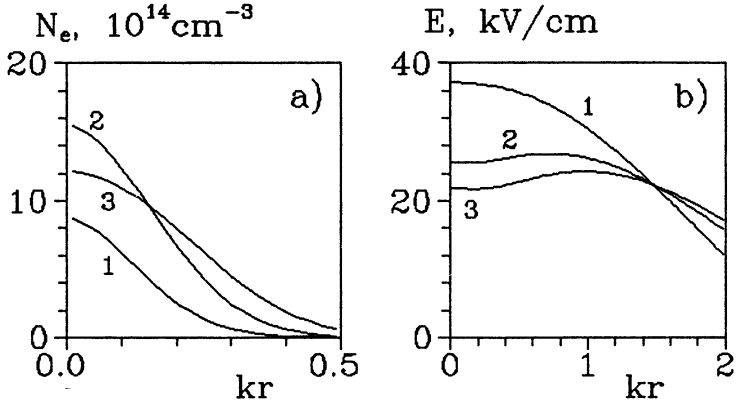

Fig.1. Dynamics of spatial distribution: a) electron density, b) electric field 1 – 13 ns, 2 – 18 ns, 3 – 30 ns p = 1 atm., E_e/p = 80 V/cm Torr

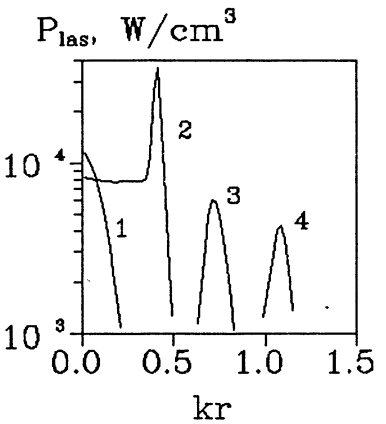

Fig.2. Spatial distribution of laser power at various time moments: 1–3ns, 2–5ns, 3–10ns, 4–15ns.

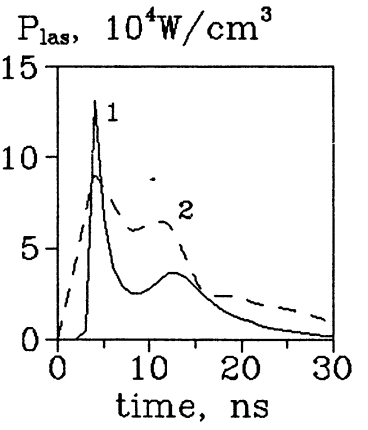

Fig.3. Laser output power: 1–calculation, 2–experiment.

tained as the result of integrating distributions shown in Fig. 2. The same figure shows an oscillogram of the laser pulse achieved in the experiment during switching-on of the microwave discharge ($\lambda = 3$ cm) in the tube placed at the focus of a parabolic mirror [6]. Comparison shows that the numerical model used in the analysis describes the shape and power of the laser pulse observed in experiment sufficiently well. When the reduced electric field increases and diameter of the tube decreases, electron density settles in the long run at the values close to the critical one N_c at the tube axis and exceeds it essentially near the walls. The increase of power leads to the fast growth of electron density near the walls and, consequently, to a higher reflection coefficient. By this , the increase of electron density near the walls is so fast that UV generation at the tube center has no time to begin due to screening of the microwave field. Spatial distribution of radiation in this case is formed as a ring with its diameter equaled to the internal diameter of the tube. Thus, calculations showed that changing the pressure of the laser mixture, diameter of the gas-discharge tube,and, the value of the incident microwave power one can efficiently control parameters of the discharge aiming at total absorption of microwave radiation and high efficiency of the laser generation.

References

1. A.J. Mendelsohn, R. Normandin, et al. Appl.Phys.Lett.,1985,38,603
2. R.W.Waynant, C.P.Christensen, J.Opt.Soc.of America,1981,71,1606
3. V.N.Slinko, A.S.Sulakshin, Quant.Electr.(Russian), 1988,15,292
4. A.A.Babin, A.L.Vikharev,et al., Pis'ma JTF (Russian) 1989,15,31
5. V.A.Flyagin, A.V.Gaponov, et al.,IEEE Trans., 1977, MTT-25,514
6. A.L.Vikharev, O.A.Ivanov, A.V.Kim, In: Relativistic High-Frequency Electronics, Issue 6, (Ed. A.V.Gaponov), Gorky, 1990, 256
7. W.A.Fitzsimmons, L.W.Anderson, G.E.Riedhauser, et al., IEEE, J.Quantum. Electronics,1976,GE-12,624
8. J.Iticawa,M.Hayachi, et al., J.Chem.Phys.Ref.Data,1986, 15,985
9. L.G.Christophorow, In: Electron-molecular interaction and their application, New York:Academ.Press. 1984, v. 1

Intracavity Laser Diagnostics of nanosecond HF-fields

Ahmedzhanov R., Polushkin I., Rostovtsev Yu.
Institute of Applied Physics, Russian Academy of Science,
46 Uljanova st., N.Novgorod 603600, Russia

This paper concerns development of measurement methods of electric field intensity in nanosecund duration. The difference from our previous papers [1] is the short pulse duration of HF fields in comparison with the laser pulse.

The experimental set-up is traditional [2]. The HF radiation (from Karsirotron [3], $P_0 = 200\ MW$, pulse duration is $\tau_{HF} = 70\ ns$, wavelength $\lambda \sim 3\ sm$) using quasioptical transformation system has a Gaussian distribution on transverse variable.

The distribution of electrical field is

$$E^2(r) = E_0^2 \exp(-\ln 2(\frac{r}{\Delta})^2),$$

$\Delta = 21sm$, E_0 - a field on beam axis (for $P_0 \sim 200\ MW$ - $E_0 \sim 6.2/;kV/cm$). The initial gas pressure is $p_0 = 3..9 \cdot 10^{-3}\ Torrom$, RF-generator created the homogeneous plasma, the electron density is $N_e = 10^{10} \cdot \cdot 10^{11} sm^{-3}$, $T_e \sim 5 \cdots 10/;eV$. We used a pulse gas shot into the plasma for creating the sufficiently high population on excited levels of hydrogen.

The investigation of absorption spectrum of hydrogen atoms in the H_α region is made by means of dye lasers; oksazin-17 concentration is $10^{-4} M/l$. The length of laser cavity is approximately 6 meters and the plasma thickness is approximately 1.5 meters. The polarization of HF-field and laser beam are parallel.

In Fig.1 a, b spectra of hydrogen atoms are shown. Using this data one can obtain the temperature of the gas in RF-discharge by means of standard procedure of ICLS-spectrum processing. It happens to be $850 \pm 100\ K$.

In Fig.1 c, d the spectrum of hydrogen atoms with the HF-field supplied are shown. To figure out these data one should remember that HF-field duration is much shorter than the laser pulse ($\tau_{laser} = 2\ \mu s,\ \tau_{HF} = 70\ ns$).

Laser mode dynamics (in accordance with [4]) is given by:

$$\frac{J_\omega(t)}{J_0(t)} = \exp(-\int^\tau \gamma_\omega dt) \tag{1}$$

The time scale of processes in plasmas is longer than laser duration τ_{laser}, so the integral in (1) can be transformed as:

$$\int^\tau \gamma_\omega dt = \gamma_\omega \cdot \tau_{laser} + \int_{\delta t}^{\delta t + \tau_{HF}} \gamma_\omega^{HF} dt = \gamma_\omega \cdot \tau_{laser} + \gamma_\omega^{HF} \tau_{HF} \theta(\tau - \delta t), \tag{2}$$

here γ_ω^{HF} - the absorption coefficient due to the present of HF-field (we use [5] to calculate the form of atom's spectral line in HF-field).

Our system of spectrum registration measures value

$$I_\omega = \int_0^\tau J_\omega(t) dt,$$

The width of instrumental contour of the spectrometer is $\delta\lambda = 0.08\mathring{A}$.

Now it is essential to take into account that there is a "memory" effect of laser generation [4]. The spectrum relaxation time is about $\sim 0.1..1 sec$. The ratio

$$\frac{I_\omega}{I_0} = \frac{\int_0^\tau J_\omega(t) dt}{\int_0^\tau J_0(t) dt},$$

depends on $\gamma_\omega, \gamma_\omega^{HF}$ and δt is time delay between the HF-field the laser pulse due to the system of synchronization.

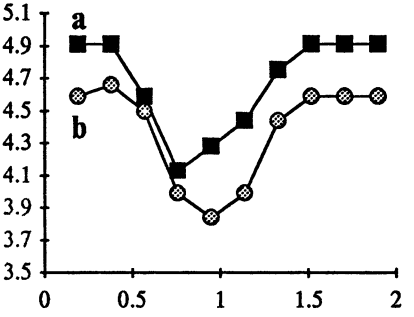

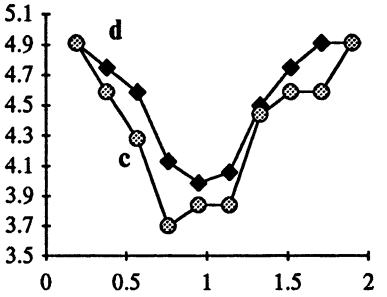

Fig. 1.
Spectra of hydrogen plasma:
a and b in the absence of HF field,
c and d in its presence.

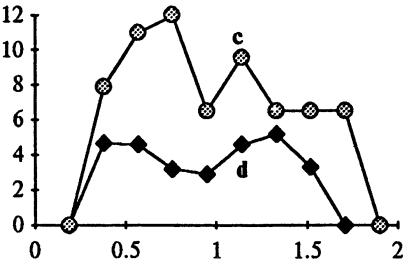

Fig. 2
Results of processing of hydrogen plasma spectra
(Fig. 1 c and d)

In the case when the uncertainties of system registration are small ($\delta t \ll \tau_{laser}$) the ratio is given by

$$\frac{I_\omega}{I_0} = \frac{1 - \exp(-\gamma_\omega \tau)}{\gamma_\omega \tau} \exp(-\gamma_\omega^{HF} \tau_{HF}) \tag{3}$$

When no HF-field is applied, one can easily obtain:

$$\frac{I_\omega}{I_0} = \frac{1 - \exp(-\tilde{\gamma}_\omega \tau_{laser})}{\tilde{\gamma}_\omega \tau_{laser}}. \tag{4}$$

Using (3) and (4) together, it is possible to find out γ_ω^{HF}, and then, knowing the profile of spectral line of hydrogen in HF-field to determine the intensity of HF-field. The integral absorption of hydrogen atoms is independent on the presence of the HF-field with regard to durations of HF-field and laser:

$$\int \gamma_\omega^{HF} d\omega = \tau_{HF}/\tau_{laser} \int \gamma_\omega d\omega \tag{5}$$

Moreover the different shots have different values of the integral (see Fig. 1 a, b) the equation (5) allows to find out easy the profile of absorption and the profile of atoms in the HF-field.

In Fig. 2 a, b one can see the profiles processed after described procedure. Using these profiles of H_α and the procedures from [5] to compare the experimental and theoretical profiles (the theoretical of atoms profiles in the HF-field are taken from [5] too) we manage to determine the intensity of electric field. It happens to be 4.0 ± 0.5 kV/cm. This value happens to be rather far from the "cold" measurements. We determine the exact position of the laser beam, and find that it is 15 cm far from the axis of the HF-filed beam. So the found intensity is in good agreement with the cold measurements.

In conclusion, we demonstrated the possibility to measure the intensity of the HF-field under these complex experimental conditions by means of Intracavity Laser Spectroscopy. It was shown that when the time duration of the HF-field was much less than the laser pulse. Besides it was the first time to use such a long cavity and the ratio of the plasma dimension to the field spatial length was extremely high.

Acknowledgments

This work was supported in part by the Soros Foundation Grant awarded by the American Physical Society.

References

1. Ahmedzhanov R., Polushkin I., Rostovtsev Yu. and etc. Zh. Exp. Teor. Fiz., 1986, v. 90, pp. 52-58.

2. Vikharev A.L., Strong HF-fields in plasmas, 1991, IAP, v.1, p.306

3. Gaponov-Grekhov A.V., Petelin M.I., Vesnik Academy of Science, 1979, n.4, p.11

4. Raspopov N., Savchenko A., Sviridenkov E., Kvant. electr. 1977, v. 4, n. 4, pp. 736-740

5. Ahmedzhanov R., Polushkin I., Rostovtsev Yu., and etc. Zh. Exp. Teor. Fiz., v.94, v. 5, pp. 52-58

Diagnostics on the Plasma Created in a Pulsed Microwave Resonator

C. Boas, G. Himmel, S. Hirsch
Institute of Experimental Physics II,
Ruhr–University of Bochum, Germany

Electron densities up to several 10^{21} m^{-3} are obtained in a 9.4 GHz resonator cavity which is made up by the movable metallic plunger at the end of a rectangular waveguide (dimensions: 2.8 cm × 7 cm) and the reflecting overdense plasma column generated three quarters of a wavelength apart. This configuration ensures that up to 95 % of the pulsed magnetron output power (120 kW, pulse duration 1 μs) are dissipated in the load resistor represented by the capillary discharge (diameter: 4 mm) operated with 20–100 Torr helium. The discharge tube is orientated parallel to the electric field of the TE10–fundamental waveguide mode and parallel to the elongated (7 cm) side of the waveguide (for more details see [1]).

Electron densities inside the waveguide are determined from He I–line profiles measured at various times during the discharge pulse and afterwards in the post–discharge [2]. The time development of the electron density resulting from measurements of the Stark broadening is shown in Fig. 1. Pictures of the discharge column taken end–on with a CCD–camera show a rather flat radial distribution of luminosity during the discharge pulse, which suggests that deviations from plasma homogeneity are not serious.

Outside the waveguide the discharge is sustained by the propagation of 9.4 GHz surface waves along the protruding parts of the quartz capillary. For probing, 2 mm–waves are irradiated side–on

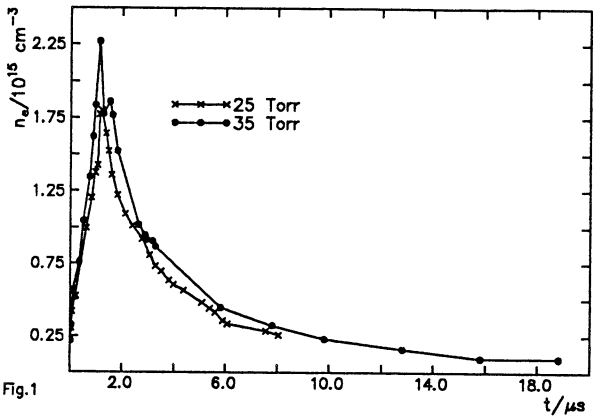

Fig.1

at various distances from the openings in the wall where the ends of the discharge tube emerge from the waveguide. The part of the test wave passing through the plasma column and the part going around constitute a two–folded interferometer together with the reference branch proper of the Mach–Zehnder device. By variation of the phase of the reference branch between 0 and $\pi/2$, the phase shift and the attenuation of the wave passing through the plasma may be determined. Phase and amplitude of the bypassing wave are known from the plateau levels of the balanced phase detector signal; these are reached whenever the electron density exceeds the critical density for 2 mm–waves.

Comparing the on–set of the magnetron pulse with the phase signal of the interferometer, the discharge ignition lag proves too small to be measured even at the largest chosen distance of the test beam from the waveguide.

In Fig. 2 the mean dissipated 9.4 GHz pulse power P is depicted against the visually determined length L of the discharge column (half of the total length) for various initial pressures p. On the assumption that ionization is most power–consuming it is expected that P is proportional to $p \cdot L^2$. For this estimate $L = n_e/(dn_e/dz)$ being proportional to N_e/p is used, where N_e denotes the maximum electron density in the middle of the waveguide [3]. It seems plausible that

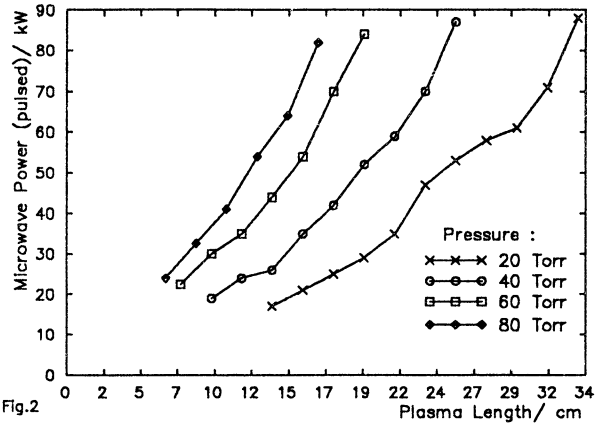

Fig.2

the value of L is mainly influenced by the end of the discharge pulse when the particle loss rate is not far from balancing the ionization rate.

As the group velocity of surface waves exceeds 2/3 of the light velocity in the given parameter range, the axial power deposition profile may be estimated to pass through a sequence of quasistationary stages near to the end of the discharge pulse. Nevertheless, the axial electron density distributions measured in the postdischarge are not represented by straight lines (see e.g. [3] for the case of weak damping) but reflect the influence of space and time dependent electron loss rates (see Figs. 3 and 4 for the pressures 40 Torr and 50 Torr respectively; $P = 110$ kW). Actually, the recombination rates (referring to the encounter of an ion with a single electron) and the electron diffusion rates also, both used for fitting theoretical time characteristics of the electron density to the afterglow measurements, increase with the distance from the waveguide. The rates in Fig. 5 (for $p = 40$ Torr; $P = 110$ kW) are quite similar to those referring to the recombination of He_2^+ with electrons [4]. Moreover, the axial variation of the diffusion rate (from $2.5 \times 10^5\ s^{-1}$ to $4.2 \times 10^5\ s^{-1}$) is indicative of the minor role of charge exchange collisions with an increasing He_2^+ percentage of the ion gas.

To sum up, pulsed high–power excitation of surface waves may

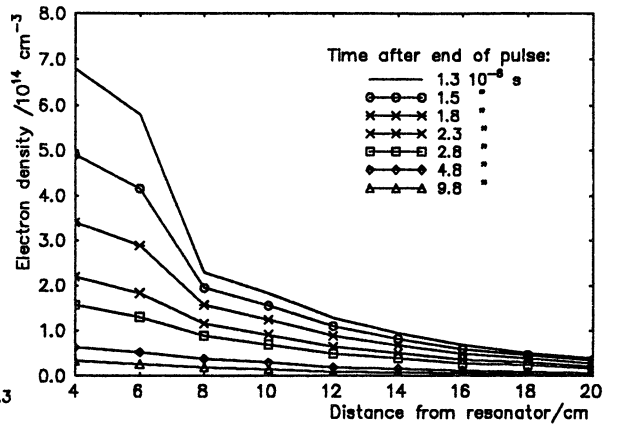

Fig.3

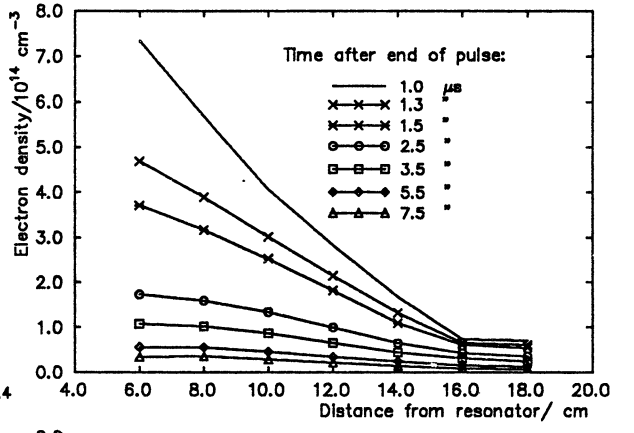

Fig.4

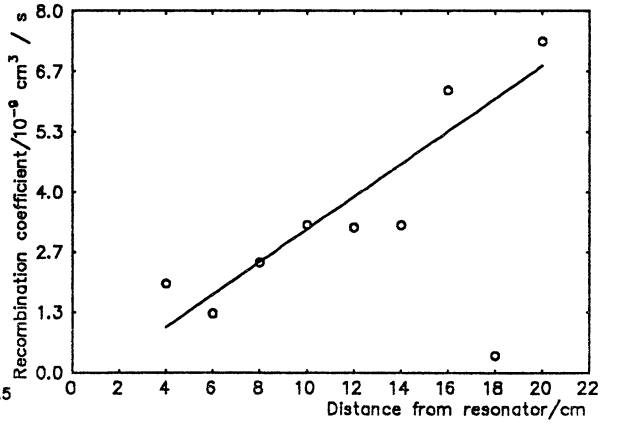

Fig.5

provide suitable starting conditions for the detailed analysis of spatially resolved afterglow measurements being useful for the extension of former low–density studies to the regime of high plasma densities.

References

[1] G. Boehm, Microwave Discharges, Fundamentals and Applications (NATO ASI series B: Physics, vol. 302). Eds. C.M. Ferreira and Moisan M., New York: Plenum Press, 1992, 215.

[2] S. Hirsch and Himmel G., submitted for publication to JQSRT.

[3] Yu.M. Aliev, A.G. Boev, and Shivarova A.P., J. Phys. D: Appl. Phys., 1984, **17**, 2233.

[4] R. Deloche, P. Monchicourt, M. Cheret, and Lambert, F., Phys. Rev. A, 1976, **13**, 1140.

OPTIMIZATION OF PULSES PARAMETERS FOR ARTIFICIALLY GENERATED PLASMAS CLOUD

Ivanov V.V.,Klopovsky K.C.,Popov A.M.,Popovicheva O.,
Rakhimova T.V.
Moscow State University, Russia

Some problems are arised as results of arfificially generated plasma cloud (AGPC) creation in atmosphere. It is necessary to choose the microwave pulse parameters. The sequence of a single pulses had to supply the regime of sustaining discharge with optimum energy density in the pulse. It is possible to produce by microwave discharge the high concentration of nitric oxides provoking the ozone depletion. The importance and complexity of this problem regures the combined consideration of air plasma kinetic processes during both microwave pulse and decay plasma [1].

This report is devoted to choice of optimum microwave pulse parameters for each altitude and radiation frequency at the condition of sustaining discharge. The calculations of plasmachemical kinetics of air plasma were conducted with the purpose of condition determination when the concentration of nitric oxides decreasing the ozone have the minumun.

The modeling of microwave discharge require the calculation of electron energy distribution function EEDF. A numerical solution of nonstationary Boltzman equation in microwave field is presented in [2]. Taking into account the nonlocality effects we solved the Boltzman equation in two-term expantion [3].

The vibration electron energy is more some ionization potentials in microwave field initiating the AGPC. So here we use the Monte Carlo method for the EEDF calculation. For each electron and on each time step the type of elementary process is considered. The prosseses of molecule exitation, dissosiation, ionization take into account.

During the ionization the second electrons are created. They are summarised and the calculation of EEDF are continued until a number of electrons increase 3 times. This time defines the pulse duration t_p. After pulse completion the plasma decay are begining. The time when the electron concentration decrease 3 times is one between pulses. So the regime of sustaining discharge is realised.

The value $Q = cE^2 t_p/4\pi$ is the energy density of radiation pulse (E is the electric field of the wave). The dependence Q on value E have the minimum produced by saturation of ionization rate dependence on E. For the $H = 30$ km Q_{opt} was $\simeq 4.2$ μJ/cm^2 at $E \simeq 1500$ V/cm and $t_p = 1$ ns. The dependence of optimum Q_{opt} on radiation frequency (from 1 to 15 GHZ) is calculated for different altitudes $H = 3 - 70$ km. The obtained values of optimum energy density are used in further calculations.

The selfconsistent calculation of EEDF and chemical kinetics processes in air plasma have been performed. More the 300 chemical reactions for 34 charged and neutral components are taken into account in our consideration. The essential components and reactions defining the rates of main processes are indicated.

The analysis of charged particles reactions shown that the plasma decay proceeds as competition of N_2^+, O_2^+ conversation to clasters N_4^+, O_4^+ and dissociated recombination. The negative ions are not important.

The special inverstigation has been conducted for indication of nitric oxides production reaction after single pulse. The concentration of NO molecules reachs to maximum value in comparison with the other oxides. In our case the energy deposition of microwave pulses is not large and small concentrations of $N_2(A^3\sum)$ and $N_2(v)$ are

created. As a consequence the reactions

$$N_2(A^3\sum) + O(^3P) \rightarrow NO + N(^2P)$$

$$N_2(v) + O \rightarrow NO + N$$

did not give the essential contributions. The main chanels of NO production were the reaction O_2 with the N atoms.

The energetic prices W for the N, O, NO production are calculated for different altitudes and radiation frequencies. The maximum prices are within area of energy density optimum. For $Q_{opt} \sim 41$ μJ/cm^2 $W_{NO} = 100$ ev/mol at $f = 1$ GHz and $H = 30$ km. So the obtained results showed the possibility of microwave pulse parameters optimization for NO production minimization in upper atmosphere.

The calculations of plasmachemical kinetics in air plasma in multipulses condisions with regards of photo and dynamical processes in the atmosphere are planed for further model development.

References

1. Gerzenshtein M.E. et al.Abstracts of ESCAMPIG 92, St.Petersburg, Russia, August 25-28, (1992).
2. Popov A.M. et al. Abstracts of IV All-Union conference on gas discharge physics. (1988).
3. Popov A.M. et al.Sov.Phys.Tech.Phys., 35,1070,(1990)

ELECTRON CYCLOTRON RESONANCE ION SOURCES FOR PRODUCTION OF MULTICHARGED IONS

P. Sortais
GANIL, 14 Bvd. Henri Becquerel,
B.P. 5027 14021 CAEN CEDEX, FRANCE

Abstract

Electron Cyclotron Resonance Ion Sources (ECRIS) now have a very wide field of applications : this paper will present different ECR ion sources and their uses for particle, nuclear, atomic and solid state physics. We will describe basic technological principles of ECR ion sources for multicharged ion production and make a brief description of multi-ionisation phenomena that can occur in an ECR plasma. Main parameters for the ion source design are the volume of the plasma chamber, the amplitude of the magnetic field, the shape of the magnetic structure, the frequency of the heating wave, and the UHF coupling system. In ECR ion sources, the wavelength of the heating wave is very close to the characteristic dimensions of the plasma (magnetic gradient and plasma density gradient) so we have no theoretical description of the coupling process. We will describe also main applications and performances of ECRIS used in the field of accelerator physics: pulsed beams for synchrotrons application (Pb 28^+, 100 μAe, 400 μs/s at CERN), high efficiency ionisation for production of radioactive beams (Louvain-la-Neuve, GANIL). We will finish by presenting some possible ion source developments in order to improve charge state distribution in regime and total current extracted from the source.

1 Introduction

Electron Cyclotron Resonance Ion Sources (ECRIS) have become the most frequently used ion sources for heavy ion accelerators. They are now used with electrostatic systems, RFQ, linacs, cyclotrons and large synchrotrons like CERN or GSI. This large success is due to the very good properties of ECRIS for accelerator applications: high charge states production (up to Ar^{18+} or Pb^{40+}), stability (over several weeks for gaseous elements), wide range of species (from any gas to W, Ta or U), reliability (no stop of operation for any

ECRIS due to internal problems), and ease of operation (only 3 tuning parameters). Since the first operational ECRIS built by Geller [1] in Grenoble (1974), consequences of studies on magnetic mirror machine for fusion research, more than 40 ECRIS are operational all over the world and many of them have been built by the Grenoble group. We will review main technical components necessary for source design, then we will recall some collision processes controlling multicharged ion production and we will finish by a survey of applications of ECRIS to low energy and accelerator physics.

2 ECR ion source principles

2.1 General structure

In order to build an ECRIS, we need four fundamental elements : 1) a minimum |B| magnetic structure, 2) a resonant surface where $|B_{hf}|=|B\omega_{ce}|$, 3) a hot and dense plasma and 4) a slow diffusion process of ions into this plasma. (Fig. 1) The minimum |B| magnetic structure is used to confine and stabilise a plasma generated by ECR discharge; then on the ECR surface perpendicular energy must be transfered to electrons in order to create a population of electron with an energy useful for the multi-ionisation of ions.

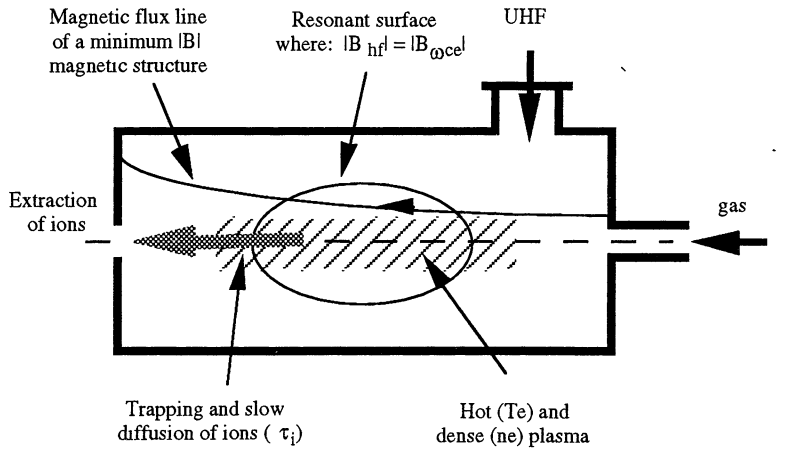

Figure 1 : Multicharged ion production in an ECRIS

This heating must also induce a population of electrons as dense (n_e) and hot (T_e) as possible in order to increase collision rates between electrons and

ions. At the same time, ions must diffuse as slowly as possible in order to stay a time (lifetime of ions in the plasma τ_i) as long as possible in the presence of ionising electrons. So we can say that the better the ($n_e\tau_i$) product for a given value of T_e, the better the multicharged ion production [2].

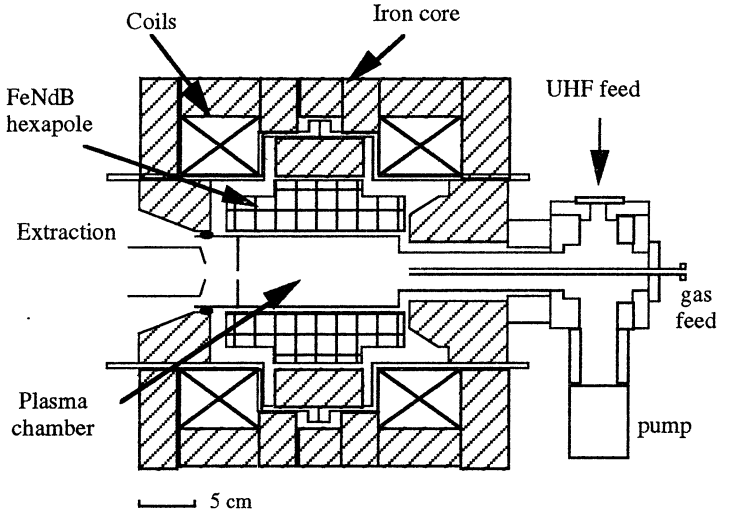

Figure 2 : Elevation view of the ECR4 14.5 GHz GANIL ion source

The minimum |B| magnetic structure is realized with the superposition of a mirror magnetic field with a multipolar structure (Fig. 2). The mirror field is created with classical coils or permanent magnets with a characteristic length between 10 to 60 cm. Except with super conducting sources radial multipolar field is made with permanent magnets placed around a plasma chamber with an inner diameter from 3 to 12 cm. It can be a quadru, hexa, octu or dodecapolar structure. The UHF power for ECR heating has a frequency between 6.4 and 28 GHz and is launched into the source radially or axially. The ion current extracted from the source is the consequence of the flux of ions diffusing spontaneously on the axis and arriving in the area of the maximum mirror field.

2.2 Magnetic parameters and minimum |B| structure

The range of ECR resonance field is between 0.2 and 1.0 T and the maximum field, for a mirror ratio of roughly 1.5 is between 0.3 and 1.5 T. (fig. 3). The feasibility of ECRIS has been largely improved by the introduction of permanent magnets used for the multipolar structure. This technology allows

the creation of a very high magnetic gradient inside a very small volume so dimensions of the source (table 1) are now largely smaller and cheaper than the first ECRIS Supermafios.

	f_{ecr} (GHz)	Ø int. (cm)	L mir. (cm)	Br_{wall} (T)	Bz_{max} (T)	$P_{elec.}$ (KW)
Minimafios[a]	18	7	30	0.8	1.0	150
CAPRICE[a]	10	6.6	16	0.8	1.1	70
Jülich ECR[b]	14.5	17	70	0.7	0.7	SC
Octopus[c]	8.5	12	50	0.45	0.4	85
ECR4[d]	14.5	6,6	16	0.9	1.1	50
RTECR[e]	6.4	14	45	0.45	0.6	20
SCECR[e]	28	14	45	2.2	2.2	SC
NANOGAN[d]	10	3	10	0.65	0.8	0

[a] Grenoble, [b] Jülich, [c] Louvain, [d] Caen, [e] MSU

Table 1 :Magnetic parameters for some typical ECRIS

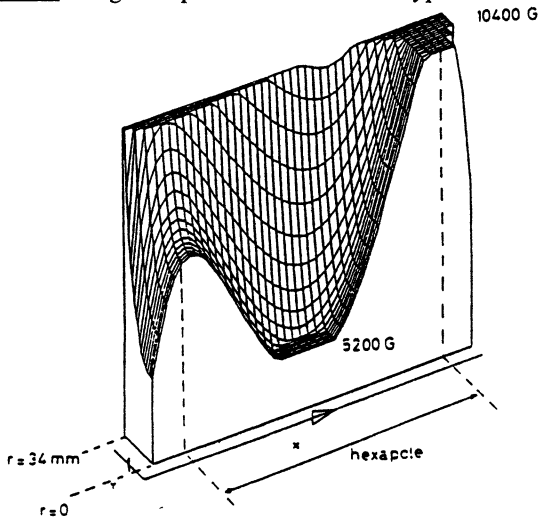

Figure 3 : Magnetic topology inside the plasma chamber with |B| limited to 0.52 T (resonance level) and 1.04 T (two times the resonance level) for ECR4 14.5 GHz

By the use of $SmCo_5$ or $Fe_{14}Nd_2B$ permanent magnets, associated to flux concentration geometry, it is now possible to create a multipolar field of respectively 0.9 T and 1.3 T, for a height of magnets of roughly 2 times the inner radius of the multipole [3]. The mirror field is created by coils generally placed inside an iron yoke and driven with 200 to 1300 A power supply. We can see in figure 3 that inside a compact source, the B_{min} structure defines a resonance zone of 3 cm in length and 4 cm in diameter. Generally the structure is designed to get a lower value of the maximum axial magnetic field near the extraction than in the area of the introduction of the UHF power, in order to optimise the loss of ions in direction of the extraction hole.

2.3 ECR process and UHF coupling systems

In ECRIS, UHF power can be introduced by coaxial lines placed on the axis of the mirror field [4], radially to the plasma chamber inside the B_{min} structure [5] (through magnets of the hexapole) outside the B_{min} structure (perpendicular [6] or parallel to the mirror field [7]). ECRIS can have very high performance with any of these systems. It is possible to find theoretical description of an ECR coupling for one particle and for a well-defined wave field near the resonance; but in the case of ECRIS ECR, coupling occurs in a hot, dense (compare to the cut-off density), inhomogeneous (density gradient), highly magnetized plasma (with magnetic gradient of the same characteristic length than the heating wave length) and finally electrons can pass several times through the resonance (stochastic heating effect). It is clear that it would be very difficult to get a theoretical prediction of plasma parameters directly from wave and magnetic components used to drive the source.

Nevertheless ECR coupling always occurs inside B_{min} structure with a relatively good efficiency. New diamagnetism measurements confirm [8] that a plasma with a density very near to the cut off density (10^{12} e/cm^{-3}) occurs inside 10 GHz devices [9] where the electronic temperature rises very rapidly with the UHF power, and then the density saturate progressively with the power increasing.

3 Ionisation process and ECR ion sources

3.1 Ionisation equilibrium and ionisation process

In order to connect plasma parameters and charge state distribution (CSD) extract from the source, it is possible to describe collisionnal processes inside the plasma as a ionisation equilibrium between creation with step-by-step ionisation and loss by charge exchange and diffusion on each charge state (i) (eq.

1).This type of description (ref. [10] to [15]) assumes that the steady state production of ions by an ECR source can be described by a homogeneous and infinite model. These assumptions neglect all in homogeneity of the process, for example wall effect on electron energy distribution (homogeneity of electron temperature), different types of diffusion for each ions, inhomogeneity of neutral density (since mean free path of neutrals can be smaller than plasma characteristic lengths). Nevertheless this type of model allows to the study of sensitivity of the CSD to mean plasma parameters, like electron energy distribution, neutral density, charge exchange process, electron density and of course τ_i lifetime of ions inside the ionising cloud of electrons.

$$\frac{dn_i}{dt} = \sum_{j=j_{\min}}^{i-1} n_e n_j \langle \sigma_{ioni.}^{j\to i} v_e \rangle + n_o n_j \langle \sigma_{exch.}^{j\to i} v_e \rangle - \sum_{j=i+1}^{j_{\max}} n_e n_i \langle \sigma_{ioni.}^{i\to j} v_e \rangle - n_o n_i \langle \sigma_{exch.}^{i\to j} v_e \rangle - \frac{n_i}{\tau_i} \qquad (1)$$

with:

n_0 the density of neutral inside the plasma

n_i the density of ions (i) in the plasma

n_e the electron density

τ_i the mean lifetime of ions with charge (i) in the plasma

$\sigma_{ioni.}^{j\to i}$ the ionisation cross section of the charge state (j) to the charge state (i) (generally limited to j_{min} = i-2 or i-3), given by Lotz formula.

$\sigma_{exch.}^{j\to i}$ the charge exchange with neutrals cross section of the charge state (j) to the charge state (i) (generally limited to j_{max} = i+2 or i+3), given by Salzborn formula.

and the requirement for charge neutralisation of the plasma : $\sum_{i=1}^{z_{\max}} i n_i = n_e$

Assuming the steady state, we have $dn_i/dt=0$. So eq. (1) becomes a set of equations easy to solve on a computer. We can see in figure 5 a typical spectrum of Argon calculated for various values of electron temperature and density. We can see those medium charge states (q<8), corresponding to the major part of extracted ions, are not very sensitive to electron temperature, but

for very high charge states (q>11) their production can be totally modified by a small amount of very energetic electrons (E>2 KeV).

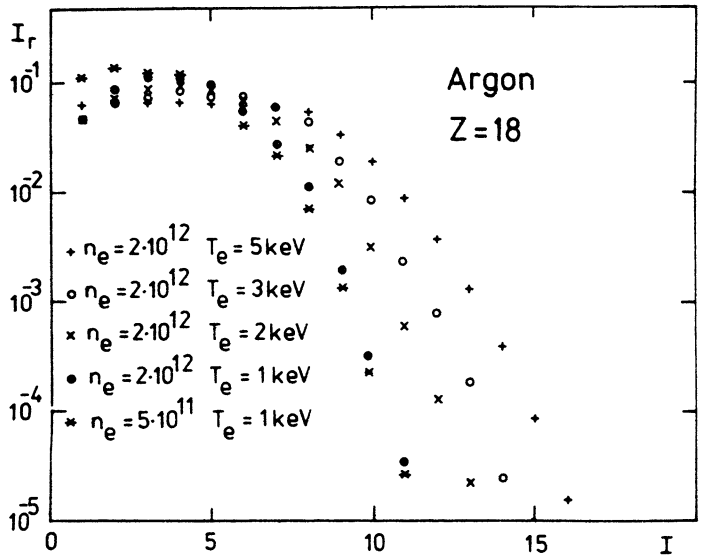

Figure 4 : Relative normalized charge distribution of Argon ions I_r as a function of electron temperature T_e and electron density n_e (from [14])

3.2 Plasma parameters and ion source performances

In multi-mirror ECRIS plasma, a density of $n_e=10^{12}$ e/cm^{-3} and an electronic temperature in the range of some KeV, can be observed [9]. According to the ionization equilibrium, a typical lifetime of 10^{-2} s is necessary to achieve the medium charge state extracted. Theses values correspond to an $<n_e\tau_i>$ product of 10^{10} s.cm^{-3}, like similar CSD, which can be observed from very different ECRIS , several "sets" of dentity, lifetime and temperature must correspond to technical characteristics of each sources. New parameters have been observed during ECR discharges induced with millimeter waves at Nizni-Novgorod [26]. Plasma Density in the range of 10^{13} to 10^{14} c/cm^{-3} inside a plasma volume similar to an ECRIS compact one Has been observed. These results seem in good agreement with Geller's scaling laws [2].

4 Application of ECRIS in accelerator physics

4.1 C.W. beams for low energy physics and cyclotron applications

The very first use of ECR ion sources has been for the production of ions with a q/m as high as possible for their acceleration to cyclotrons. At the same time, ECRIS has opened up the possibility of producing fully stripped ions up to Neon (now up to Argon) at very low energy (from 0.1 to 30 KV of extraction voltage). These kind of beams are very useful for atomic physics experiments in order to study the charge exchange process, metastable level, X ray spectroscopy, and other low energy processes.

$^{15}N^{7+}$	$^{18}O^{8+}$	$^{22}Ne^{10+}$	$^{27}Al^{13+}$	$^{40}Ar^{18+}$
50 [a]	10 [b]	5 [c]	10^{-5} [d]	10^{-3} [e]

[a] CAPRICE 10 GHz 2 wce (Grenoble)
[b] AECR 14.5 GHz (Berkeley)
[c] ECR4 14.5 GHz (GANIL)
[d] Minimafios 10 GHz (Grenoble)
[e] Minimafios 16 GHz (Grenoble)

Table 2 : C.W. maximum currents (μAe) for light fully stripped ions

Ar $^{6+}$	400	Pb $^{20+}$	25
Ar $^{7+}$	400	Pb $^{22+}$	25
Ar $^{8+}$	500	Pb $^{24+}$	25
Ar $^{9+}$	300	Pb $^{26+}$	(25)
Ar $^{10+}$	150	Pb $^{28+}$	20
Ar $^{11+}$	100	Pb $^{30+}$	12
Ar $^{12+}$	50	Pb $^{32+}$	6
Ar $^{13+}$	30	Pb $^{34+}$	3
Ar $^{14+}$	5	Pb $^{36+}$	1

Table 3 : Typical C.W. maximum currents (μAe) for Argon and Lead useful for cyclotron applications (ECR4 GANIL)

The particle energy (in Mev/A) delivered by cyclotrons is given by :

$$W = K\left(\frac{q}{M}\right)^2$$

where q and M are the charge and mass of the accelerated ion, and K is a characteristic parameter of the cyclotron depending of the size of the machine and its magnetic field value. So, if we increase the charge state of the particle by a factor 2 to 3, we can increase the energy of the particle by a factor 4 to 9 without any modification of the machine. Except for GANIL where the charge useful for the acceleration is defined by the stripping ratio made between the two cyclotrons, practically all heavy ion cyclotrons use the ion extracted from the source with the highest charge state corresponding to a current compatible with acceleration technology (generally in the range of 1 μAe)[16]. For light ions, it is now possible to produce fully stripped ions (i.e. with the maximum q/m), but for very heavy elements like Lead or Uranium, charge state extracted from the source are very far away from the maximum q/m. The objective of the superconducting source design at National Super Conducting Cyclotron Laboratory (USA) (fig. 5) consisted in use the high frequency effect in order to improve the CSD [25]. The limit of 1 μAe would be around the charge 45^+ for Uranium ions.

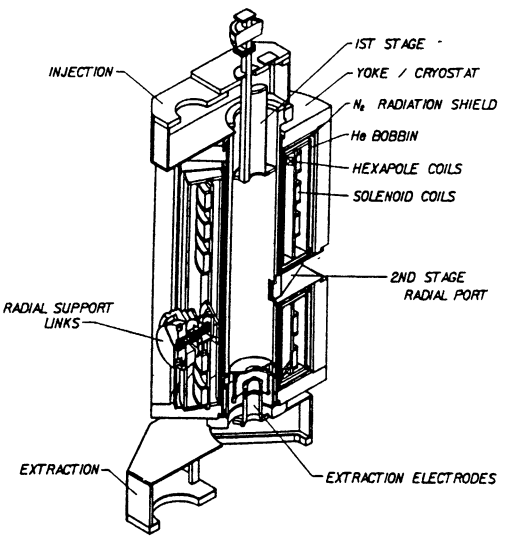

Figure 5 :MSU superconducting source design for 2.2 T minimum |B| structure for 28 GHz functioning

At GANIL (complex of 2 cyclotrons with change of the charge state of the ions between the two cyclotrons by stripping) the charge useful for acceleration is lower than with a single cyclotron but this situation, associate to very good transmission allows the production of very high currents. A beam up to 5 10^{13} p/s for elements up to Ar (5 KW of heavy ion beam power) is planned for the on line production of radioactive species [17].

4.2 Afterglow pulsed beams for synchrotron applications

ECR ion sources can produce C.W. current, but at the same time and without any physical modification, they can be tuned to produce short pulses of intensity much higher than during the C.W. tuning called "afterglow pulsed currents". This phenomenon can be understood as a plasma potential disruption inducing a rapid diffusion of highly charged ions of the plasma when we stop the UHF power [18].

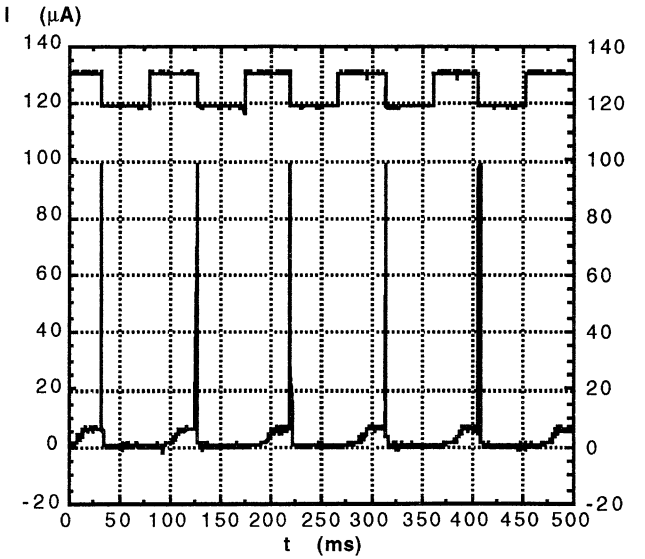

Figure 6 : Afterglow peak currents of Pb^{28+} produced with the ECR4 14.5 GHz at GANIL

The ECR heating of to electrons gives perpendicular energy which improves their confinement in the magnetic mirror field, compared to a classical

thermalized electronic population. Ions are confined in the electronic cloud by a self-electrostatic well, so at the cancellation of the RF power, the "plugging effect" induced by high energy electrons disappears and the deconfinement of thermal electrons induces the axial release of the ions [19].

This effect has been observed for the first time by the team of the DRFMC, at Grenoble in 1988, on the MINIMAFIOS, 16.6 GHz, but the same time structure can be now observed on many other ECR ion sources: MINIMAFIOS 14.5 GHz at CERN, ECR4, 14.5 GHz at GANIL and CAPRICE, 14.5 GHz at GSI

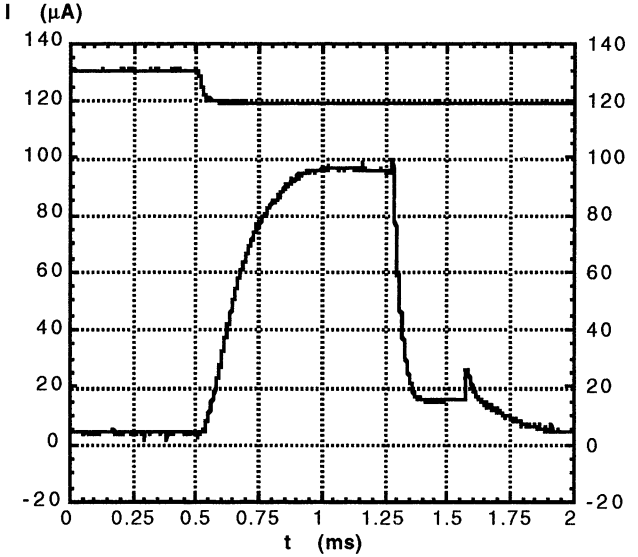

Figure 7 : Afterglow pulsed current of Pb^{28+}
with 400 μs of useful time for acceleration at CERN

Since then, we have tried to develop a working mode for its use for accelerator application. Acceleration of heavy ions in synchrotron accelerators demands very short pulses (≤ 1 ms) and a charge state as high as possible. The CERN demand (Fig. 7), for the acceleration of Lead ions are the following : high pulsed current of around 100 μAe of Pb^{28+}, corresponding to 10^{10} ions in the pulse of 400 μs and a repetition frequency of 1 to 5 Hz [20]. This production process is also planned to be use on the GSI synchrotron complex.

4.3 Permanent magnet ECRIS for high voltage applications

The technical environment of an ECRIS is relatively important: high power alimentations, emitter driving a klystron, high pressure water cooling for coils and a relatively big size (1 m in length,0.7 m in diameter). So the design of a permanent magnet ECRIS can be very useful if we want use it with a relatively complex environment like high voltage platform, Van De Graaf machines or highly radioactive on line production systems. The first permanent magnet ECRIS for production of highly charged ions is NEOMAFIOS 8 GHz [21] designed by P. Sortais and P. Ludwig (Fig. 8). This development has been made in connection with the 100 KV injection system from GANIL, in order to study the possibility to build a high performance ECRIS without power to create the magnetic structure. This one has a Minimafios like structure where a Ø 7 cm plasma chamber is magnetized up to 0.55 T. But the UHF power still remains high, (some hundred of Watts), so klystron emitter (> 5 KW of primary power) is necessary to run the source at its maximum performance.

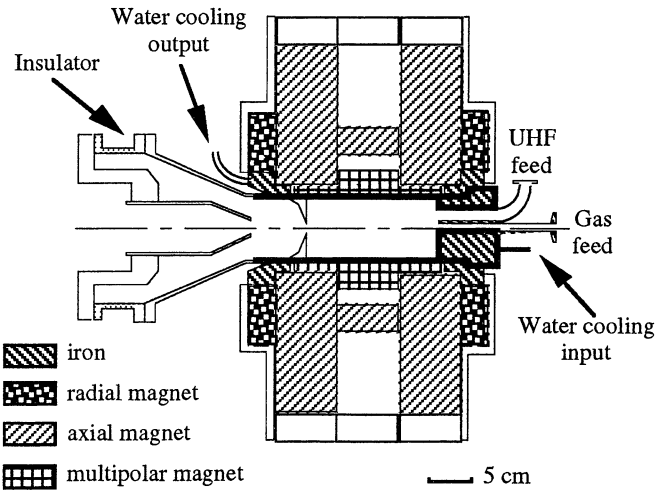

Figure 8 : NEOMAFIOS 8 GHz : the first purely permanent magnet ECRIS operational on an high voltage platform at RIKEN (Japan)

The two next permanent magnet ECRIS are BECRIS at HMI (Berlin) [22] and NANOGAN at GANIL (Caen) (Fig. 9). Becris is the first multicharged ECR ion source specially designed for its implantation on the terminal of a Van de Graaf machine. Its implantation is planned by the end of 1993. NANOGAN has been developed for an on-line production experiment of radioactive species,

but it can also be used on a high voltage platform. Its outer diameter is only 12 cm and it can produce ions up to fully stripped Oxygen (≈10 nAe) with an UHF power of only 4 W. Its installation on an 200 KV implantation device (CNET Grenoble) is planned by the end of 1993 in order to produced P^{5+} for Mev implantation.[23]

$^{14}N^{2+}$	$^{16}O^{8+}$	$^{40}Ar^{4+}$	$^{40}Ar^{8+}$	$^{86}Kr^{15+}$	$^{129}Xe^{17+}$
300	0,01	110	60	10	8,5

Table 4 : Ion currents (μAe) produced with NANOGAN (Ø 6mm, 13.5 kV)

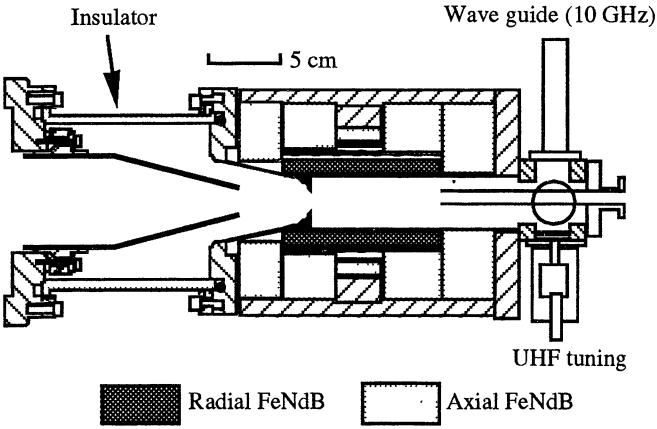

Figure 9 : NANOGAN 10 GHz: An ultra compact ECRIS for on line and high voltage applications at GANIL (France)

4.4 High efficiency ECRIS for on line production of radioactive species

Another new field of application for ECRIS is the on-line production of radioactive species. Generally, radioactive elements are produced in very small amounts, so in order to transform them into ions the gas efficiency of the source is a very important parameter. This one can be defined as: ratio of radioactive atoms of a given species arriving into the source to the number of radioactive ions of the same species (eventually by charge state) coming from the source (eventually inside a given emittance). ECR ion sources are the only ones to produce good efficiency ions from N and noble gases. A first source,

totally dedicated to on line production has been designed and is now operational at Louvain-la-Neuve (Belgium) [24]. This source (Fig. 10) is used to post accelerated ions of gaseous elements up to energy of astrophysics interest : 0.2 to 1 Mev/A.

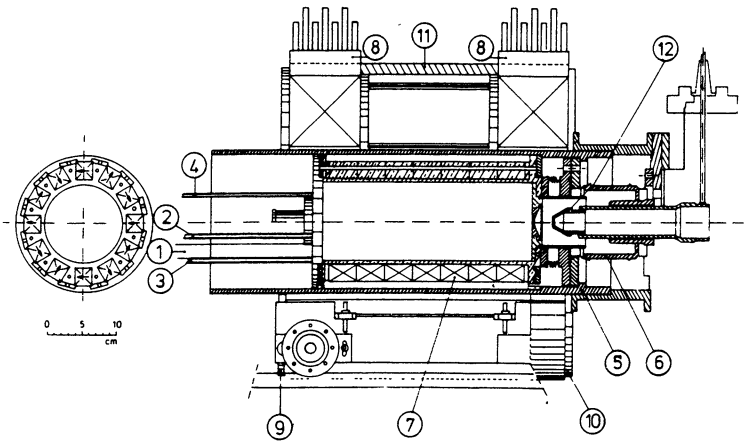

(1) micro wave guide
(2,3) cooling water in/outlet
(4) gas input
(5,6) HV insulator
(7) permanent magnets
(8) solenoids
(9,10,11) iron yoke
(12) extraction electrode

Figure 10 : Louvain-la-Neuve ECRIS for on line production of N and Ne low charge state ions

Two other prototypes began to be operational at TRIUMF (source TISOL) and GANIL (source NANOGAN). Theses ECRIS are directly connected to an on-line production target, where multicharged ions have to be extracted from the source [23] (Fig. 11). These developments are made in order to produce beams ready for their acceleration up to energy of nuclear interest : 2 to 30 Mev/A. We observed, as predicted, the production of "light" Neon (^{19}Ne,^{18}Ne) coming from projectile fragmentation and at the same time, "heavy" Neon (^{23}Ne,^{24}Ne) coming from target fragmentation. We have also observed that it is possible to produce it with high charge state (>3) corresponding to a suitable Q/M value for post acceleration in the cyclotron SPIRAL of the GANIL project. These results, obtained without any optimisation of parameters of the isotopic separator, show

very clearly that the concept of production of radioactive ions with heavy ion primary beams and on line system based on ECR ion source is operational.

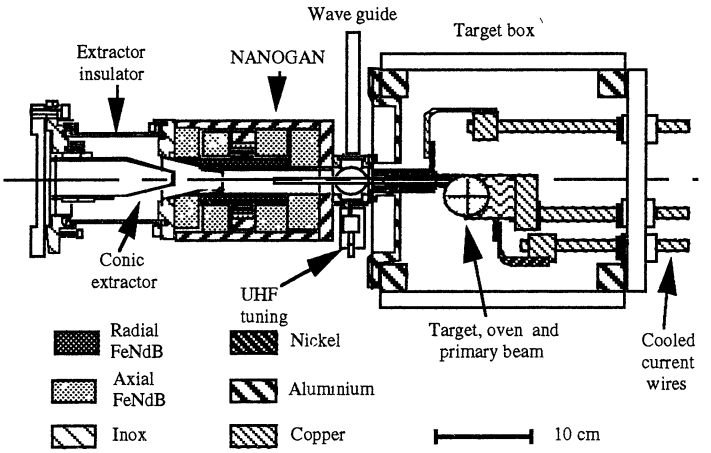

Figure 11 : Target production and transfer system used for on line production of noble gas with NANOGAN at GANIL

5 Conclusion

After 15 years of development, it is clear that ECRIS can now give an answer to the main demands of heavy ion beams. In spite of the fact that we have no theoretical description, it seems that it is possible to further the improvement of plasma parameters. Ionisation equilibrium shows that density increasing can be very benefit to current and charge state distribution extracted from the source. At the same time, very high density plasma generated by millimetre waves inside a quasi ECRIS plasma chamber shows that it is possible to go on the field/frequency scaling. So a new generation of ECRIS working with 10^{13} to 10^{14} e/cm^{-3} seems possible and could open new applications: very high currents of multicharged ions beams (C.W. or pulsed), very high efficiency source working at high pressure for on line production of radioactive species or improvement of charge state distribution of very heavy elements.

References

1. Geller R., IEEE Trans. Nucl. Sci.,1976, NS-**23,** 904.
2. Geller R., Annu. Rev. Nucl. Part. Sci.,1990, **40,** 15.
3. Schiemenz P. et al., N.I.M., **A305**, 1991, p.15-18.
4. B. Jacquot et al., 10th Int. Work. on ECRIS, Knoxville, USA, Nov. 90, 133
5. Antaya A. et al. Int. Conf. on ECRIS and Appl., East Lansing, USA, 1987, 334
6. R. Geller et al., N.I.M., **A243**, 1986, 224
7. Lyneis C.,Proc. 10th Int. Work. on ECRIS, Knoxville, 1990, USA, p 13
8. Meulin G. et al., Rev. Sci. Inst., **61**, 1990, 236.
9. Girard , Proc. 11th Intern. Work. on Electron Cyclotron Resonance Ion Sources, Groningen, 1993, 86.
10. Jongen Y., pre-prints LC-8001, Univ. Catholique de Louvain-La-Neuve, (Belgium), 1980
11. West H.I., preprints UCRL-53391, Lauwrence Livermore National Lab., (USA), 1982
12. Bliman S. and Chang-Tung N., Journal de Physique, 1981, **42**, 1247
13. Sortais P., note scientifique n° 586, DRFG-PADSI Grenoble, (France), 1986
14. Shirkov G., Mühle C., Musiol G. and G. Zschornack, Nucl. Instrum. and Meth., 1991, **A302**, 1.
15. Shirkov G., Proc. 4th Int. Conf. on Ion sources, Bensheim, 1992, Rev. Sci. Instrum., **63**, (4), 2894.
16. Lyneis C., 13th Int. Conf on Cyclotrons and theirs Appl., Vancouver 1992.
17. Chabert A. et al., 2th Int. Conf. on Radio. Nucl. Beams, Louvain-la-neuve, Belgium, Aug. 91, 115.
18. Melin G. et al., 10th Int. Work. on ECRIS, Knoxville, USA, Nov. 90, 1.
19. Sortais P. , 4th Int. Conf. on Ion Source, Bensheim, Germany, Rev .Sci .Inst., **63**, 1992.
20. Amendola G. et al., E.P.A.C., Berlin, 1992
21. Sortais P. et al., Int. Conf. on ECRIS and Appl., East Lansing, USA, 1987, 334
22. Arndt P. et al., 11th Int. Work. on ECRIS, Groningen, The Netherlands, 1991, 127.
23. Sortais P. et al., 11th Int. Work. on ECRIS, Groningen, The Netherlands, 1991, 97.
24. Loiselet C. et al., 10th Int. Work. on ECRIS, Knoxville, USA, Nov. 90, p 133-155.
25. Antaya A. et al., 10th Int. Work. on ECRIS, Knoxville, USA, Nov. 90, p 133-155.
26. Golubev B. et al., Rus. Jour. Appl. Phys., 1990, **16**, 4, 487.

INVESTIGATION OF ECR DISCHARGE WITHIN THE BASEBALL AND CUSP GEOMETRY WITH LONGITUDINAL INPUT OF GYROTRON POWER

A.A.SKOVORODA, A.V.TIMOFEEV

RSC "Kurchatov Institute", Moscow, Russia

Results are presented of experiments on electron cyclotron heating with longitudinal in put of gyrotron power in nonuniform magnetic fields in open systems of two types: nonaxisymmetric baseballs and axisymmetric systems with oppositely directed fields (cusps). These data thus far do not have a unique theoretical explanation. The main results are presented from experimental measurements of the hot electron population resulting from ECR heating of the plasma in baseball OGRA-4B. A theoretical model is developed which describes the hot electron dynamics and the propagation of electromagnetic oscillations in the plasma self - consistently. The results obtained with this model are in agreement with experimental data.

Introduction

In spite of the long history of experimental and theoretical studies of ECR plasma heating, it is only recently that we have begun to understand the mechanism by which the hot-electron population (HEP) forms. In mirror systems these electrons determine the basic energy content (β) of the plasma. Even the earliest experiments on ECR plasma heating in mirrors [1] showed that it was possible to obtain a plasma with β=0.5 due to formation of HEP with energy greater than 1 MeV. But up to now we can not made the safe predictions about the distributions of HEP in space and energy in specific conditions.

Any prospective explanation of this phenomenon must answer the *basic* question: How is the resonance maintained between the cyclotron gyration, the frequency of which undergoes large changes during acceleration to relativistic energies, and electromagnetic (EM) oscillations with a very narrow spectral linewidth such as that typically found in present–day generators,e.g.,gyrotrons. It is natural to expect that once we have solved this problem we will likewise understand what factors determine the energy of EHP, density and spatial distribution.

In the course of studies over many years, a number of factors have been discovered which essentially affect the process by which the HEP forms:

–amplitude of EM waves. In ideal situation (electrons no collide, plasma is quiescent, EM wave is actually monochromatic) the interaction between confined in mirror electron and EM wave assumes a chaotic character (electrons diffuse in energy with the familiar quasilinear diffusion coefficient (QDC)) only at enough large power (see,e.g.,[2]). In real experiments none of these ideal conditions is satisfied; consequently, heating takes place even in the superadiabatic regime and no restrictions on the energy are observed [3]. At large power QDC decreases due to nonlinear relativistic effects and electron total energy begins to oscillate (known cyclotron oscillations) about some average value E, which can be determined from ECR condition $\omega=eBc/E$.

–electron motion across nonuniform magnetic field. The enough slow changes in magnetic field B give rise to changes in E. This phenomena is known as autophasing in accelerator theory and *relativictic autoresonance* (RA) in plasma theory. In stationary mirrors this phenomenon can occur at ECR with HEP confined close to B minimum. If these electrons are displaced transverse to the magnetic field lines,e.g.,due to any plasma instability, E can increase. This mechanism can give rise to the formation of rings or disc of HEP in the

midplane of the system [4].

–bounded transverse dimensions of the EM beam. This becomes important when beam is transverse to the field lines and there is no EM background. If B within EM beam varies within the range B_1,B_2, then from ECR condition the maximum electron energy can acquire is equal $\varepsilon=mc^2(B_2/B_1-1)$. But in experiments were observed electrons with larger energies and it was necessary to include for explanations any other effects,e.g., collisions [5].

–effect of EM background. The presence of high level EM background is typical for majority of experiments. Scattering increases the volume occupied by microwave radiation,and hence facilitates the growth of ε (see above). If within the volume B changes by more than a factor two, then simultaneous ECR at several harmonics becomes possible, which in turn creates the preconditions for unlimited heating [3].

–Doppler effect. It is known that ECR interaction extremely strong depends on longitudinal refractive index $N\|=k\|c/\omega$. If $N\|\ll 1$ only the transverse electron energy changes and electron trajectory in mirror tightens up in the region of small B. When the energy

$$\varepsilon \approx \sqrt{2\varepsilon_{\|o}mc^2} \qquad (1)$$

is reached ($\varepsilon\|o$ –initial longitudinal energy) the trajectory is found within the region where ECR interaction ceases [6]. The situation is radically different for $N\| > 1$, when the change in the longitudinal energy due to ECR interaction is quite large [7]. The case $N\| = 1$ is known as *Doppler autoresonance* (DA) [8]. In DA the position of ECR does not vary as a function of ε. Thus the amplitude of hot–electron bounce oscillations along mirror grows and unlimited acceleration shuts off when the electron abandons the trap. The maximum energy to which the electron can be accelerated is given by

$$\varepsilon_{max} = 2mc^2(B_{max}/B_r - 1), \quad (2)$$

where B_r is the resonant magnetic field for cold – electron. The same expression for maximum energy holds also for $N_{||} > 1$, but the position of ECR varies on ε and acceleration is possible only in inhomogeneous magnetic field. We call this regime *inhomogeneous Doppler autoresonance* (IDA).

In this work we investigate ECR discharge at low pressure within the baseball and cusp geometry with longitudinal input of gyrotron power, when $N_{||}$ is of order 1. The experiments were carried out on two devices OGRA–4B (superconducting baseball) and OGRA–4K (superconducting cusp). In the first section we summarize the parameters and the basic experimental results on OGRA–4B. The theoretical analysis and discussion is represented in the second section. The basic experimental results on OGRA–4K are summarized in the third section.

1.OGRA–4B

The OGRA–4B device is a superconducting single *minB* open trap with a mirror ratio $\approx$ 2 (longitudinal and transverse) and minimum B=1.7 T [9]. Figure 1 shows curves of constant B in one of the planes of symmetry. On the same figure are shown the two microwave inputs used in the experiment. The longitudinal input 1 was connected to gyrotron 1, which had wavelength of 8 mm (fundamental harmonic), and the transverse input 2 was connected to gyrotron 2 which had wavelength of 4.8 mm (second harmonic). The gyrotron produce EM power level at the output of the line in the form of a Gaussian pulse of up to 0.2 MW for 0.1 s with linear polarization. The microwave radiator was tube of diameter 8.5 cm, terminating in ceramic windows. The waveguides were filled with dry nitrogen at pressures up to atmospheric, flowing continuously.

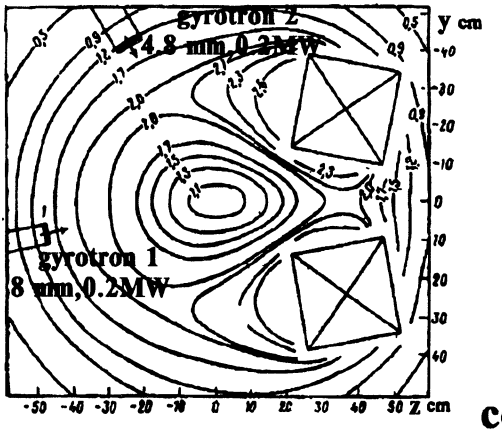

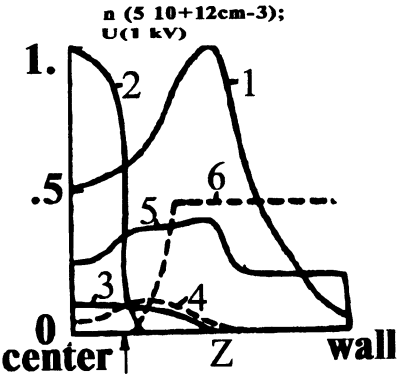

Fig.1.Contours of constant B in OGRA–4B

Fig.2.Profiles along axis:1–B; 2–4 warm, hot, cold electron density; 5–potential;6–microwave power; arrow–ECR for cold electrons

The diagnostics used in the experiment is described in Ref. [10]. Here we say little about the behavior of the EM propagating in the chamber where the plasma is confined. The measurements were carried out directly in the chamber using the technique described in Ref.[11]. They exhibited a well – developed directivity diagram, slightly exceeding the EM input in diameter. The background (the average power level in the chamber) was less than 10%. Subsequently, [11] sensors were positioned in the chamber across from each EM input in order to measure the transmitted power and determine the fraction absorbed in the plasma.

For microwave breakdown of hydrogen at pressure of (1.–5.)E–6 torr a hot–electron plasma formed with $\beta \approx 0.1$ [12]. Investigation of this plasma revealed the presence of tree groups of electrons: cold, warm and

hot. Table 1 and figure 2 give the measured plasma parameters and their distribution along mirror axis.

Table 1. Plasma parameters in OGRA–4B

Central plasma density	0.6 10+13 cm–3
Warm electron density	0.5 10+13 cm–3
Warm electron energy	1–3 KeV
Warm electron life time	1 msec
Volume of warm plasma	5 liters
Cold electron density	1–4 10+11 cm–3
Cold electron energy	20–80 eV
Cold electron life time	10 μsec
Hot electron density	0.8–1.5 10+12 cm–3
Hot electron energy	0.1–0.4 MeV
Hot electron life time	0.5 sec
Volume of hot plasma	20 liters
Maximum β in B=1T	15%
Ion energy	10–40 eV
Plasma potential	+(150–300)V
Ionization degree n_e/n_g	5000
Longitudinal plasma current	2A

Note that results we obtained (see details in Ref.[12]) coincide in large measure with many results obtained in experiments on open systems and on bumpy tory. Here we summarize the basic experimental results underlying our theoretical model [13] for ECR discharge with longitudinal EM input.

Figures 3 and 4 show dynamics in time of signals connected with hot electrons. The steady state is not reached in our time scale limited by gyrotrons power supply. The signal from diamagnetic pickup shows no spread when the gyrotron is switched off and the HEP density does not change at time. At that time hot–electron flux out the end of system obtained with x–ray sensor decreased very rapidly. One can see on figure 4 that 5 msec. gyrotron switching off leads to the x–ray signal disappearing, and then to its rapid

restoring up to previous level while a diamagnetic signal does not undergo noticeable changes.

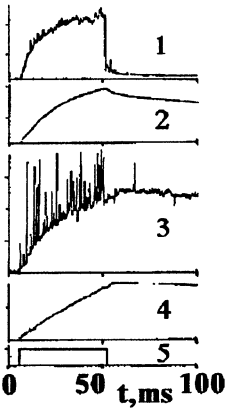

Fig.3.HEP dynamics:
1-end x-ray;2-diamagnetic signal;
3-cyclotron 4mm radiation;
4-cyclotron 0.3-2mm radiation;
5-gyrotron1.

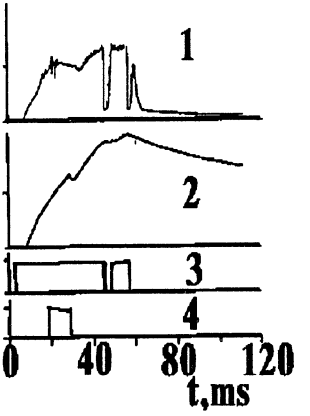

Fig.4.HEP dynamics:
1-end x-ray;2-diamagnetic signal;
3-gyrotron 1;4-NB injection.

Figure 2 shows that HEP is distributed throughout the trap. In contrast the warm electrons are concentrated in the mirror center within the region bounded by the ECR surface. When the position of this resonant surface changes the volume occupied by warm electrons varies too (e.g., when the magnetic field is increased the volume decreases).

The measurements show that the bulk of the microwave power is absorbed by the HEP. Figure 2 shows that calculated microwave power is decreased rapidly along axis and never reaches the ECR point of cold electrons. The warm electrons do not interact intensively with EM wave. The cold electrons arisen as a result of neutral gas ionization are "locked out" of resonant interaction too. The special experiment with

a plate at the one end of mirror, which collected the entire plasma flux and acquired a negative potential greater than the energy of the cold electrons leaving the end of trap, showed that in this case their energy did not change (cold electrons passed through the entire system and two ECR points).

Figure 5 shows energetic spectrum of electron flux on the end of mirror. Because of their short lifetime the density of the cold electrons is low, but they constitute the major part of the electron flux leaving trap. The presence of cold electrons gives rise to a positive plasma potential to be measured. Note that the average energy of electron flux is lower than the temperature of warm electrons in mirror center to be measured by means of laser scattering.

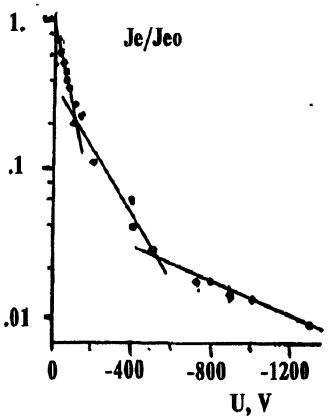

Fig.5.Energetic spectrum of end electron flux.

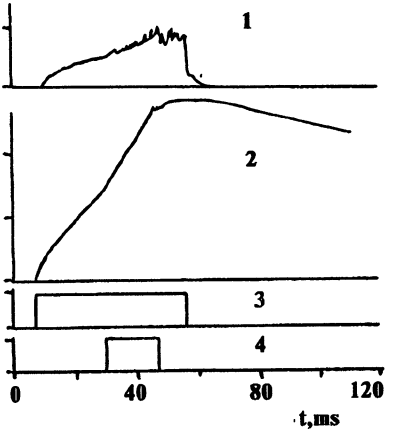

Fig. 6.Two gyrotron working
1-end x-ray;2-diamagnetic signal;
3-gyrotron 1;4-gyrotron 2

Figure 6 shows the result of two gyrotrons working together, which resulted in a substantial

increase in plasma pressure and a change in the way the diamagnetic signal grows. The efficiency which is possible with two – frequency heating has been known, but we do not see the sharp drop in x–ray signal when the second gyrotron (4.8 mm) is switched off.

Figure 7 shows the x–ray intensity from two opposite ends of mirror and from plasma volume (the attenuation of signals is different). We can see that HEP detrapping from mirror along field lines by acting of EM waves is higher in the direction of wave propagation (note, that the x–ray signals from ends are equal after gyrotron switching off).

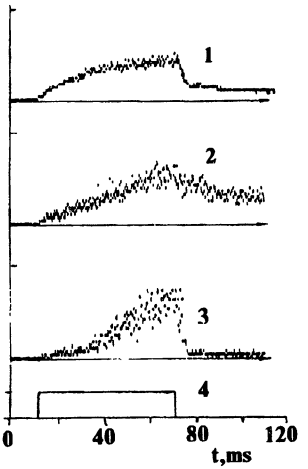

Fig.7.X-ray signals from: 1-end wall with EM input; 2-plasma ;3-end wall opposite input;4-gyrotron 1 switch on

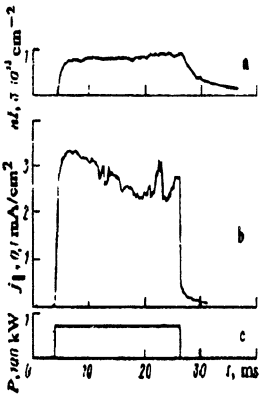

FIG.8 Oscillograms: a) line density nl; b) flux of electrons to the end of the system with energies greater than 0.4 keV; c) gyrotron power.

Figure 8 shows the sharp drop in the warm – electron flux without drop in linear density when gyrotron is shut off. Figure 4 shows the complicate behavior of x–ray signal from mirror end after gyrotron switching off. We observe the unusual afterglow.

2.Theoretical model and discussion

In our conditions the index $N\|$ of right–polarized waves propagating along the magnetic field is given by

$$N_{\|} \approx 1 + \omega_{pe}^{c2}/\omega(\omega_{eo}-\omega) > 1, \qquad (3)$$

where ω_{pe}^{c}–cold electron plasma density, ω_{eo}– cold electron cyclotron frequency. When monochromatic EM waves undergo ECR interaction we have

$$\varepsilon - \mu\omega = \varepsilon_{\|o}, \qquad (4)$$

where $\mu=\varepsilon\perp/\omega e$ is magnetic moment. This relation with well known ECR condition enables us to describe the acceleration process in mirror (details see in Ref.[13]).

Consider the phase plane (figure 9) of the variables $p_{\perp o}$, $p_{\|o}$ (transversal and longitudinal electron momenta at the center of mirror). In this

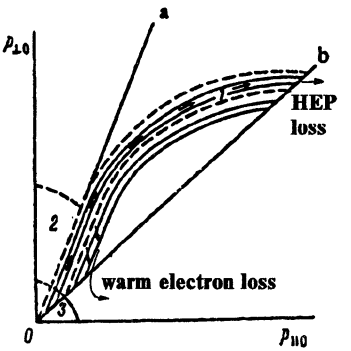

FIG. 9. Electron populations confined in the system: 1) hot electrons; 2) warm electrons; 3) cold electrons; b) boundary of the loss cone; a) boundary of the resonant cone defined by the condition $\omega = \omega_{e0}$; $p_{\|0}$ and $p_{\perp 0}$ are the electron momentum components relative to the center of the system.

plane the light lines denote trajectories along which electrons diffuse under the influence of the EM field. In the nonrelativistic region they are nearly straight and parallel to the resonant cone (line *a*) and intersect the loss cone (line *b*) in the low– energy region. In the high– energy region the diffusion trajectories intersect the loss cone due to relativism. If the electron phase density on line *b* vanishes for all values of energy, then the main result of EM diffusion will be to expel electrons from mirror. In order that EM diffusion lead to heating and acceleration, the electron phase density in the low – energy region must be maintained by some nonmagnetic means. The figure 2 shows that cold electrons, which interact weakly with EM field are confined by the self – consistent ambipolar potential and have a Maxwellian distribution function (region 3). The cold electrons, which are "stretched" by microwave field, form "acceleration jets" in the phase plane. Coulomb collisions smear out the "jets" in the transverse direction. Electrons which arise inside the resonant cone form the warm electron group (region 2). Most of the warm electrons do not interact directly with the EM field, since they do not reach the ECR point in their motion within trap. The phase volume occupied by warm electrons is large. Consequently, when the phase densities of the electrons in regions 2 and 3 are comparable, the number of warm electrons in the trap can be considerably larger than the number of cold electrons, as is observed experimentally.

Coulomb smearing of the "jets" takes place not only in the direction of the resonant cone but also in the opposite direction. This process gives rise to electrons which reach the EM diffusion line, intersecting the last cone, and consequently to ejection of electrons from mirror. Figure 9 shows that the energy of the lost electrons must be considerably greater than the energy of the cold electrons and smaller than the energy of the warm ones.

These qualitative considerations explain a number of experimentally observed facts: existence of three groups of electrons; their space distribution; the sharp drop in flux without any drop in density when gyrotron is shut off; the decrease in the warm – electron energy in the flux from trap relative to the measured in the center of plasma by Thompson scattering and so on. The model predicts not only qualitative but also quantitative results. Figure 10 shows a comparison between simulation and experiment for hot–electron energy spectrum, which is completely satisfactory. Figure 11 permits a comparison of calculated by Eq.2 maximum electron energy as a function of $B\max/Br$ and the experimentally observed dependence.

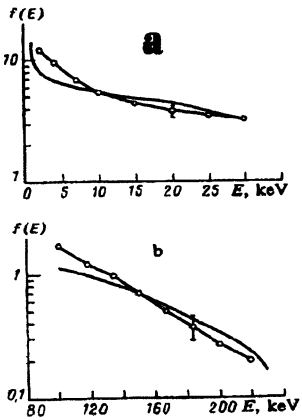

FIG. 10. Hot-electron energy spectrum: calculation – solid trace (resonant mirror ratio 1.6 $\varepsilon_{\parallel 0}$ = 0.5 keV, α = 0.01); experiment – trace marked with circles: a) x-ray photoelectron spectrometer; b) x-ray analyzer.

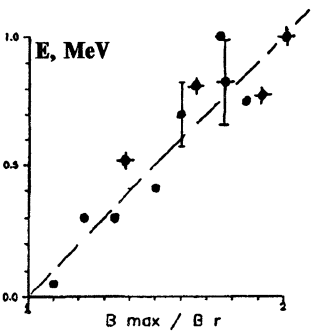

Fig.11. Dependencies of x-ray maximum energy (points with crosses) and normalized diamagnetic signal on ECR point (dashed line Eq.2)

Now we discuss in detail two facts: unusual afterglow and asymmetry of HEP detrapping.

1.When gyrotron is shut off the warm electrons can not abandon the trap at once. It is necessary for these electrons to diffuse with Coulomb time to mirror loss

cone at first. This explains the sharp drop in the warm – electron flux and the appearance of intensive short – lived x–ray signal after gyrotron switching off (see fig.4,8). The time delay of this signal is in good comparison with Fokker – Planck calculations of warm – electrons afterglow and depends on B_{max}/B_r.

2.The theoretical model [13] predicts the detrapping of HEP from a magnetic well along the field lines in the direction of wave propagation in the symmetric trap (B_{max} on field line are equal in two mirror plugs). It is related with the fact that hot – electrons are accelerated in ECR point, when their motion is directed towards the wave propagation (vice versa for cool electrons). The theoretical model gives the value of δR – the change of mirror ratio for hot – electron in one act of ECR interaction (in detail see Ref.[14]). In our experimental conditions we have $\delta R \approx 0.02$ and the asymmetric baseball mirror. In such trap B_{max} are unequal and the relation between them changes with azimuthal angel. If inequality is greater then δR the detrapping should be symmetric. In our condition we have the intermediate case and figure 7 can be good explained including quantitative relation [14].

The observed asymmetry of HEP detrapping can result in the emergence of a current along axis. This possibility is of great importance in closed trap of tokamak type. In our experiments we demonstrate that for $N_{\|} > 1$ the relativistic decrease of cyclotron frequency as a result of heating is compensated by the shift of resonance point to the higher magnetic field region (IDA regime). In a tokamak such compensation is more difficult because of smaller magnetic field variation along the electron trajectory. But requirements to the magnetic field inhomogeneity become weaker in DA regime $N_{\|} = 1$. In Ref.[15] we investigate this possibility in tokamak. In DA monochromatic ECR wave can accelerate electrons infinitely without formation of plateau on

distribution function and besides electrons gain parallel momentum from the wave along with the energy. As a result a "jets" is formed in velocity space. Figure [15] shows level lines of electron distribution as a result of model Fokker – Planck calculations in tokamak.

3.OGRA-4K

ECR discharge in cusp geometry is practically noninvestigated [16].

The OGRA–4K device is a superconducting single cusp. A cusp configuration was produced by two coils with counter – directed magnetic fields. Figure 12 shows counters of constant *B*. Any longitudinal asymmetry is connected with nonequivalence of coils which was used early in customary open trap in magnetic system OGRA–4. Maximum field in axial plugs is 3T, in magnetic gap is 1.85T. On the figure 12 are shown the two microwave inputs. The longitudinal input 1 was connected to gyrotron 1, which had a wavelength of 8 mm, and the transverse input 2 is connected to gyrotron 2, which had a wavelength of 10mm.

Figure 13 shows the magnetic field geometry, gyrotron 1 power P_g distribution and the position of ECR for two harmonics. The zones of warm electron production are shaded. The distance *l* across the field lines is counted off along lines passing through magnetic field minima points at field lines. The field rise gradient along *l* is 13 T/m.

The main purpose of experiment on OGRA – 4K are: (1) achievement a few percent of β; (2) demonstration of stable confinement of plasma with low pressure at cusp center; (3) investigation of the influence of nonadiabatic effects on plasma losses. Table 2 gives the measured plasma parameters [17]. Figure 14 shows the transversal distribution of ion axial (circles) and from slit (points) flux out of trap. Figure 15 shows the time dynamic of average plasma pressure at

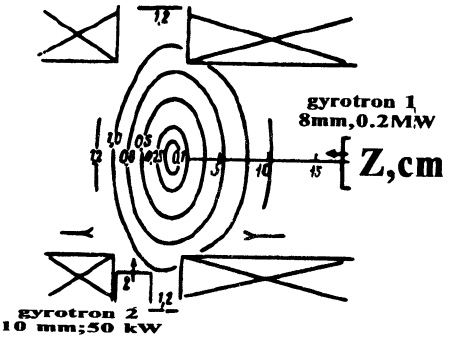

FIG12 Countours of constant B in OGRA-4K

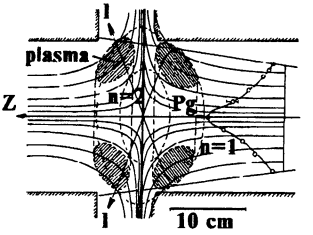

Fig.13. Field geometry and gyrotron power Pg distribution. The zones of warm plasma production are shaded

Table 2. Plasma Parameters in OGRA–4K.

Maximum density in ring	0.5 10+13 cm–3
Warm electron density	0.5 10+13 cm–3
Average energy warm elect.	(2–20) keV
Typical ring dimensions:	
along l	from 4 to 8 cm
along field line	4 cm
radius	7cm
Volume of warm plasma	1 liter
Cold electron density	(1–6) 10+11 cm–3
Cold elect. temperature	(20–80) eV
β (B=1T)	3%
Warm elect.lifetime	2 ms
Cold elect.lifetime	10 μs
Averige ion energy	(10–20) eV
Plasma potential	+(80–120) V

periodic gyrotron switch on/off. In experiments with great β we found that the continuous grow of diamagnetic signal is limited by global instability (disruptions) which can be stabilized by additional controlled gas puffing [18]. Figure 16 demonstrates this situation (*D*–diamagnetic signal; *Puff* – moment of additional gas puffing;*Hα* – intensity of Hα radiation; *P* – gas pressure in cusp).

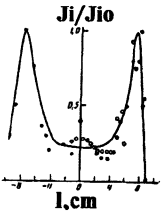

Fig.14.End ion flux along axis(circles) and slit(point)

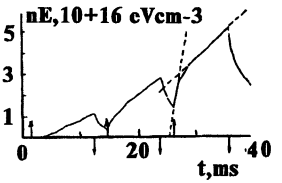

Fig.15.Plasma presssure vs.t pointer up-gyrotron switch on; pointer down-switch off.

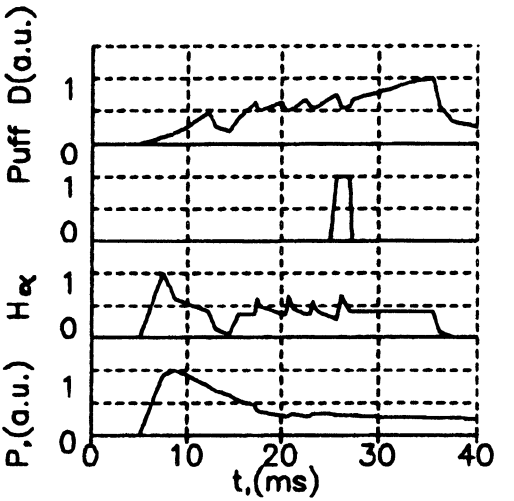

Fig.16.Stabilization of global instability by gas puffing.

Figures 17 and 18 show the *l*–profiles of electron and ion flux, plasma potential and cold electron temperature at low $\bar{l}$ there the nonadiabatic effects may be important. One can see that for electron nonadiabatic zone (l<1 cm) we have any little peculiarity, but for ion nonadiabatic zone l>1 peculiarities are absent.

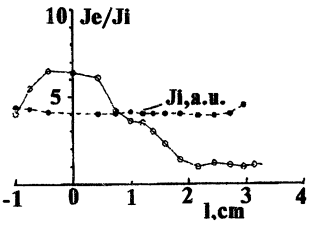

Fig.17.Electron and ion flux in slit vs.l

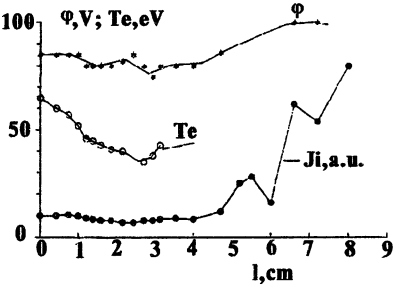

Fig.18.Plasma potential, cold electron temperature Te and ion flux vs.l

The main conclusion from these investigations is fact of MHD stable plasma confinement with high β in cusp with rather steep pressure profiles. It was demonstrated by measurements of plasma flux along field lines out of trap that the nonadiabatic particle and energy losses were small.

The interesting peculiarity of ECR in cusp is the absent of hot electrons with energy greater then 100 keV. On figure 13 we see that electrons concentrate in points where ECR condition for fundamental harmonic is close to the minimum of magnetic field along field line. In these points we have $N_{\|} < 1$ and the maximum electron energy is limited. The measured energy is close to obtained by Eq.1. When gyrotron was switched off the x–ray signals changed monotonously without sharp drops. We do not receive any peculiarities connected with second harmonic zone.

References

1.Alikaev V.V. et al., Plasma Phys., 1968, **10**, 753;
Dandl R.A. et al., Nucl. Fusion, 1973, **13**, 693.

2.Timofeev A.V., in: Reviews of Plasma Physics, B. B Kadomtsev (ed.),Vol.**14**,Consultants Bureau, N.Y.,p.56

3.Hokin S.A.,MIT Pl. Fus. Center,PFC/RR–87–17, 1987

4.Hiroe S. et al., Nucl. Fusion, 1988, **28**, 2249;
Chen X. et al., Phys. Fluids, 1989, **B1**, 615.

5.Cho T. et al., Nucl. Fusion, 1987, **27**, 1421;
Saito T. et al., Proc. 16th Europ. Conf. Contr. Fus. and Plasma Phys.,Venice,1989,ECA 13B, Pt.III, p.1127

6.Timofeev A.V. and Zvonkov A.V., Sov. J. Plasma Phys., 1986, **12**, 238.

7.Hafizi B. and Aamodt R.E., Phys.Fluids, 1987,**30**,3059

8.Davydovskii V.Ya.,Sov.Phys. JETF, 1963, **16**, 629;
Kolomenskii A.A. and Lebedev A.N. ibid. 1963,**17**,179.

9.Belavin M.I. et al.,Sov.J.Plasma Phys., 1990,**16**,568 and 572.

10.Belavin M.I. et al.,Plasma Phys. and Contr. Nucl. Fusion Res.1988 (Nice Conf.), Nucl. Fusion Suppl. 1989, **2**, 691;
Belavin M.I. et al. , Topics in Atomic Science and Technology, Thermonuclear Fusion Series [In Russian],1988, **1**, 51 and ibid. 1988,**3**,7.

11.Kosarev P.M. and Skovoroda A.A., Prib. Tekh. Eksp. 1989,**1**,148 (Sov. Instruments and Techniques of Experiment).

12.Skovoroda A.A., Zhil'tsov V.A. et al. Proc. 17th Europ. Conf. Contr. Fus. and Plasma Heating, Amsterdam,1990,ECA 14B, Pt.II,593 and Pt.III, 1072;
Belavin M.I. et al., Thesis. Int. Workshop Strong Microwaves in Plasma, Suzdal, 1990,H–22;
Skovoroda A.A., Timofeev A.V. et al., Proc. 18th Europ. Conf. Contr. Fus. and Plasma Phys., Berlin, 1991,ECA 15C, Pt.II, p.C13–265;
Skovoroda A.A., Zhil'tsov V.A. et al., Sov.J. Plasma Phys.,1991, **17**, 456 and 365.

13.Kharitonov K.Yu., Skovoroda A.A., Timofeev A.V. et al., Sov.J.Plasma Phys., 1991,**17**,447.
14.Kuyanov A. Yu., Skovoroda A. A. et al., Sov. J. Plasma Phys., 1993, **19** (to be published).
15.Kuyanov A.Yu., Skovoroda A.A., Timofeev A.V. et al., Proc. 19th Europ. Conf. Contr. Fus. and Plasma Phys., Innsbruck,1992, ECA 16C,Pt.II,p.1521;
Kuyanov A.Yu., Skovoroda A.A., Timofeev A.V. et al., Proc. 14th Int. Conf. on Plasma Phys. and Contr. Nucl. Fus. Res., Wurzburg, 1992, E–3–5.
16.Physics of Multiply Charged Ions, J. de Physique.1989,**50**,C1,Suppl.1.;
Kunze J.F. et al.,Fus.Technol.1986,**10**,Pt.2a, p.1034
17.Belavin M.I. et al., Proc. 12th Int. Conf. on Plasma Phys. and Contr. Nucl. Fus. Res., Nice, 1988, Nucl. Fus. Suppl. **2**, p. 691;
Belavin M.I. et al.,Sov.J.Plasma Phys.1990,**16**,447;
Belavin M.I. et al., Proc. 13th Int. Conf. on Plasma Phys. and Contr. Nucl. Fus. Res., Washington,1990, Nucl. Fus. Suppl. **2**, p. 747
18.Skovoroda A.A., Zhil'tsov V.A. et al. Proc. 17th Europ. Conf. Contr. Fus. and Plasma Heating, Amsterdam, 1990, ECA 14B, Pt.II, p.593;
Skovoroda A.A., Zhil'tsov V.A. et al., Sov.J. Plasma Phys.,1991, **17**, 365;

Production and Application of ECR Plasma Discharge with Relativistic Electron Component

S.V.Golubev, V.E.Semenov, E.V.Suvorov, M.D.Tokman
Institute of Applied Physics, Nizhny Novgorod, Russia

1 Introduction

Interaction of microwave field with plasma electrons under electron-cyclotron resonance (ECR) conditions proved to be a rather simple and efficient way to increase essentially the energy of plasma electron component. The most impressive application of this type is at present ECR plasma heating in fusion toroidal devices [1] the main aim of which is the heating of bulk plasma ions up to fusion temperatures of order of 10-20 keV. Success in this field became possible due to achievements in the design and manufacturing of powerful microwave generators - gyrotrons (see e.g.[2]). At the same time in recent years ECR phenomenon was successfully used in simple mirror magnetic traps to get plasma with high energy content in electron component for non-fusion applications. ECR sources are used (or there are detailed proposal to use them) for multi-charged ion production [3], for isotope separation, for collective ion acceleration in plasma accelerators [4], for generation of SXR radiation [5], for material processing [6] etc. ECR is also used for production of hot electron "rings", "disks" and other specific electron distributions in space and velocity space for plasma stabilization in sophisticated magnetic traps like bumpy-tori and tandem-mirrors [7] (this may be considered as semi-fusion applications). Many of these applications are presented here at

the Workshop both at Plenary sessions and in the Discharge section session.

Two distinguished specific features are typical of the ECR discharge in small or moderate-size mirror traps used for applications. The first is that due to a small volume of plasma it is possible to achieve a rather large energy deposition per unit plasma volume with microwave generators of moderate power. The second is that due to short energy (and particle) life-time in a trap the energy exchange between electron and ions is rather weak and the energy content in the electron component may be essentially greater than that in ion component.

The ECR discharge in a simple mirror trap possesses a number of advantages for the applications such as:

a) low break-down conditions (practically without threshold),

b) easy and reliable cw operation (steady-state ECR discharge),

c) high efficiency of energy transformation from microwave radiation to electron component of a plasma which is essentially easy with longitudinal launch of radiation into the trap,

d) good energy and particle confinement in radial direction for simple axisymmetric traps;

e) easy realization of unidirectional energy flow in one-mirror geometry.

The contemporary tendency in the development of ECR discharge for applications to use higher frequencies in order to get higher electron density in the plasma results in a natural change from cavity modes to quasi-optical microwave beams which gives opportunity to vary plasma volume independently of the radiation wavelength.

In the present communication we consider mainly the problem of electron distribution function formation in the ECR discharge in a mirror magnetic trap under the action of intense microwave field. In this problem different aspects of ECR discharge physics are important. First of all it is electron - microwave field interaction in the situation when electron bouncing between the plugs crosses the section in which ECR condition is satisfied. When considering the energy gain of electron resulting from many passages through the

resonant zone it is necessary to take into account shifting of resonance zone into the plug due to relativistic variation of electron mass and forcing of electron out of the plug due to increase in its magnetic momentum. An important circumstance is that (especially in steady-state ECR discharge) electron distribution function is influenced by plasma life-time in magnetic trap which is defined by joint behavior of both electron and ion components of plasma. We draw specific attention to the induced electron precipitation into the loss-cone due to the interaction with microwave field which plays an important role in the resulting life-time and which usually is not taken into account. Some aspects of ECR discharge applications are also considered.

2 The main peculiarities of ECR heating of electrons in the mirror trap

It seems useful to start the discussion of ECR heating of plasma in mirror traps with specifying some general features of electron-microwave resonant interaction. Let there be a monochromatic electromagnetic wave propagating at some angle to the axis of trap with frequency ω being equal to the N-th harmonic of nonrelativistic electron cyclotron frequency at some section of mirror Z_R^0 cited further as "cold" resonant section (see Fig. 1). Then the effective interaction takes place in the vicinity of "hot" resonant section Z_R where the following equality is satisfied:

$$N\omega_H = \gamma\omega(1 - n_\parallel\beta_\parallel) \qquad (1)$$

(1) where $\omega_H = eH/mc$ is nonrelativistic gyrofrequency of electron, $H = H(Z_R)$ is magnetic field strength in the section Z_R, e, m, and c are the charge and rest mass of electron, and light velocity respectively, $n_\parallel$ is the longitudinal (with respect to magnetic field) refractive index of electromagnetic wave, $\gamma = 1/\sqrt{1-\beta^2}$ is relativistic factor, $\beta^2 = \beta_\parallel^2 + \beta_\perp^2$, $\beta_\parallel = V_\parallel/c$, $\beta_\perp = V_\perp/c$, $V_\perp$, $V_\parallel$ are the transverse and longitudinal (with respect to magnetic field) components of electron velocity.

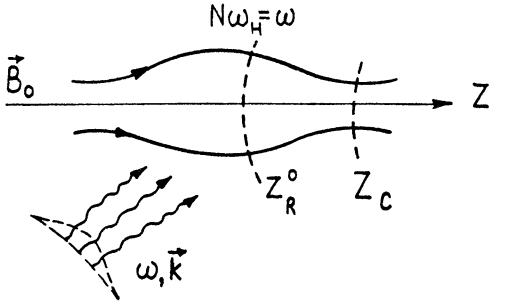

Figure 1: The scheme of ECR heating in the mirror trap

In contemporary experiments on ECR in mirror traps (end traps of tandem mirrors, ECR source of multicharged ions and others) free path of electron is much greater compared to distance between the plugs and electrons perform many bounce oscillations before leaving the trap. Therefore, we shall consider electron distribution function averaged over period of these oscillations to describe ECR heating of plasma. The distribution function will be reduced to the cold resonant section, which, in principle, is sufficient to determine it in every section[1]. In this connection some peculiarities of ECR interaction are shown below as applied to electrons in the section Z_R^0.

First of all it should be noted that not all electrons available in section Z_R^0 reach section Z_R and participate in resonant interaction. Specifically, when $n_\parallel^2 < 2$ the fulfillment of resonant equality (1) is possible inside the trap only for electrons with the transverse velocity not too large in the cold resonant section. In the case of weakly relativistic electrons to which we confine our consideration here, the above condition can be represented in rather simple form:

$$\beta_\perp^2 < 2\beta_\parallel / \sqrt{2 - n_\parallel^2} \qquad (2)$$

Certainly this limitation can be more severe if the microwave beam

[1]Since the averaged distribution function depends on the integrals of electron motion in the inhomogeneous magnetic field of the trap.

width is small enough but we are not going to analyze specially this problem.

To analyze the evolution of electron distribution function in time it is also important to know the relation between the changes of transverse and longitudinal components of electron velocity in the course of ECR interaction. In terms of electron parameters in the cold resonant section this relation is determined by conservation of the following value [8-10]:

$$2\gamma - \gamma^2\beta_\perp^2 = const \tag{3}$$

With taking into account this relation one can see that increase in electron energy up to infinity is possible without violation inequality (2) if $n_\parallel > 1$. However, with $n_\parallel < 1$ increase of electron energy is limited above. The maximum energy which electron can reach is determined by initial conditions and can be expressed as follows [11]

$$\beta_m^2 = 2\beta_{\parallel 0}/\sqrt{1 - n_\parallel^2} \tag{4}$$

if at the early stage transverse component of electron velocity is of order of longitudinal one in the section Z_R^0. Here $\beta_{\parallel 0}$ corresponds to the initial value of electron longitudinal velocity.

It should be noted that there are some other mechanisms [10-15] of energy limitation for electrons heated under ECR conditions in magnetic mirror (including the case of quasi-longitudinal launch of the radiation, when $n_\parallel > 1$). Omitting the details we underline only that electrons can remain weakly relativistic within a wide variety of conditions; this circumstance will be used in future consideration.

In the most cases, being averaged over many passages through the resonant region, the interaction of electrons with microwave field can be considered as a diffusion process in the velocity space (so called quasilinear diffusion [8,10,13]). The diffusion occurs along the lines at which the integral (3) is conserved. In a weakly relativistic limit these lines are almost perpendicular to the axis of longitudinal velocity which results in kinetic equation with the diffusion over transverse

velocities [8,16]:

$$\frac{\partial f}{\partial t} = \tau_b^{-1} \frac{1}{\beta_\perp} \frac{\partial}{\partial \beta_\perp} \left\{ \beta_\perp (\tilde{\beta}^2/2) \frac{\partial f}{\partial \beta_\perp} \right\} \tag{5}$$

Here $f(\beta_\perp, \beta_\parallel, t)$ is electron distribution function in resonant section Z_R^0 , $\tau_b(\beta_\perp, \beta_\parallel)$ is the bounce oscillation period of trapped electrons, $\tilde{\beta}^2$ corresponds to the averaged over cyclotron phases "jump" in the value of $\beta_\perp^2$ due to the single pass of electron through the ECR region. The mentioned above limitation of electron energy corresponds (see equation (5)) to the presence of definite boundary of diffusion region:

$$\beta_\perp \leq \beta_m(\beta_\parallel) \tag{6}$$

out of which the value $\tilde{\beta}^2$ equals zero .

For the full description of ECR discharge in mirror systems it is also necessary to take into account the processes of particle "birth" inside the trap (due to ionization), particles losses through the plugs, and particle collisions. Within our model it is possible to include the ionization process into kinetic equation as a source term in the region of velocity space ($\beta_\perp^2 + \beta_\parallel^2 \leq \beta_i^2$) corresponding to energies of order of ionization potential of neutrals or of ions (if we deal with multicharged ions). Respectively the process of electron losses can be included in the model as some sink term in the kinetic equation. Usually the region corresponding to the particle losses is associated with loss-cone in the velocity space[2]:

$$\beta_\perp \leq \beta_{\perp c} = \beta_\parallel / \sqrt{R-1} \tag{7}$$

where R is the mirror ratio for the cold resonant section Z_R^0 . However, when dealing with ECR heating it is necessary to remember that

[2]To be more precise we should note that it is necessary to take into account the effect of ambipolar electric field when investigating electron losses at the developed stage of ECR discharge. This field, arising due to charge separation, does not permit the electrons to leave the trap if their longitudinal velocity $\beta_\parallel$ is below some definite value β_φ. Due to this the sink term equals zero in the region where $\beta_\parallel < \beta_\varphi$.

before reach the plug from section Z_R^0 electron have to pass section Z_R where its transverse velocity is changed due to resonant interaction. If at the boundary of the loss-cone $\tilde{\beta}$ is much less compared to dimensionless value of transverse velocity component ($\tilde{\beta}_c \ll \beta_{\perp c}$) the mentioned above effect is unessential and the loss-region for electron in cold resonant section coincides with the loss-cone. But in the opposite limiting case ($\tilde{\beta}_c \gg \beta_{\perp c}$), the changes of transverse electron velocity in ECR region results in the enlargement of the loss-region up to that one determined by inequality $\beta_\perp \leq \tilde{\beta}_c$.

Electron collision scattering can be also represented as a diffusion in velocity space. This diffusion occurs mainly along the lines at which electron energy is conserved. The frequency of Coulomb collisions ν declines rather fast with increasing of electron energy ($\nu \propto \beta^{-3}$). Therefore, the quasilinear diffusion is always dominant in the velocity space region corresponding to sufficiently high energy of electron with the exception of the region where $\beta_\perp > \beta_m$.

Thus, besides the region of electron birth due to ionization we can distinguish at least two other characteristic regions in the velocity space (see Fig. 2). One of them ("cold" region, or "C-region") is associated with cold electrons. Here the collisional diffusion is stronger than quasiliner one, i.e. $\nu\beta^2 > \tilde{\beta}^2/\tau_b$. Using formula $\nu = \nu_c\beta^{-3}$ the last inequality can be represented as follows:

$$\begin{gathered} \beta < \beta_\nu \\ \beta_\nu \sim \nu_c \tau_{b\nu}/\tilde{\beta}_\nu^2 \end{gathered} \tag{8}$$

where $\nu_c = 4\pi Z e^4 n \Lambda m^{-2} c^{-3}$, Z is the charge number of ion, n is electron density of plasma, Λ is Coulomb logarithm, $\tilde{\beta}_\nu \equiv \tilde{\beta}(\beta_\perp = \beta_\nu, \beta_\parallel = \beta_\nu)$, $\tau_{b\nu} \equiv \tau_b(\beta_\perp = \beta_\nu, \beta_\parallel = \beta_\nu)$. Due to strong scattering one can expect the isotropic electron distribution over velocities will be formed in the C-region with the exception of the vicinity of loss-cone, where the drop of distribution function may occur. As for the ECR interaction this process influences only electron heating in this region determining the characteristic scale β_T of electron distribution over energies.

Another characteristic region ("hot" region, or "H-region") is connected with the rest part of velocity space ($\beta > \beta_\nu$). In the defi-

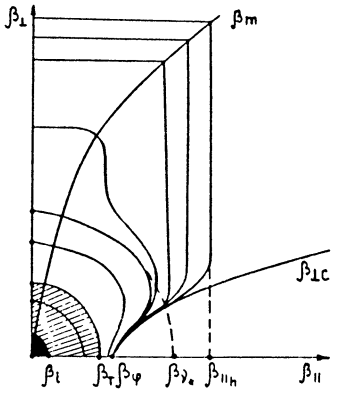

Figure 2: The characteristic structure of electron distribution function over velocities under the condition of powerful ECR heating in the mirror trap.

nite domain of H-region, where $\beta_\perp < \beta_m$, the quasilinear diffusion is stronger compared to collisional one. This provides the electron distribution with $\beta_\perp \gg \beta_\parallel$ in the H-region. At the same time there is only collisional diffusion in the domain with $\beta_\perp > \beta_m$. This diffusion can be considered as diffusion over longitudinal velocities and provides quasi-homogeneous electron distribution over longitudinal velocities here.

The isotropy of the electron distribution function in the C-region results in the quasi-uniformity of this function in that part H-region where $\beta_\parallel < \beta_\nu$, $\beta_\perp < \beta_m(\beta_\parallel = \beta_\nu)$. It should be noted that in general case the quasi-uniformity of the distribution function can occur also out of the mentioned part of H-region. Specifically, when $\beta_\varphi > \beta_\nu$ this peculiarity features the distribution function in the domain where $\beta_\parallel < \beta_\varphi$, $\beta_\perp < \beta_m(\beta_\parallel = \beta_\varphi)$ because there are no electron losses here. In other part of H-region (further we shall denote it as "HH-region") the quasilinear diffusion, being strong (compared to the process of collisional scattering) results not only in the significant anisotropy of electron distribution over velocities but in plasma escape from

the mirror trap as well [16,17]. In this domain due to the process of electron losses the electron distribution function decreases with energy increase.

We can estimate the rate of electron precipitation into the loss-region (which is due to ECR interaction) considering quasilinear diffusion in fixed plane $\beta_\parallel = const$ with taking into account the sink term in the kinetic equation. When this diffusion is relatively weak ($\tilde{\beta}_c \ll \beta_{\perp c}$) the electron losses are strong enough to provide essential drop of the distribution function inside the loss-cone. In this case the problem can be reduced to solution of equation (5) with boundary condition $f = 0$ when $\beta_\perp = \beta_{\perp c}$. The result is dictated by $\tilde{\beta}(\beta_\perp)$ dependence. In the case of ECR heating at the first harmonic of electron gyrofrequency the value of $\tilde{\beta}$ is not changed considerably with $\beta_\perp$ increase and the characteristic time τ_p of electron precipitation into the loss-cone can be expressed as [18]:

$$\tau_p(\beta_\perp, \beta_\parallel) \sim \tau_\perp \ln\left(\beta_\perp^2/\beta_{\perp c}^2\right) \tag{9}$$

where $\tau_\perp(\beta_\perp, \beta_\parallel)$ corresponds to the characteristic time of transverse diffusion over the distance in velocity space of order of $\beta_\perp$:

$$\tau_\perp \sim \tau_b(\beta_\perp/\tilde{\beta})^2 \tag{10}$$

On the other hand, if the value of $\tilde{\beta}$ rises as the transverse velocity component increases (which is typical for ECR heating at the second harmonic) then another estimate of τ_p is valid [18]:

$$\tau_p(\beta_\perp, \beta_\parallel) \sim \tau_\perp \tilde{\beta}^2/\tilde{\beta}_c^2 \tag{11}$$

As it follows from the comparison between (10) and (9),(11), the precipitation time τ_p is less than $\tau_\perp$ if $\beta_\perp \gg \beta_\parallel$. It implies that in the considered case (when $\tilde{\beta}_c \ll \beta_{\perp c}$) the plateau over transverse velocities is formed at the electron distribution function f in the region $\beta_\perp \leq \beta_m$ (the exception is the vicinity of loss-cone where there is the drop of the distribution function).

In the opposite limiting case (when $\tilde{\beta}_c \ll \beta_{\perp c}$) the sink term is not large enough to produce considerable drop of distribution function in

the loss-region, i.e. the plateau over transverse velocities is formed in the whole region $\beta_\perp < \beta_m$. The estimate of the rate of electron losses can be performed on the basis of assumption that all electrons, which occupy some domain with area $\pi\beta_{\perp c}^2$ in the velocity space region $\beta_\perp \leq \tilde{\beta}_c$, leave the trap during a half of bounce oscillation period τ_b. This results in the following expression for the characteristic time of the electron precipitation into the loss-region [14,18][3]:

$$\tau_p(\beta_\perp, \beta_\parallel) \sim \beta_\perp^2 \tau_b / \beta_{\perp c}^2 \qquad (12)$$

3 Solving technique

As it is clear from above analysis, the sufficiently complete information about the electron distribution function is associated with the parameters β_ν (which features the intensity of microwave radiation), β_T (which corresponds to the scale of electron distribution function in the cold region of velocity space), β_φ (which is determined by ambipolar electric field), $\Delta\beta_\parallel$ (which corresponds to the characteristic scale of electron distribution over longitudinal velocities in the HH-region[4]), and with the dependence $\beta_m(\beta_\parallel)$.

Naturally, in order to find all these parameters it is necessary to specify the mirror trap geometry and the characteristics of microwave field such as its intesity, frequency, polarization (specified by used normal wave), launching angle, etc. The particular results will be left until different applications will be considered in Sec. 4,5. Here we shall discuss only the general way to estimate $\Delta\beta_\parallel$, β_T , β_φ , under the assumption that the dependencies $\tau_b(\beta_\perp, \beta_\parallel)$ and $\tilde{\beta}(\beta_\perp, \beta_\parallel)$ are known.

First of all we note that $\Delta\beta_\parallel$ is in fact determined by the process of relatively weak collisional diffusion during the time of electron precipitation into the loss-region. With taking into account the anisotropy

[3]Considered case has much in common with so called "strong diffusion case" [17] corresponding to the loss-cone filled with electrons.

[4]To be more precise we should note that $\Delta\beta_\parallel$ is introduced only for that part of velocity space where $\beta_\parallel > \beta_i$.

of the distribution function ($\beta_\perp \gg \beta_\parallel$) and plateau over transverse velocities one can obtain the following estimate:

$$(\Delta\beta_\parallel)^2 \sim \langle \nu\tau_p\beta_\perp^2 \rangle \sim \nu_c\beta_h^{-1}\tau_{ph} \tag{13}$$

Here and further the brackets $\langle\rangle$ corresponds to averaging of parameters over electron distribution we are interested in, $\beta_h = \beta_m(\beta_{\parallel h})$, $\beta_{\parallel h} = \beta_l + \Delta\beta_\parallel$, $\beta_l = max\{\beta_i, \beta_\varphi, \beta_\nu\}$, $\tau_{ph} = \tau_p(\beta_\perp = \beta_h, \beta_\parallel = \beta_{\parallel h})$.

The most appropriate way to estimate the characteristic energy of cold electrons is the analysis of their energy balance. It should be noted however that this way may be used only in the case when the intensity of microwave radiation is low enough to provide validity of inequality[5]

$$\beta_\nu \gg \beta_\varphi \ , \ \beta_T \tag{14}$$

In this case within the quasilinear approximation microwave power P_a absorbed by cold electrons can be represented as

$$P_a \sim N_e mc^2 \tilde{\beta}_T^2/\tau_{bT} \tag{15}$$

$$N_e = S_R c \int_0^\infty 2\pi\beta_\perp d\beta_\perp \int_0^\infty \beta_\parallel \tau_b f(\beta_\perp, \beta_\parallel, t) d\beta_\parallel \tag{16}$$

where $\tilde{\beta}_T \equiv \tilde{\beta}(\beta_\perp = \beta_T, \beta_\parallel = \beta_T)$, $\tau_{bT} \equiv \tau_b(\beta_\perp = \beta_T, \beta_\parallel = \beta_T)$, N_e is the total number of electrons in the magnetic field tube with area S_R in the cold resonant section. On the other hand the energy flux from the trap, which is connected with the cold electrons in the field tube, can be presented by the following expression:

$$P_e \sim \tau_e^{-1} N_e mc^2(\beta_i^2 + \beta_T^2 + \beta_\varphi^2) \tag{17}$$

where τ_e is the average lifetime of electrons in the trap.

[5]In the opposite case when the inequalities (14) are reversed (further we shall see that both of them are reversed collectively) the specification of cold electron component becomes a matter of convention because the electron distribution function becomes quasi-uniform in the whole region in the velocity space with $\beta_\parallel \leq \beta_\varphi$, $\beta_\perp \leq \beta_m(\beta_\parallel = \beta_\varphi)$. This region is much greater compared to the C-region which allows to identify the parameter β_T with β_φ without serious consequences.

In order to estimate the ambipolar effect it is necessary to find the total flows of electrons J_e and ions J_i from the trap as the functions of β_φ . Thereafter the condition of zero electric current from the trap results in the equation for the unknown β_φ :

$$J_e(\beta_\varphi) = ZJ_i(\beta_\varphi) \tag{18}$$

Corresponding calculations can be considerably simplified in two limiting cases. In particular, one can neglect the contribution of hot electrons to the total electron flow from the trap if microwave radiation is sufficiently small (see (14)). On the other hand, when microwave intensity is high enough and $\beta_\nu < \beta_\varphi$ the cold electrons cannot leave the trap at all and the only losses of hot electrons should be taken into account.

In the first case the electron losses are almost completely determined by collisions and assuming the Maxwellian distribution of cold electrons over velocities we can use well known Pastuhov's formula [19] for electron lifetime τ_e :

$$\tau_e \sim \nu_c^{-1}\beta_T^3 e^\mu/(1+\mu) \quad , \quad \mu = (\beta_\varphi/\beta_T)^2 \tag{19}$$

In the second case the electron lifetime is governed by the process of hot electron precipitation into the loss-region. At the same time it is clear that the characteristic value of electron longitudinal velocity $\beta_{\|h}$ is determined by the process of relatively weak collisional diffusion during the their whole lifetime. Therefore, in a similar manner like (13) we can obtain the following expression:

$$(\beta_{\|h} - \beta_i)^2 \sim \nu_c \beta_h^{-1}\tau_e \tag{20}$$

which will be used further for the estimates of τ_e. In both cases the total electron flow from the magnetic field tube with area S_R in the resonant section can be expressed as:

$$J_e = \tau_e^{-1} N_e \tag{21}$$

As for the ion lifetime a rather simple way to estimate it can be proposed when ions are sufficiently "cold" and the quasi-neutrality

of plasma is mainly provided by ions redistribution inside the trap. In this case the ambipolar electric field arising near the magnetic plugs is strong enough to neglect the thermal motion of ions and diamagnetic force action on them but it does not disturb the spatial distribution of electrons which is mainly determined by their distribution over velocities and magnetic field inhomogeneity. It should be noted here that the confinement of electrons in the loss-cone is caused not only by ambipolar electric field inside the trap but essentially by the field outside of it (in particular by the potential drop in the double layer at the plasma boundary). As a result the problem of ion escape through the plugs can be considered within a hydrodynamic approach. Qualitatively the solution may be described as follows. The ions flow through the "throat" of mirror with the hydrodynamic velocity of order of the ion sound velocity C_s corresponding to the average longitudinal velocity of electrons inside the loss-cone: $C_s \sim c\sqrt{Zm/M}\beta_\varphi\beta_T/(\beta_\varphi+\beta_T)$, where M is the mass of ion. At the same time the plasma density n_c in the throat is determined by those electrons which in the resonant section belong to the loss-cone. Taking into account the main peculiarities of electron distribution over velocities the total ion flow J_i from the magnetic field tube with area S_c in the throat of the mirror may be estimated as:

$$J_i \equiv Z^{-1}S_cC_sn_c \sim Z^{-1}S_cc\beta_T\sqrt{Zm/M}n_R\mu^2(1+\mu)^2 \qquad (22)$$

if the intensity of microwave radiation is low enough (see (14)), or as:

$$J_i \sim Z^{-1}S_cc\beta_\varphi\sqrt{Zm/M}n_R\beta_\varphi^3/(\beta_h^2\beta_{\|h}) \qquad (23)$$

if the intensity of microwave radiation is sufficiently high. Here n_R and n_c are the electron densities in the cold resonant section and in the throat of the mirror respectively.

4 Application to the calculation of ECR breakdown threshold

Usually under ECR conditions it is not difficult to heat electrons up to the energy in excess of ionization potential of neutral particles.

In typical mirror systems electrons gain such energy due to single passage through the resonant region. It should be also noted that transport cross-section σ_t is much less than ionization one σ_i for sufficiently energetic electrons. In this case the ionization is more fast process as compared to collisional scattering. Therefore in the mirror trap the breakdown threshold may exist only is some process providing faster electron losses comparing to usual scattering. Such process is the electron precipitation into the loss-cone, which has been considered above. In this connection the commonly accepted condition of the breakdown $\nu_i \tau_e > 1$ can be represented as follows[6]:

$$\nu_i \langle \tau_p \rangle > 1 \tag{24}$$

where ν_i is the frequency of electron impact ionization.

Not interesting in the problem of the threshold value of microwave power we shall consider it being sufficiently high to provide validity of inequalities $\tilde{\beta}_c \gg \beta_{\perp c}$ and $\beta_\nu \ll \beta_i$. In this case the electron distribution function is quasi-homogeneous over transverse velocities in the region with $\beta_\perp \leq \beta_m$. This peculiarity simplifies considerably all calculations. Firstly, the relation (12) yields:

$$\langle \tau_p \rangle \sim (R-1)(\beta_h/\beta_{\|h})^2 \tau_{bh} \tag{25}$$

where $\tau_{bh} = \tau_b(\beta_\perp = \beta_h, \beta_\| = \beta_{\|h})$. Secondly taking into account the approximations for the ionization and transport cross-sections ($\sigma_i \sim \sigma_{i0}(\beta_i/\beta)^2$, $\sigma_t \sim \sigma_{t0}(\beta_i/\beta)^4$), which is appropriate for energetic electrons, one can calculate ν_i and $\Delta\beta_\|$:

$$\nu_i = n_m c \langle \sigma_i \beta \rangle \sim n_m c \sigma_{i0} \beta_i^2 / \beta_h \tag{26}$$

$$(\Delta\beta_\|)^2 \sim \langle \nu \beta_\perp^2 \rangle / \nu_i \sim \beta_i^2 \sigma_{t0}/\sigma_{i0} \tag{27}$$

where n_m is the density of neutrals, and we have supposed following dependence for the period of bounce oscillations: $\tau_b \sim \tau_c/\beta_\|$, $\tau_c =$

[6]At the initial stage of breakdown when plasma density is small enough one can neglect the influence of ambipolar electric field on electron confinement reasoning thereby $\tau_e = \langle \tau_p \rangle$.

L/c , L is the characteristic longitudinal scale of the trap[7]. Within this supposition one can obtain from (24)-(27) the final result for the breakdown condition as:

$$(R-1)n_m\sigma_{i0}c\tau_c\left(\sigma_{i0}/\sigma_{t0}\right)^{3/2}\beta_h/\beta_i > 1 \qquad (28)$$

The threshold value of the density of neutrals n_m depends on the mechanism of electron energy limitation (i.e. on the function $\beta_m(\beta_\parallel)$) in this case. It is interesting to note that in the case of quasi-parabolic spatial distribution of magnetic field intensity in the trap, when the approximation $\tau_b \sim \tau_c/\beta_\perp$ is valid, the threshold value of n_m does not depend on β_h within a logarithmic factor [14,20] and can be expressed in a rather general form:

$$n_m L(R-1) \geq Q \sim 10^{13}\mathrm{cm}^{-2} \qquad (29)$$

The breakdown condition (23) involves only the neutral gas pressure and two geometric parameters (by the length of mirror machine and by the position of ECR region with respect to magnetic plug). This was carefully verified in experiment [20] (see also the corresponding paper in this book [21]); it is in agreement with the results of early experiment [22] too.

One more interesting inference follows from the above results. The value of ratio σ_{t0}/σ_{i0} is not too high compared to unity. Therefore, the relation (27) is demonstration that the scattering of electrons is not significant in the case of ECR breakdown and the characteristic value of longitudinal electron velocity remains of order of its initial value: $\beta_{\parallel h} \sim \beta_i$.

[7]Such approximation is typical for square-well spatial distribution of magnetic field intensity in the trap. The other typical approximation $\tau_b \sim \tau_c/\beta_\perp$ is used in the case of quasi-parabolic spatial distribution of magnetic field intensity.

5 Application to the investigation of steady-state of ECR discharge. Characteristic values of plasma lifetime and of electron energy

In this section the main attention will be paid to the estimates of plasma lifetime and of characteristic parameters of electron distribution over velocities in steady-state of ECR discharge in the mirror magnetic traps. The results will be presented for ECR at the first and at the second cyclotron harmonics for microwave radiation launched nearly transverse to the trap axis (which means nearly perpendicular to dc magnetic field).[8]

When $n_{\|} \approx 0$ the relation (2) yields:

$$\beta_m \sim \sqrt{\beta_{\|}} \tag{30}$$

Having in mind practical applications we shall consider heating by O-mode at the first harmonic and by X-mode at the second harmonic. In this case it is possible to use following approximate relation for $\tilde{\beta}$ [13-16]:

$$\tilde{\beta}^2 \sim G \begin{cases} \beta_{\|} & \text{for } O\text{-mode} \\ \beta_{\perp}^2/\beta_{\|} & \text{for } X\text{-mode} \end{cases} \tag{31}$$

where $G = (eEn_{\perp}/mc\omega)^2 \omega l/c$, $n_{\perp}$ is the transverse (with respect to magnetic field) refractive index of electromagnetic wave, l corresponds to the scale of magnetic field inhomogeneity at hot resonant section, E is respectively the amplitude of linearly polarized (in the dc magnetic field) component of microwave electric field for O-mode, or the amplitude of transverse to the magnetic field circular component of microwave electric field rotating in the same direction as

[8] As for the solution of the same problem with quasi-longitudinal launch of radiation into magnetic trap it is essentially more complicated due to possible presence of evanescent region, additional effect of X- and O-modes coupling and singularity of X-mode refractive index near the cyclotron resonance region; this problem still remains to be far from a complete solution (see for example [23]).

electrons for X-mode. As for the $\tau_b(\beta_\perp, \beta_\parallel)$ dependence we shall mainly consider the spatial distribution of magnetic field intensity to be quasi-parabolic assuming thereby that $\tau_b \sim \tau_c/\beta_\perp$.

On the basis of presented here relations for $\beta_m(\beta_\parallel)$, $\tilde{\beta}$, and τ_b one can estimate all particular parameters of electrons (β_ν, β_T, β_φ, $\Delta\beta_\parallel$, β_h, and τ_e) just following the way discussed in Sec.3.

Actually, taking into account the isotropy of electron distribution function in the C-region we obtain from (31) that independently of the heating mode of microwave radiation

$$\tilde{\beta}_\nu^2 \sim G\beta_\nu \tag{32}$$

Respectively the characteristic value $\tau_{b\nu}$ can be presented as

$$\tau_{b\nu} \sim \tau_c/\beta_\nu \tag{33}$$

independently on the spatial distribution of magnetic field inside the trap. As a consequence we are able to rewrite the expression (8) for the boundary of the cold region in the explicit form:

$$\beta_\nu \sim (\nu_c\tau_c/G)^{1/3} \tag{34}$$

On the other hand the relations (9)-(13) yield in the case of relatively weak quasilinear diffusion, when $\tilde{\beta}_c \ll \beta_{\perp c}$:

$$(\Delta\beta_\parallel)^2 \sim \nu_c\tau_c \begin{cases} \frac{\ln[(R-1)/\beta_{\parallel h}]}{G\beta_{\parallel h}} & G \ll \beta_{\parallel h}/(R-1) \quad \text{for } O\text{-mode} \\ \frac{R-1}{G\beta_{\parallel h}} & G \ll \beta_{\parallel h} \quad \text{for } X\text{-mode} \end{cases} \tag{35}$$

In the opposite limiting case the corresponding results are the same for both modes under consideration:

$$(\Delta\beta_\parallel)^2 \sim \nu_c\tau_c(R-1)/\beta_{\parallel h}^2 \qquad G \gg \beta_{\parallel h}\ ,\ \beta_{\parallel h}/(R-1) \tag{36}$$

Quantitative analysis of (35) and (36) shows that the characteristic width of electron distribution over longitudinal velocities is completely determined by the position of boundary of HH-region: $\beta_{\parallel h} \sim \beta_l$. The characteristic scale $\Delta\beta_\parallel$ is about of the value β_l ($\Delta\beta_\parallel/\beta_l \sim$

$\{\ln[(R-1)/\beta_l]\}^{1/3} \sim 1$, for O-mode, or $\Delta\beta_\parallel/\beta_l \sim (R-1)^{1/3} \sim 1$, for X-mode) in the case of weak intensity of microwave radiation (when $\beta_l = \beta_\nu \gg \beta_\varphi$), and it is much less compared to β_l in the opposite limiting case (when $\beta_l = \beta_\varphi \gg \beta_\nu$). Another important conclusion is that there are no significant difference between two considered modes of microwave radiation in terms of the main specific features of electron distribution function. Therefore we shall not distinguish them further.

As it was mentioned previously, plasma contains mainly cold electrons when microwave power is sufficiently small (see (14)). Due to the isotropy of cold electron distribution over velocities, we can use the obvious relation $N_e \sim n_R S_R L$ which, in accordance with the conditions of ambipolar plasma flow from the trap (see (18),(19),(21),(22)) gives us the following equation in the unknown β_φ and β_T:

$$\beta_T^4 \frac{e^\mu \mu^2}{(1+\mu)^3} \sim \nu_c \tau_c R \sqrt{M/Zm} \tag{37}$$

where $\mu = (\beta_\varphi/\beta_T)^2$ (cf. (19)). The second equation in these unknowns can be obtained when equating the values of microwave power absorbed by the plasma in the trap and of energyflux from the trap (see (15) and (17)):

$$\frac{\beta_i^2 + \beta_T^2(1+\mu)}{\beta_T} \frac{\mu^2}{(1+\mu)^2} \sim GR\sqrt{M/Zm} \tag{38}$$

If we are interested in the physical solution of the equations (37)-(38) then it is necessary to choose those which are in agreement with the requirement of stability. It implies that a variation of absorbed power P_a, caused by positive variation of β_T, must be less compared to corresponding variation of the rate of energy loss P_e (the variation of μ is supposed to be consistent with equation (37)). Such a solution can be realized only in the case when the parameter $\xi = \nu_c \tau_c R\sqrt{M/Zm}/\beta_i^4$ is sufficiently high in magnitude:

$$\xi > \xi_m \sim 25 \tag{39}$$

When $\xi \gg \xi_m$ the stable solution does not exist if the intensity of microwave radiation is too small:

$$G < G_0 \approx \beta_i \sqrt{Zm/M}\sqrt{\mu_0}/R$$

where μ_0 is the largest root of the equation $\mu_0 - 3\ln\mu_0 \approx \ln\xi$. In this sense we can consider the value G_0 as corresponding to threshold value of microwave intensity needed to sustain steady-state of ECR discharge in the mirror trap in the absence of external source of ionization. The equations (37)-(38) have the stable solution satisfying the inequality $\beta_\nu > \beta_\varphi > \beta_T$ during the increase of G from G_0 up to $G_c \approx G_0 \xi^{1/4}\sqrt{5/\mu_0}$. According to this solution the characteristic energy of cold electrons increases approximately in proportion to G^2 and there is a slow logarithmic drop of parameter $\mu = (\beta_\varphi/\beta_T)^2$:

$$\begin{aligned} \beta_T &\sim \beta_i(\sqrt{\mu_0}/\mu)(G/G_0) \\ \mu - \mu_0 - 5\ln(\mu/\mu_0) &\sim 4\ln(G/G_0) \end{aligned} \tag{40}$$

Plasma lifetime or more specifically the characteristic lifetime of cold electrons decreases as $1/\beta_T$ in this case:

$$\tau_e \sim R\tau_c\sqrt{M/Zm}/\beta_T$$

When G reaches the critical value G_c the value of β_φ becomes comparebale with β_ν. In this case cold electrons cannot leave the trap and our consideration is violated. The limiting value of μ corresponding to $G \sim G_c$ is $\mu_c \approx 7$. The limiting values of β_ν and β_T equal respectively $A^{1/4}$, and $A^{1/4}/\sqrt{\mu_c}$, where $A = \nu_c\tau_c R\sqrt{M/Zm}$.

In the considered case ($G_0 < G < G_c$) there is, certainly, a small fraction of "hot" electrons besides the cold electron component. The hot component corresponds to electrons in the H-region of the velocity space, where the distribution function is quasi-homogeneous[9].

[9]It means that distribution function of all electrons in the trap over energies has a slowly diminishing "tail" in the range of energy from $mc^2\beta_\nu^2$ up to $mc^2\beta_h^2 \sim mc^2\beta_\nu$, where this distribution function is inversely proportional to square root of energy

According to (20) the characteristic lifetime of hot electrons τ_{eh} decreases with incresing microwave power similar to the lifetime of the cold component:

$$\tau_{eh} \sim \nu_c^{-1} \beta_{\|h}^{5/2} \sim \nu_c^{-1} \beta_\nu^{5/2} \propto G^{-5/6}$$

But in contrast with cold electrons the characteristic energy of hot component decreases in this case: $\beta_h \sim \sqrt{\beta_l} \sim \sqrt{\beta_\nu} \propto G^{-1/6}$ (cf.(34)). At the same time the total amount of hot electrons N_{eh} increases sharply with the growth of the microwave intensity. Due to this the total energy content in the hot component increases with microwave intensity increse, which results in the additional growth (as compared with (40)) of average electron energy in the trap.

One can estimate the value of N_{eh} assuming, for instance, the Maxwellian distribution of cold electrons over velocities and the continuity of electron distribution function at the boundary $\beta = \beta_\nu$:

$$N_{eh}/N_{ec} \sim \frac{\beta_\nu^{5/2}}{\beta_T^3} \exp(-\beta_\nu^2/\beta_T^2)$$

where N_{ec} is total amount of cold electrons in the trap.

The limiting values of τ_e/τ_{eh} and N_{ec}/N_{eh} (attained when $G \sim G_c$) equal $A^{1/8}\mu_c^{1/2}$ and $A^{1/8}\mu_c^{3/2}$ respectively. It should be noted that the value $A^{1/8}$ is weakly dependent on all the parameters and it is about 0.1 in the cases of practical interest. Therefore, the contribution of hot component to particle and energy losses from the trap is not very significant in the whole range $G_0 < G < G_c$ [10]. In other words, we can state that above consideration is reasonable up to $G = G_c$.

When G becomes more than G_c the value of β_φ exceeds β_ν, as it was mentioned above. In this case detailed analysis shows that

[10]Such is not the case for the contribution of hot component to the total energy of electrons. When $G \sim G_c$ the energy content in this component is more than one in cold component by a factor of $A^{-3/8}\mu_c^{-1/2} \gg 1$. However the hot electrons leave the trap when they precipitate into the loss cone. So the characteristic energy carried away with each electron of hot component is about of $mc^2\beta_l^2$, i.e. it is much less than the average energy of hot electrons

microwave power absorbed by cold electrons increases with increasing β_T more rapidly than energy flux from cold electron component to the hot one. Therefore, the steady-state with $\beta_T < \beta_\varphi$ becomes unstable and specific cold component of electrons disappears in the sense that the electron distribution function becomes quasi-homogeneous in the velocity space region with $\beta_\perp < \beta_h$ and $\beta_\parallel < \beta_l \sim \beta_\varphi$. As a result we can use the formulas (20) and (23) for the analysis of plasma escape from the trap. Taking into account the fact that $\beta_{\parallel h} \sim \beta_l = \beta_\varphi$ and the relation $N_e \sim cS_R n_R \tau_c \beta_{\parallel h}/\beta_h$ which follows from (16) in the case of quasi-parabolic spatial distribution of magnetic field intensity, one can obtain the expressions for all unknown parameters: τ_e, β_h, β_φ

$$\begin{aligned} \tau_e = \tau_{ec} &\sim \nu_c^{-1} A^{5/8} \\ \beta_h &\sim A^{1/8} \\ \beta_\varphi &\sim A^{1/4} \end{aligned} \tag{41}$$

Thus, it may be concluded that there is a cosiderable change in characteristics of the steady-state of ECR discharge when the intensity of microwave radiation exceeds some critical value. This corresponds to the disappearance of pronounced cold component of electrons and results in jump-like variations of the value of average electron energy (which is due to the change in the value of N_{eh}/N_e by the factor $\mu_c^{3/2} A^{1/8}$) and of the value of plasma lifetime (by the factor $A^{-1/8}\mu_c^{-1/2}$). It is rather important that plasma lifetime and characteristic energy of electrons becomes independent of the microwave field intensity when it is high enough (cf. (41)). As it is clear from (41) the electron energy is weakly dependent on all the other parameters such as plasma density charge and mass of ion and geometry of trap. Specifically, the characteristic value of electron energy is about $5 \div 10$keV for a rather wide range of parameters, e.g. for electron density within $10^{11} \div 10^{12}\text{cm}^{-3}$, the trap length L - $10 \div 100$cm, mirror ratio not more than 10 , and the value of Zm/M within $10^{-3} \div 10^{-5}$. The critical value of microwave radiation intensity corresponding to G_c depends mainly on the radiation frequency ω and on the scale of magnetic field inhomogeneity l in the hot resonant section. Assuming the radiation wavelength of order of 1cm, and $l \sim$ 10cm, one can esti-

mate the critical density of microwave energy flux as $30 \div 100 \mathrm{kW/cm^2}$.

When plasma density is too small and the inequality $\xi \ll \xi_m$ takes place the similar as presented above analysis shows that only steady-state without pronounced cold component of electrons is possible. In this sense the threshold value of microwave intensity coincides with its critical value. Corresponding estimates results in $G_0 = G_c \sim \beta_i \sqrt{Zm/M} \ln(1+\xi)/R$. As for the main parameters of electrons such as τ_e, β_h, and β_φ they can be estimated using (41) if $\xi > 1$, but when $\xi < 1$, we should use quite different relations:

$$\begin{aligned} \beta_\varphi &\sim \beta_i \\ \beta_h &\sim \sqrt{\beta_i} \\ \tau_e &\sim \nu_c^{-1} A/\beta_i^3 \end{aligned} \tag{42}$$

6 Production of relativistic electron population

There is a considerable interest in production of relativistic (and ultra-relativistic) electrons in simple mirror traps in view of possible applications such as generation (bremsstrahlung [5] or synchrotron [24]) of radiation in wavelength range from UV to SXR, collective acceleration of heavy ions in plasma accelerators [4,25], creation of specific distributions of hot electrons in end traps of tandem-mirrors [11,26] etc.

The main problem in ECR acceleration of electrons up to relativistic energies is to overcome frequency detuning due to variation of electron relativistic mass with the increase of its energy. Using monochromatic radiation this may be done by two ways. The first is to distribute microwave field over the region of electron motion with essentially inhomogeneous magnetic field. In this case in the process of energy increase the region of resonance interaction is shifting in the direction of more intense magnetic field. The second is to provide variation of magnetic field in time correspondingly to variation of electron gyrofrequency with energy increase.

We used the first idea in the design of ECR complex for production of hot electron "disks" with the density more than $10^{12} \mathrm{cm^{-3}}$ and

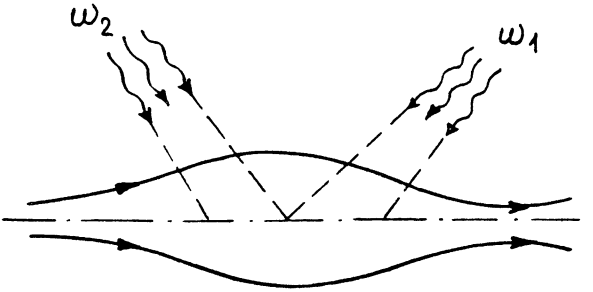

Figure 3: The scheme of two frequency ECR heating in the end cell of the tandem mirror trap

energies in the region of hundreds keV in the end traps of Novosibirsk tandem-mirror AMBAL-M [26]. The geometry of plasma irradiation by two quasi-optical microwave beams of finite cross-section is shown in Fig. 3. Since the magnetic field inhomogeneity is not sufficient to compensate the detuning two-frequency scheme was used. With launch angle about 45 deg. and beam apertures about 10 cm the use of two frequencies corresponding to wavelength of radiation 4.0 and 5.5 mm provides step-by-step resonant interaction with changing the number of cyclotron harmonic in resonance and the microwave field frequency [11,26]:

$$\begin{aligned} 2\omega_H/\gamma &\approx \omega_1 \\ 2\omega_H/\gamma &\approx \omega_2 \\ 3\omega_H/\gamma &\approx \omega_1 \end{aligned} \tag{43}$$

Here γ is the relativistic factor. The overlapping of higher harmonics is more easily provided. The estimate for energy boundaries of resonant interaction at fixes harmonic number with microwave field of a fixed frequency was obtained for the "pitch-angle width" of hot electron disk near purely transverse velocities $\Delta\Theta^2 \approx 0.2$. This value was obtained from the model analysis of Fokker-Plank equation with collisional and quasi-linear terms corresponding to plasma density $n \approx 2 \cdot 10^{13}\text{cm}^{-3}$ and microwave power $P \approx 0.5\text{MW}$ for the geometry corresponding to AMBAL-M conditions [16].

Another idea of relativistic electron production under ECR conditions will be below a subject of more detailed theoretical investigation. This idea is based on the well known in accelerator technique phase stability effect (PSE) [27] (in Russian papers it is often called cyclotron autoresonance effect) which in the case of electron - microwave field interaction may be treated in a following way. Electron in the presence of dc magnetic field and ac electric field rotating with the frequency ω in the plane orthogonal to the magnetic field can move along the circular stable orbit satisfying the condition of relativistic cyclotron resonance

$$\omega \approx \omega_H/\gamma \tag{44}$$

which becomes the exact equality with electric field amplitude diminishing to zero (this corresponds to the case of free gyration of electron with relativistic gyrofrequency in a dc magnetic field). A very nice property of phase stability effect is that whatever small is microwave field amplitude with slow enough ("adiabatic") variation of dc magnetic field resonance condition (44) in automatically maintained in the process of magnetic field increase. That means that increase in electron energy is determined only by the ratio of final magnetic field intensity to its initial value and the relativistic energy of electron varies during this process proportionally to this ratio. Energy gain in this case is essentially greater than in the case of adiabatic magnetic compression without microwave field both in weakly relativistic and ultra-relativistic regions of electron energies. In ref.[4] it was proposed to use phase stability effect at the initial stage of magnetic compression using microwave field excited in microwave cavity and to reach electron energies of order of the rest energy; final stage of magnetic compression without microwave field was supposed to provide further increase of electron energy proportional to square root of the "magnetic compression" ratio. In [25] the possibility was considered to reach essentially higher electron energies applying microwave field during the full stage of magnetic compression. We present here the main featured of this scheme.

The principle idea is very simple: it is necessary to provide continuous interaction of plasma electrons with quasi-optical microwave

beam in a slowly increasing dc magnetic field. To realize this idea it is necessary to satisfy a number of conditions and limitations which are sometimes contradictory to each other. They are the following.

• The final energy E_f of electrons is defined by the ratio of final and initial values of magnetic field intensity:

$$E = mc^2(H_{max}/H_{min}) \tag{45}$$

• The radiation frequency must be close to the initial value of nonrelativistic electron gyrofrequency:

$$\omega \approx \omega_{H_0} \tag{46}$$

• Plasma cross-section is reduced in the course of magnetic compression as

$$S(t)/S_0 \approx H_0/H(t). \tag{47}$$

This implies that the cross-section of quasi-optical microwave beam should be of the order of initial plasma cross-section to provide continuous interaction of electrons with microwave field. Taking into account that the fraction of microwave beam participating in the electron acceleration diminishes in the course of magnetic compression but equal amount of energy is also subtracted from the increasing magnetic field we obtain estimate for the minimum amount of microwave energy needed for PSE acceleration of N_e electrons:

$$\int P dt \approx \frac{1}{4} N_e mc^2 (H_{max}/H_0)^2 \tag{48}$$

In the final state plasma radius should be a few relativistic electron gyroradius ($r_H \approx c/\omega_{H0}$) in order to neglect the collective effects in electron PSE acceleration.

• The length of the region with dc magnetic field should be long enough in order to provide electron confinement during acceleration process. The favorable circumstance is that electron inertial confinement is related to plasma expansion along the magnetic field with the ion-sound velocity. In reality this means that electron perform many bounces between the boundaries of expanding plasma.

• The rate of magnetic compression should be high enough in order to provide interaction during plasma confinement time but low enough to satisfy the adiabaticity condition:

$$T_{ad} \ll T \ll L/V_s \tag{49}$$

where $T = \left(\frac{1}{H}\frac{\partial H}{\partial t}\right)^{-1}$ is the time of magnetic compression, L is the longitudinal size of dc magnetic field region, V_s is the ion-acoustic velocity. The characteristic time defining adiabaticity condition in the most unfavorable case is defined by (see [28]):

$$T_{ad} = \omega^{-1}\left(\sqrt{1-n_{\|}^2}\frac{eE}{mc\omega}\right)^{-4/3} \tag{50}$$

where ω is the radiation frequency, E is microwave field amplitude, $n_{\|}$ is the longitudinal refractive index of microwave radiation.

• There is also additional condition of electron trapping into the stable orbit corresponding to PSE. In the case when electrons are weakly relativistic at the initial stage these conditions can be presented as

$$\Delta\beta_{\perp}^2 \ll \left(\frac{eE}{mc\omega(1-n_{\|}^2)}\right)^{2/3} \tag{51}$$

where $\Delta\beta_{\perp}$ corresponds to the initial diversity of transverse velocity of electrons.

• Limitation to plasma density arises from the condition that plasma with relativistic electron component should be transparent for microwave radiation propagating along the magnetic field at all stages of magnetic compression[11] :

$$n_{\|}^2 = 1 - \frac{\omega_p^2}{\omega_H^2}\frac{mc\omega}{eE} > 0$$

[11]Presented here expression for the nonlinear refractive index $n_{\|}$ is obtained withing the assumption that all electrons of plasma rotates with the velocity of order of light velocity

where ω_p is plasma frequency. Taking for estimates $n_\parallel^2 \approx 0.5$ we get limitation for the plasma density which is most essential in the final stage:

$$n\ (\mathrm{cm}^{-3}) \sim 0.5 \cdot 10^{11} \frac{P^{1/2}\ (\mathrm{MW})}{\lambda\ (\mathrm{cm})\ D\ (\mathrm{cm})} \qquad (52)$$

where λ is the radiation wave length and D is the diameter of microwave beam.

Having in mind the achievements in the design of microwave radiation generators based on the use of relativistic electron beams ($10 \div 1000$ MW of microwave power in a pulse of $10 \div 0.1$ μsec duration in wavelength region $3 \div 10$ cm - see e.g.[2]) we take as reference the following numbers $P = 10$ MW at $\lambda = 3$ cm, pulse duration $\tau = 5$ μsec, magnetic field compression $H_{max}/H_0 \approx 30$ and the diameter of microwave beam $D \approx 5\lambda$. These numbers satisfy all the above conditions if the length of magnetic trap is of the order of 1 meter with the total number of ultra-relativistic electrons (with the energy about 15 MeV) about $3 \cdot 10^{12}$. In the final compressed stage plasma diameter would be about 3 diameters of relativistic electron circular orbit and the magnetic field intensity would be about about 10 Tesla.

References

1. V.V.Alikaev, A.G. Litvak, E.V.Suvorov. Electron cyclotron plasma heating in toroidal system. In High-Frequency Plasma Heating (A.G. Litvak, Ed), American Institute of Physics, New York, (1992), 1 - 61.
2. M.I.Petelin, Int. J. Electronics, **67**, (1989), p.37.
3. R.Geller. *Journal de Physique*, **50**, (1989), No 1, C1-887 - C1-892.
4. R.Geller, K.S.Golovanivsky. Prelimenary project of a compact ECRPAC divice for 1-400 Mev/amu heavy ion bunches production. Note PSI N301, Center d'Etudes Nucleaines de Grenobl, 1991.
5. J.H.Booske, F.A.Aldabe, R.F.Ellis, W.D.Getty. Journal of Applied Physics, **64**, (1988), No 3, 1055.
6. A.M.Howald et al. *Phys. Rev.*, **A33**, (1986), 3779.
7. H.L.Berk, H.V.Wong, K.T.Tand, *Phys. Fluids*, **30**, (1987), 2681
8. A.V.Timofeev, V.D.Tokman, *Fizika Plazmy*, (1994), in print

9. B.Hafizi, R.E.Aamodt, *Phys. Fluids*, **23**, (1987), 3059.
10. T.D.Rognlien, *Nucl. Fusion*, **23**, (1983), 163
11. M.Yu.Gljavin, E.V.Suvorov, M.D.Tokman, et al. *Voprosy atomnoy nauki i tehniki (VANT)*, serija Termojadernyi sintez, No 4, (1990), 65- 70.
12. A.I.Neishtadt and A.V.Timofeev, *Sov. Phys. JETP*, **66**, (1987), 973.
13.A.V.Timofeev, In: *Reviews of Plasma Physics* (Ed. by B.B.Kadomtsev, translation Editor D.ter Haar) New York: Consultant Bureau, **14**, (1989), 63
14. E.V.Suvorov, M.D. Tokman. *Fizika Plasmy*, **15**, (1989), 934 - 943. (*Sov. J. Plasma Phys*, **15** (8), (1989), 540 - 545).
15. P.Jaeger et al, *Phys. Fluids*, **14**, (1972), 1073.
16. M.D.Tokman, *Preprint No 297*, Inst. of Appl. Phys., (Nizhny Novgorod, 1991)
17.P.A.Bespalov and V.Yu.Trakhtengets, In: *Reviews of Plasma Physics* (Ed. by M. A. Leontovich, Translation Editor D. Ter Haar) New York: Cousultant Bureau **10**, (1986), 155
18. S.V.Golubev et al, Proc. of Int. Conf. on Open Plasma Confinement Sistems for Fusion, June 14-18, (1993), Novosibirsk, Russia.
19. V.P.Pastukhov. *Nuclear Fusion*, **14**, (1974), 3.
20. S.V.Golubev, V.G.Zorin, I.V.Plotnikov, S.V.Razin, M.D.Tokman. Experimental investigation of initial stage of ECR discharge sustained by millimeter wavelength radiation in mirror trap. Proceeding of Simposium'92 of Research Center for Ultra High Energy Density Heat Source, p.17, Osaka University Japan, 1992.
21. S.V.Golubev et al, Experimental Investigation of Initial Stage of ECR Discharge Sustained by Millimeter Wavelength Radiation in Mirror Trap, II Inter. Workshop, Strong Microwaves in Plasma, Nizhny Novgorod, Russia, 1993, p. D30.
22. V.N.Bocharov et al, *Voprosy atomnoy nauki i tehniki (VANT)*, serija Termojadernyi sintez, N3, (1985), 64.
23. V.A.Zhiltsov et al., *Fizika Plazmy* **17**, (1991). 771
24. V.V.Andreev et al., in (Litvak A.G., Ed.), (Proc. Int. Workshop on Strong Microwaves in Plasmas. Suzdal (USSR), 1990). Vol.1,

Nizhny Novgorod (1991), p. 479.
25. S.V.Golubev, V.E.Semenov, E.V.Suvorov, M.D. Tokman. On the application of power microwave beams for ECR production of hot anisotropic plasma in the plasma accelerater. Proc. of First Kharkov Intern. Seminar on Plasma, Laser and Linear Collective Accelerators. Kharkov, Ukraina, Octob. 1992. Publ. by KPTI, Kharkov, Ukraina, 1993.
26. G.I.Dimov, Prep. 89-151, INF, Novosibirsk, USSR, 1989.
27. A.N.Lebedev, A.V.Shal'nov, Background of Accelerater Physics and Technique, Moscow, Energoatomizdat, 1991.
28. E.V.Suvorov, M.D. Tokman. *Fizika Plasmy*, **14**, (1988), 950-957. (*Sov. J. Plasma Phys.* **14** (8), (1988), 557 - 561).

PLASMA SYNCHROTRONS GYRAC: RELATIVISTIC PLASMA GENERATORS, PLASMA ACCUMULATORS AND SOURCES OF RADIATION

V.V. Andreev and A.M. Umnov
Plasma Physics Laboratory, Russian Friendship University, 117198, Moscow, Russia.

1 Introduction (ECR and SGA)

It is well known that Electron Cyclotron Resonance (ECR) is an effective method of plasma heating. Meanwhile maximum energy which electrons gain under ECR is limited due to relativistic detuning of the resonance. The upper level of achievable energy in case of ECR is determined by the electric field strength. Therefore obtaining high electron temperature requires high microwave power. But if ECR is produced in a slowly growing in time magnetic field the relativistic change of the electron mass is compensated with the change of the magnetic field in time $B(t) = B[1 + b(t)]$ ($B_0 = m_0 c\omega/e$, m_0 and e are the rest mass and the charge of the electron, ω -angular frequency of HF field, $b(t)$-monotonously growing in time function). As a consequence the resonant condition $\omega \simeq \omega_{ce}$ ($\omega_{ce} = \frac{eB(t)}{m_0 \gamma c}$, $\gamma = (1 - v^2/c^2)^{-1/2}$, v-velocity of the electron) is maintained automatically unlike the ECR- phenomenon. It was shown the possibility of such a process theoretically [1] and experimentally [2,3] and it was named Synchrotron Gyromagnetic Autoresonance (SGA).

Under SGA the electron phase φ (φ - is the angle between the vectors of electric field strength **E** and impulse of the electron **U** is being trapped into such an interval that average time energy of the electron grows in accordance with the law of the magnetic field growth $W(t) \simeq b(t)$, where $W = \gamma - 1$ - kinetic energy in $m_0 c^2$ units γ - relativistic factor. The maximum value of energy of the electron gained

during SGA is limited only by radiation loss. The achievable energy is determined by the terminal value of the magnetic field and doesn't depend on the microwave field strength. The SGA-phenomenon has been studied experimentally and by means of numerical simulation using particles (CIC-method).

2 Experimental devices and results

GYRAC-0. The first device - plasma synchrotron GYRAC-0 was built to demonstrate the phenomenon and to study its general properties. The scheme of GYRAC-0 is sketched in Fig.1.

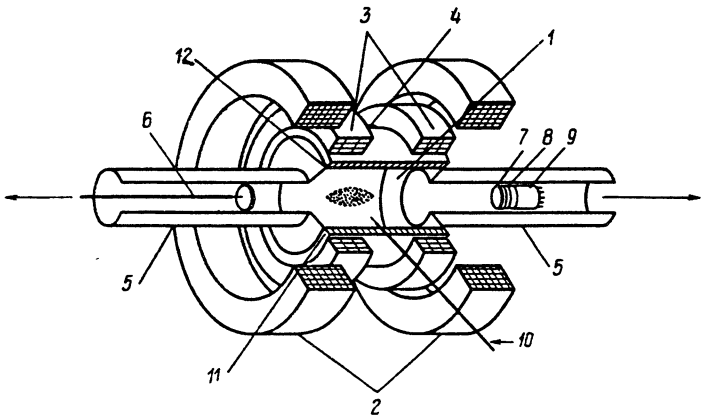

Fig.1. Scheme of the GYRAC-0

The static magnetic mirror field ($R = 1.4$, $L = 23cm$), produced by two coils 2, allows to keep ECR condition in the midplane of the system. The pulse magnetic field (build up time $(1.5 - 2)ms$, decay time $(4.5 - 6)ms$ is generated by a capacitor bank discharge through coils 3. The maximum value of the pulse magnetic field is determined by the charging voltage of the capacitor bank. The vacuum TE_{111} cylindrical resonant cavity 1 is excited by a microwave source in a single pulse operation mode with a power $150W$ and duration $1.5ms$ at the frequency $2.4GHz$. A discharge appears within the cavity

at the residual gas pressure $1 \times 10^{-5} Torr$. This discharge produces initial nonrelativistic plasma in the static magnetic field during the first $100 \mu s$ of the microwave pulse. The interaction of electrons with electromagnetic field in growing in time total magnetic field leads to generation of relativistic plasma formation - relativistic electron vortex filled with ions.

Diagnostics of the relativistic plasma were performed by analyzing bremsstrahlung and synchrotron radiations and by studying longitudinal losses from the trap. The obtained experimental and numerical simulation data allowed us to find the dependence of trapping efficiency $I = N_{tr}/N_t$ (N_t - total number of initial plasma electrons, N_tr - a number of trapped electrons) on initial plasma parameters and SGA - parameters. It was found [2] that trapping efficiency strongly depended on initial plasma density and a relative shift of initial magnetic field. SGA-process is no longer possible when n_{e0} is above some marginal value, that is due to strong ambipolar field appearing in plasma during SGA. A similar effect was found under varying of initial magnetic field value.

The obtained experimental results show that in optimum trapping conditions $(50 - 80)\%$ of initial plasma electrons are trapped in SGA-regime. Average energy of electrons $W \simeq 400 keV$, lifetime of obtained plasma $t = 100 ms$.

Experiments performed on the GYRAC-0 demonstrated SGA-phenomenon and allowed to study general properties of SGA but obtained plasma density was too low in order to use it in some applications.

GYRAC-D. In the next device using SGA-principle - GYRAC-D the regime of plasma accumulation was realized as a result of plasma heating under SGA and subsequent throwing SGA-plasma into the central region of the magnetic mirror trap in the regime of the SGA-pulse packet.

The principle scheme of the GYRAC-D is shown in Fig.2. The vacuum TE_{111} resonant cavity 1 with two pulse coils 2 is placed symmetrically with three pairs of coils 3 forming static mirror magnetic field ($R = 1.2$, $L = 100 cm$). The resonant cavity is exited by a mi-

crowave source in a pulse operation mode with a power of $300W$ at the frequency of $2.45GHz$ and duration of $500\mu s$. The pulsed magnetic field is generated by a capacitor bank discharge through pulse magnetic coils.

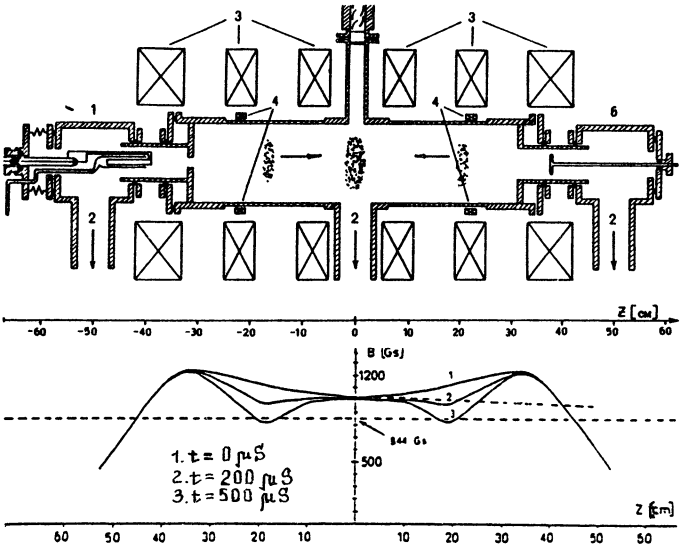

Fig.2. Scheme of the GYRAC-D and magnetic field configuration

An initial plasma created by LaB_6 source is injected into the cavity along the axis through a mirror throat and a channel of differential pumping. Injector operates well in continuous and pulsed regimes, pressure in the cavity $(0.8-1)\times 10^{-5}Torr$. Parameters of plasma injection: plasma's diameter $6mm$, $n_{e0}=(0.5-1)\times 10^{10}cm^{-3}$, $T_{e0}=(5-15)eV$.

The current running in the pulsed magnetic coils generates the reverse magnetic field which reduces the static magnetic field down to the nonrelativistic ECR value and lower (see Fig.2) in the local areas of maxima of the cavities electric field. At the moment when the pulsed magnetic field reaches the maximum, the pulse $(0.2ms)$ of injection and the HF pulse $(0.6ms)$ come to action and two e-vortexes emerge as a result of SGA. Then e-vortexes are thrown into the central region of the trap due to axial gradient of the magnetic

field and are confined in it.

The installation allows to run the process in the regime of a pack of pulses (number of SGA-pulses is till 8 at different repetition rate) in a working cycle that makes it possible to realize an accumulation regime as well as a regime of a single pulse heating.

The experimental and numerical simulation data show that there exist an optimum phase of plasma injection (duration of injection and a time shift between the injection start and the SGA-stage start) and optimum trapping conditions (microwave field strength, rate of magnetic field growth, repetition rate and duration of injection, gas pressure, mirror ratio, relative shift of starting value of magnetic field) which realize an accumulation regime [3].

Optimum parameters of accumulated plasma are as follows: $n_e \simeq 8 \times 10^9 cm^{-3}$, average energy of trapped electrons $W \simeq 200 keV$, lifetime is about $400 ms$. Experiments also show that for the above mentioned SGA-parameters there is no need for further increase of SGA-pulses because plasma density reaches it's saturation value. This may be explained by plasma build-up time becoming equal to typical decay time.

GYRAC-X. GYRAC-X is a plasma X-ray source in which kinetic energy of relativistic electrons obtained under SGA converts into X-ray by falling e-vortex on a heavy metal target. The principle of the GYRAC-X is seen from Fig.3. It is similar to GYRAC-0. The differences are that permanent magnets are used and that GYRAC-X acts in a regime of a magnetic field pulse packet under constant level of HF-power. The cavity is exited by microwave at frequency $2.4 GHz$, $350W$. The static magnetic mirror field satisfies ECR- condition in the midplane of the cavity. The pulse magnetic field: $t_{incr} = (100 - 500)\mu s$, $B_{max} = 500 Gs$.

Diagnostics of produced relativistic plasma were performed making analysis of the bremsstrahlung radiation from gas as well as from a W-target placed into relativistic plasma location. Values of density and average energy of trapped electrons are obtained by integral measurement and amplitude analysis. Experiments and numerical modelling of the process showed that such a regime allowed to obtain

dense short-life relativistic electron swarms. Life time and density of swarms were determined by initial plasma parameters, HF electric field strength, velocity of magnetic field growth and repetition rates of SGA-pulses.

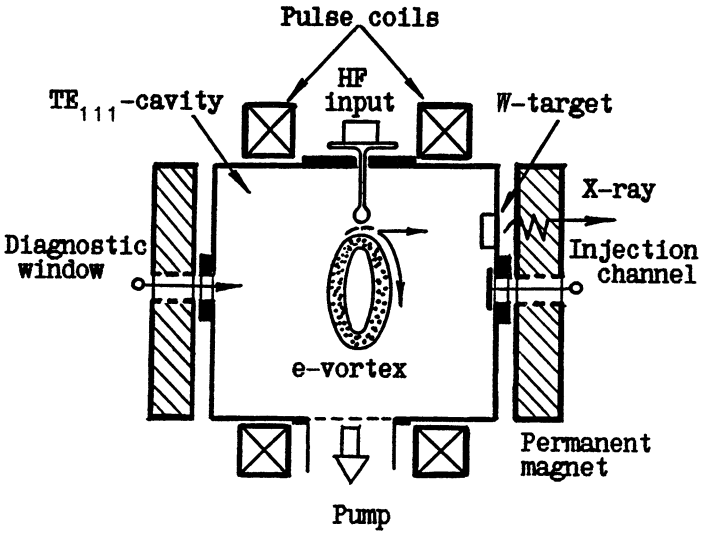

Fig.3. Scheme of the GYRAC-X

The measurement of intensity of radiation from a gas a W-target showed that its maximum power is equal to $6 \times 10^4\, MeV/s$ at rise time of magnetic field $300\mu s$ (relativistic electron density $\simeq 10^9 cm^{-3}$). Radial slight insertion of a target in e-vortex location shows that only small part of trapped particles ($\simeq 5 \times 10^6$) falls on a target and deeper target insertion leads to detuning of the resonance. That is why another technique is currently applied - throwing an e-vortex on a target placed by the side wall of the cavity (see Fig.3). Preliminary experimental data show that in the last case a sharp increase of X-ray intensity takes place. Now experiments in a progress.

3 Conclusion

Obtained experimental and numerical modelling data show that the most salient feature of SGA is the possibility of obtaining Gyrac produced plasma with parameters (average electron energy, plasma density and dimension) which can be varied in wide intervals. The SGA-regime can be used to obtain a controlled beam of relativistic electrons as well as relativistic plasma. Thus the SGA phenomenon belongs both to plasma physics and charged particle accelerator physics and the sphere of its applications may be very wide. Interest to Gyrac produced plasma may be enhanced by the prospect of a multicharged ion source, a synchrotron radiation source or bremsstrahlung source to be created with its use.

References

1. K.S. Golovanivsky, 1985, Physica Scripta **24**, 126.
2. V.V. Andreev and A.M. Umnov, 1991, Physica Scripta **43**, 490.
3. V.V. Andreev and A.M. Umnov, 1992, Rev. Sci. Instr. **63**(4), 2907.

ECR-sourse of metallic plasma

A.I.Karchevsky, Yu.A.Muromkin, A.L.Ustinov
RRC Kurchatov Institute, Moscow, Russia
M.Yu.Glyavin, E.V.Suvorov, M.D.Tokman
Institute of Applied Physics , Russian Academy of Sciences,
Nizhny Novgorod, Russia

A new method of isotope separation in plasma - method of ion-cyclotron heating achieved an intensive development in recent years. Practical use of this method is possible in large size magnetic systems. Intensive magnetic fields about 2-3 T with the length of uniform field region about 3-5 m are required for high isotopic selectivity in isotope separation of elements with middle and heavy mass. Plasma flows with transverse size of 10-40 cm and plasma density of $10^{11} - 10^{14} cm^{-3}$ are necessary for high productivity achievement.

The plasma sources must satisfy the set of requirements: plasma must be of minimum initial temperature, the bulk of ions must be singly ionized. Those factors as energy cost, possibility of universal application for various elements, possibility of operation with metallic plasma are of great importance too. A plasma source with such parameters can be created on the base of ECR using powerful (up to tens of kW) stationary generators with frequency about tens of GHz [1,2]. Breakdown initiation is possible with the use of rare gases (Ar) with its further substitution in discharge by metallic vapor. The metallic vapor can be produced with Joule heating (for such easy vaporized metals as Cd, Zn, etc.), or by sputtering of the target with energetic ions (for such elements as Cr, Ni, rare earth elements etc.). In the latter case negative potential 1-4 kV is applied to the target (cathode), and longitudinal discharge could be initiated. Such ECR plasma sources are perspective also for some microelectronics

tasks [3].

To study parameters of such type plasma source an experimental installation including microwave generator - gyrotron, waveguide system and superconducting solenoid with vacuum chamber was constructed (Fig. 1).

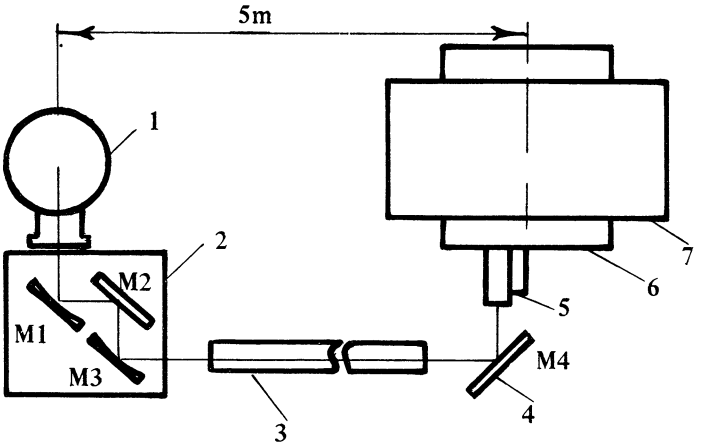

Fig. 1 Microwave transmission system

The continuous wave gyrotron (1) with wavelength about 8 mm ($f = 37$ GHz) and power up to 20 kW was used as microwave generator. Parameters of the radiation emitted from the gyrotron require special mirror system (2). This system focuses the radiation into cylindrical waveguide as quasi-Gaussian profile and eliminates parasite modes. Bimetallic tube (3) with diameter of 70 mm is used as basic waveguide. It's length is about 4.5 m (4 beats of base modes TE_{11} and TH_{11}), that allows to place gyrotron far from strong magnetic field of solenoid (7). The basic waveguide with great diameter is unsuitable for transmission of microwave power into vacuum chamber (6) with inner diameter about 300 mm. Due to this reason additional mirror M_4 is used for refocusing the radiation into additional waveguide (5) with diameter 40 mm.

Maximum efficiency of microwave coupling of extraordinary wave with plasma can be expected under quasi-parallel input towards the ECR surface from stronger magnetic field region. In our case for

low-temperature plasma the condition of quasi-parallel input $\theta < (V_{T_e}/c)^{1/3}$ (θ is angle with magnetic field, V_{T_e} is electron thermal velocity, c is the light velocity) gives input angle $\theta < 10°$. Waveguide system components responsible for quasi-parallel input of radiation are shown in Fig. 2.

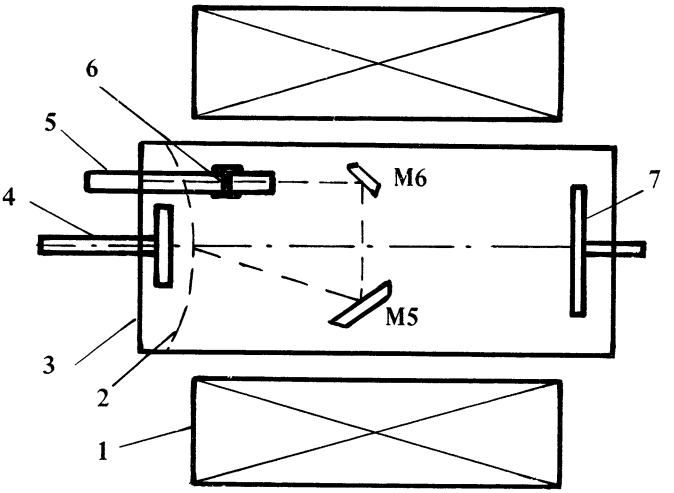

Fig. 2 Vacuum chamber with microwave system intertor

When using the single mirror M_5 a portion of reflected radiation is inevitably captured by the waveguide if $\theta < 35°$. Using of mirror M_6 allows to diminish input angle to 10° and less. In this case the radiation in the mode of ordinary wave intersects the plasma flow in the high field region ($2f_G \simeq \omega_H/2\pi$, where ω_H is cyclotron frequency) where refractive index of plasma is $n \simeq 1$. Ceramic window (8) is placed in additional waveguide in the high field region beyond the ECR surface (2) to avoid initiation of discharge inside the waveguide. Longitudinal discharge necessary for sputtering, is initiated between cathode (4) and grounded beam collector (7).

It is suggested [4] that this installation will be used to investigate plasma source with plasma density up to 10^{12} cm^{-3}, diameter of plasma column about 50-100 mm, and with equivalent ionic current up to 10 A.

REFERENCES

1. T.E.Romesser, V.Vanek, J.Tang et al. *IEEE Int. Conf. on Plasma Science, San Diego, Calif., USA*, 1993.

2. A.Compant La Fontaine, P.Louvet. *Separation Phenomena in Liquids and Gases, Second Workshop*, 1989, V.1, p.139.

3. P.Kidd. *J.Vac.Sci.Technol.*, A 9(3). 1991, p.486.

4. E.V.Suvorov, M.D.Tokman. *Sov. J. Plasma Phys.*, 15(8), 1989, p.540.

EXPERIMENTAL INVESTIGATION OF INITIAL STAGE OF ECR DISCHARGE SUSTAINED BY MILLIMETER WAVELENGTH RADIATION IN MIRROR TRAP

S.V.Golubev, I.V.Plotnikov, S.V.Razin, E.V.Suvorov, M.D.Tokman, V.G.Zorin

Institute of Applied Physics, Russia Academy of Science,
46 Uljanov Street, 603600 Nizhny Novgorod, Russia

1.Possibilities of increasing efficiency of ECR sources of multiply charged ions (MCI) by increasing the frequency of microwave pumping has recently been actively studied. This line of investigation has been developed after a series of experimental works was published (see, e.g., [1]) that demonstrates essential increase of intensity of MCI beam when the pumping frequency changed from 10 to 18 GHz. On the basis of these experimental investigations a semi-empirical scaling has been found; according to it, current of ions with an average charge Z must increase in proportion to the squared frequency. This yields the supposition that creation of ECR sources using powerful millimeter wave radiation generated by modern gyrotrons will permit one to make operation of MCI source more efficient [2,3,4].

Along with this, ECR discharge is considered as a source of incoherent soft X-ray radiation for lythography[5]; the possibility to obtain unique properties of semiconductors when their surface is modified by multiply charged ions was discussed in [6].

First experimental investigations of the ECR discharge sustained by millimeter wavelength radiation are described in [3,4,7-10]. Of interest and importance for design of ECR sources of MCI are the problem of discharge produced in the mirror trap and problem of influence of the dielectric HF window, which transmits the microwave power into the mirror trap. The present paper describes the investigations of these problems. There are comparison of the experimental and theoretical estimations here and the electron losses mechanism in the presence of the powerful microwave field is discussed.

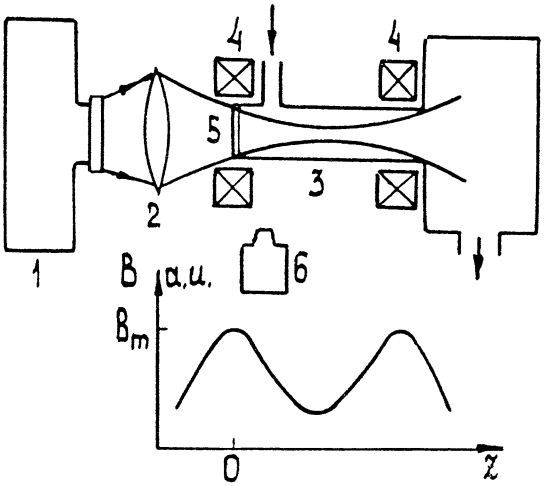

Figure 1

2.Figure 1 shows the scheme of the experimental setup. Microwave radiation of a pulse gyrotron (1) (pulse duration τ = 1ms, power was S = 120kW, frequency 37.5 GHz) was focused by a dielectric lens (2) into a glass vacuum chamber (3). The vacuum chamber was placed into a mirror trap produced by two pulse coils (4). The distance between mirrors was 20cm, and the mirror ratio equaled 3. The vacuum chamber could move relative to the magnetic system; by this, position of the quartz window (5) (7cm in diameter) for launching of the microwave radiation varied relative to the maximum of the magnetic field B_m. To eliminate statistic straggling of discharge formation time we used a special set of electrodes (preionizer) providing initial density of primary electrons in the trap. Spatio-temporal characteristics of the discharge luminescence was investigated with a streak camera (6). To estimate plasma density in the discharge, the transmission factor of the diagnostic microwave (frequency 35,52GHz) through plasma was measured.

3.Figure 2 presents the experimentally determined boundaries of the regions of existence (curve 1) of an ECR discharge where p is pressure of the residual gas in the chamber, and B_m is magnetic field

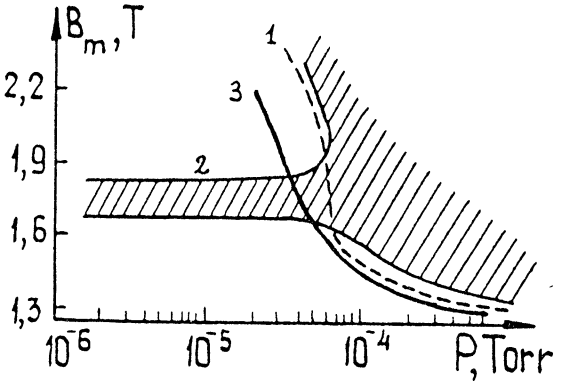

Figure 2

strength in the mirror. Curve 1 was obtained with the case of the input window placed outside the trap at the distance $z = -5$cm from mirror and not influencing discharge evolution.

To the right of this curve the discharge arises during the microwave pulse and there is no discharge to the left of this curve.

The experiments showed essential influence of the input dielectric window on discharge evolution when the window is placed inside the trap (as a rule, to the maximum of the magnetic field, i.e. mirror). Curve 2 shows regions of discharge existence in the presence of a dielectric. The discharge takes place in the hatched area, and there is no discharge existence outside this region. It is necessary to note that region corresponding to the discharge under low pressures down to 10^{-6}Torr, changes its boundary in dependence on the quality of the dielectric surface and power of the pre-ionizer. Estimations of discharge evolution time with optimal electron temperature and without electron losses show that when gas pressure is about 10^{-6}Torr, this time is essentially longer than pulse duration, i.e., discharge ignition is impossible if no additional amount of gas in the trap. Hence, there is gas flow from the window surface in the experiments.

The presence of gas flow from the dielectric window surface is confirmed by observation of spatial developments of the discharge

under low gas pressures. The streak photos at low pressures ($p = 1.2 \cdot 10^{-5}$Torr) showed that discharge luminescence appeared near the dielectric surface and spreaded into the trap with velocity about $7 \cdot 10^4$cm/s. This velocity is of the order of magnitude of sound velocity and corresponds to the spread of neutrals from the window. Then (in some tens of microseconds) plasma is produced and velocity of luminescence motion increase up to ion-acoustic velocity. Under high gas pressures (10^{-3}Torr and higher) the luminescence appears over the whole trap practically simultaneously, and that means that the dielectric has no influence on the discharge evolution. Besides, measurements of transmissivity of the diagnostic microwave through the plasma confirmed the existence of gas flow from the window too. The cut-off plasma density was observed under pressure $p = 10^{-5}$Torr when the density of neutral gas was 50 times lower than the cut-off plasma density. Existence of such dense plasma is hardly explained without ionization of the gas emitted into the trap from the dielectric window.

3.Thus, the experiments showed that there are two regimes for plasma generation in the trap. One corresponds to the input dielectric window influences the discharge evolution and other to absence of influences. In the second case (window is outside the trap), experimental investigation of the discharge existence can be compared to the results of the theory developed in [12]. In this work the situation is discussed when the main mechanism of electron losses is their scattering into the loss cone by interaction with powerful resonance microwave pumping in the ECR zone. Just this situation is realized under the conditions of our experiment since all of approximations used in [12] are satisfied. The result of calculation is shown on Fig.2, curve 3. This calculation agrees qualitatively with the experimental data (see Fig.).This agreement confirmed the assumption that particle losses from the trap on the stage of gas breakdown are essentially determined by scattering under interaction with microwave pumping. Evidently this electron loss mechanism plays a leading role in a completely ionized plasma when the structure of a steady-state ECR discharge in magnetic trap has been formed.

When the influence of the dielectric window on the discharge evolution is essential, gas flow from the window surface into the mirror trap takes place. Discharge ignition is caused by ionization of the additional gas. Formation mechanism of such a discharge is not completely clear; the following scheme is discussed as a hypothesis. Even after first passing through the resonance zone primary electrons can acquire the energy of the order of magnitude of several hundreds eV. These electrons can leave the trap if the ECR zone is sufficiently close to the magnetic mirror. When these electrons get to the surface of the dielectric window, they cause secondary emission. This process can be repeated till dissipation of microwave power in the electron layer near the window finally leads to gas emission from the dielectric due to its heating by electron flow and evolution of a spatial discharge in the vaporized gas. Simple estimations (see, e.g., [13]) show that even when electron density is of the order of magnitude $N \simeq 10^9$ cm^{-3} power flow to the dielectric window will be about one tenth of the microwave source power.

REFERENCES

1 R.Geller, B.Jacquot, P.Sortais. Nuclear Instruments and Methods in Physics Research, A243, p.224, 1986.

2 K.S.Golovanivsky. Prib.Tekh.Eksp., N.5, p.7, 1985.(in Russian)

3 S.V.Golubev, V.G.Zorin, T.N.Zorina, S.V.Razin. Int. Workshop on Strong Microwaves in Plasmas. Suzdal, 1990. Contr. papers, p.D-37.

4 Y.Arata, S.Miyake, H.Kishimoto, N.Abe, Y.Kawai. Japanese Journal of Applied Physics, v.27, N 7, p.1281, 1988.

5 J.H.Booske, F.A.Aldabe, R.F.Ellis, W.D.Getty. Journal of Applied Physics, v.64, N.3, p.1055, 1988.

6 A.M.Howald et al. Physics Review., A33, p.3779, 1986.

7 A.G.Demekhov, B.G.Eremin, A.V.Kostrov, E.V.Suvorov, A.A. Fraiman, A.L.Chekanov, Yu.M.Shagiev. Preprint IAP , N 146, 1986.(in Russian)

8 Y.Arata S.Miyake, H.Kishimoto. Japanese Journal of Applied Physics, v.28, N 2, p.234, 1989.

9 V.N.Bocharov et al. Vopr. Atom. Nauki i Tekh. Ser. Termoyad. Sintez, N 3, p. 64, 1985.(in Russian)

10 Yu.V.Bykov, S.V.Golubev, A.G.Eremeev, V.G.Zorin. Physics of Plasma, v.16, N 4, p.487, 1990. (in Russian)

11 T.A.Antaya. Journal de Physique, v.50, N 1, p. 707, 1989.

12 E.V.Suvorov, M.D.Tokman. Sov. Journal of Plasma Physics, v.15, N 8, p.540, 1989.

13 V.L.Ginzburg. Propagation of electromagnetic waves in plasma. Nauka, M., 1967.(in Russian)

The calculation of the efficiency of the production of multiply charged ions in an ECR source at high plasma density

S.V.Razin, V.G.Zorin, T.N.Zorina, M.V.Yulpatova

Institute of Applied Physics , Russian Academy of Sciences,
Nizhny Novgorod, Russia

The possibility of increasing the efficiency of the ECR sources of multiply charged ions (MCI) by increasing plasma density has been intensively studied recently [1,2]. The most reliable way of obtaining more dense plasma is the use of the pumping at higher frequency. The creation of powerful gyrotrons of the millimeter wavelength band [3] has provoked interest in the study of plasma in mirror trap with density $10^{13}-10^{14}cm^{-3}$[4,5,6]. The present paper is dedicated to the calculation of the efficiency of production of MCI in the ECR source with such plasma density.

The efficiency of the production of MCI in plasma is calculated using a nonstationry (in contrast to [4]) system of differential equations describing the ionization balance for neutral atoms and ions with each ionization state. The sequential multiple-step

ionization by the electron impact and only longitudinal losses of plasma from a trap are taken into account:

$$\frac{dN_i}{dt} = N_e \cdot (k_{i-1,i}N_{i-1} - k_{i,i+1}N_i) - \frac{N_i}{\tau_i}$$

Here N_e is electron density, N_i is density of ions with charge i, $k_{i-1,i}$ are the electron impact ionization rates calculated using the model of Lotz [7], τ_i is the mirror ion confinement time. All calculations were made for oxygen, i=1...8. Estimation of contribution charge-exchange processes between ions and neutrals to ionization balance showed that it could be ignored in plasma with density $10^{13} - 10^{14} cm^{-3}$.

The electron temperature T_e is defined from the solution of the energy balance equation under the assumption of Maxwellian electrons energy distribution function and that microwave power is entirely absorbed by plasma (this can be provided with axial launch of microwave energy through the magnetic mirror into plasma). We assumed also that ion temperatures are identical for all ion charge states.

$$\frac{dE_e}{dt} = \frac{S}{L} - 3\delta\nu_{ei}(T_e - T_i)N_e - \frac{E_e}{\tau_e},$$

where $E_e = 3T_eN_e/2$, S-intensity of microwave radiation, L - distance between mirrors of the trap, δ - part of the electron energy lost after one collision, ν_{ei} is the collision frequency between electrons and ions, T_i is ion temperature, τ_e is electron confinement time.

Unfortunately there is no adequate model of the confinement of dense (with the electron density of the order of $10^{13} cm^{-3}$ and more) nonequilibrium plasma in the mirror trap at present. The given calculation use the expression for τ_i obtained in [8] on the basis of experimental results:

$$\tau_i = L \text{ æ}/V_{T_i}$$

Where æ is mirror ratio, V_{T_i} is the thermal ion velocity (see [4] too).

Now let us consider a pulse regime of microwave generator operation. The time evolution of some ion densities when S=100 kW/cm^2 is shown on Fig.1 (Note that pulse gyrotrons allowed to obtain this and even higher level of intensity operate in Institute of Applied Physics now).

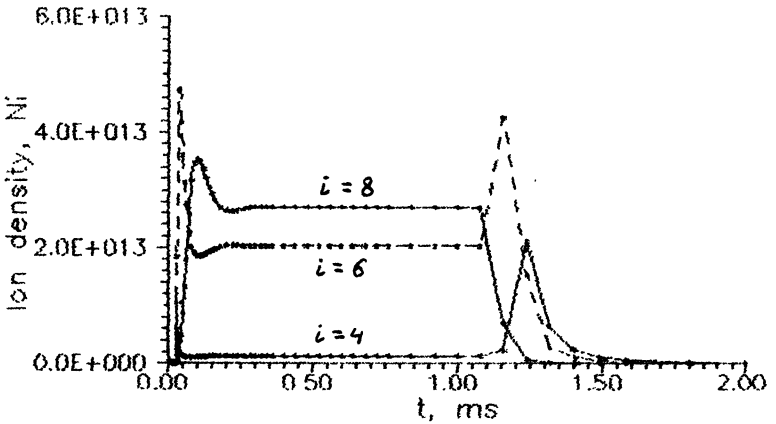

Figure 1

In this Figure you can see that build-up time of the steady-state ion density is approximately 0.2 ms, so pulse duration of HF generation under the pulse regime must be chosen much more than this build-up time. In our case pulse duration was 1 ms.

Figure 2 shows the charge state distribution (CSD) of oxygen ions in the plasma of ECR ion source under pulse regime.

We see that a maximum of distribution of ions corresponds to the charge plus seven.

Under continuous-waves (CW) regime intensity of microwave radiation was assumed 5 kW/cm^2. Figure 3 showes the CSD of ions. In this case maximum of distribution corresponds to the charge plus six and according to calculations densities of highly charged ions are several tens times lower than under pulse regime

with S=100 kW/cm^2.

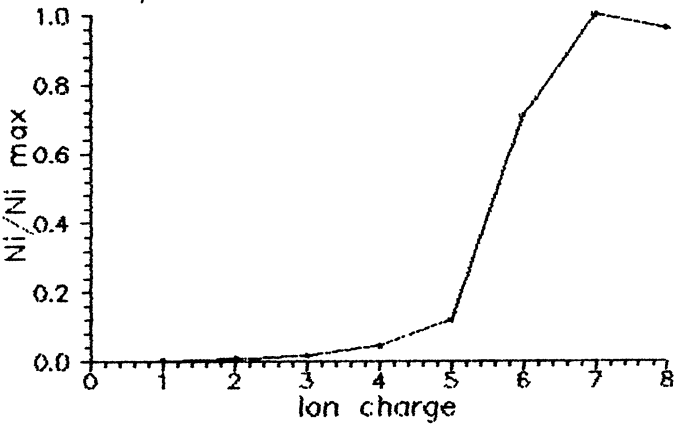

$N_e \simeq 5 \cdot 10^{14} cm^{-3}, T_e \simeq 1.6 keV, S = 100 kW/cm^2$

Figure 2

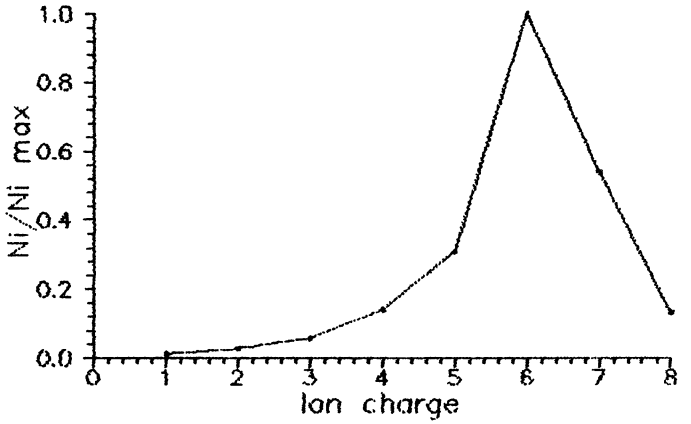

$N_e \simeq 5 \cdot 10^{13} cm^{-3}, T_e \simeq 1.8 keV, S = 5 kW/cm^2$

Figure 3

Now we can compare the efficiency of production of MCI in the cases of pulse-periodic and CW-regimes. Let us suppose

that time-averaged pulse microwave radiation intensity and CW-intensity equals 5 kW/cm^2. To compare these two regimes from the point of view of ion generation, it is necessary to compare following fluxes of ions:

$$F_i = (\frac{N_i}{\tau_i})_{CW}, \hat{F}_i = \frac{1}{T}\int_0^T \frac{N_i(t)}{\tau_i(t)}dt,$$

where T is repetition period of microwave pulses. According to calculations the ratio $\hat{F}_i/F_i$ equals to 1.6 for i=7 and to 6.2 for i=8.

Thus, the calculations have showen that the pulse-periodic regime of microwave generator operation is more efficient for production of highly charged ions than CW-regime. With increased electron density up to 10^{14} and more by means of powerful millimeter-wave gyrotrons one can obtain very high densities of MCI and CSD of ions with maximum on charge 7. The current of such ions will essentially exceed corresponding currents of MCI of the best modern electron cyclotron resonance sources.

REFERENCES

1. R. Geller, B. Jacquot, P. Sortais. *Nuclear Instruments and Methods in Physics Research*, 1986, A243, p.224.

2. W. Halverson et al. *Journal de Physique*, 1989, v.50, p.C1-751 - C1-758.

3. A.V. Gaponov, V.A. Flyagin, A.L. Gol'denberg et al., *Int. Journal Electronics*, 1981, v.51, N 4, p.277-302.

4. S.V. Golubev, V.G. Zorin, T.N. Zorina, S.V. Razin. *Proc. of the Int. Workshop "Strong microwaves in plasmas"*, Suzdal, 18-23 september, 1990. Nizhny Novgorod, 1991, v.1, p.485.

5. Yu.V. Bykov, S.V. Golubev, A.G. Eremeev, V.G. Zorin. *Phys. of Plasma*, 1990, v.16, N 4, p.487 (in Russian).

6. Y. Arata, S. Miyake, H Kishimoto, N. Abe, Y. Kawai. *Japanese Journal of Applied Phisics*, 1988, v. 27, N 7, p. 1281.

7. W. Lotz. *Zeit. fur Physik*, 1968, v.216., N 3, p.241.

8. A.G. Demekhov, B.G. Eremin, A.V. Kostrov, E.V. Suvorov, A.A. Fraiman, A.L. Chekanov, Yu. M. Shagiev. *Preprint IAP*, 1986, N 146 (in Russian).

The SCECR 6.4 GHz High B Mode and Frequency Scaling in ECR Ion Sources

T.A. Antaya
National Superconducting Cyclotron Laboratory,
Michigan State University,
E. Lansing, MI 48824 USA
and
S. Gammino
INFN–Laboratorio Nazionale del Sud,
VI. A Doria (ang. V.S. Sofia),
95123 Catania, Italy

1 Introduction

Since the presentation of the first results of the Grenoble 16.6 GHz ECRIS (Electron Cyclotron Resonance Ion Source) at the Berkeley ECRIS Workshop in 1984 [1], the possibility of $n_e \propto f^2$ frequency scaling has been one of the major driving forces of ECRIS designs for highly charged ions. Several higher frequency sources have been built and they do indeed have very high performance: the 14 GHz ECRIS ICIS at Jülich [2], AECR at LBL [3], ECR4 of Ganil [4] and the 18 GHz Minimafios of Grenoble [5]. Two of these sources, AECR and ECR4, have operated at lower frequency as well with poor results. On the other hand, there is Caprice 2B of Grenoble [6], a 10 GHz source with essentially equivalent performance. There are also very high density singly-charged sources , like the Chalk River ECRIS [7], operating at 2.45 GHz. Given these conflicting results, do we need to raise the frequency to get higher performance, and if so, is this really a signature of the $n_e \propto f^2$ density cut off limit?

In order to help resolve this issue, we built a developmental source, the SCECR, at NSCL. The SCECR was designed to permit the frequency opertion scaling in a single geometry by using a full superconducting coil set to scale the magnetic topology from 5-35 GHz. [8] At the lower end of this frequency range, the wide magnetic range would also permit the study of new regimes of magnetic confinement, like that exhibited in Caprice 2B-type ECRIS. In addition, the SCECR design parameters were based on the optimized RTECR at NSCL[9], so the starting point would be a well known performance. Hence, in one geometry, both frequency scaling and magnetic confinement scaling could be studied, with no instrumental bias toward either mode of operation.

The initial results with the SCECR are that it matches or exceeds the performance (peak charge states and/or intensity), of nearly all other existing ECRIS, but at the low operating frequency of 6.4 GHz. In addition, the SCECR is stable, reproduceable, and has a very high ionization efficiency ($\geq$ 80%). These results have been obtained by raising both the axial and radial magnetic confinement substantially above the design values, while maintaining a normal 6.4 GHz ECRH resonance zone. The frequency scaling argument, while not invalidated by these results, is now much less clear. While at the same time, these results open up the new possibility of high performance, low frequency sources.

2 SCECR 6.4 GHz High B Mode

The SCECR is shown schematically in Fig. 1. There are five superconducting solenoid coils, clustered 2 and 3, to produce two axial mirrors. These mirrors are split to permit fine mirror ratio adjustment. (This subdivision has in fact allowed the field configuration responsible for the results to be reported here.) The superconducting hexapole resides in the bore of the tandem mirror. The plasma chamber, microwave injection and beam extraction systems are the same as the RTECR. The plasma chamber bore is 14 cm, and the axial mirror-to-mirror length is 50 cm. The field design that follows

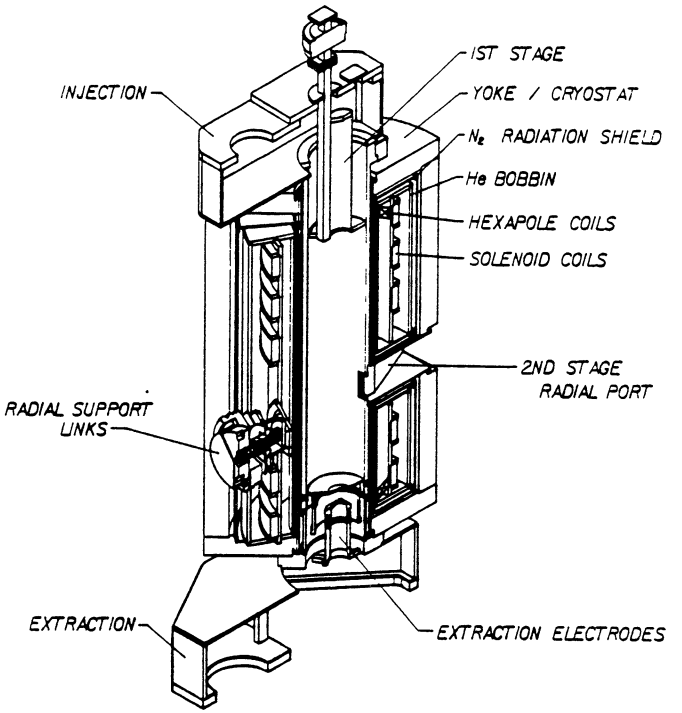

Figure 1: The SCECR is shown in schematic form.

that of the " 2 mirror " operating configuration of the RTECR. The design axial and radial magnetic fields are labelled '6.4 GHz design' in Figures 2 and 3. Here, the SCECR is effectively the same ECRIS as the RTECR, and we found the performance to be similar as well (compare column 1 and 2 in Table 8.) Figures 2 and 3 also show the optimal magnetic field of the SCECR at 6.4 GHz. By 'optimized' we mean, the field at which the best multiply-charged ion production is obtained. Table 1 summarizes the characteristics of these two magnetic configurations. Figure 4 compares the performance of the SCECR for the optimized field to that of the RTECR for noble gases. As can be seen in Fig. 4, there is a large improvement in the per-

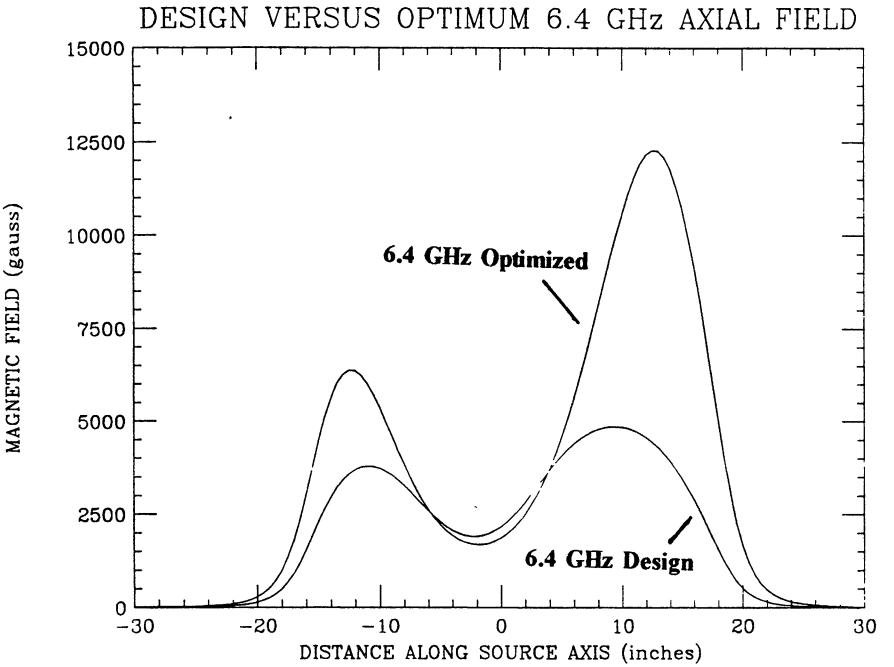

Figure 2: A comparison between the 'Design' axial magnetic field and the 'optimized' field at which the best performance of the SCECR is observed.

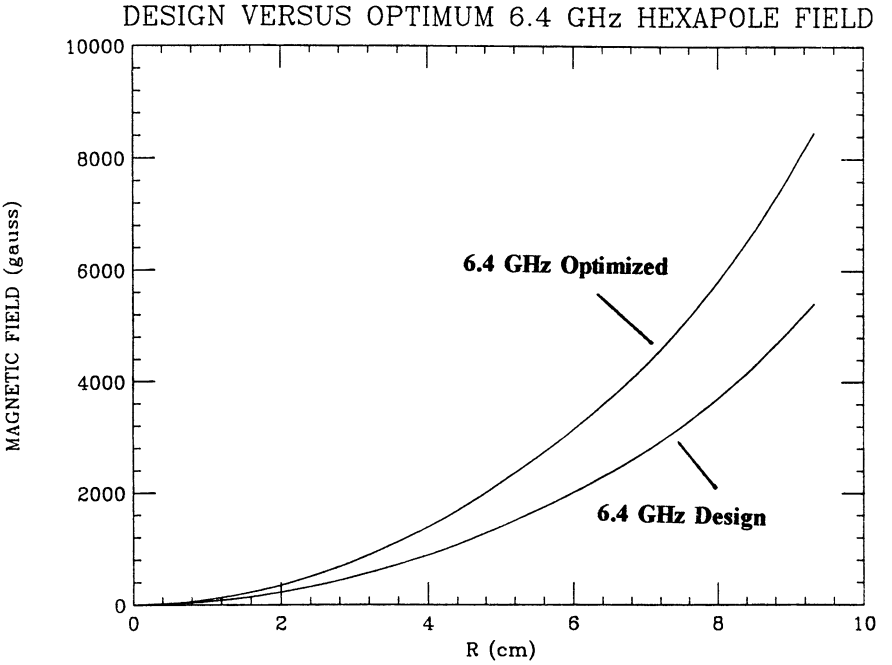

Figure 3: The 'Design and 'Optimized' radial magnetic fields are shown.

	6.4 GHz Design	6.4 GHz Optimized
Injection Mirror Ratio	3	7 2
Extraction Mirror Ratio	2	3 8
Wall Mirror Ratio	1 7	2 9
Mirror peak-to-peak Separation	0 52m	0 65m
Confined Plasma Volume	8L	10L

Table 1: A comparison of design vs. optimal magnetic field parameters of the SCECR for operation at 6.4 GHz

formance of the SCECR over that of the RTECR. Yet the SCECR is operating at the same frequency as the RTECR, but with higher peak fields, mirror ratios and a larger confined plasma volume.

3 The Classical Frequency Scaling Argument

Since field resonant microwave heating of electrons is the plasma drive in ECRIS, microwave transmission into the plasma is essential under all operating conditions. The propagation of electromagnetic waves in a conductive medium follows the dispersion relation:

$$k^2 = \mu\epsilon\frac{w^2}{c^2}(1 + \frac{4\pi i\sigma}{\omega\epsilon}) \tag{1}$$

For tenuous non-collisional plasmas ($g \approx 0$), the conductivity σ can be expressed as:

$$\sigma = \frac{in_e e^2}{m_e\omega} \tag{2}$$

where n_e is the plasma density. Assuming a non-dielectric, non-

magnetic plasma ($\epsilon \approx 1, \mu \approx 1$), then we have:

$$k^2 \simeq \frac{\omega^2}{c^2}(1 - \frac{\omega_p^2}{\omega^2}) \tag{3}$$

where we have defined the plasma frequency ω_p as:

$$\omega_{p^2} \equiv \frac{4\pi e^2}{m_e} n_e \tag{4}$$

one can see that when:

$$\omega > \omega_p \qquad \text{k is real–wave propagates} \tag{5}$$

$$\omega < \omega_p \qquad \text{k is imaginary–wave attenuates} \tag{6}$$

In ECR sources, we choose $\omega = \omega_{ecr}$, and then the limit on microwave propagation into an ECRIS would be $\omega_{ecr} > \omega_p$, which thru Eq.(4), sets a limit on the maximum plasma density:

$$n_{e,max} = \frac{m_e}{4\pi e^2} \omega_{ecr}^2 \tag{7}$$

Table 2 shows some calculated cutoff densities as a function of ECR frequency. As one can see from Table 2, a 30-fold increase in cutoff density is possible when going from 6.4 GHz to 35 GHz.

Why would one expect that raising the maximum allowed plasma density would be important for ion production in ECR sources? Consider the step-wise ionization of species X from charge state i+ to charge state (i+1)+; thru successive electron impact ionization:

$$X^{i+} + e \rightarrow 2e + X^{(i+1)+} \tag{8}$$

If $\sigma_{i,i+1}(E_e)$ is the cross-section for this reaction, and τ_c is the average ion confinement time in the plasma, one can show that for this step to occur, then:

$$n_e \tau_c \geq \sigma_{i,i+1}(E_e) v_e >_{v_e}^{-1} \tag{9}$$

That is, the product $n_e \tau_c$ must be greater than a characteristic rate for the atomic process driving the reaction. All other factors being

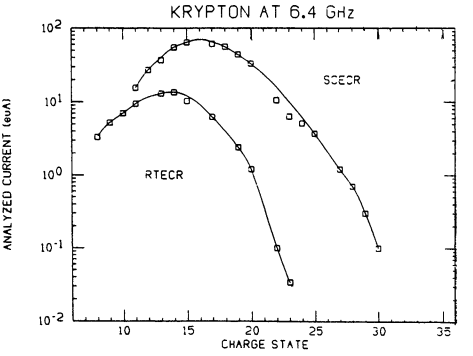

Figure 4: A comparison between the RTECR and SCECR for krypton ion production– both sources are operating at 6.4GHz.

ω_{ecr}	$n_{e,max}$
6 4 GHz	5 1 10^{11} cm^{-3}
14 GHz	2 4 10^{12} cm^{-3}
35 GHz	1 5 10^{13} cm^{-3}

Table 2: Maximum cutoff density for microwave transmission into an ECR plasma.

equal, raising the plasma density raises the maximum charge state that can be produced in an ECR plasma. Since the maximum plasma density $n_e \propto f^2$ by Eq.(6), it follows that raising the ECR frequency is an obvious way to scale up the performance of these ion sources.

4 Comparison with Higher Frequency Sources

In Tables 3-8, we compare the DC performance of several sources in the frequency range of 10-18 GHz with the High-B mode performance of the SCECR. (Limited published data on the dc performance of the 18 GHz minimafios make it impossible to include this source in comparisons for all species.) As can be seen, the SCECR results fit reasonably well into the performance interval of these other sources. That is, there is no evidence that they have substantially higher ion

O	SCECR	AECR/LBL	CAPRICE
4+	320	375	*
5+	410	442	*
6+	625	475	400
7+	120	131	47
8+	12	~13	3.0

Table 3: A comparison between the SCECR and higher frequency sources for the production of Oxygen ions.

Ne	SCECR	AECR/LBL	CAPRICE
4+	105	*	*
5+	155	*	*
6+	193	121	*
7+	155	90	*
8+	105	86	90
9+	11	7.5	7
10+	1.1	*	0.3

Table 4: A comparison between the SCECR and higher frequency sources for the production of Neon ions.

production rates or higher extracted currents, which would be the signature for the frequency scaling effect.

One issue that is often not addressed in comparing source performance is ion source brightness, and we try to address this in Table 8. The total extracted current should scale as:

$$I \propto V^{3/2} a^2 \tag{10}$$

where V is the source bias voltage and a is the diameter of the extraction aperature. (We assume that the extraction gap has been chosen to match the space charge.) Using $V = 10kV$ and $a = 8mm$, the standard extraction parameters of the SCECR, sources with higher voltage or larger extraction areas would be expected to have enhanced

Ar	SCECR	AECR/LBL	ECR4/GANIL	CAPRICE
6+	61	*	*	*
7+	150	*	*	*
8+	325	210	500	550
9+	200	231	300	270
10+	120	*	*	120
11+	100	141	80	60
12+	55	78	36	30
13+	20	34	13	12
14+	10	17	5	4
15+	*	*	*	1
16+	1.5	1.4	0.5	0.3

Table 5: A comparison between the SCECR and higher frequency sources for the production of Argon ions.

extracted current, and this is indicated by the enhancement factor, the last entry in Table 8. The RTECR, SCECR, ICIS and AECR all have the same extraction parameters, and so can be directly compared, while one would expect that the extracted current of the others is enhanced by the extraction parameters and should be scaled by 1/(enhancement). Compared this way, the SCECR and AECR have the highest performance of all ECRIS, but these two sources differ in frequency by a factor of 2.27, or in cut off density, by a factor of 5.

5 A Possible Correct Interpretation of ECRIS Performance

One can see from Figure 4 that the performance of the SCECR at 6.4 GHz greatly exceeds that of the RTECR. Yet both sources have the same plasma hardware and the same operating frequency. One can see also from Figs. 2 and 3 that the optimized magnetic field of the SCECR is much higher than the RTECR equivalent design field. In fact, peak operating fields of the SCECR are similar to

Kr	SCECR	AECR/LBL	ECR4/GANIL	CAPRICE
11+	15.5	*	*	*
12+	27	*	*	*
13+	37	*	115	*
14+	55	*	*	*
15+	64	44	90	*
17+	61	48	50	40
18+	56	45	*	30
19+	44	36	20	20
20+	33	23	8.5	15
21+	*	13	*	7
22+	10.5	10	*	4
23+	6.3	6.8	*	2
24+	5.1	~4	*	*
25+	3.7	2.2	*	*
26+	*	~1	*	*
27+	1.2	*	*	*
28+	0.7	0.25	*	*
29+	0.3	*	*	*
30+	0.1	*	*	*

Table 6: A comparison between the SCECR and higher frequency sources for the production of Krypton ions.

those of the high frequency sources, and this is a clue to why the SCECR performance is higher. The condition for a quiet plasma in a magnetic trap is:

$$\beta = P_{particle}/P_{magnetic} \ll 1 \tag{11}$$

where $P_{particle}$ is the pressure related to the momentum of the particles in the trap. Since it is true that, when comparing temperatures, $T_e \gg T_i, T_o$ in ECRIS plasmas, and the neutral density n_o must satisfy $n_o \ll n_i$ to produce highly charged ions, then the condition expressed in Eq.(11) can be reduced to a condition relating the electron

Xe	SCECR	AECR/LBL	ECR4/GANIL	CAPRICE
10+	1.8	*	*	*
11+	4	*	*	*
12+	4.5	*	*	*
13+	6.2	*	*	*
14+	8.9	*	*	*
15+	12	*	*	*
16+	*	*	*	*
17+	19.3	*	70	*
18+	27	20	*	*
19+	32	24.5	55	*
20+	41	27	41	42
21+	43	28.5	30	40
22+	45	29.5	30	33
23+	50.5	29.5	30	30
24+	*	30	*	25
25+	44	*	17	20
26+	32	*	14	18
27+	14.2	12	*	8.5
28+	7	6.8	*	4
29+	5	*	3	2
30+	1.4	~2.5	*	*
31+	*	1	*	*
34+	1.2	*	*	*
38+	0.6	*	*	*

Table 7: A comparison between the SCECR and higher frequency sources for the production of Xenon ions.

	RTECR	SCECR	SCECR	RIKEN [1]	CAPRICE [2]	JULICH [3]	GANIL [4]	AECR [5]	AECR	MINIMAFIOS [6]
	6.4 GHZ	6.4 GHZ	6.4 GHZ	10 GHZ	10 GHZ	14.4 GHZ	ECR4	14GHZ	14GHZ	18 GHZ
		low field	high field	biased disk	2 omega	supercon.	high field	no E-gun	E-gun	
O 6+	52	90	625	150	400	135	•	170	475	800
O 7+	12.2	25	120	60	47	50	•	51	131	180
O 8+	1	4	12	6	3	6	•	6	13	•
Ar 11+	12.1	13	100	100	60	30	80	44.5	141	140
Ar 12+	8.1	8	60	40	30	23	36	22.6	78	80
Ar 13+	3.8	5.2	20	15	12	13	13	9.8	34	45
Ar 14+	1.4	1.4	10	8	4	6.3	5	4	17	20
Ar 16+	0.1	0.1	1.5	1	0.3	0.8	0.5	0.28	1.4	1.4
Extr. Aper.	8 mm	8 mm	8mm	10mm	10mm	8mm	6mm	8mm	8mm	8mm
Extr. Volt.	10 KV	10 KV	10 KV	10 KV	20 KV	10 KV	15 KV	10 KV	10 KV	15 KV
Enhancement	1	1	1	1.25	3.53	1	1.38	1	1	1.84

[1] T. Nakagawa, et.al., Proc of the 11th Int. Workshop on Electron Cyclotron Resonance Ion Sources (ECRIS 11), Groningen, The Netherlands (1993) 208.

[2] G. Melin, et.al , Proc. of the 11th Int. Workshop on Electron Cyclotron Resonance Ion Sources (ECRIS 11), Groningen, The Netherlands (1993) 91.

[3] H. Beuscher, Proc. of the Int. Conf. on the Physics of Multiply Charged Ions and Int. Workshop on ECR Ion Sources, Grenoble, France, les editions de physique 50 (1989) 883.

[4] P Sortais, et.al., Proc. of the 10th Int. Workshop on ECR Ion Sources, Oak Ridge, Tennessee, CONF-9011136 (1991) 35.

[5] C.M. Lyneis, et.al., Proc of the 10th Int. Workshop on ECR Ion Sources, Oak Ridge, Tennessee, CONF-9011136 (1991) 47.

[6] C Barue, et.al., Proc. of the 4th Int. Conf on Ion Sources, Benshiem, Germany, CONF-910943 (1992) 2844

Table 8: Several sources are compared for high charge state oxygen and argon ions. An effort is made to estimate brightness: sources with a lower 'Enhancement Factor' have higher brightness.

temperature and plasma density to the magnetic pressure,

$$\sum N_e k T_e \ll B^2/2\mu o \tag{12}$$

for a stable, well confined, quiescent plasma. From Eq.(12), one can argue that the one must raise the magnetic field to raise the density. Since the first harmonic resonance is used to heat the electrons in an ECRIS, then raising the field would require raising the frequency if the minimum field is raised too high. Also, if it is possible to raise the magnetic confinement without raising the frequency, i.e. the SCECR High-B mode, then the same performance gain should be possible at low frequency.

6 Summary and Conclusions

Our preliminary conclusion is that the performance scaling of ECRIS with increasing frequency is an effect of the increase in magnetic confinement of the plasma. This permits higher n_e and T_e, both of which will result in higher source performance, but enhancing the ion production rate for highly charged ions. There is no evidence at present for the $n_e \propto f^2$ frequency scaling, as one of the highest performance sources, the SCECR, has a low operating frequency relative to other ECRIS. As was shown, the frequency scaling argument starts from the assumptions of a collisionless, non-magnetic plasma, and therefore may be inappropriate as a scaling argument for the type of plasma found in an ECRIS for highly charged ions.

On the other hand, the magnetic field required in the SCECR to obtain such high performance at 6.4 GHz is not so high that it would not be possible with conventional magnetic technology, using a suitable coil design, though it would have been difficult to achieve in any presently existing conventional ECRIS. Since the cost and difficulty of microwave generators increases dramatically with increasing frequency, this High-B mode operation represents an important new low frequency ECRIS concept, and we expect that some groups will attempt to extend these results to a conventional magnet based ECRIS. At the same time, it is clear that higher frequency operation

with a scaling of the High-B mode topology is likely to lead to further significant increases in performance. There are at present two efforts to further explore this regime. The next step in the SCECR program will be to extend these results to 14.5 GHz. To accomplish this, the field of the source must be raised substantially higher than the present operating level. Additionally, the serse ECRIS, under construction for INFN/LNS in Catania, Italy, which follows the SCECR design [10], will also be able to operate in this High-B mode.

References

[1] R. Geller, et.al., Workshop on the Sixth International ECR Ion Source, Berkeley, Californai (1985).

[2] H. Beuscher, Proc. of the Int. Conf. on the Physics of Multiply Charged Ions and Int. Workshop on ECR Ion Sources, Grenoble, France, les editions de physique 50 (1989).

[3] C.M. Lyneis, et.al., Proc. of the 10th Int. Workshop on ECR Ion Sources, Oak Ridge, Tennessee, CONF-9011136 (1991).

[4] P. Sortais, et.al., Proc. of the 10th Int. Workshop on ECR Ion Sources, Oak Ridge, Tennessee, CONF-9011136 (1991).

[5] C. Barue, et.al., Proc. of the 4th Int. Conf. on Ion Sources, Benshiem, Germany, CONF-910943 (1992).

[6] G. Melin, et.al., Proc. of the 11th Int. Workshop on Electron Cyclotron Resonance Ion Sources (ECRIS 11), Groningen, The Netherlands (1993).

[7] T. Taylor, Proc. of the 4th Int. Conf. on Ion Sources, Benshiem, Germany, CONF-910943 (1992).

[8] T.A. Antaya, Proc. of the Int. Conf. on the Physics of Multiply Charged Ions and Int. Workshop on ECR Ion Sources, Grenoble France, les editions de physique 50 (1989).

[9] T.A. Antaya, 7th Workshop on ECR Ion Sources, Jülich, Germany, Jül-Conf-57 (1986).

[10] S. Gammino and G. Ciavola, Proc. of the 4th Int. Conf. on Ion Sources, Benshiem, Germany, CONF-910943 (1992).

CERAMICS SINTERING USING MILLIMETER WAVE RADIATION

Yu.V.Bykov, A.G.Eremeev, V.E.Semenov
Institute of Applied Physics, Nizhny Novgorod, Russia

The last years are marked by a significant growth of interest to microwave processing of materials. It seems that using of microwave energy for practical application is well-defined and settled area of technology based on rather simple physical fundamentals. The volumetric character of microwave absorption in most non-metallic materials makes it possible to enhance greatly the heating rates in comparison with conventional processes based on surface heating and penetration of heat into the depth of specimen by fairly slow thermal conductivity. As a consequence, the microwave technological processes can, in principle, have such recognized advantages over their conventional counterparts as

- energy and time savings,
- improved quality of product,
- reduction in labor-content and operating floor and so on.

These features are common attributes of those industrial microwave technologies dealing with the heating of the microwave-sensitive materials up to not very high temperatures (drying, food processing, curing polymers and rubber and etc.).

The real reason for reanimation of interest in this field is connected with the attempts to develop new kinds of applications which are not restricted to heating of a large mass of material characterized by rather strong microwave absorption. Although this search is promoted partly by the same factors - energy and time savings - special attention is paid to processes that have potential for producing

materials with new properties and values not achieved by any other methods of processing.

Here we will consider the trends in microwave processing of materials taking as example one of its branches - namely the microwave ceramic sintering. The choice of this area of activity seems quite justified due to many factors - growing tendency to use ceramics in modern industry, especially large energy savings in implementation of high-temperature processes and the possibility to produce new ceramic materials with unique properties, being probably the main reason.

Let us outline in several words the process of ceramics sintering as it is. Usually the initial material for sintering is non-organic crystalline powder compacted to somewhat about 40-60 % of the theoretical density of material. The grain size in this powder is about one micrometer as a rule. When one bears in mind the ordinary sintering without application of the external pressure the main driving force for densification is the surface tension. At high temperatures the viscosity of material is low enough and relative motion and accommodation of grains is possible. At higher values of temperature the diffusion mass transport leads to practically complete exclusion of pores or emptiness out of the specimens. In essence, producing dense ceramic materials by high temperature sintering is the result of the compromise between the process of removing porosity by mass transport effects and the growth of grains due to recrystallization. Advanced structural ceramics are practically poreless material with grain size as small as possible and without any flaws. Such ceramics have the highest working parameters (strength, hardness, fracture toughness) allowing to use it in severe environment (high temperature, oxide or aggressive atmosphere). In this sense fine microstructure of ceramics signifies the overcoming to some extent main disadvantage of this materials - their high brittleness. The essential facts are the casual sequence of the sintering process, the resulting microstructure and the final properties which are functions of the microstructure. And microwave ceramic sintering is endowed with unique potential due to the possibility of the fast, controllable and inertia less heating which

yield the confined growth of grains.

Figure 1 represents the typical microstructures of microwave- and conventionally- sintered alumina. Comparison of this micrographs does not need comments. We only underline that the most severe flaws in a ceramics are large pores or pore agglomerates and abnormally large grains which are conspicuous in the microstructure of the conventionally sintered sample. In polycrystalline materials the resistance to fracture increases as the grain size diminishes because the grain boundaries hinder crack propagation. Table 1 shows the dependence of the mean grain size in alumina (the purity 99.7 %) upon the rate of microwave heating.

Table 1

Heating rate (deg. C/min)	50	100	200	300
Average grain size (μm)	2.15	1.9	1.3	0.85

Note that fast microwave sintering allows to obtain alumina with density $\sim$ 0.98 of the theoretical value and with mean grain size only slightly above the initial value (0.5 μm). As result of the finer microstructure the microwave sintered samples have improved mechanical properties compared to their conventional counterparts (See Table 2).

Table 2

Sintering process	Density, g/cm^3	Porosity, %	Micro-hardness, MPa	Fracture toughness, MPa$\cdot m^{1/2}$
M-wave T = 175 deg. C/min 1625° C * 15 min	3.9	1.0–1.5	22000	4.5
Conventional T = 40 deg. C/min 1625° C * 15 min	3.88	1.0–1.5	19000	3.3

What are those major specific features of microwave heating which are most essential for microwave processing of materials and in particular for ceramic sintering?

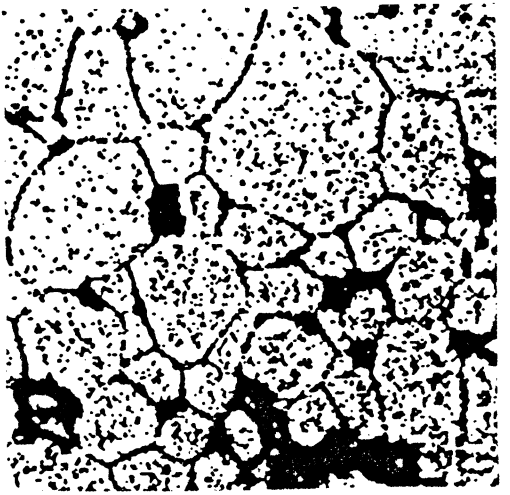

a) Heating rate
10° C/min
1620°C * 120min

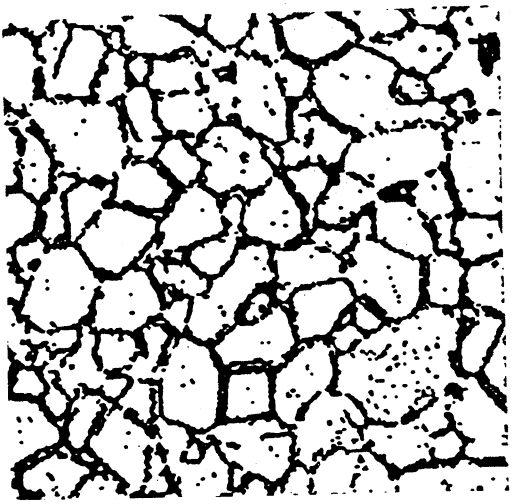

b) Heating rate
100° C/min
1550°C * 10min

Fig.1. Electron micrographs
of conventionally (a) and microwave (b) sintered alumina

1. The volumetric character of the microwave absorption is the principle one, of course. As a function of dielectric properties of processed materials and frequency of radiation, the distribution of the internal thermal sources could be formed in accordance with requirements of the peculiar kind of processing. In this sense transfer to centimeter and millimeter wave radiation from decimeter band traditionally used in the microwave technology means the possibility of considerable broadening of the variety of materials that could be subjected to efficient heating by microwaves. Specifically, for ceramic processing this will make possible the effective sintering of the most prospective ceramic materials based on pure oxides, nitrides - materials with very low values of microwave absorption.

2. Selectivity is another distinctive property of the microwave heating. The various constituents of composite materials have naturally the different ability to absorb microwave radiation. As result the microwave sensitive constituents may have larger temperature then the mean value within the sample. That kind of overheating is very essential for processes having restrictions on the upper allowable value of temperature and, in particular, for low-temperature processing of materials. It is known, for example that advanced polymer composites are those reinforced by conductive inclusions and fibers. The local overheating of the inclusions gives rise in number of chemical bonds between inclusions and the matrix and to enhanced adhesion. In microwave assisted chemistry this effect leads to the increase in the rates of the chemical reactions on the surfaces of catalysts and promotes the reduction of the resulting product decomposition. As for high-temperature microwave ceramics sintering and synthesis of new materials the selective heating would be of great importance due to the leading role played by mass transport processes on the surfaces and boundaries of the grains. Therefore the effect of selective microwave absorption must be taken into consideration when choosing the optimal composite's constituents for achieving the improved properties of materials. It is worth noting that mass transport processes reliable for densification of powder compacts and forming the intergrain linkages could depend not only on the non-uniform tem-

perature pattern but thermal elastic stresses also.

3. The other specific feature of heating with microwaves lies in exploiting such properties of electromagnetic field as coherency and polarization. These factors can be beneficially used when dealing with workpieces of materials with regular structure, for instance multilayer ceramic-metals composites. These materials are of primary concern for manufacturing of various kind of electron devices - multilayer capacitors, ceramic substrates for integrated circuits and so on. It is clear that a transfer to using radiation with shorter wave length allows to attain efficient processing of the regular structure composites with reduced space scale of regularity.

4. One of the most intriguing experimental results in microwave ceramics sintering is the decrease in temperature of sintering in comparison with values typical for correspondent conventional processes. For some ceramic materials this reduction in temperature can be as large as three hundred degrees [1]. And if the short time of microwave sintering can be more or less conceived in terms of eliminating the slow thermal conductive process then the decrease in temperature badly needs explanation.

There are several hypotheses pretending to give such an explanation. It seems the most of these attempts do not stand against the critics. Not discussing them in details we will note briefly only their failures.

* Grain boundaries overheating. In fact, what is necessary for sintering is to have rather soft or movable boundaries of grains. It is evident that microwave absorption within many powder substances, especially the low-absorptive ones, is localized predominantly within the near-surface layer of grains. This fact gave impetus to the idea on the influence of boundaries overheating on the process of sintering. But because of small size of the grains ($\sim 1\ \mu m$) the thermal conductivity would make the temperature distribution even within the grains and the temperature of their boundaries could not differ considerably from the mean temperature of the sample.

* Thermal stresses. As a consequence of volumetric heating and the surface cooling of the microwave heated samples the temperature

distribution within them would be of dome-like type. The corresponding thermal stresses could achieve rather high values and be even close to values of pressures typical for method of hot pressure sintering. However, at high temperatures the role of thermal stresses diminishes greatly because of fast relaxation of stresses in media of the enhanced viscosity and thermal stresses can not be considered as an additional driving force for densification.

* Non-thermal or non-equilibrium effects. This hypothesis assume that absorption of intensive coherent microwave radiation can significantly perturb the phonon spectrum within crystallites and the enhanced mass transport can be explained by the non-equilibrium distribution of the phonon energy [2]. It is necessary to say the scanty information on the relevant parameters allows to be arbitrary in the estimates of such an effects. In any case, although the perturbation of the phonon energy spectrum by microwaves could not be excluded at all, however due to the fast relaxation of phonon excitation the amount of thermal energy stored in the perturbed part of spectrum seems to be not large in comparison with the total absorbed energy to effect mass transport processes.

* Drift of charge vacancies. In their recent paper Rybakov and Semenov [3] proposed the mechanism allowing to take into account the influence of high frequency electromagnetic field on mass transport in polycrystalline materials. The theoretical consideration is relied on an assumption about the asymmetry in the penetration of the charged vacancies under applied electric field through the layer of charge occurring at the boundaries of grains - that is a kind of the diode effect. The main hindrance to be assured in the relevance of this mechanism to microwave sintering is the lack of the pertinent data on the parameters of materials at high temperatures. Note that at zero-frequency approximation this theory is able to explain the fact of pore deformation within monocrystalline samples in dc electric field [4].

It is necessary to stress that not nearly all researchers support the very idea of the existence of the specific microwave effects in sintering. The main arguments are connected with the absence of the pre-

cise knowledge of the temperature distribution within the microwave heated samples. Nevertheless, there is plenty of experimental results witnessing to the favor of the occurring rather conspicuous specificity of the microwave sintering.

As an example, the experiments on sintering $BaTiO_3$ - samples can be taken. Figure 2 presents the dependencies of the linear shrinkage of samples on their temperature for conventional (curve 1) and microwave (curve 2) processes of sintering respectively. The temperature was measured by the thermocouple positioned on the lower edge of the samples. The direct comparison of presented results is hampered by the fact that temperature distributions within the samples are not the same in these two cases. Specifically, temperature was uniform inside the sample heated conventionally, but there was a temperature drop $\Delta T \approx 100$ K between the center and surface of the sample heated by microwave radiation. However, the results of the conventional densification permit to determine the values of the apparent activation energy of sintering E_a and the diffusion coefficient D in the expression describing the densification. Having found these parameters, one is able to calculate the expected shrinkage of the microwave-heated sample assuming that the local densification is completely determined by the local temperature and the distribution of temperature along the height of the sample is parabolic. The temperature dependence of the shrinkage obtained in such a manner is depicted by curve 3. And comparison of the curves 2-3 shows that the densification at microwave heating occurs at temperatures less by 100 degrees than it could be expected according to the model of non-uniform conventional heating.

Microwave sintering at radiation frequencies widely disparate from each other could give additional information on the origin of the specific microwave effects. The results on the densification of Al_2O_3 - samples when heating at frequencies 30 and 83 GHz are represented on Fig.3. There is steady although rather small shift to lower temperatures within the region close to the temperature of sintering. But the lack of precise knowledge on the temperature distribution inside the samples does not allow to make any definite conclusion on the

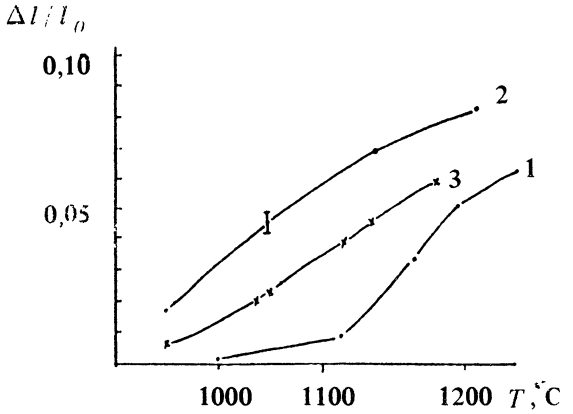

Fig.2. Linear shrinkage $\Delta l/l$ via temperature T for $BaTiO_3$ - samples. (1) - thermal heating, (2) - microwave heating at frequency 83 GHz , (3) - calculated curve

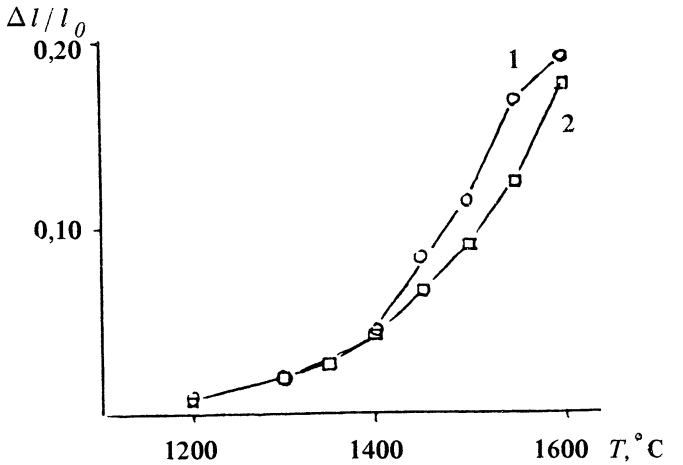

Fig.3. Linear shrinkage of alumina (99.3% Al_2O_3 + 0.5% MgO , heating rate $\dot{T} = 50$ deg. C/min) at two different frequencies f of microwave radiation: (1) - $f = 30$ GHz , (2) - $f = 83$ GHz

influence of the frequency of radiation on the result of sintering.

However, along with the beneficial features inherent to microwave sintering there are also negative moments regarded usually as challenges to this method [5]. In what way the passing to higher frequency of electro-magnetic fields could affect the problems specific to microwave sintering?

* sintering low-absorptive materials. We have discussed this issue above already and underline here only the technical aspect of it. Growth of an absorptivity with increasing frequency annuls the necessity to use such sophisticated methods as hybrid heating (that is heating with microwaves and thermal flows) or adding the microwave-sensitive substances to the matrix ceramic material. On the other hand the heating of materials at two rather distinctive frequencies (for instance 2.45 and 30 GHz) makes it possible not only to create the desirable distribution of temperature inside the sample but to control this distribution in the optimal manner during implementation of the process.

* sintering large size specimens is in the first turn the problem of an attainment of quasiuniform spatial distribution of the electromagnetic field within an applicator. It is more or less clear that rather uniform distribution can be achieved within a really oversized untuned cavity with the ratio of its dimensions to wavelength somewhat about 100 and in which several hundred modes can be excited simultaneously [6]. In practice, such microwave furnaces of reasonable size and fed by a power of moderate level become feasible with using centimeter and/or millimeter wave radiation only. The experience gained in the laboratories of USA, Germany, Japan and Russia proves that transfer to short wave radiation is the most straightforward way to solving this problem.

* thermal runaway is a typical thermal instability caused by a strong dependence of the microwave absorption on the temperature of material. This instability is a very serious hindrance especially in the case of fast microwave heating. Leaving aside the events when the runaway is derived from the non-uniform density of the initial material one can easily see those advantages provided by passing

to the higher frequencies. Due to a short wavelength the resulted interference pattern of the electric field within the sample placed inside the oversized cavity would be more shallow and of smaller space scale. As consequence, the threshold for thermal instability would increase because of the dispersing effect of the thermal conductivity.

* arcing and plasma ignition threshold can be also shifted to the higher processing temperatures. An increase of the microwave absorption with frequency allows to decrease the level of microwave power needed for the achievement of a designated value of temperature.

Thus, radiation of centimeter/millimeter wave range appears to be very promising for the high-temperature processing of materials inasmuch as it has potential to overcome the most serious problems obstructing the use of the longer wavelength radiation. Certainly, the solving of physical and technical issues is only the first step on the way to achieve the economically viable application of the shortwave radiation. Nevertheless, even at this point it is possible to indicate the most prospective areas of the further development and among them there are:

* sintering of large - sized and intricate - shaped specimens of advanced ceramic materials with thin microstructure,

* joining ceramic specimens of intricate shapes and joining ceramics with metals,

* sintering of nanocrystalline ceramic materials. This problem seems very intriguing since its solving can to some extent promise to defeat brittleness - the main disadvantage of ceramic materials.

References

1. Kimrey H.D., et al. Mat.Res.Soc. Symp.Proc. (Ed. W.B.Snyder,Jr. W.H.Sutton, M.F.Iskander, D.L.Johnson). Pittsburgh: 1990, **189**, 243.

2. Booske J.H., et al. Ceram.Trans., 1991, **27**, 185.

3. Rybakov K.I., Semenov V.E., Preprint 340, IAP, Nizhny Novgorod, 1993.

4. Geguzin J.E., Ovcharenko N.N., Dokl.Akad.Nauk SSSR, 1965, **163**, 621.
5. Sutton W.H., Mat.Res.Soc.Symp.Proc. (Ed. R.L.Beatty, W.H.Sutton, M.F.Iskander). Pittsburgh: 1992, **269**, 3.
6. Kimrey H.D., Janney M.A., Mat.Res.Soc.Symp.Proc. (Ed. W.H.Sutton M.H.Brooks, I.J.Chabinsky). Pittsburgh: 1988, **124**, 367.

CONTENTS OF VOLUME 1

Creation and heating of plasma by microwaves in fusion devices

Microwave discharge and its applications